Universidad de Santiago de Compostela
Facultad de Física
Departamento de Física Aplicada

Propiedades magneto-ópticas y plasmónicas entrelazadas en multicapas magnetoplasmónicas de metal y metal/dieléctrico (Intertwined magnetooptical and plasmonic properties in metal and metal/dielectric magnetoplasmonic multilayers).

Memoria de tesis presentada para optar al grado de Doctor en Física por:

Elías Ferreiro Vila

Tesis dirigida por:

Prof. Alfonso Cebollada Navarro
Dr. José Miguel García Martín

Tutor:

Prof. José Rivas Rey

Mayo 2012

Instituto de Microelectrónica de Madrid. Centro Nacional de Microelectrónica (IMM-CNM)
Consejo Superior de Investigaciones Científicas (CSIC)
Tres Cantos, Madrid

D. **Alfonso Cebollada Navarro** y D. **José Miguel García Martín**, Profesor de investigación y Científico Titular respectivamente del Consejo Superior de Investigaciones Científicas (CSIC), como directores y D. **José Rivas Rey**, CAT-EU del Área de Electromagnetismo del Dpto. de Física Aplicada de la Universidad de Santiago de Compostela, como tutor:

CERTIFICAN QUE:

Que el trabajo titulado: "Intertwined magnetooptical and plasmonic properties in metal and metal/dielectric magnetoplasmonic multilayers.", realizado por D. Elías Ferreiro Vila dentro del grupo de *Nanoestructuras magnéticas y magnetoplasmónica*, del Instituto de Microelectrónica de Madrid (IMM-CNM-CSIC) situado en Tres Cantos (Madrid), ha sido revisado y está en disposición de ser presentado para optar al grado de Doctor en Física.

Fdo.: Alfonso Cebollada Navarro

Co-director del trabajo

Fdo.: José Miguel García Martín

Co-director del trabajo

Fdo.: José Rivas Rey

Tutor del trabajo

Fdo.: Elías Ferreiro Vila

Estudiante de doctorado

Tres Cantos, 08 de Mayo 2012

La presente Tesis Doctoral ha sido llevada a cabo gracias a la financiación por parte del Consejo Superior de Investigaciones Científicas (CSIC) a través de una beca predoctoral perteneciente al programa de Junta de Ampliación de Estudios (JAE preDoc).

La presente Tesis Doctoral ha sido realizada en:

Instituto de Microelectrónica de Madrid (IMM-CNM-CSIC).

C/ Isaac Newton 8, PTM 28760 Tres Cantos (Madrid).

RESUMEN

1.- OBJETIVOS Y CONTEXTO DE ESTA TESIS

Esta tesis estudia la fenomenología asociada a multicapas magnetoplasmónicas (MP) metálicas y metal/dieléctrico, las cuales combinan metales nobles y metales ferromagnéticos, y exhiben efectos interrelacionados entre la excitación del Plasmón-Polaritón Superficial (SPPs) y su actividad magneto-óptica (MO). Además, en esta tesis, algunos de estos sistemas MP fabricados han sido seleccionados para emplearse como transductores en aplicaciones sensoras.

Las estructuras magnetoplasmónicas son importantes por varias razones. Por un lado, nos permiten alcanzar un conocimiento mayor de las resonancias de plasmón en nanoestructuras metálicas (elementos clave en disciplinas emergentes como la nanofotónica y la plasmónica), puesto que la actividad MO puede actuar como una sonda local del campo electromagnético asociado a una resonancia de plasmón. Desde el punto de vista de las aplicaciones, las estructuras magnetoplasmónicas también pueden ser utilizadas como dispositivos activos plasmónicos debido a la modulación del vector de onda del SPP aplicando un campo magnético externo; o también pueden ser utilizadas como transductores en una nueva clase de sensores, con sensibilidad mayor que los sensores plasmónicos convencionales, basados en el uso del aumento de la actividad MO debido a la excitación del SPP como señal transductora. Además, la modulación magnética de la señal detectada consigue aumentar la relación señal-ruido, la cual determina el límite de detección de un sensor.

Desde el punto de vista contextual, este trabajo de tesis supone la continuación natural de los estudios llevados a cabo en el grupo de investigación en el cual se ha llevado a cabo la misma, principalmente por el anterior miembro del grupo el Dr. J.B. González-Díaz, quién estudió esta fenomenología magnetoplasmónica para una variedad de sistemas: nanoestructuras homogéneas de metal noble o ferromagnético, nanoestructuras heterogéneas Au/Co/Au y multicapas heterogéneas Au/Co/Au donde las resonancias de plasmón superficial localizado (LSP) o de SPP y la actividad MO se encuentran relacionadas.

Por otro lado, las aplicaciones mencionadas para sensores de estas estructuras MP estudiadas en este trabajo de tesis, prosiguen los estudios sobre sensores magnetoópticos llevados a cabo por los Dres. B. Sepúlveda y D. Regatos, quienes trabajan actualmente en el NanoBiosensors and Bioanalytical Applications Group dirigido por la profesora L. Lechuga en el Centro de Investigación en Nanociencia y Nanotecnología (CIN2-CSIC) y anteriormente situado en el Instituto de Microelectrónica de Madrid (IMM). El desarrollo del primer sensor de resonancia de

plasmón superficial magneto-óptico (MOSPR) fue realizado por el Dr. B. Sepúlveda, mostrando un aumento de la sensibilidad de este sensor con respecto a la sensibilidad del sensor de resonancia de plasmón superficial (SPR). Muy recientemente, el Dr. D. Regatos ha continuado con estos estudios sobre el sensor MOSPR. Más concretamente, ha analizado y optimizado la estructura de las multicapas MP utilizadas como transductores para estos sensores con dos tipos de tricapas (Au/Fe/Au y Au/Co/Au), obteniéndose una sensibilidad mayor para este sensor MOSPR optimizado comparado con el primer sensor MOSPR diseñado por el Dr. Sepúlveda. Además, el Dr. Regatos ha detectado analitos de bajo peso molecular, por ejemplo la hibridación de cadenas de ácido desoxirribonucleico (ADN).

En particular para esta tesis, centraremos nuestra atención en las propiedades MP de heteroestructuras de capa continua, las cuales combinan metales nobles y ferromagnéticos. Los resultados principales de este trabajo incluyen: Una mejora de las propiedades MP gracias al control de las propiedades ópticas, rugosidad de las intercaras y cristalinidad de estas heteroestructuras. Se presenta también un novedoso sensor de gases funcionalizado con una película delgada porosa de TiO_2 usado para la detección de vapores de alcohol. Finalmente, se estudia un diseño innovador de cavidad metal-aislante-metal (MIM) MP, la cual ofrece nuevas posibilidades para la realización de moduladores magnéticamente controlados para SPPs, tomando como punto de partida el inspirador trabajo sobre el sistema complementario aislante-metal-aislante (IMI) realizado por el Dr. B. Sepúlveda.

Durante las últimas décadas, una gran cantidad de investigaciones se dedicaron a una nueva área de investigación, denominada Plasmónica. Las resonancias de plasmón superficial son ondas electromagnéticas acopladas a oscilaciones resonantes del plasma de los electrones localizados en las intercaras de un metal y un dieléctrico o en nanoestructuras metálicas, que dan lugar a un aumento del campo óptico cercano, y además pueden usarse para sobrepasar el límite de difracción de la luz en determinadas circunstancias. Gracias a estas propiedades, muchos estudios se han centrado en la posibilidad de implementar circuitos nanofotónicos y para desarrollar sensores químicos o biosensores que exploten estos fenómenos plasmónicos.

Avances prometedores e imprescindibles en el progreso de la Plasmónica están vinculados con el desarrollo de dispositivos plasmónicos activos, en otras palabras, la realización de combinaciones de materiales o configuraciones que permitan el control de las propiedades de los plasmones mediante un agente externo. Para este fin, además del uso de puntos cuánticos, materiales termo-ópticos y electro-ópticos, una opción interesante para ser utilizado como agente de control externo para los plasmones propagantes (SPP) es el campo magnético, el cual será usado en esta tesis.

Es conocida desde hace bastante tiempo la capacidad del campo magnético para variar las propiedades de los SPPs en los semiconductores InSb altamente dopados. Este efecto está gobernado por los elementos no diagonales del tensor dieléctrico (ε_{ij}) responsables de la actividad MO y cuyos valores están controlados por el mencionado

campo magnético, los cuales resultan ser relativamente altos en la presencia de campos magnéticos moderados para esta clase de semiconductores. Aun así, para metales nobles (como oro y plata), los normalmente empleados para estructuras plasmónicas (debido a su baja absorción óptica comparados con los demás metales en el visible), se necesitan campos magnéticos extremadamente altos (decenas de Tesla) para obtener elementos ε_{ij} con valores medibles, y por lo tanto con propiedades significantes para la modulación de los SPPs. Los metales ferromagnéticos, al contrario, poseen una gran actividad MO asociada con su imanación y podrían convertirse en elementos adecuados para la realización de estructuras plasmónicas activas. No obstante, los metales ferromagnéticos presentan una desventaja importante causada por su alta absorción óptica en el visible, la cual implica que las resonancias asociadas a estos plasmones se vuelven demasiado difusas y las pérdidas en la propagación de los plasmones pasan a ser demasiado altas. Una manera factible de reducir tal problema, sin perder la actividad MO, sería combinar metales nobles y ferromagnéticos, formando lo que se denomina un sistema magnetoplasmónico.

Cuando un material plasmónico está combinado con uno MO activo, las propiedades plasmónicas y MO del sistema MP resultante se entrelazan. Por ejemplo, Safarov et al. han mostrado que la actividad MO puede aumentarse cuando se excita la resonancia SPP en una tricapa Au/Co/Au. Estos estudios fueron extendidos más tarde en el grupo en el que se ha realizado esta tesis por el Dr. González-Díaz et al. variando el espesor de Co: se comprobó que el aumento observado de la actividad MO cuando se excita el SPP es debido a la acción combinada de la gran disminución de la reflectividad y a un aumento en la componente magnética de la actividad MO, lo que en conjunto provoca el aumento global en la respuesta MO. Además, se mostró también que el vector de onda del SPP en tricapas Au/Co/Au se puede modificar con un campo magnético externo debido a su dependencia con los elementos no diagonales del tensor dieléctrico, que son dependientes del campo magnético en estos sistemas. Incluso, el aumento de la actividad MO con la excitación del SPP ofrece la posibilidad de un nuevo sensor que usa multicapas MP. Sepúlveda et al. han desarrollado un novedoso sensor de resonancia de plasmón superficial magneto-óptico (MOSPR) que ofrece una sensibilidad más alta que el sensor de resonancia de plasmón superficial (SPR) convencional.

2.- RESULTADOS DE ESTA TESIS

Multicapas Ag/Co/Ag:

A pesar de que el Au es el material más común usado en la Plasmónica, la Ag está convirtiéndose en un material típico para la fabricación de estructuras plasmónicas en forma de nanohilos, resonadores ópticos, nanoparticulas, guías de onda, etc. El uso

de la Ag en vez del Au es principalmente llevado a cabo en experimentos donde el factor de calidad (factor Q) de la resonancia del plasmón es un parámetro clave, gracias a que la Ag exhibe resonancias de plasmón más intensas que el Au en la región visible debido a su más baja absorción óptica y más alta frecuencia de plasma. Por lo tanto, podemos esperar que la Ag proporcione rendimientos superiores para la magnetoplasmónica respecto al Au, ya que las resonancias más estrechas de la Ag otorgarán longitudes de propagación mayores de los SPPs excitados (interesante para dispositivos plasmónicos activos) y sensibilidades mayores con las variaciones del índice de refracción en el medio dieléctrico (interesante para aplicaciones en sensores) a los sistemas plasmónicos que usen este metal noble. Desafortunadamente, la Ag presenta un grave problema como es su deterioro químico en condiciones ambientales, lo cual obliga a la deposición de una capa extra de protección para estas multicapas MP basadas en Ag como material plasmónico.

En particular para esta tesis, se fabricaron y caracterizaron dos series de tricapas Ag/Co/Ag con diferentes tipos de capa de protección para prevenir las reacciones químicas de la Ag y el Co con la atmósfera. La capa de protección de 2 nm de Pt demostró un rendimiento pobre para mantener invariables las propiedades MP del sistema Ag/Co/Ag. Sin embargo, las multicapas Ag/Co/Ag con 5 nm de Au como capa de recubrimiento presentaron una resonancia intensa y estrecha de la actividad MO con la excitación del SPP (de hecho, exhibiendo un rendimiento mejor que las anteriormente mencionadas tricapas Au/Co/Au) y una modulación magnética significativa del vector de onda del SPP (similar a la modulación magnética mostrada por las tricapas Au/Co/Au). Además, estos sistemas con recubrimiento de Au mantienen las propiedades MP en condiciones ambientales para largos períodos de tiempo (confirmado hasta dos años). En contraste, las tricapas Ag/Co/Ag sin capa de protección sufren modificaciones importantes después de dos años expuestas a condiciones ambientales, perdiendo sus propiedades MP originales. Por lo tanto, se puede concluir que la capa de 5 nm de Au ha demostrado experimentalmente que mantiene las mejores propiedades ópticas y MO (respecto a la tricapa Au/Co/Au) para las resonancias de plasmón de la tricapa Ag/Co/Ag y además evita las reacciones químicas dentro de esta estructura en condiciones ambientales.

La importancia de la estructura y la rugosidad interfacial:

En esta tesis también se estudia el efecto clave de la cristalinidad (tamaño de grano o dispersión de electrones o fotones en las fronteras de grano) y la rugosidad superficial o interfacial sobre las propiedades magnéticas, ópticas, MO y principalmente MP de estas heteroestructuras en forma de multicapas. De hecho, existen muchos trabajos anteriores mostrando que las superficies muy planas, los tamaños de grano y el

crecimiento epitaxial tienen un papel importante en las constantes ópticas de las nanoestructuras plasmónicas. Por ejemplo, Kuttge et al. han analizado las diferencias entre las longitudes de propagación de SPPs excitados en películas de Au monocristalino y en dos películas de Au policristalinas con tamaños de grano diferente, observando longitudes de propagación mayores para la estructura monocristalina y, en el caso de la comparación entre las dos estructuras policristalinas, obteniéndose mayores longitudes de propagación del SPP para la estructura con tamaño de grano mayor.

Por otro lado, otros trabajos diferentes indican que las propiedades magnéticas y MO de las estructuras multicapa también pueden cambian por la morfología y la rugosidad interfacial de la capa ferromagnética dentro de una heteroestructura. Como ejemplo de este fenómeno, Clavero et al. han estudiado las diferencias de las constantes MO para películas de Co nanoparticulado, variando su morfología por medio de la temperatura durante la deposición del Co. La reducción del tiempo de relajación electrónico para nanopartículas de Co menores da lugar a una disminución de las constantes MO, de acuerdo al modelo óptico para metales de Drude debido a los efectos de confinamiento de estas nanopartículas dentro de una matriz dieléctrica. De hecho, se encontró un menor rendimiento MO respecto a lo esperado por la teoría para tricapas Au/Fe/Au policristalinas, utilizadas para aplicaciones biológicas como sensores MOSPR. Esto se debe probablemente a las peores propiedades MO del Fe en contacto con el Au. Todos estos hechos indican que si las características estructurales y morfológicas pueden determinar fuertemente las constantes MO de un sistema multicapa MP, es razonable pensar que por tanto la actividad MO y la modulación magnética del vector de onda del SPP, ambas dependientes de las constantes MO, serán también modificadas notablemente.

En esta tesis se ha realizado un estudio sistemático comparando las propiedades estructurales, morfológicas, magnéticas, ópticas, MO y MP de tricapas Au/Fe/Au epitaxiales y policristalinas en función del espesor de la capa intermedia de Fe. Encontramos un efecto directo de la cristalinidad y la calidad de interfaz de las estructuras epitaxiales en las constantes MO del Fe, que como consecuencia da lugar a un aumento del valor de la actividad MO sin la excitación del SPP (un factor x3) y otro aumento en la modulación magnética del vector de onda del SPP ($\Delta k/k$) (un factor x2) con respecto a los valores de las estructuras policristalinas equivalentes. Por otro lado, la actividad MO con la excitación del SPP depende principalmente de la obtención del espesor de capas exacto que produce óptimas excitaciones de plasmon, y como consecuencia un mínimo en la reflectividad y un máximo en la actividad MO. A partir de la longitud de propagación del SPP (L_{SPP}), se puede definir la figura de mérito $FoM \equiv (\Delta k \times L)_{SPP}$. La estructura epitaxial con espesor óptimo para la excitación del SPP presenta el doble rendimiento que la estructura óptima policristalina para esta figura de mérito. Finalmente, se presentan también los valores de la estructura Au/Ag/Co/Ag policristalina con espesor óptimo, para considerar la posibilidad de futuras estructuras Au/Ag/Co/Ag epitaxiales que ofrezcan mayor rendimiento.

Aplicaciones como sensores:

Como es bien sabido, la excitación de ondas SPP produce regiones donde los campos electromagnéticos (EM) son confinados e intensificados en la intercara de un metal y dieléctrico. Estas resonancias de plasmón son extremadamente sensibles a los cambios locales del índice de refracción que ocurre en dicha intercara, y este hecho proporciona una capacidad para la detección analítica de compuestos ubicados en la parte dieléctrica. Como resultado, esta técnica se extendió para la detección de biomoléculas que se inmovilizan en superficies de Au o Ag, así como para controlar interacciones entre biomoléculas de diferente naturaleza en el rango nanomolar a picomolar en tiempo real. Las aplicaciones de esta tecnología abarcan la biología, la seguridad alimentaria, los diagnósticos médicos y el control medioambiental.

Esta aplicación sensora de los SPPs se basa en las variaciones de las constantes ópticas efectivas en la superficie del transductor metálico debido a la interacción con el analito investigado, las cuáles pueden detectarse por el sensor como cambios en la curva de reflectividad cuando la excitación del SPP tiene lugar. Estas variaciones en la excitación del SPP también se trasladan a la actividad MO bajo la excitación del SPP. Por ejemplo, el aumento o resonancia de la actividad MO alrededor de la excitación del SPP exhibe un desplazamiento angular cuando varía el índice de refracción del dieléctrico de la intercara compartida con la multicapa MP. En un ángulo de incidencia fijo, este cambio angular se traduce en un cambio en la señal MO. Esta configuración de sensor basada en la medida del la actividad MO bajo la excitación del SPP es llamada Resonancia de Plasmón Superficial Magneto-Óptico (MOSPR), como se ha mencionado con anterioridad propuesto por primera vez por Sepulveda et al.

En esta tesis se ha mostrado cómo las diferentes multicapas MP desarrolladas a lo largo de la misma se han utilizado con éxito como transductores en configuraciones de sensor SPR y MOSPR para la detección de vapores de alcohol y la formación específica del complejo anticuerpo-proteína, en medio aéreo y acuoso respectivamente. Con respecto a los experimentos sobre detección de gases, una innovadora capa porosa de TiO_2 depositada a ángulo rasante (GLAD) se ha utilizado como capa sensora o captadora de las moléculas de alcohol, presentando un buen rendimiento para captar moléculas de metanol, etanol e isopropanol gracias a su gran porosidad (gran proporción de superficie frente a volumen). Además, el sensor MOSPR demuestra una sensibilidad mayor frente a los sensores SPR que utilizan tricapas Au/Co/Au o películas delgadas de Au (SPR "clásico") como capas transductoras para la detección de dichos vapores del alcohol.

Por otro lado, con respecto al experimento inmunológico, el protocolo usado para inmovilizar las biomoléculas sobre la capa superior de Au de los transductores MP se basa en el fuerte enlace que surge entre los átomos de Au de la capa MP y el grupo tiol (-SH) de las capas autoensambladas (SAMs) alcanotioladas. Se utilizó un transductor MP funcionalizado con una capa de proteína albúmina bovina (BSA) para el reconocimiento del analito: el anticuerpo complementario de esta proteína (antiBSA). A

concentraciones altas de analito, las respuestas de los sensores SPR y MOSPR presentaron el estado de saturación típico en un proceso de adsorción superficial (comportamiento de la isoterma de Langmuir). La sensibilidad de una multicapa Au/Ag/Co/Ag resultó menor que la de una tricapa Au/Co/Au como transductoras MOSPR debido a una oxidación parcial de las capas de Ag y Co en el medio líquido, como se dedujo a partir de la observación de una disminución general de señal MO en la curva angular. Además, la sensibilidad normalizada es mayor para el sensor MOSPR (tricapa de Au/Co/Au como transductora) comparada con la correspondiente para el sensor SPR "clásico" (película delgada de Au como transductor) en estos experimentos de detección de anticuerpos.

Multicapas MP metal/dieléctrico:

Las cavidades ópticas son potentes herramientas que permiten controlar la interacción de luz y materia y por tanto se han empleado en una gran variedad de investigaciones, desde dispositivos ópticos cuánticos a sensores ópticos ultrasensibles. Estas aplicaciones se basan en el confinamiento eficaz de la luz en un volumen de modo de la cavidad muy pequeño. Aunque la mayoría de las cavidades ópticas están basadas en estructuras de materiales dieléctricos, el confinamiento de la luz utilizando nanoestructuras metálicas se ha convertido recientemente en un tema de gran interés. En contraste con las cavidades dieléctricas, las cavidades plasmónicas pueden sobrepasar el límite de la difracción de la luz y en principio alcanzar volúmenes de modo por debajo de la longitud de onda.

Se puede conseguir un fuerte confinamiento de la luz en SPPs guiados en un dieléctrico nanométrico entre dos metales. Esta geometría metal-aislante-metal (MIM) sirve como una guía de onda plasmónica (PGW), por lo que la compresión de los campos del SPP en un núcleo dieléctrico podría ser una manera de resolver el problema para el acoplo de la luz a una guía de onda de dimensiones transversales nanométricas, tal como Gizburg et al. han propuesto. De hecho, Dionne et al. han realizado estudios experimentales sobre MIM-SPPs propagados en guías de onda con núcleos dieléctricos de dimensiones transversales nanométricas. Como resultado, la longitud de onda a lo largo de la dirección de propagación disminuye significativamente para estos MIM-SPPs y esto ofrece la posibilidad de crear nanocavidades con volúmenes de modo extremadamente pequeños, o dispositivos ópticos no lineales. Además, el coste de pérdidas adicionales que es inherente al aumento en confinamiento es relativamente bajo en comparación a otras geometrías para guiar SPPs.

Con respecto a las ventajas para aplicaciones en sensores, hay que recordar que estos MIM-SPPs se dividen en dos modos (simétrico y antisimétrico) con distribuciones diferentes del campo electromagnético, lo que permite discernir variaciones de índice de refracción ocurridas en la superficie objeto de estudio de las variaciones de índice de refracción globales (debidas a cambios de temperatura, fluídica,…). Slavík et al. han

estudiado un sensor SPR de modo simétrico/antisimétrico (S/A), proponiendo una estructura con una película delgada de Au entre el medio de detección y una película de Teflon como el otro dieléctrico, formando así un sistema aislante-metal-aislante (IMI) (el cuál exhibe las propiedades recíprocas del sistema MIM).

Se han diseñado, fabricado y caracterizado cavidades magnetoplasmónicas metal-aislante-metal (MP-MIM) para esta tesis. Se llevó a cabo un estudio sistemático comparando las propiedades morfológicas, magnéticas y magnetoplasmónicas de estas cavidades en función del espesor de SiO_2 y la posición de una o dos capas de Co para el sistema MIM. Se ha probado mediante experimentos y simulaciones la existencia de modulación magnética del vector de onda en estos sistemas MIM para sus dos modos plasmónicos: antisimétrico (AM) y simétrico (SM). Las diferencias en la relación de dispersión y en las propiedades de confinamiento del campo EM de ambos modos, producen un comportamiento drásticamente diferente para la modulación magnética del vector de onda en función del espesor de SiO_2: Un aumento dramático de la señal de modulación para el modo AM con núcleos dieléctricos muy pequeños, mientras esta señal de modulación permanece casi constante para el modo SM. De hecho, se ha medido una señal de modulación tres veces mayor para el modo AM con respecto a la del modo SM a espesores bajos de SiO_2 (180 nm). Además, nuestros resultados muestran que en cavidades MP-MIM perfectamente simétricas esta modulación se anula, pero cuando se introduce alguna asimetría en la estructura de la cavidad no es posible cancelar por completo esta modulación. Finalmente, los sistemas MIM con dos capas de Co fabricados exhiben diferentes campos de saturación para la imanación de cada capa ferromagnética. Esto provoca que las estructuras MP-MIM con dos capas de Co puedan presentar dos comportamientos para la señal de modulación: En un caso se obtiene una alta modulación para el modo AM, y por tanto similar a las estructuras con solo una capa de Co, aplicando campos magnéticos bajos (cuando solo saturamos magnéticamente una capa de Co). Por otro lado se tienen señales de modulación muy bajas para los dos modos aplicando campos magnéticos altos (con las dos capas ferromagnéticas saturadas). Todo esto podría tener aplicaciones prometedoras para el desarrollo de moduladores magnéticos de los SPPs con varios estados de modulación.

Index of Contents

Chapter I: Introduction

I.1.- MOTIVATION AND SCOPE OF THIS TESIS 6

I.2.- MAGNETOPLASMONICS 7

I.3.- ORGANIZATION OF THE THESIS 11

I.4.- REFERENCES 12

Chapter II: Experimental methods

II.1- INTRODUCTION 16

II.2.-FABRICATION TECHNIQUES 16

II.2.A-Sputtering deposition 16

II.2.B- E-beam evaporation 18

II.2.C-Fabrication systems 19

II.3.-STRUCTURAL CHARACTERIZATION 26

II.3.A-X-Ray diffraction (XRD) 26

II.3.B-Atomic Force Microscopy (AFM) 28

II.4.-OPTICAL CHARACTERIZATION 31

II.4.A.-Spectroscopic ellipsometry (SE) 31

II.5.-MAGNETIC, MAGNETOOPTICAL AND MAGNETOPLASMONIC CHARACTERIZATIONS 34

II.5.A.- The magnetoopical Kerr effect. 34

II.5.B- Polar Kerr loops and spectroscopy 37

II.5.C- The transverse Kerr loops system. 42

II.5.D- TMOKE measurements in Kretschmann configuration. 43

II.5.D (i) Magnetoplasmonic characterization (Madrid system) 47

II.5.D. (ii) Magnetoplasmonic sensing (Lecce system) 49

II.6.-REFERENCES..... 50

Chapter III: Ag/Co/Ag multilayers

III.1.- INTRODUCTION 54

III.2.- DETERIORATION OF THE MULTILAYERS IN AMBIENT CONDITIONS..... 56

III.2.A.- Surface morphology 56

III.2.B.- Magnetoplasmonic characterization 57

III.2.C.- X-Ray photoelectron spectroscopy (XPS) 59

III.3.- Pt CAPPING LAYER STRUCTURES 62

III.3.A.- Fabrication and morphology 62

III.3.B.-Magnetic characterization 63

III.3.C.-Magnetooptical characterization 63

III.3.D.-Magnetoplasmonic characterization 65

III.4.- Au CAPPING LAYER STRUCTURES..... 69

III.4.A- Motivation of the structures 69

III.4.B.- Morphology 70

III.4.C.- Magnetic characterization 71

III.4.D.- Optical and Magneto-Optical characterization..... 72

III.4.E.- Magnetoplasmonic characterization 74

III.4.E.(i)- Surface plasmon resonance effects on the MO activity 75

III.4.E.(ii)- Magnetic modulation of the SPP resonance 77

III.4.F.- Comparison of the different magnetoplasmonic multilayers studied..... 79

III.6.-CONCLUSIONS..... 80

III.7.-REFERENCES 81

Chapter IV: The role of the structure and interface roughness: A comparison between epitaxial and polycrystalline multilayers

IV.1- INTRODUCTION 87

IV.2- FABRICATION TECHNIQUES 88

IV.3.- STRUCTURE AND MORPHOLOGY 89

IV.4.- MAGNETIC CHARACTERIZATION 92

IV.5. OPTICAL CHARACTERIZATION 96

IV.6. MAGNETOOPTICAL CHARACTERIZATION 97

IV.7. MAGNETOPLASMONIC CHARACTERIZATION 100

IV.7.A.-Surface plasmon resonance effects on the MO activity 100

IV.7.B.- Magnetic modulation of the SPP resonance 103

IV.7.C.- Propagation length of the SPPs 105

IV.8.-CONCLUSIONS 107

IV.9.-REFERENCES 107

Chapter V: Sensing applications

V.1- INTRODUCTION 110

V.2.- GLAD TiO_2 FUNCTIONALIZED GAS SENSOR 111

V.2.A.-Preparation of magneto-optical transducing layers and TiO_2 sensing layer 113

V.2.B.-Morphological characterization 114

V.2.C.-Magnetoplasmonic characterization 115

V.2.E.-Gas sensing 119

V.3.- BIOSENSING 123

V.3.A.-Surface functionalization of the biosensor 123

V.3.B.-Biosensing experiment (antiBSA recognition) 124

V.3.C.-Comparison of different multilayers as transducers 128

V.4.. -CONCLUSIONS 130

V.5.. - REFERENCES 131

Chapter VI: MP-MIM cavities

VI.1.- INTRODUCTION 134

VI.2.- DESIGN OF STRUCTURES 135

VI.3.- EXPERIMENTAL AND THEORETICAL METHODS 141

VI.4.- PLASMONIC MIM CAVITY 141

VI.4.A. -Morphology and plasmonic characterization ($Ag/SiO_2/Ag$) 142

VI.5.- MAGNETOPLASMONIC MIM CAVITIES 144

VI.5.A.- Samples and multilayer optimization 144

VI.5.B.- Morphological characterization 146

VI.5.C.- Magnetic characterization 148

VI.5.D.- Magnetoplasmonic characterization 149

VI.5.D.(i)-Optical characterization of the modes 149

VI.5.D.(ii)- Magnetic modulation of the modes 152

VI.6.- CONCLUSIONS 158

VI.7.- REFERENCES 159

Conclusions and future perspectives 161

Appendix I 165

References 167

Appendix II 169

References 173

List of publications: 175

Chapter I:

Introduction

I.1.- MOTIVATION AND SCOPE OF THIS TESIS 6

I.2.- MAGNETOPLASMONICS 7

I.3.- ORGANIZATION OF THE THESIS 11

I.4.- REFERENCES 12

I.1.- MOTIVATION AND SCOPE OF THIS TESIS

This thesis studies the phenomenology associated to with metal and metal-dielectric *magnetoplasmonic (MP)* multilayers, which combine noble metals and ferromagnetic metals, exhibiting interrelated effects between the excitation of Surface Plasmon-Polaritons (SPPs) and their magnetooptical (MO) activity. Additionally, in these thesis, selected fabricated MP systems have been used as transducers in sensing applications.

Magnetoplasmonic structures are important for a number of reasons. On one hand, they allow achieving a better understanding of plasmon resonances of plasmonic nanostructures (key elements in emergent disciplines such as nanophotonics and plasmonics) since the MO activity can act as local probe of the electromagnetic field associated to a plasmon resonance[1]. From the viewpoint of applications, magnetoplasmonic structures can also be used as active plasmonic devices due to the modulation of the SPP wavevector via an external magnetic field[2]; or as new kind of sensors, with higher sensitivity than conventional plasmonic ones, based in the use of an enhanced MO activity due to the SPP excitation as transduction signal[3]. Additionally, the magnetic modulation of the detected signal facilitates increasing the signal-to-noise ratio, which determines the limit of detection of a sensor.

From the contextual point of view, this thesis work supposes the natural continuation of the studies carried out at the host research group, mainly by the former member Dr. J.B. González-Díaz, who studied this MP phenomenology for a variety of systems: pure ferromagnetic and pure noble metal nanostructures, Au/Co/Au nanostructures and Au/Co/Au multilayers where localized Surface Plasmon (LSP) or SPP resonances and the MO activity can be interrelated[4].

On the other hand, the sensing applications of these MP structures studied in this thesis work pursue the sensing studies carried out by Dr. B. Sepúlveda and D. Regatos, who work now at the NanoBiosensors and Bioanalytical Applications Group directed by Prof. L. Lechuga at CIN2-CSIC and was previously located at IMM. The first development of the MagnetoOptical Surface Plasmon Resonance (MOSPR) sensor was elaborated by B. Sepúlveda, proving an enhancement for the sensitivity for this sensor with respect to the sensitivity of the Surface Plasmon Resonance (SPR) sensor[5]. Very recently, D. Regatos has analyzed and optimized the layer structure of the MP multilayers used as sensor transducers for both Au/Fe/Au and Au/Co/Au trilayers, obtaining a higher sensitivity than that obtained in the pioneer experiments performed by Dr. Sepúlveda. Besides, D. Regatos has detected analytes of low molecular weight as it is the hybridization of Deoxyribonucleic acid (DNA) chains[6].

In particular for this thesis, we will focus our attention on the MP properties of continuous layered heterostructures that combine noble and ferromagnetic metals. The

main outcome of this work include: An improvement of the MP properties achieved by the control of the optical properties, interface roughness and crystallinity of these heterostructures. A novel gas sensor functionalized with a porous TiO_2 thin film is also presented for the detection of alcohol vapours. Finally, an innovative MP metal-insulator-metal (MIM) cavity is studied in the last chapter offering new possibilities for the implementation of magnetic driven modulators of SPPs, taking as an origin point the inspiring work about the complementary MP-IMI system by B. Sepúlveda[7].

I.2.- MAGNETOPLASMONICS

During the last decades, a large amount of investigations have been performed in a new area of research known as Plasmonics[8,9,10]. Surface Plasmon resonances are electromagnetic waves coupled to resonant oscillations of the electron plasma located at metal–dielectric interfaces[11] or in metallic nanostructures, giving rise to an enhanced optical near field, which may allow in specific circumstances overcoming the diffraction limit of light[12]. Many studies have been focused on the possible implementation of nanophotonic circuits[13,14,15] and the development of chemical sensors and biosensors[16,17,18] exploiting plasmonic phenomena.

Further advances in the progress of plasmonics are associated with the development of active plasmonic devices, that is, the realization of materials combinations or configurations that allow the control of the properties of plasmons by an external agent. For that purpose, and in addition to the use of quantum dots[19], thermo-optic[20] and electro-optic[21,22] materials, an interesting option for being used as SPP external control agent is the magnetic field.

The magnetic field ability to affect the properties of SPPs in highly doped InSb semiconductors has been known for a long time[23,24]. This effect is governed by the non-diagonal elements of the dielectric tensor, ε_{ij}, responsible for the MO activity and whose value is controlled by the magnetic field, which in this kind of semiconductors turns out to be relatively high under the presence of moderate magnetic fields. However, for noble metals (such as gold and silver), the ones usually employed in plasmonics due to their lowest optical absorption, extremely high magnetic fields (tens of Tesla) would be needed to obtain ε_{ij} elements with a sizeable value, and therefore enough SPP modulation properties[25]. On the contrary, ferromagnetic metals possess large MO activity associated with their magnetization and could be suitable elements for active plasmonics. Nevertheless, ferromagnetic metals present an important drawback in their high absorption, which implies that the associated plasmon resonances are too broad and the propagation losses happen to be too high. A feasible way to reduce such damping without losing MO activity is to combine noble and ferromagnetic metals, forming what is known as magnetoplasmonic systems.

When a plasmonic material is combined with a MO active one, both the plasmonic and the MO properties of the resulting magnetoplasmonic system become interrelated. For example, Safarov et al. have reported that the MO activity can be enhanced when the SPP resonance is excited in the Au/Co/Au system[26]. Later, Herman et al. have explained this enhancement of the MO activity (Figure I.1. (a)) due to the fact that the electromagnetic field of the light is highly enhanced at the MO active layer (Co in this case) when the SPP is excited[27](Figure I.1. (b)). These studies were later extended in our group by J. B. González-Díaz et al. varying the Co thickness: the observed increase of the MO activity when the SPP was excited was shown to be due to the combined action of the intense decrease of the reflectivity and to an enhancement in the magnetic component of the MO activity, which altogether are responsible of the enhanced global MO response in Au/Co/Au trilayers (see Figure I.2.[(a)-(f)]). Moreover, it was also shown that the SPP wavevector, in Au/Co/Au trilayers could be modified by an external magnetic field due to its dependence with the off-diagonal elements of the dielectric tensor, which in turn are magnetic field dependent in these systems (this leads to a magnetic modulation of the incidence angle for the SPP excitation called $\Delta\theta$ and shown in figure I.3.(g))[28,29,2].

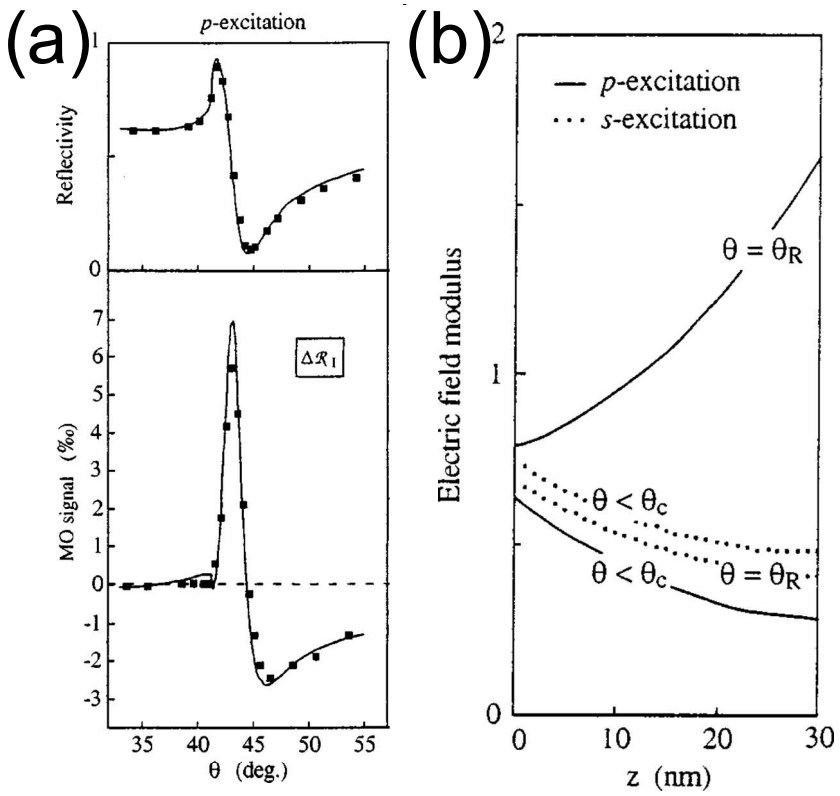

Figure I.1.(a) Variation with the incidence angle θ of the reflectivity (top panel of the figure) and of the intensity for the MO response (ΔR_I), in the transversal configuration (bottom panel of the figure). The symbols correspond to the measurements, the lines represent the theoretical fits. (b) Variation with the distance z to the prism/metal interface of the light electric field modulus inside of the noble metal layer for unit s and p excitations and for two values of the incidence angle: one lower than θ_C , the other θ_R corresponding to the resonant excitation of the SPPs. Figure extracted from Ref.[27].

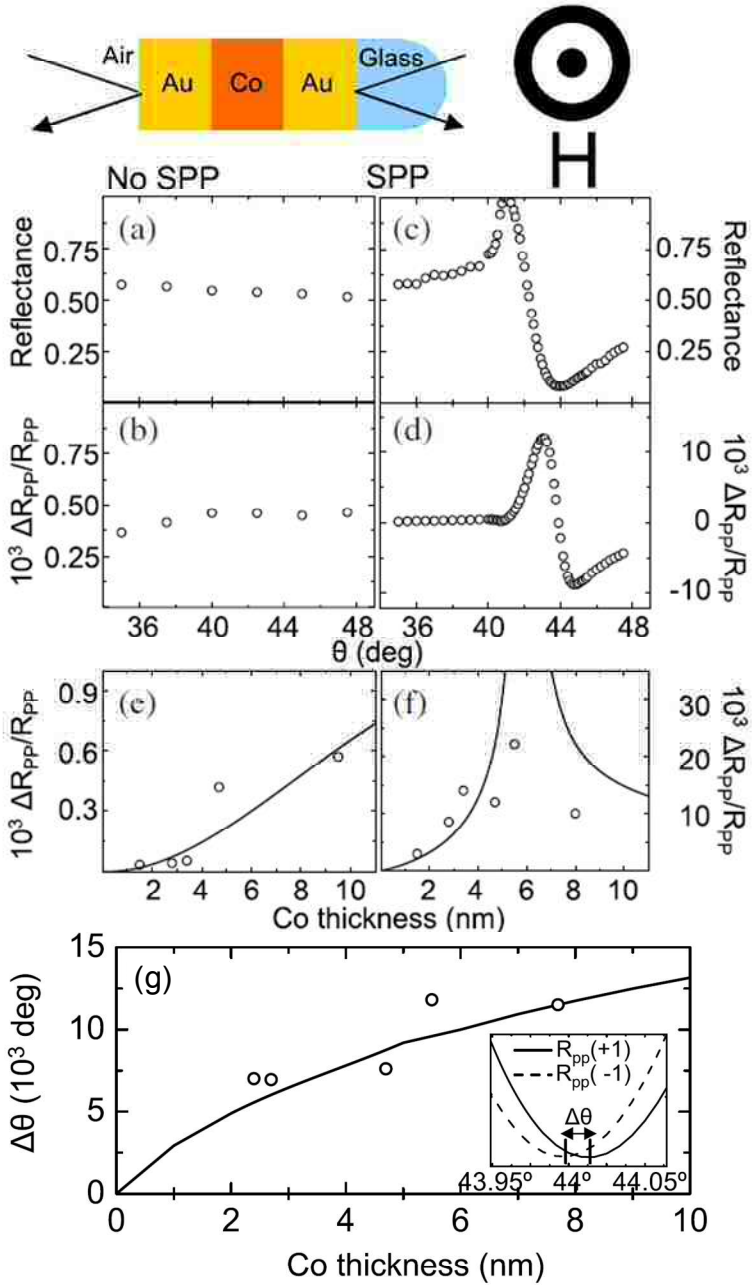

Figure I.2. Top: schematic view of the sample configuration. If the light is incident from the left, no SPP excitation occurs; if light is incident from the right the prism allows SPP excitation (Kretschman configuration). [(a–d)] Experimental behavior of the reflectivity R_{pp} and transverse Kerr signal $\Delta R_{pp}/R_{pp}$ as a function of the incidence angle for the 4.7 nm Co trilayer sample. No surface plasmon modes are excited in the left hand panels, whereas the right hand panels show the corresponding data with SPP excitation; (e) and (f) correspond to experimental (dots) and theoretical values (solid line), of the transverse Kerr signal intensity as a function of the Co layer thickness, without (e) and with (f) SPP excitation. (g) Angular shift of the minimum in reflectivity as a function of Co thickness. The circles correspond to the experimental values of Δθ. The line is a theoretical calculation. The inset shows the angular shift observed in the 6 nm thick Co sample. Extracted from ref. [28].

Besides, this magnetic modulation scales with the thickness of the ferromagnetic layer and enhances with the addition of a dielectric overlayer[30]. Thus, different magnetoplasmonic structures open interesting possibilities for the elaboration of active

devices in plasmonics and potentially at high speed, as the magnetism dynamics is very fast[31]. In fact, a great deal of intertwined plasmonic and magnetooptical (MO) phenomena have been studied in a variety of magnetoplasmonic structures within the last years[1,32,33,34,35,36,37,38,39].

Moreover, the enhancement of the MO activity with the SPP excitation offers the possibility of a new sensor using the MO activity from a magnetoplasmonic multilayer. Sepúlveda et al. have developed this new MagnetoOptical Surface Plasmon Resonance (MOSPR) sensor using a Au/Cr/Co/Cr multilayer as transducer and obtaining a sensitivity higher than in conventional Surface Plasmon Resonance (SPR) sensors for the detection of a protein (see Fig. I.3.)[3]. Later, Regatos et al. have also reported a higher sensitivity of the MOSPR sensor compared to the SPR one using both Au/Fe/Au[40] and Au/Co/Au[41] trilayers for variations of the bulk refractive index and the detection of DNA chains hybridization, respectively.

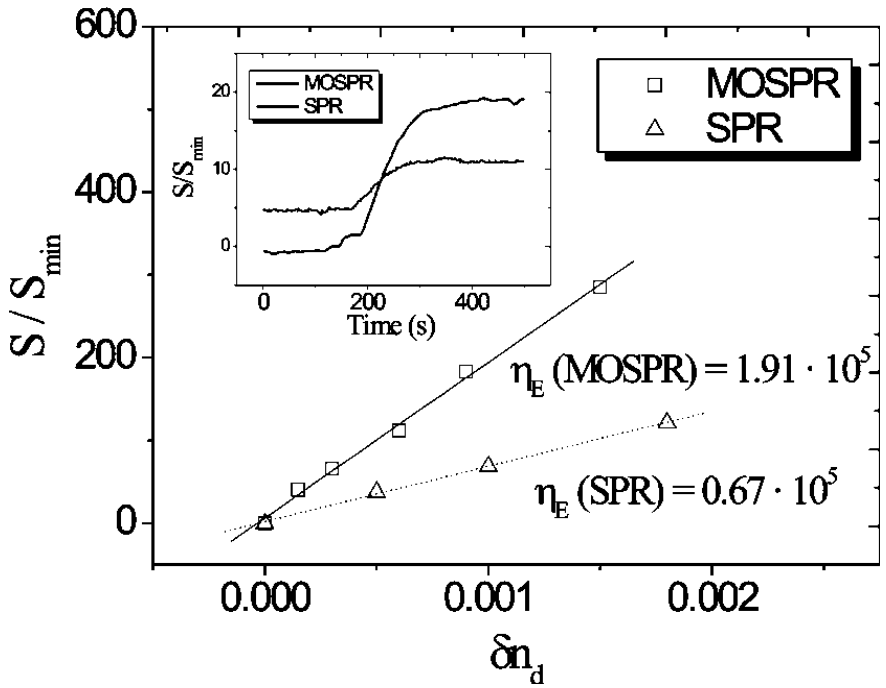

Figure I.3. Comparison of the experimental normalized signals of the MOSPR and the SPR sensors that are due to refractive-index changes, and evaluation of their experimental sensitivities. Inset, Normalized signal of the detection of the physical adsorption of bovine serum albumin proteins. Figure extracted from ref. [3].

I.3.- ORGANIZATION OF THE THESIS

The thesis is divided in six chapters:

Chapter I: Where the aim of this thesis work and an introduction to the history of magnetoplasmonics are presented.

Chapter II: A high number of experimental techniques are necessaries for the fabrication, complete (structural, morphological, optical, magnetooptical and magnetoplasmonic) characterization and sensing applications of the magnetoplasmonic multilayers. This chapter describes the techniques used during this thesis work and the physics involved.

Chapter III: The use of Ag instead of Au as plasmonic material to improve the performance of the magnetoplasmonic multilayers is studied in this chapter. Due to the chemical deterioration of Ag in room atmosphere, two types of capping layers (Pt and Au) have been used to protect the studied Ag/Co/Ag trilayers. Two series of these trilayers have been fabricated and characterized. We will conclude that the Au capped Ag/Co/Ag trilayers exhibit the best results, with even better performance than Au/Co/Au trilayers previously studied.

Chapter IV: Another issue to study is the importance of the crystallinity and interface roughness on the optical and magnetooptical properties of these magnetoplasmonic multilayers. Epitaxial and polycrystalline Au/Fe/Au series of samples have been fabricated and characterized in this chapter. The epitaxial Fe layer exhibits higher magnetooptical constants than the polycrystalline ones, which leads to higher magnetic modulation of the SPP wavevector.

Chapter V: These magnetoplasmonic multilayers can be used as optical (SPR sensor) or magnetooptical (MOSPR sensor) transducers in sensors. In this chapter, SPR and MOSPR sensors have been compared for gas and biosensing applications: alcohol vapour detection using a porous TiO_2 film as sensing layer and the specific recognition of the antibody by their complementary protein that actuates as the sensing layer. Finally, the higher sensitivity of the MOSPR configuration compared to the SPR one will be confirmed for this two sensing experiments.

Chapter VI: A novel metal-insulator-metal (MIM) magnetoplasmonic multilayers will be proposed, designed and developed for the implementation of magnetically driven active plasmonic devices. These structures divide the SPP resonance in two optical modes, which exhibit different electromagnetic field distribution and therefore different magnetic modulation. $Ag/SiO_2/Ag$ multilayers have

been grown with different SiO_2 layer thickness and positioning a thin Co layer near either the Ag/SiO_2 or the SiO_2/Ag interfaces (Co down and Co up series), as well as on both sides (Co double series). The asymmetric and symmetric structures show high and low modulation values respectively. This opposite behaviour is explained by the nonrecipocity effects for the two SPP excited at the two metal/insulator interfaces for each structure.

Finally, the most important results achieved from each part of the thesis are summarized in the conclusions section. Addittionally, the thesis is complemented with two appendices detailing some technical aspects used all along this work.

I.4.- REFERENCES

[1] Meneses-Rodríguez, D., Ferreiro-Vila, E., Prieto, P., Anguita, J., González, M. U., García-Martín, J. M., Cebollada, A., et al. (2011). Probing the electromagnetic field distribution within a metallic nanodisk. *Small*, *7*(23), 3317-23.

[2] V. V. Temnov et al., Nat. Photonics **4,** 107-111 (2010).

[3]Sepúlveda, B., Calle, A., Lechuga, L. M., & Armelles, G. (2006). Highly sensitive detection of biomolecules with the magneto-optic surface-plasmon-resonance sensor. *Optics letters*, *31*(8), 1085-1087.

[4] PhD thesis: "**Magnetoplasmonics.MagnetoOptics in Plasmonics Systems",** Juán B. González Díaz, Universidad Autónoma de Madrid (2010).

[5] PhD thesis: "**Efectos Magneto-Ópticos en dispositivos biosensores de campo evanescente",** Borja Sepúlveda, Universidad Complutense de Madrid (2005).

[6] PhD thesis: "**Biosensores ópticos de alta sensibilidad basados en técnicas de modulación plasmónica",** David Regatos, Universidade de Santiago de Compostela (2012).

[7] Sepulveda, B., Lechuga, L. M., & Armelles, G. (2006). Magnetooptic effects in surface-plasmon-polaritons slab waveguides. *Journal of Lightwave Technology*, *24*(2), 945-955.

[8] Maier S. A., Plasmonics: Fundamentals and Applications (Springer, Berlin, 2007).

[9] Raether H., *Surface Plasmons on Smooth and Rough Surfaces and on Gratings*, vol. 111 of *Springer Tracts in Modern Physics* (Springer-Verlag, Berlin, 1988).

[10]Barnes, W. L., Dereux, A., & Ebbesen, T. W. (2003). Surface Plasmon subwavelength optics. *Nature*, *424*(August), 824-830.

[11]Sambles, J., Bradbery, G., & Yang, F. (1991). Optical excitation of surface plasmons: an introduction. *Contemporary physics*, **32**(3), 173–183.

[12]Ebbesen, T. W., Lezec H. J., Ghaemi H. F., Thio T. & Wolff P. A.(1998). Extraordinary optical transmission through sub-wavelength hole arrays. *Nature*, *391*, 667.

[13] S. I. Bozhevolnyi, V. S. Volkov, E. Devaux, J. Y. Laluet and T. W. Ebbesen, Nature **440**, 508-511 (2006).

[14] B. Steinberger, A. Hohenau, H. Ditlbacher, A. L. Stepanov, A. Drezet, F. R. Aussenegg, A. Leitner and J. R. Krenn, Appl. Phys. Lett. **88**, 094104 (2006).

[15] J.-C. Weeber, Y. Lacroute and A. Dereux, Phys. Rev. B **68**, 115401 (2003).

[16] Homola, J. (2008). Surface plasmon resonance sensors for detection of chemical and biological species. *Chemical reviews*, *108*(2), 462-493.

[17] Anker, J., Hall, W., Lyandres, O., & Shah, N. (2008). Biosensing with plasmonic nanosensors. *Nature materials*, *7*(June), 8-10.

[18] Treviño, J., Calle, a, Rodríguez-Frade, J. M., Mellado, M., & Lechuga, L. M. (2009). Determination of human growth hormone in human serum samples by surface plasmon resonance immunoassay. *Talanta*, *78*(3), 1011-6.

[19] D. Pacifici, H. J. Lezec and H. A. Atwater, Nature Photonics **1**, 402-406 (2007).
[20] T. Nikolajsen, K. Leosson and S. I. Bozhevolnyi, Appl. Phys. Lett. **85**, 5833 (2004).
[21] M. J. Dicken et al., Nano Lett. **8**(11), 4048-4052 (2008).
[22] J. A. Dionne, K. Diest, L. A. Sweatlock and H. A.Atwater, Nano lett., 9(2) (2009).

[23] Brion, J., Wallis, R., Hartstein, A., & Burstein, E. (1972). Theory of surface magnetoplasmons in semiconductors. *Physical Review Letters*, *28*(22), 1455–1458.

[24] Wallis, R., Brion, J., & Burstein, E. (1974). Theory of surface polaritons in anisotropic dielectric media with application to surface magnetoplasmons in semiconductors. *Physical Review B*, *9*(8), 3424-3437.

[25] Sepúlveda, B., González-Díaz, J. B., García-Martín, A., Lechuga, L. M., & Armelles, G. (2010). Plasmon-Induced Magneto-Optical Activity in Nanosized Gold Disks. *Physical Review Letters*, *104*(14), 1-4.

[26] V.I. Safarov, V. A. Kosobukin, C. Hermann, G. Lampel, J. Peretti and C. Marlière, Phys. Rev. Lett. **73**, 3584-3587 (1994).
[27] C. Hermann, V. A. Kosobukin, G. Lampel, J. Peretti, V.I. Safarov and P. Bertrand, Phys. Rev. B **64**, 235422 (2001).
[28] J. B. González-Díaz, A. García-Martín, G. Armelles, J. M. García-Martín, C. Clavero, A. Cebollada, R. A. Lukaszew, J. R. Skuza, D. P. Kumah and R. Clarke, Phys. Rev. B **76**, 153402 (2007).
[29] E. Ferreiro-Vila et al., Phys. Rev. B **80**(12), 125132 (2009).
[30] D. Martín-Becerra,J. B. González-Díaz, V. V. Temnov, A. Cebollada, G. Armelles, T. Thomay, A. Leitenstorfer, R. Bratschitsch, A. García-Martín and M. U. González, Appl. Phys. Lett. **97,** 183114 (2010).

[31] Temnov, V. V., Nelson, K., Armelles, G., Cebollada, A., Thomay, T., Leitenstorfer, A., & Bratschitsch, R. (2009). Femtosecond surface plasmon interferometry. *Optics express*, *17*(10), 8423-32.

[32] González-Díaz, J. B., García-Martín, A., García-Martín, J. M., Cebollada, A., Armelles, G., Sepúlveda, B., Alaverdyan, Y., et al. (2008). Plasmonic Au/Co/Au nanosandwiches with enhanced magneto-optical activity. *Small (Weinheim an der Bergstrasse, Germany)*, *4*(2), 202-5.

[33] Bonod, N., Reinisch, R., Popov, E., & Nevière, M. (2004). Optimization of surface-plasmon-enhanced magneto-optical effects. *Journal of the Optical Society of America B*, *21*(4), 791.

[34] G. Armelles, J. B. González-Díaz, A. García-Martín, J.M. García-Martín, A. Cebollada, M. U. González, S. Acimovic, J. Cesario, R. Quidant and G. Badenes, Optics Express **16**, 16104-6112 (2008).

[35] Papaioannou, E. T., Kapaklis, V., Giersig, M., Fumagalli, P., Garcia-Martin, a., Ferreiro-Vila, E., & Ctistis, G. (2010). Magneto-optic enhancement and magnetic properties in Fe antidot films with hexagonal symmetry. *Physical Review B*, *81*(5), 1-12.

[36] Sepúlveda, B., González-Díaz, J. B., García-Martín, a., Lechuga, L. M., & Armelles, G. (2010). Plasmon-Induced Magneto-Optical Activity in Nanosized Gold Disks. *Physical Review Letters*, *104*(14), 1-4.

[37] C. Clavero et al., Opt. Express **18**(8), 7743-7752 (2010).
[38] C. Clavero et al., Opt. Lett. **35**(10), 1557-1559 (2010).

[39] Belotelov, V. I., Akimov, I. a, Pohl, M., Kotov, V. a, Kasture, S., Vengurlekar, a S., Gopal, A. V., et al. (2011). Enhanced magneto-optical effects in magnetoplasmonic crystals. *Nature nanotechnology*, *6*(6), 370-6.

[40] Regatos, D., Fariña, D., Calle, a., Cebollada, a., Sepúlveda, B., Armelles, G., & Lechuga, L. M. (2010). Au/Fe/Au multilayer transducers for magneto-optic surface plasmon resonance sensing. *Journal of Applied Physics*, *108*(5), 054502.

[41] Regatos, D., Sepúlveda, B., Fariña, D., Carrascosa, L. G., & Lechuga, L. M. (2011). Suitable combination of noble / ferromagnetic metal multilayers for enhanced magneto- plasmonic biosensing. *Optics Express*, *19*(9), 8336-8346.

Chapter II: Experimental methods

II.1- INTRODUCTION 16

II.2.-FABRICATION TECHNIQUES 16

II.2.A-Sputtering deposition 16

II.2.B- E-beam evaporation 18

II.2.C-Fabrication systems 19

II.3.-STRUCTURAL CHARACTERIZATION 26

II.3.A-X-Ray diffraction (XRD) 26

II.3.B-Atomic Force Microscopy (AFM) 28

II.4.-OPTICAL CHARACTERIZATION 31

II.4.A.-Spectroscopic ellipsometry (SE) 31

II.5.-MAGNETIC, MAGNETOOPTICAL AND MAGNETOPLASMONIC CHARACTERIZATIONS 34

II.5.A.- The magnetoopical Kerr effect. 34

II.5.B- Polar Kerr loops and spectroscopy 37

II.5.C- The transverse Kerr loops system. 42

II.5.D- TMOKE measurements in Kretschmann configuration. 43

II.5.D (i) Magnetoplasmonic characterization (Madrid system) 47

II.5.D. (ii) Magnetoplasmonic sensing (Lecce system) 49

II.6.-REFERENCES 50

II.1- INTRODUCTION

This chapter presents both fundamental physics and setup details of the experimental techniques used for the elaboration of this thesis work. Magnetoplasmonic multilayer films require a large variety of experimental methods for their fabrication and complete characterization (structural, magnetic, optical and magnetooptical). The chapter is divided in three subchapters. The first one is devoted to the fabrication techniques: magnetron sputtering and e-beam evaporation. In the second one, the structural (X-Ray Diffraction), morphological (Atomic Force Microscopy) and optical (Spectroscopic Ellipsometry) characterization techniques are described. Finally, the third and main subchapter presents the magnetooptical (MO) Kerr effect, which is used for both the magnetic and MO characterizations, and the Kretschmann configuration that allows the SPP excitation in those multilayers for their magnetoplasmonic characterization and sensing applications.

II.2.-FABRICATION TECHNIQUES

The multilayers used in this thesis work have been fabricated using two Ultra-High Vacuum (UHV) deposition systems with e-beam evaporation (mainly for the insulator film deposition) and magnetron sputtering (for the metal film deposition) techniques. The precise control of the nanometer thickness of the layer by only a few parameters is a great advantage of these techniques. Moreover the UHV conditions allow the preservation of the material purity after the deposition.

II.2.A-Sputtering deposition

Sputtering deposition is one of the most widely used methods for the fabrication of thin films in both fundamental and industrial investigation[1]. Its popularity is based on the accurate control of deposition rate, high degree of reproducibility of the deposited films, versatility of the technique and the simplicity of the physical processes involved. It also allows the deposition of high melting point metals, such as refractory metals, and also insulators through AC sputtering or reactive sputtering using different gases. The physical mechanism of the sputtering deposition is purely mechanic, since it is produced when the highly energetic ions from a low pressure plasma of an inert gas (such as Ar) hit the surface of a solid target causing the isotropic emission of neutral atoms by momentum transfer. Then, the neutral atoms, emitted in every direction, arrive to the substrate forming a deposit. The energy of the arriving atoms is in the range of 10-100 eV. That energy can be modified not only varying the sputtering pressure, but the accelerating power supplied to the target (cathode) as well. For example, the typical

values for those parameters used for the sputtering process with a Au target are $1.5*10^{-3}$ mbar and 20 W respectively. The Fig.II.1. shows a sketch of the sputtering process, where a number of atoms are ejected when the plasma ions collide with the target material. Some of the impinging atoms are also reflected back and neutralized, but may still be energetic enough to reach the surface of the substrate where the thin film is being formed. That back-scattering affects the resulting film properties.

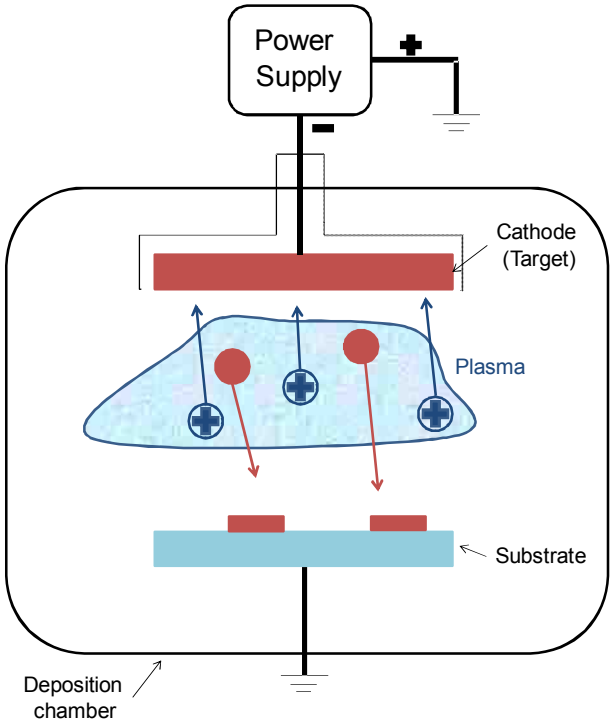

Fig. II.1. Scheme of a sputtering deposition. The Ar ions of the plasma strike the material target (cathode) and the material atoms are ejected towards the substrate.

In this thesis work, commercial *sputtering magnetrons* (AJA International, INC) have been used for the deposition of thin films of noble and ferromagnetic metals (see fig. II.2.(a)). In this sputtering configuration, a magnetic field generated by a set of permanent magnets located below the target is used to confine the electrons in the proximity of the target surface (see figure II.2.(b)). The electrons follow helicoidal trajectories along the magnetic field, causing a higher number of collisions with the gas atoms and therefore enhancing the ionization process. The main advantage of this configuration is that it allows the use of stable plasmas at lower working gas pressures and thus it leads to the possibility of a deposition rate increase. Moreover, this sputtering method can be used with DC and AC voltages allowing the deposition of both metals and insulators.

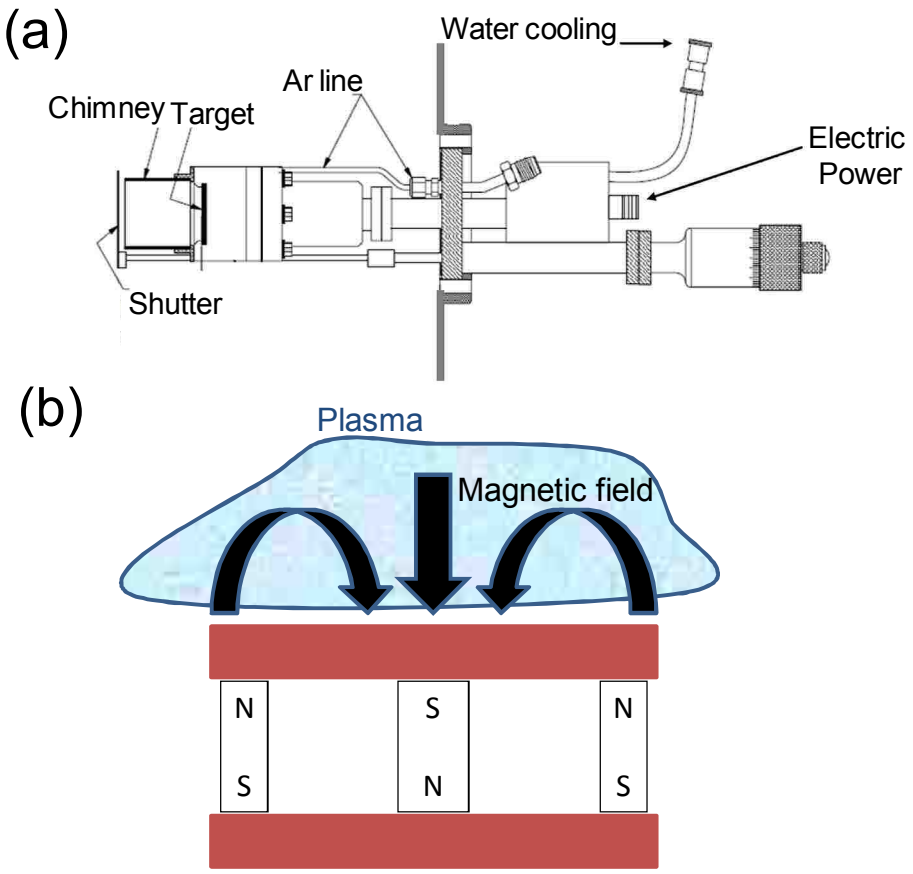

Fig. II.2.(a) Scheme of a magnetron sputtering of AJA International, INC.(b) Magnetic field lines on the surface of the magnetron target.

II.2.B- E-beam evaporation

Electron beam evaporation is a deposition technique based on the use of a flux of electrons as the heater for the thermal evaporation of a material[2]. The heating energy is supplied to the surface of the material to be deposited, contained in a water cooled cavity, by the kinetic energy of a high current electron beam. The temperatures reached by the e-beam heating are only limited by the radiation and conduction to the water cooled cavity. Materials contained in the water cooled cavity do not significantly react with it, therefore providing a universal evaporant container. The bent electron beam evaporation source was first envisioned by L Holland[3] as it is now used in thin film fabrication for electronics, optics and research; but the modern 270º gun was developed in the 1960s by Hugh Smith and Charles Hanks[4]. Today the development of the new generation of hard multilayer optical coatings has made electron beam evaporation the technology of choice in optics.

The electron beam evaporation source, as used for thin film fabrication, has three basic sections: the electron gun, the beam deflection magnetic lens and the evaporant-containing cavity (see Figure II.3). The e-beam is formed in the gun, which is a hot filament providing free electrons by the thermionic effect, passes through the magnetic lens and is focused upon the evaporant material. For useful evaporation to happen, the evaporant surface must achieve a temperature such that the surface vapour pressure is greater than the pressure inside the deposition chamber. A stable thermal equilibrium between the evaporant and the energy dissipation is required in order to achieve stable evaporation rates. The evaporant mainly dissipates the heat by conduction to the cool water cavity, then by evaporant phase change and finally by thermal radiation. A portion of the beam, with important energy, is also reflected by the evaporant surface. For an ideal conductor (Ag, Au, Al, Cu), the rate is increased with increasing power until the evaporant pressure over the beam impact point achieves the viscous flow range ($7.5*10^{-2}$ mbar). Because the temperature variation is relatively small from the point of first evaporation to instability, the heat losses by conduction to the cool water cavity and radiation do not increase fast. Therefore, the evaporation rate increases exponentially with increasing power until being limited by the vapour density over the evaporant surface.

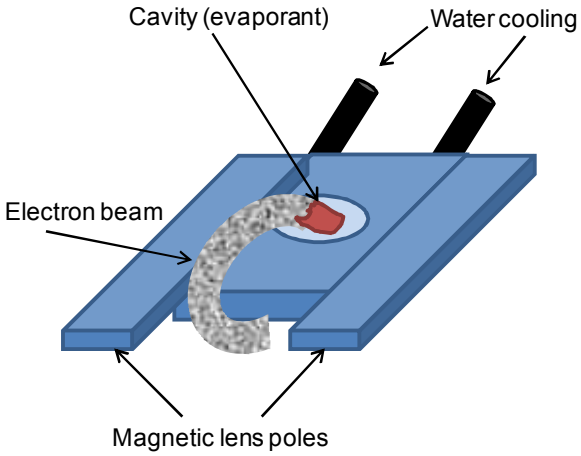

Fig. II.3. Sketch of an electron beam evaporator.

II.2.C-Fabrication systems

Two deposition systems have been used for the fabrication of the samples: A system to grow multilayers only via sputtering deposition named sputtering system (fig. II.4.(a)) and other system to deposit layers via sputtering deposition or e-beam evaporation named deposition system (fig. II.4.(b)).

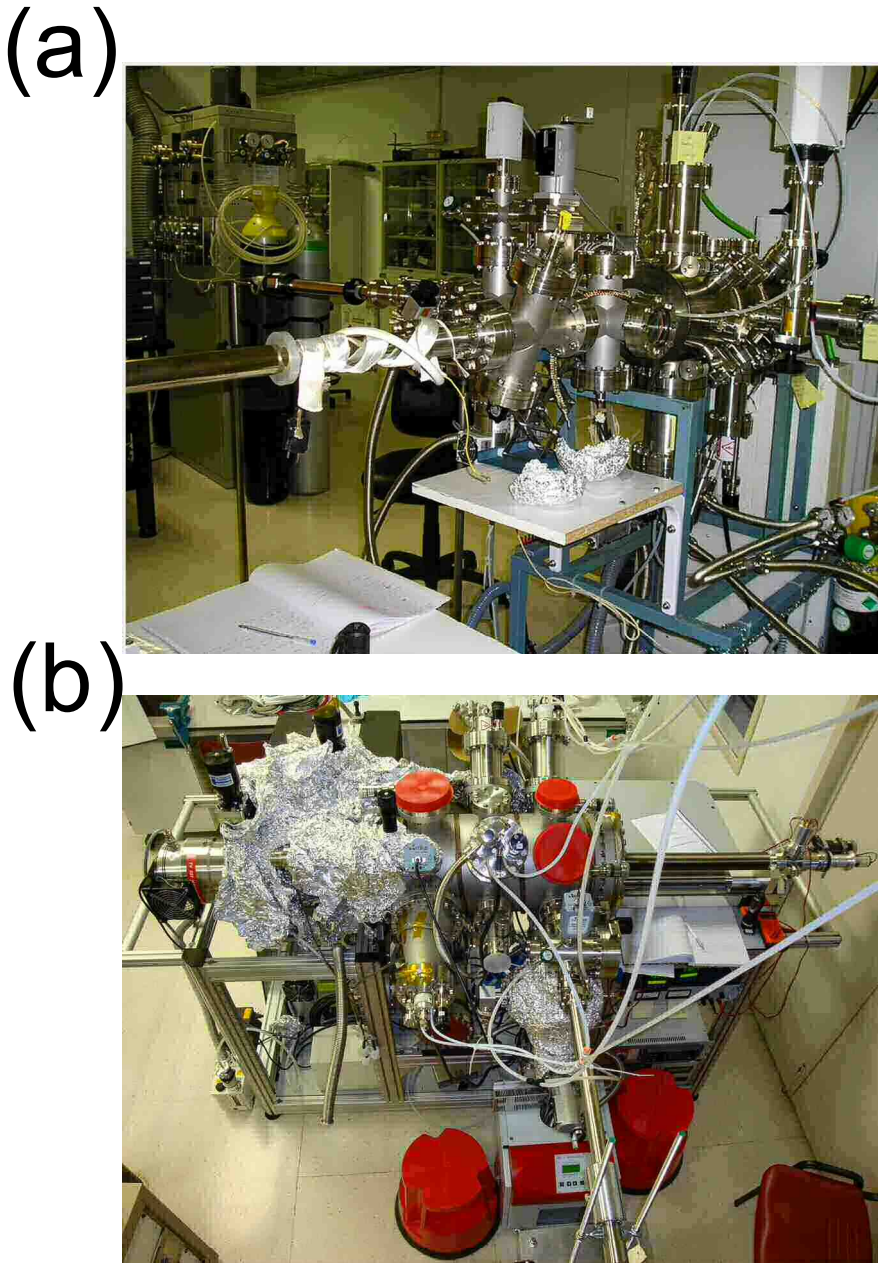

Fig. II.4. Views of the sputtering system (a) and the deposition system (b).

A scheme of the sputtering deposition system is shown in the figure II.5. It consists of a cylindrical chamber, that is evacuated by a turbo-pump with the support of a mechanical rotary pump (Pfeiffer D-35614 Asslar with a pump velocity of 520 l/s and 12 m^3/hour respectively) achieving a base pressure in the 10^{-9} mbar range after a previous baking of 120 ºC within 3 days of the deposition chamber. The chamber pressure was monitored by dual gauge sensor: a Pirani gauge, in the range of 10^{3}-10^{-2} mbar, and a hot cathode Bayard-Alpert gauge for the 10^{-2}-10^{-10} mbar (Pfeiffer PBR260 pressure sensor). The deposition chamber is connected to a load lock chamber through a gate valve. Pumping system in the load-lock chamber consists of a turbo-pump with the support of a mechanical rotary pump (Pfeiffer D-35614 Asslar with a pump velocity of

60 l/s and 6 m^3/hour respectively), achieving a base pressure of $2*10^{-8}$ monitorized by other Pfeiffer PBR260 sensor of dual gauge.

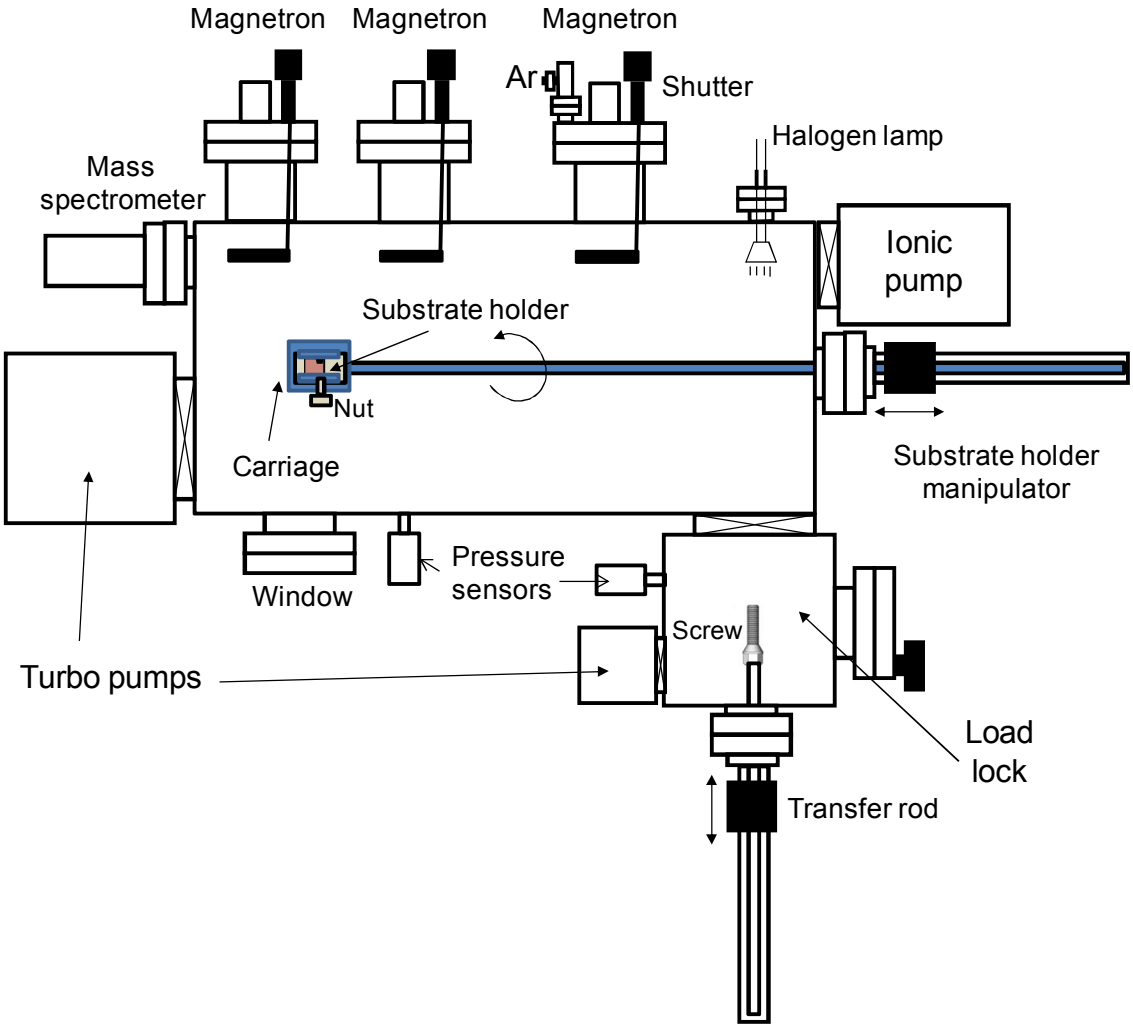

Fig. II.5. Scheme of the sputtering system.

The substrate holder (upper sample holder of the figure II.6.(a)) is composed of: a steel plate with Ta flanges to hold the substrates and a steel nut to screw into the load-lock manipulator, which is a transfer rod with magnetic components. The substrate holder is transferred from the load-lock to a carriage with lateral flaps to maintain the sample holder (see fig.II.6.(b)) and its own transfer rod (substrate holder manipulator) that allows linear and rotation movements inside the deposition chamber. A halogen lamp is located inside the deposition chamber to degas the substrates during 30 minutes. There are two gas inlet ports to admit Ar into the deposition chamber directly connected to the Co magnetron. The gas flow was controlled by a needle valve. The deposition chamber is connected to a mass spectrometer (Pfeiffer Prism QMS 200) that allows leak test and residual gas analysis by the ionization and discrimination of the atoms and molecules located inside the chamber as a function of their charge-mass ratio, applying electric fields.

Inside the deposition chamber, the magnetron sputtering deposition has been available for different metallic targets: Au, Ag, Co and Cr. The plasma conditions were controlled only by the Ar pressure and the target power. The Ar pressures used for the plasma ingnition were Au: $1*10^{-3}$ mbar, Ag: $3*10^{-3}$ mbar, Co: $6.6*10^{-3}$ mbar and Cr: $3*10^{-3}$ mbar. The target power used was 20 W for all the targets except for the Ag deposition that was done with 100 W. Using these plasma conditions for each target, the deposition ratios obtained were Au: 1.84 Å/s, Ag: 1.67 Å/s, Co: 0.26 Å/s and Cr: 0.3 Å/s.

The deposition system with sputtering deposition and e-beam evaporation will be detailed in the next paragraphs. A scheme of the deposition system is shown in the figure II.7. It consists of a cylindrical chamber, that is evacuated by a turbo-pump (Varian TV 551 Navigator with a pump velocity of 550 l/s) with the support of a mechanical rotary pump (Varian DS 102 with a pump velocity of 12 m^3/hour) achieving a base pressure in the low 10^{-9} mbar range after a previous baking of 120 ºC within 3 days of the deposition chamber. The chamber pressure was monitored by a dual gauge sensor (MKS 979B pressure sensor). The deposition chamber is connected to a load lock chamber through a gate valve. Pumping system in the load-lock chamber consists of a turbo-pump with the support of a mechanical rotary pump (Pfeiffer D-35614 Asslar with a pump velocity of 60 l/s and 6 m^3/hour respectively), achieving a base pressure of $2*10^{-8}$ monitorized by other MKS 979B sensor of dual gauge.

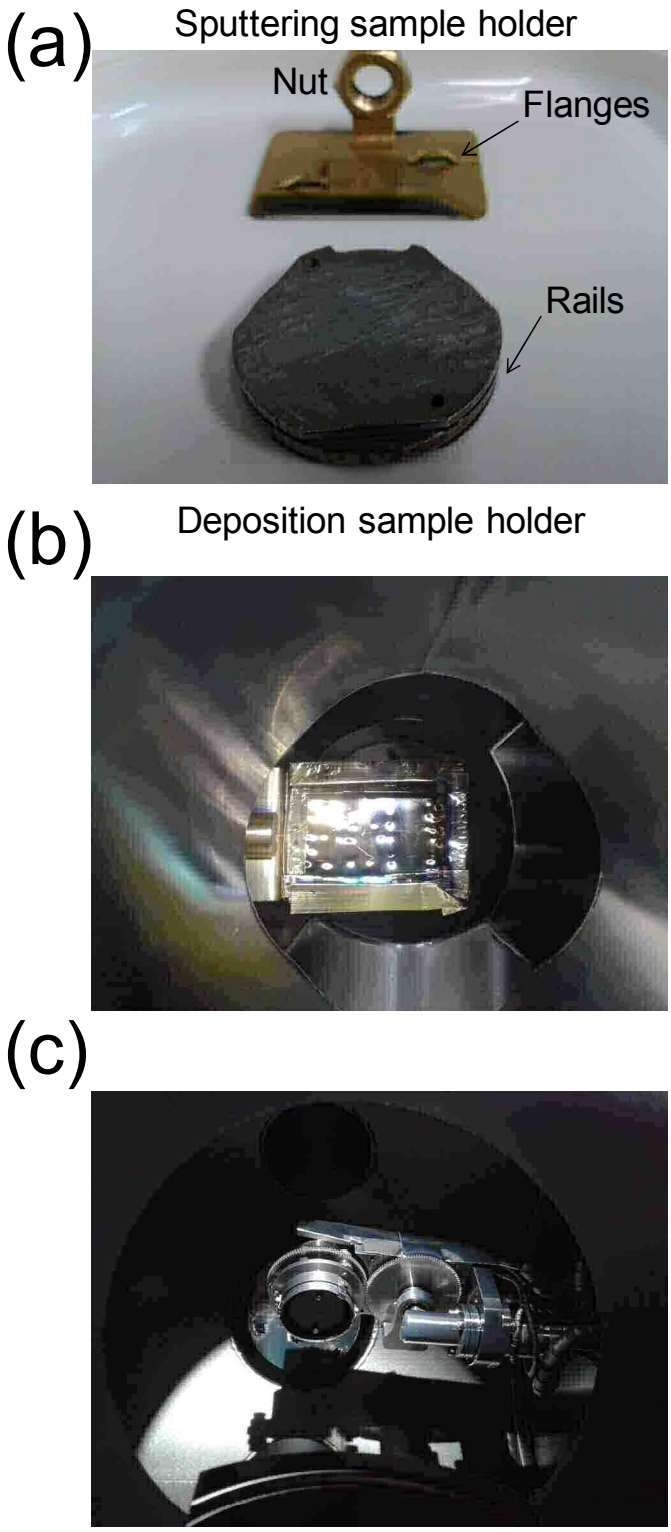

Fig. II.6. (a) Views of both sample holders for the sputtering system (at the top of the figure) and the deposition system (bottom of the figure). (b) Carriage inside the deposition chamber of the sputtering system. (c) Heater inside the deposition chamber of the deposition system.

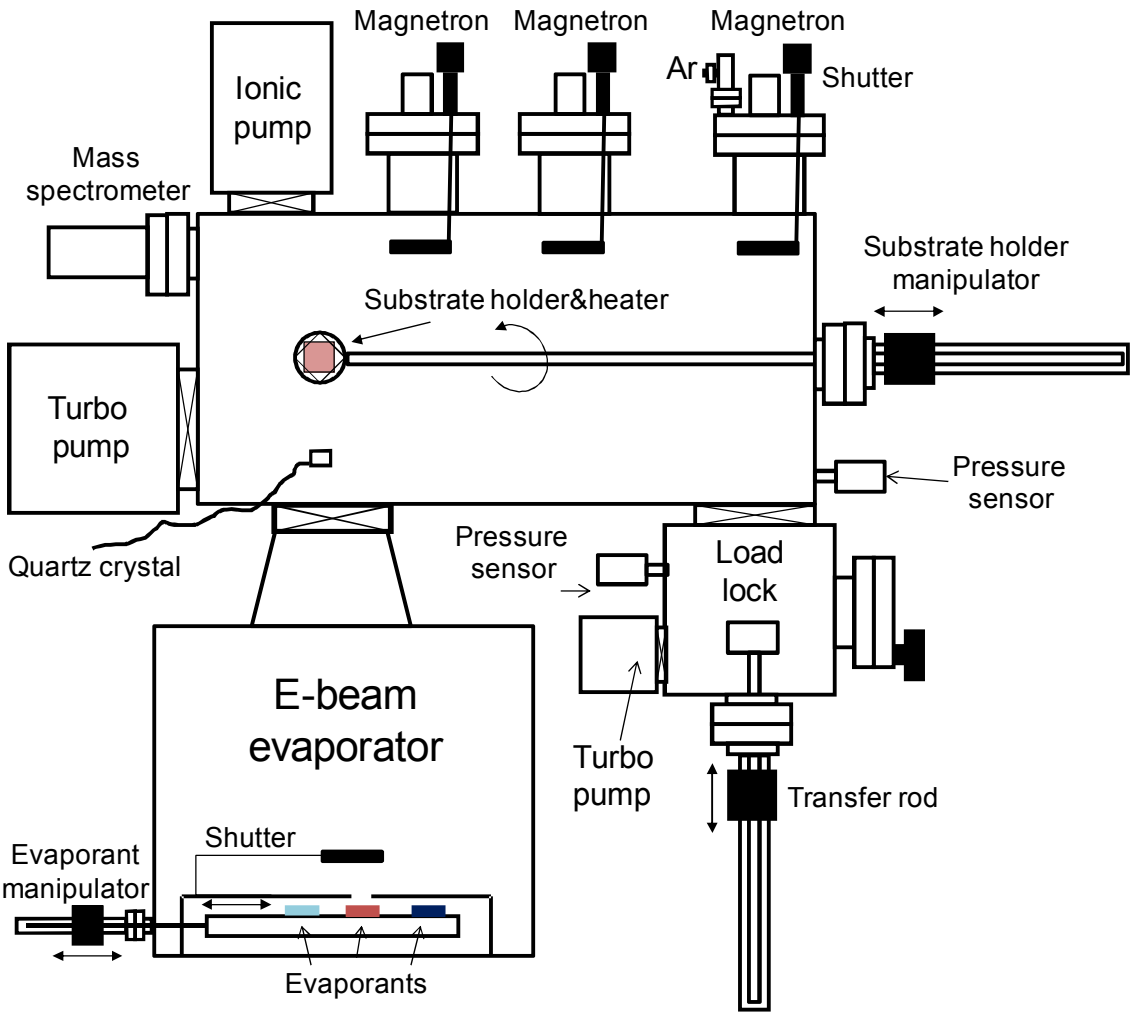

Fig. II.7. Scheme of the deposition system.

The substrate holder is a steel circular platform (substrate holder of the bottom of the figure II.6.(a)) where the substrates are attached by W wires of 0.5 mm diameter to the metallic platform. This substrate holder is screwed (by means of external rails) in a cavity of the transfer rod inside the load lock. The substrate is transferred to a heater (the substrate holder is attached to the heater by a pair of flanges and a mechanism) inside the deposition chamber by this transfer rod. The heater is under the substrate holder to degas the substrates at 160ºC within 30 minutes and also allowing for deposition with hot substrate and/or in-situ annealing: the maximum temperature that can be achieved is 800ºC with 3.2 A and 24 V. Moreover, the circular cavity of the heater can rotate with angular speed from $2.5*10^{-3}$ revolutions per minute (rpm) to 3.6 rpm. Such azimuthal rotation allows a deposition with improved homogeneity over the sample surface respect to the static one and, in combination with tilt, can be used to prepare a variety of nanostructures: nanocolumns, helicoidal structures,…(see section V.2. of the chapter V). There are two gas inlet ports to admit Ar into the deposition chamber directly connected to the Co and Fe magnetrons. The gas flow was controlled

by a needle valve. The deposition chamber is connected to a mass spectrometer that allows leak test and residual gas analysis.

The sputtering deposition has been available for five different metallic targets inside the deposition system: Au, Ag, Co, Cr and Ti. Again the plasma conditions were controlled only by the Ar pressure and the target power. The Ar pressure was $1.5*10^{-3}$ mbar for all the targets. The target powers used were Au: 20 W, Ag: 20 W, Co: 150 W, Cr: 20 W and Ti: 100 W. Using these plasma conditions for each target, the deposition ratios obtained were Au: 1.1 Å/s, Ag: 0.66 Å/s, Co: 0.33 Å/s, Cr: 0.23 Å/s and Ti: 0.26 Å/s. In both fabrication systems, the targets are protected by a shutter that allows the plasma ignition without material deposition onto the substrate. This allows for performing a 2 min pre-sputtering of each target which removes any possible contaminant from the target surface.

The deposition system allows e-beam evaporation for three different materials, in our case Co, Ti and SiO_2. The e-beam evaporation is carried out with the base UHV conditions of the system. A working voltage of 7 kV is used for all the materials. Two e-beam parameters have been adjusted in order to control the deposition ratio of the evaporant (which is monitorized by a quartz balance): the current and the scan shape of the e-beam. The scan shape of the e-beam is highly relevant when the evaporant is a poor heat conductor, for instance SiO_2, in order to distribute the e-beam energy within the material for obtaining stable evaporation ratios, whereas the scan shape is almost irrelevant for metals such as Co and Ti. Taking into account the different thermal conductivity for the three evaporant materials, a spiral beam shape has been used to focus the beam at the center of the Ti and Co cavities; and a triangular beam shape has been used to widely distribute the heat within the SiO_2 material and consequently obtaining stable evaporation. Moreover, the three materials exhibit different evaporation temperatures, thus different powers or currents have been used to obtain similar evaporation rates. The currents used were Co: 55 mA, Ti: 40 mA and SiO_2: 25 mA. Finally the deposition rates obtained with these e-beam conditions were Co: 0.7 Å/s, Ti: 0.2 Å/s and SiO_2: 1.5 Å/s.

II.3.-STRUCTURAL CHARACTERIZATION

The layer structure and interface roughness will leads to variations on the optical and MO characteristics of the multilayers systems fabricated for this thesis work. Thus the structural and morphological characterizations have been performed by X-Ray diffraction (XRD) and Atomic Force Microscopy (AFM) respectively.

II.3.A-X-Ray diffraction (XRD)

The X-rays diffraction (XRD) is one of the most important experimental techniques for the analysis of the crystalline structure. It was discovered by Laue, Friedrich and Knipping in 1912 and developed by W. H. Bragg and W. L. Bragg[5]. Moreover, this non-destructive analytical technique provides also information about the thickness and roughness of different layers in a multilayer structure (which are studied in this thesis work). This technique is based on the measurement of the scattered intensity of an X-ray beam impinging in a sample as a function of incident and scattered angle.

The XRD system used is a Philips Xpert MRD of four circles with a copper anode [Fig. II.8.]:

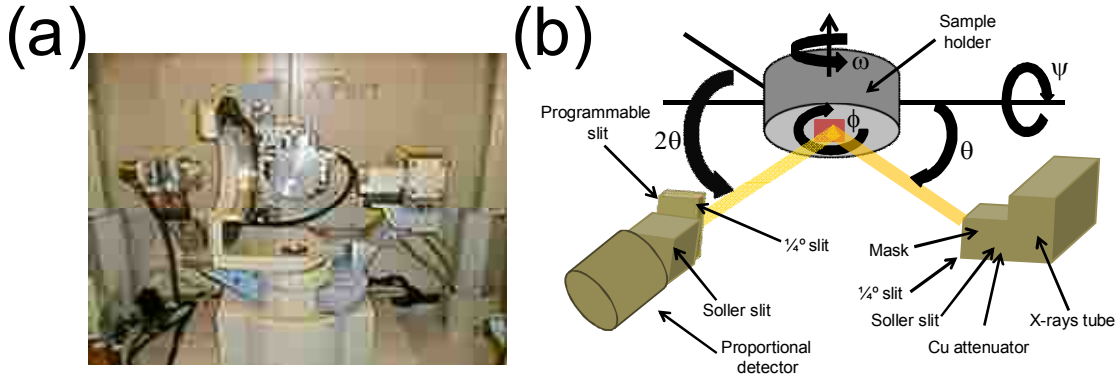

Fig. II.8. Photograph (a) and schem (b) view of XRD system located at IMM.

The work conditions of the X-rays tube were 45 kV and 40 mA. The system uses a goniometer with Euler geometry, thus the sample can be positioned at the three Euler angles[6] (ϕ,ψ,ω):ϕ is the rotation on the plane of the sample, ψ is the rotation around the axis parallel to the incidence plane and ω is the incidence angle of the x-rays on the sample. The fourth angle or 2θ circle accounts for the rotation of the detector in the scattering plane. On the other hand, a XYZ translation stage coupled to the goniometer

allows moving the sample in the three directions of the space. The Bragg-Brentano configuration was used for the measurements. The wavelength used in that configuration was λ=1.5418 Å that is a weighted mean value of the $K_{\alpha 1}$ and $K_{\alpha 2}$ lines of Cu. A Cu attenuator of 0.1 mm thickness is also used to decrease the beam intensity. Subsequently it travels across a set of Soller slits, which are a series of horizontal plane sheets that provides a collimated beam with a vertical angular divergence of 0.04 rad. Next, a ¼º slit, which limits the horizontal angular divergence, and a 0.5 mm mask that controls the beam size. After the beam reflection on the sample, the beam goes through a ¼º slit again, a programmable slit with an aperture of 0.5 mm and a Soller slit set as in the incident optics. Finally a proportional detector of Xe measures the reflected X-rays.

Two kinds of XRD measurements can be performed taking into account the X-rays incidence angle: low angle ($2\theta<15º$) and high angle ($2\theta>15º$) ranges. In the low angle range, known as X-rays reflectometry (XRR) the X-rays interact with the material as a continuous medium therefore it is possible to use the Fresnel equations from Optics. On the other hand, the X-rays discriminates the atomic structure of the material in the high angle range therefore the Bragg equation governs the X-rays diffraction (XRD). Crystalline phases, lattice parameter, epitaxial relations between the substrate and the other layers, mismatch of the crystalline orientations and the grain size can be determined using that configuration.

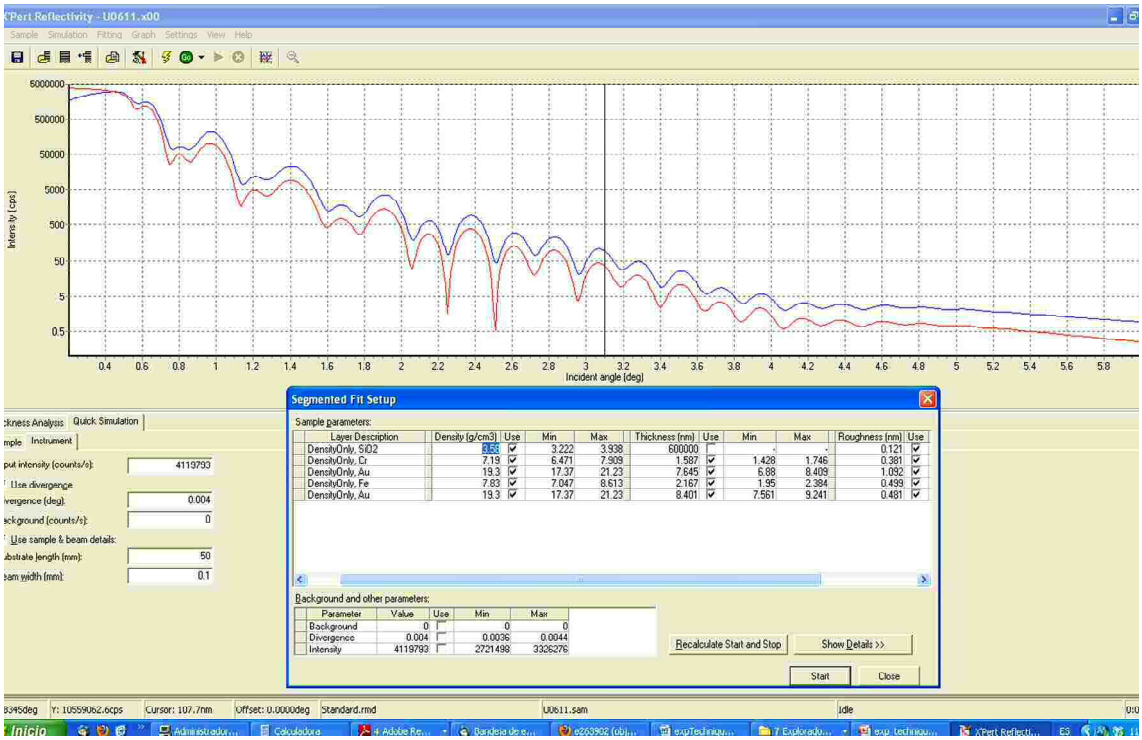

Fig. II.9. X'Pert Reflectivity program of PANalytical to fit the experimental XRR measurements with simulated ones from a model.

To perform the XRR measurements specific optics was used to decrease the horizontal divergence of the beam. Besides the use of the mentioned soller slit sets (for the two optics) to decrease the vertical divergence, a parabolic mirror and a 1/32º slit were used to improve the horizontal collimation of the beam for the incidence optics. The reflected beam is also horizontally collimated by another soller slit set and a 0.24º slit after that being collected by the detector. Once the XRR measurement is obtained, a fit to a structure model can be performed with a commercial program X'Pert Reflectivity by PANalytical (see figure II.9. with a fit for a Au/Fe/Au/MgO substrate system). Information of thickness, interlayer roughness and densities of each layer of the multilayer can be obtained by the fit between the experimental and simulated curves.

II.3.B-Atomic Force Microscopy (AFM)

The Atomic Force Microscopy (AFM[7]) has become a fundamental tool for nanotechnology since 1986, mainly in the surface morphology characterization with nanometric resolution. It emerged in order to explore insulator surfaces, which are not available by Scanning Tunneling Microscopy (STM).

This topographic technique consist in scanning across the sample surface a tip of nanometric size, located in the apex of a micro cantilever, maintaining a fixed tip-sample distance. To do this, in the majority of commercial equipments, a laser spot is reflected off the backside of the cantilever onto a four segment photodiode. The surface topography is obtained from the cantilever deflection variations, which combined with a feedback and control system, allow maintaining constant the tip-surface distance. These vertical variations are detected by the photodiode using the differential signal between the upper and lower parts of the four segment photodiode, whereas the lateral variations, detected by the difference between the left and right parts of the photodiode, can be used to measure the lateral forces due to the surface friction (see figure II.5.).

The AFM can operate in contact (static) mode or in various non-contact (dynamic) modes where the cantilever is vibrated. In the dynamic mode, the cantilever is externally driven to oscillate close to its fundamental resonance frequency. The oscillation amplitude, phase and resonance frequency are varied by the tip-surface interaction; those variations of the oscillation with respect to the external reference oscillation provide information about different properties of the sample. In this work the AFM was used in the amplitude modulation[8] or tapping mode although AFM can operate also in the frequency modulation[9] where the feedback system maintains the resonance frequency constant.

In the amplitude mode a piezoelectric mounted in the AFM cantilever holder drives the cantilever to oscillate close its resonance frequency. The amplitude of this oscillation is usually from 10 to 100 nm. The amplitude of the oscillation decreases as the tip gets closer to the surface of the sample due to the interaction forces (van der Waals forces, electrostatic forces, etc) with the tip of the cantilever. Another

piezoelectric tube, where the sample is mounted (in a sample-scanning microscope) or where the tip holder is mounted (in a tip-scanning microscope), changes the tip-sample distance to control the setpoint amplitude as the cantilever is scanned over the surface of the sample. Finally, an AFM measurement is achieved by imaging those piezoelectric height variations. It is worth to mention that the topography, obtained for the rough surfaces presented in this thesis work, is the result from a convolution of the actual surface of the sample with the shape of the tip. Therefore the lateral and vertical resolutions are limited to values around 10 nm and 2 Å respectively for standard tips. The tapping mode improves over the contact mode, in which the cantilever drags across the surface at constant force and therefore it damages the surface of the sample.

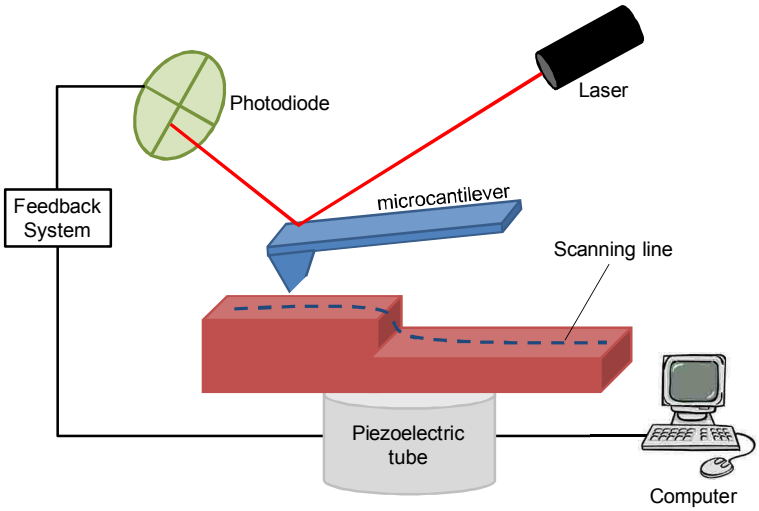

Fig. II.10. Sketch of the sample-scanning AFM following the lineshape of the surface of the sample.

The AFM images of this thesis were taken using either Veeco™ (tip-scanning) and Nanotec™ (sample-scanning) microscopes operating in noncontact dynamic mode (see figure II.11). Besides, silicon cantilevers from NanoSensors™ were used with a force constant, resonance frequency and tip radius of 5 N/m, around 75 kHz and 10 nm respectively.

Veeco AFM

Nanotec AFM

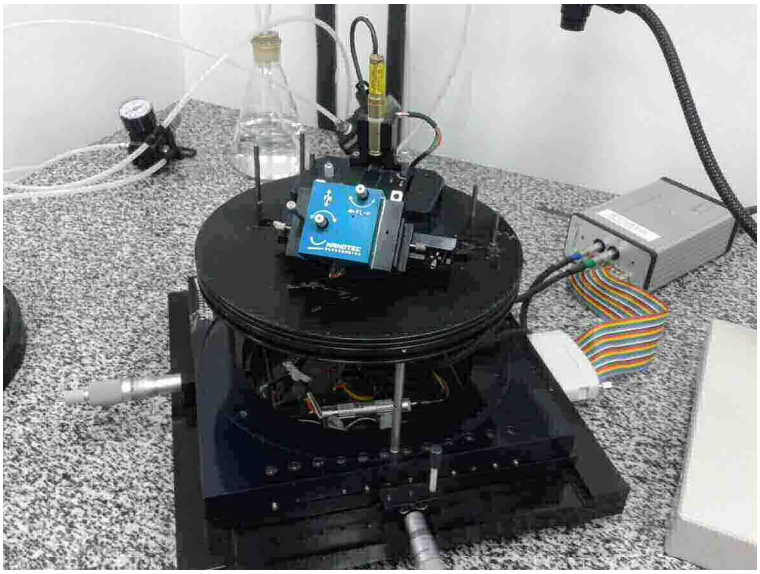

Fig. II.11. Photographs of the two commercial AFM used: Veeco™ and Nanotec™ .

II.4.-OPTICAL CHARACTERIZATION

The electromagnetic response of a macroscopic material with the light is encoded in the dielectric tensor (at visible frequencies the magnetic permeability for a material is approximated to that of the vacuum). The dielectric tensor is a symmetric tensor ($\varepsilon^{ij}= \varepsilon^{ji}$) with complex components for i,j=x,y and z thus it can be diagonalized. Nevertheless, taking into account the MO effects, the symmetry of the dielectric tensor is broken by the presence of a magnetic field (i.e. $\varepsilon^{ij}(M)=\varepsilon^{ji}(-M)$). Therefore the dielectric tensor of a magnetized material is antisymmetric[10]:

$$\varepsilon = \begin{pmatrix} \varepsilon^{xx} & \varepsilon^{xy} & \varepsilon^{xz} \\ -\varepsilon^{xy} & \varepsilon^{yy} & -\varepsilon^{yz} \\ -\varepsilon^{xz} & \varepsilon^{yz} & \varepsilon^{zz} \end{pmatrix} \quad \text{[II.1]}$$

The diagonal components are usually called “optical constants”, whereas the non-diagonal ones are called “MO constants”. Besides, the real “ε^{ii}_1” and imaginary “ε^{ii}_2” parts of each diagonal component for the dielectric tensor are related to the refractive index “n” and absorption coefficient “κ” by the next expression:

$$\varepsilon_1^{ii} = n^2 - \kappa^2$$
$$\varepsilon_2^{ii} = 2n\kappa \quad \text{[II.2]}$$

II.4.A.-Spectroscopic ellipsometry (SE)

Spectroscopic ellipsometry (SE) is a fast, non destructive and powerful characterization technique for the determination of the optical properties of materials systems (in our case mainly for metallic films). Compared with other techniques for obtaining information of the optical properties, the main advantage is that it does not require preparation of the sample for performing the measurements (Ohmic contacts, immersion oil, …).

SE is based on the study of the variations for the polarization state of the reflected light from the sample compared to that of the incident light[11]. From these measurements it is possible to obtain information of the refractive index of a material taking into account its thickness, roughness, anisotropy,….

Usually, the electric field of the reflected light can be separated in two orthogonal components: parallel (r_p) and perpendicular (r_s) to the incidence plane (see figure II.12.). Besides, these two Fresnel complex reflection coefficients can be expressed as a ratio ρ:

$$\rho = \frac{r_p}{r_s} \quad \text{[II.3]}$$

and it is conventionally expressed as a function of the angles Ψ and Δ:

$$\rho = \tan(\Psi) e^{i\Delta} \quad \text{[II.4]}$$

Therefore, the Ψ and Δ angles are measured by the ellipsometer and they determine the variations on the amplitude and phase for the orthogonal components of the electric field, respectively[12]. The ellipsometry measurements were performed with a M200FI J. A, Woollam Co.™ ellipsometer between 500 nm and 1.69 μm for the wavelength, for angles of incidence ranging from 45 to 75º (see figure II.6.), which allow extracting both real and imaginary parts (ε^{ii}_1 and ε^{ii}_2, respectively) of the diagonal elements of the dielectric tensor (or equivalently the "n" and "k" of the complex refractive index).

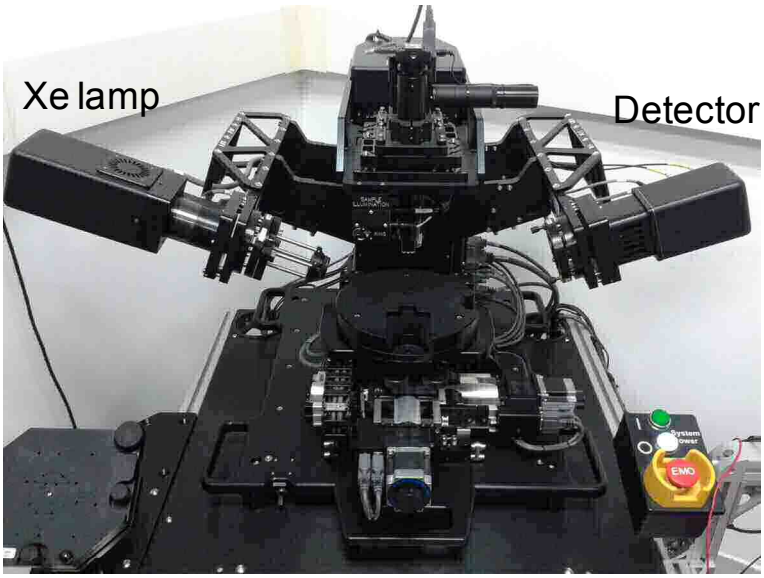

Fig. II.11. Spectroscopic ellipsometer with variable angle at IMM.

Ideally in a bulk sample without any oxide, surface roughness, or any overlayer, the optical constants of the sample can be extracted from the elipsometric data using the following expression:

$$\left\langle \varepsilon^{xx} \right\rangle = \left\langle \varepsilon_1^{xx} \right\rangle + i \left\langle \varepsilon_2^{xx} \right\rangle = \left(\langle n \rangle + i \langle k \rangle \right)^2 = \sin(\phi)^2 \left[1 + \tan(\phi)^2 \left(\frac{1-\rho}{1+\rho} \right)^2 \right] \quad \text{[II.5]}$$

where ϕ is the angle of incidence and ρ is defined in equation [II.3].

For a real situation, the previous assumptions (a sample without oxide, surface roughness or overlayers,…) are not realistic, thus the measurements of the Ψ and Δ angles cannot provide direct information about the properties of the sample. In order to do that, simulation and regression programs with classical optical models, which describe the physical properties of the materials, are required.

First a theoretical model is proposed for the structure of the system under investigation building a layered optical model with the nominal sample structure. Each layer is parameterized by its thickness and optical constants. Then the Fresnel reflection coefficients are calculated using the classical optics laws[13] (Snell's law, Fresnel equations,…). Finally the program can generate or predict elipsometric data. If the model is a good representation of the sample, the model-generated elipsometric data will fit well with the experimental ones.

It is important to remark that the fitting will be more complicated if we request too much parameters since the probability of correlation between them will be higher. Thus easy models are recommended to construct our systems. The metallic multilayers grown over glass substrates of this thesis (with an interface roughness similar to the thickness layer) are complex systems exhibiting a general structure of the optical constants for each layer quite different from those of the bulk. It means that the use of parametric models is not appropriated for obtaining the optical constants fit. The alternative approach used in this thesis work to deduce the optical constants from the elipsometric data is based on a B-Spline model. This model exhibits an arbitrary flexibility for the optical constants as a function of the wavelength taking as initial conditions the optical constants of the bulk material for each layer. Nevertheless, the optical constants obtained via the B-Spline model require a study of their physical meaning.

One physical property of the components of the real optical constants is that they must obey the Kramers-Kronig relations, since the respective real and imaginary components are connected by the next expressions:

$$n(E)-1=\frac{2}{\pi}P\int_0^{\infty}\frac{E'\kappa(E')}{E'^2-E^2}dE'$$

$$\varepsilon_1(E)-1=\frac{2}{\pi}P\int_0^{\infty}\frac{E'\varepsilon_2(E')}{E'^2-E^2}dE' \quad \text{[II.6]}$$

where n and ε_1 are the real parts of the complex refractive index and dielectric constant, κ and ε_2 are the imaginary parts of the complex refractive index and dielectric constant respectively. Therefore knowing one component of the refractive index (or dielectric constant) we automatically obtain the other component.

Once we have fitted the experimental data, the "goodness" of the fitting is analyzed by the Mean Squared Error (MSE) value, also called Root Mean Squared Error[14]. This value is the square root of the error summation divided by the number of measurements points minus the number of fit parameters. It is quatified by the next equation:

$$MSE=\sqrt{\frac{1}{3n-m}\sum_{i=1}^{n}\left[\left(N_{E_i}-N_{G_i}\right)^2+\left(C_{E_i}-C_{G_i}\right)^2+\left(S_{E_i}-S_{G_i}\right)^2\right]}x1000 \quad \text{[II.7]}$$

where n is the number of wavelengths, m is the number of fit parameters and N=Cos(2Ψ), C= Sin(2Ψ)Cos(Δ), S= Sin(2Ψ)Sin(Δ). The parameters subscripted with E and G are the experimental and generated data respectively. Therefore the lower the MSE value, the better the fit between the measured and the theoretically generated data. The usual accuracy of the elipsometric measurements is around 0.001, by this reason it is included the factor 1000 in order to get a MSE around 1 for an ideal model fit. However, this MSE value is only possible for elementary samples such as single thin films on Si substrates, but MSE values higher than 10 are achieved for the best model fits of multilayers (the case of this work).

II.5.-MAGNETIC, MAGNETOOPTICAL AND MAGNETOPLASMONIC CHARACTERIZATIONS

This section describes the MO Kerr effect with its three different configurations, which is the measurement principle of the polar and transverse Kerr setups that provides the magnetic and the MO characterization for our multilayers. Moreover the Kretschmann configuration added to a transverse Kerr setup leads to both the measurement of the MO Kerr effect with the SPP excitation in these multilayers (magnetoplasmonic characterization) and their use as transducers in MagnetoOptical Surface Plasmon Resonance (MOSPR) sensors .

II.5.A.- The magnetoopical Kerr effect.

The rotation of the polarization plane of the light when it travels through a glass with an applied magnetic field (parallel to the direction of the light beam), was discovered by Michael Faraday in 1846[15]. Later, John Kerr reported a similar change in the polarization plane of the light, when the light was reflected by an electromagnet in 1876[16]. Kerr observed tiny rotations with a magnetization dependence, since a maximum rotation was reached when the magnetization was saturated. The Kerr effect can be measured in three configurations, as Voight[17] proposed, depending of the orientation of the magnetization relative to the incidence plane of the linearly polarized light and the plane of the magnetooptical material: these are the transversal, polar and longitudinal configurations. In transversal configuration a variation of intensity is measured whereas in the polar and longitudinal configurations, the reflected light is elliptically polarized. I will explain in detail the configurations used in this thesis work: the transversal and polar ones.

Transversal configuration: In this configuration the magnetization is placed perpendicular to the incidence plane of the light and it is on the plane of the magnetized medium ($\mathbf{M_y}$ in the figure II.7. (a))). If the magnetization is parallel to the *y* axis, the dielectric tensor of the magnetic material is given by:

$$\varepsilon = \begin{pmatrix} \varepsilon^{xx} & 0 & \varepsilon^{xz} \\ 0 & \varepsilon^{yy} & 0 \\ -\varepsilon^{xz} & 0 & \varepsilon^{zz} \end{pmatrix} \quad \text{[II.8]}$$

Since the electric field of the electromagnetic wave must have a perpendicular component to the magnetization in the magnetooptical activity, there is no effect for s polarization. A tiny variation of the reflection coefficient for the p polarized component of the light is produced by the Kerr effect in this configuration and therefore that variation gives rise to an intensity change of the light reflected without a rotation of the polarization plane or ellipticity. Thus the transverse magnetooptical Kerr effect (TMOKE) can be defined as the normalized variation of reflectivity relative to the p polarization:

$$\frac{\Delta R_{pp}}{R_{pp}} = \frac{R_{pp}(+M_s) - R_{pp}(-M_s)}{R_{pp}(+M_s) + R_{pp}(-M_s)} \approx \frac{R_{pp}(+M_s) - R_{pp}(-M_s)}{2R_{pp}(0)} \quad \text{[II.9]}$$

where $R_{pp}(+M_S)$ and $R_{pp}(-M_S)$ are the reflectivities with the magnetization saturated of the magnetic material in both opposite directions of the magnetic field; and $R_{pp}(0)$ is the reflectivity with null magnetization. With this definition, the maximum value that $\Delta R/R$ can reach is 1. If we consider a system of two semi-infinite, non-magnetic and magnetic media, the TMOKE adopts the following form:

$$\frac{\Delta R_{pp}}{R_{pp}} = 2sen(2\theta)\,\mathrm{Re}\left(\frac{\varepsilon_{xz}}{\left(\varepsilon_{xx}^2 - 1\right)\cos^2(\theta) - \varepsilon_{xx} + 1} \right) \quad \text{[II.10]}$$

being θ the incidence angle of the light and ε_{xx} or ε_{xz} components of the dielectric tensor.

Polar configuration: When the magnetization is perpendicular to the plane of the magnetic material ($\mathbf{M_z}$ in the figure II.7.(b)), the light reflected in the perpendicular direction of the sample surface rotates its polarization plane an angle θ_K and it acquires an ellipticity, which are proportional to the perpendicular component of the

magnetization[18]. The ellipticity is defined by ε_K=arctan(a/b) where a and b are the minor and major axes respectively of the polarization ellipse (see figure II.12.).

$$\varepsilon \equiv \begin{pmatrix} \varepsilon^{xx} & \varepsilon^{xy} & 0 \\ -\varepsilon^{xy} & \varepsilon^{yy} & 0 \\ 0 & 0 & \varepsilon^{zz} \end{pmatrix} \quad \text{[II.11]}$$

The origin of the rotation and ellipticity of the polarization state of the light can be explained by the diagonalization for the basis of the circular polarized light eigenvectors[19], being the dielectric constants $\varepsilon^{+}=\varepsilon^{xx}+i\varepsilon^{xy}$ and $\varepsilon^{-}=\varepsilon^{xx}-i\varepsilon^{xy}$ their respective eigenvalues. It means that the two components of the circular polarized light probe media with different complex refractive constants N^{+} and N^{-}: $N^{\pm} = n^{\pm} + i\,k^{\pm} = (\varepsilon^{\pm})^{1/2} = (\varepsilon^{xx} \pm i\varepsilon^{xy})^{1/2}$. Thus the complex Fresnel coefficients, which determine the amplitude and polarization state of the reflected light, are different. Differences between the refractive index $\Delta n=n^{+}-n^{-}$ give rise to a phase shift $\Delta\theta=\theta^{+}-\theta^{-}$ between the right-handed and left-handed circular polarized components of the light (magnetic cicular birefringence[20]), leading to the rotation of the polarization plane (Kerr rotation θ_k). On the other hand, differences between the absorption coefficients $\Delta k=k^{+}-k^{-}$ give rise to differences on the modulus of the Fresnel coefficients and thus lead to different reflectivities for the right-handed and left-handed circular polarized components (magnetic circular dichroism) causing elliptical polarization light (Kerr ellipticity ε_k).

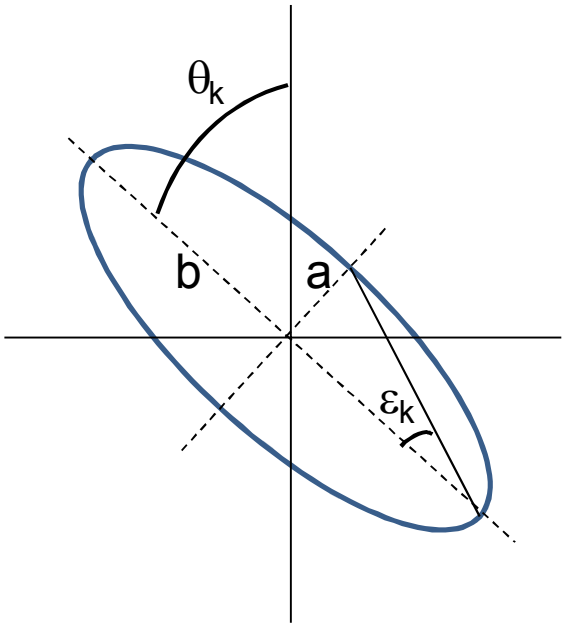

Fig. II. 12. Polarization ellipse with the major (b) and minor (a) axes including the Kerr rotation (θ_k) and ellipticity (ε_k) angles.

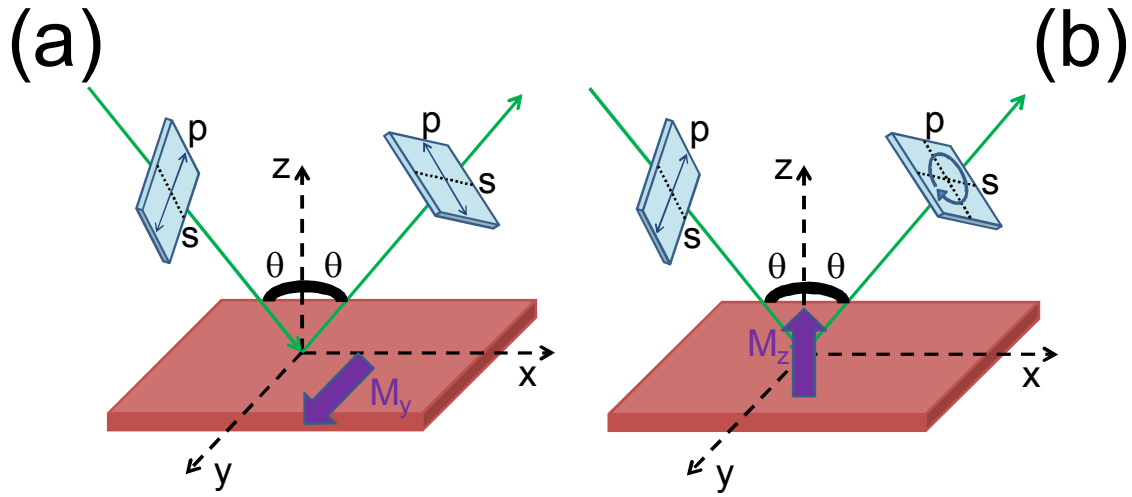

Fig. II. 13. Transverse (a) and polar (b) configurations of the magnetooptical Kerr effect.

II.5.B- Polar Kerr loops and spectroscopy.

The experimental setup described in what follows allows measuring both rotation and ellipticity in polar configuration, obtaining MO hysteresis loops at a particular wavelength or alternatively MO spectra at saturation.

The MO activity shows, in first approximation, a linear dependence with magnetization. Therefore hysteresis loops with information of the magnetization reversal process and saturation and coercive fields of the material can be obtained from rotation and ellipticity Kerr measurements as a function of the magnetic field. Besides, the Polar Kerr spectra provide a great amount of information about the spectral properties and electronic structure of the material since the Polar Kerr effect depends of the optical and MO properties of the system.

The polarization modulation technique is used in our setup due to its high sensitivity (around 10^{-3} degrees) [21,22,23]. Figure II.14. (a) shows a scheme of the setup for measuring the Kerr rotation and ellipticity signals. The light source is a Xe lamp with a spectral range from 240 nm to 2 μm approximately. The light is reflected in a series of concave mirrors (not depicted in the scheme) and focused onto the aperture of a monochromator (SpectraPro 150 model). Thet monochromator has dual indexable gratings of 600 and 1200g/mm, a 150 mm focal length and a spectral resolution of 0.4 nm with 10 μm wide slit. Once the wavelength is selected, the beam crosses a polarizer that has its principal axis oriented at 45º with respect to the setup plane. Subsequently, a PEM-90 photoelastic modulator periodically modulates the light between linear and circular polarized states. The p-polarized component of the light is affected by a phase $\varphi = \varphi_0 \operatorname{sen}(\omega_m t)$, where ω_m is the angular frequency of the modulation ($\omega_m = 2\pi \cdot 50$ kHz)

and φ_0 the phase amplitude; whereas the s-polarized component of the light is not affected. Next, the beam is focused by a set of two lenses onto the sample which is located in between the two polar pieces of an electromagnet, one of which has a hole drilled through its axis. This way, magnetic fields of up to 1.6T perpendicular to the sample plane can be reached. The light reflected off the sample reaches another set of two lenses that collimates the beam. A second polarizer, used as analyzer with adjustable principal axes for the calibration measurements, is found in the setup. After the lens and the polarizer, the focus and linearly polarized beam is impinged on the photodetector which is a photon multiplier tube (PMT). Both signals from the photodetector and from the photoelastic modulator (reference signal) are sent to a lock-in amplifier for filteringthe signal, allowing to determine both rotation (second harmonic of the reference signal) and ellipticity (first harmonic) signals with the help of a computer.

The Jones matrix method is used for describing the polarization state of the light inside the system[22]. Each optical component in fig.II.8 is expressed by a Jones matrix. The electric field amplitude of the reflected beam E^r at the photodetector is represented by the equation:

$$E^r = P_2 \cdot S \cdot M \cdot P_1 \cdot E^i \quad \text{[II.12]}$$

where E^i is the amplitude of the incident light. The P_2, S, M and P_1 Jones matrices represent the second polarizer (analyzer), the sample, the photoelastic modulator and the first polarizer respectively. Those matrices are:

$$P_1 = \begin{pmatrix} 1/2 & 1/2 \\ 1/2 & 1/2 \end{pmatrix} \qquad M = \begin{pmatrix} 1 & 0 \\ 0 & e^{i\varphi} \end{pmatrix}$$

$$S = \begin{pmatrix} r_p & r_{ps} \\ r_{sp} & r_s \end{pmatrix} \quad P_2 = \begin{pmatrix} \cos^2\beta & sen\beta\cos\beta \\ sen\beta\cos\beta & sen^2\beta \end{pmatrix} \quad \text{[II.13]}$$

where the axis of the second polarizer can rotate an angle β, the axis of the first polarizer has been fixed to 45º and the reflectivity of the sample is described by the complex Fresnel coefficients, defined as:

$$\begin{aligned} \mathbf{r}_p &= r_p e^{i\delta_p} \\ \mathbf{r}_s &= r_s e^{i\delta_s} \\ \mathbf{r}_{ps} &= -\mathbf{r}_{sp} = r_{ps} e^{i\delta_{ps}} = r_{sp} e^{i\delta_{sp}} \end{aligned} \quad \text{[II.14]}$$

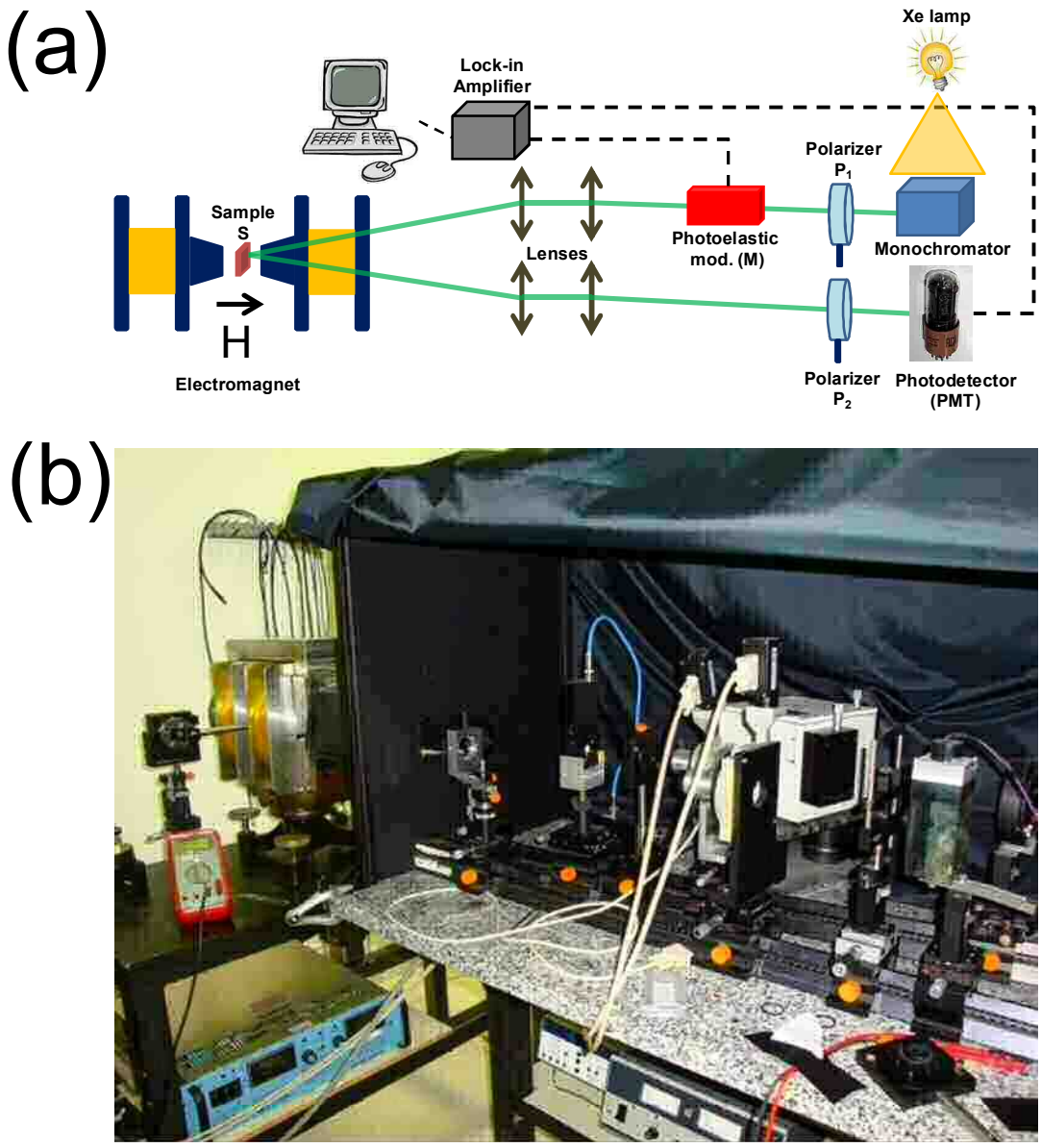

Fig. II. 14. Scheme (a) and photograph (b) of the Polar Kerr spectrograph.

These coefficients can be related to the Kerr rotation and ellipticity using the following expresions:

$$\theta_k^p + i\varepsilon_k^p = \frac{\mathbf{r}_{sp}}{\mathbf{r}_{pp}}$$

$$\theta_k^s + i\varepsilon_k^s = \frac{\mathbf{r}_{ps}}{\mathbf{r}_{ss}} \quad \text{[II.15]}$$

The PMT measures the reflected intensity; taking into account that the incident intensity is given by:

$$E_p^i = E_s^i = \left(\frac{I}{2}\right)^{\frac{1}{2}} \text{ [II.16]}$$

The equation [II.11] can be operated to obtainin the reflected intensity that reaches the PMT:

$$I^r = \left(E_p^r\right)^2 + \left(E_s^r\right)^2 = \frac{I^i}{2}\left(A + B\cos\varphi + Csen\varphi\right) \text{ [II.17]}$$

where the coefficients A, B and C when the axis of P_2 is positioned in the p direction (β=0) are given by:

$$\begin{aligned} A &= r_p^2 + r_{sp}^2 \\ B &= -2r_{sp}r_p\cos(\delta_p - \delta_{sp}) \\ C &= 2r_{sp}r_p sen(\delta_p - \delta_{sp}) \end{aligned} \text{ [II.18]}$$

The intensity measured by the PMT is a function of the sine and cosine of the phase-shift applied by the photoelastic modulator. Moreover, that phase-shift exhibits a sinusoidal dependence with the modulation frequency ω_m. Due to the filtering of the lock-in amplifier, the first terms of the Fourier series for the intensity of the equation [II.16] will only be analyzed:

$$\begin{aligned} sen\varphi &= sen(\varphi_0 sen\omega_M t) = 2J_1(\varphi_0)sen(\omega_M t) + 2J_3(\varphi_0)sen(3\omega_M t) + \ldots \\ \cos\varphi &= \cos(\varphi_0 sen\omega_M t) = J_0 + 2J_2(\varphi_0)\cos(2\omega_M t) + \ldots \end{aligned} \text{ [II.19]}$$

where $J_n(\varphi 0)$ are the Bessel functions of the *nth* kind. Applying the equation [II.18] in [II.16], we can obtain:

$$I = I_0 + I_1 sen(\omega_M t) + I_2\cos(2\omega_M t) + I_3 sen(3\omega_M t) + \ldots \text{ [II.20]}$$

with

$$\begin{aligned} I_0 &= A + BJ_0(\varphi_0) \\ I_1 &= 2CJ_1(\varphi_0) \\ I_2 &= 2BJ_2(\varphi_0) \end{aligned} \qquad \text{[II.21]}$$

where A, B and C are the coefficients shown in the equation [II.17], I_0 is the DC component of the intensity, I_1 is the amplitude of the first harmonic in ω_M and I_2 is the amplitude for the second harmonic in $2\omega_M$. The lock-in amplifier can measure I_0, I_1 e I_2 taking ω_M as the reference frequency. Normalizing both amplitudes I_1 and I_2 to the DC component I_0 and considering the equations [II.14] that relate the Fresnel coefficients with the Kerr rotation and ellipticity, we can obtain two different expressions proportional to those Polar Kerr parameters:

$$\begin{aligned} \frac{I_2}{I_0} &= -4J_2(\varphi_0)\left(\frac{r_{sp}}{r_p}\right)\cos(\delta_{sp}-\delta_p) = -4J_2(\varphi_0)\theta_p \\ \frac{I_1}{I_0} &= 4J_1(\varphi_0)\left(\frac{r_{sp}}{r_p}\right)sen(\delta_{sp}-\delta_p) = 4J_1(\varphi_0)\varepsilon_p \end{aligned} \qquad \text{[II.22]}$$

where the next approximations $r_{sp}^2 << r_p^2$ and $J_0(\varphi_0)\sim 0$ for φ_0=2.2 rad (phase amplitude commonly used) have been considered. Therefore, leaving apart numerical factors, the normalized intensities I_1 and I_2 measured by the lock-in amplifier provide us the Kerr ellipticity and rotation respectively. However, the values of $J_2(\varphi_0)$ and $J_1(\varphi_0)$ cannot be directly calculated since the actual phase shift of the photoelastic modulator exhibits a wavelength dependence[24] $\varphi_0=\varphi_0(\lambda)$ due to its piezo-optical coefficients and to the deviations from the paraxial geometry (real incidence angle ~10º). Anyway, those values can be obtained by a calibration of the system at different angles (β) of the P_2 polarizer (analyzer).

II.5.C- The transverse Kerr loops system.

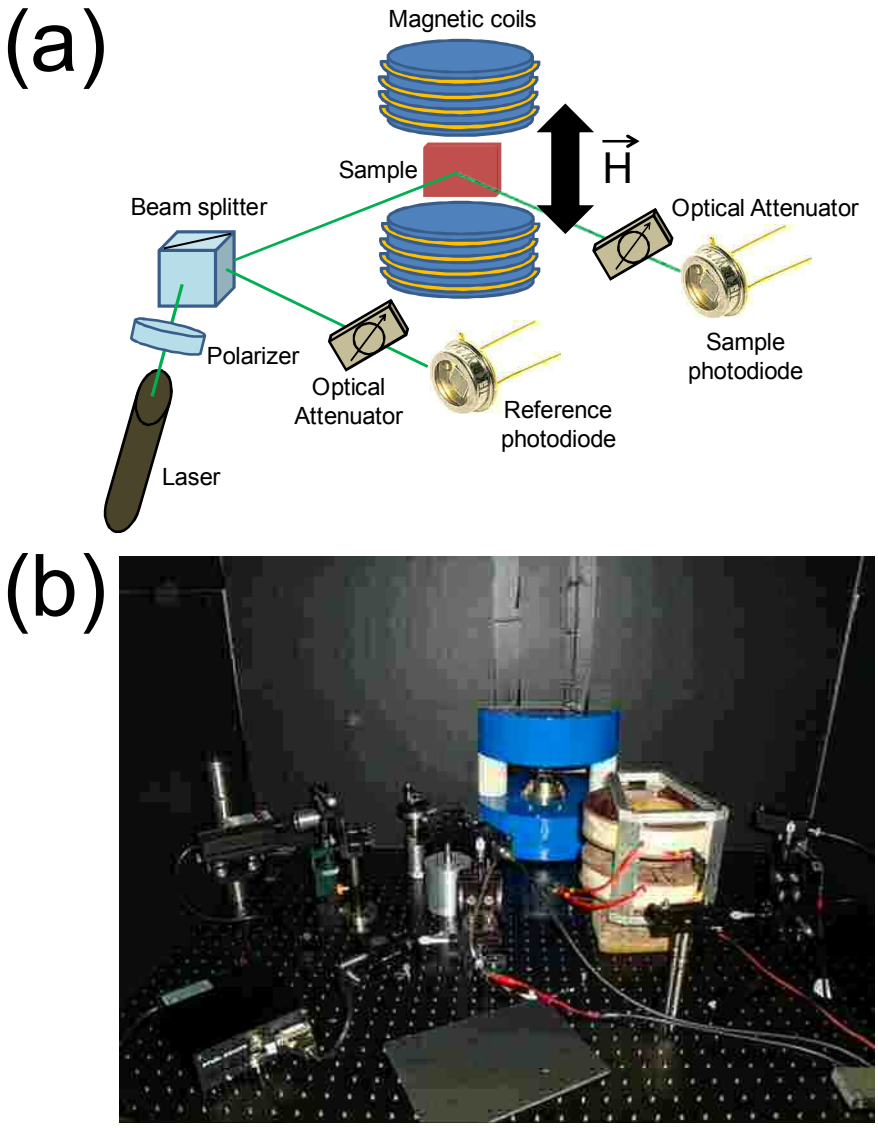

Fig. II. 15. Scheme (a) and photograph (b) of the TMOKE loops system.

Magnetic hysteresis loops with inplane magnetization have been obtained using the transverse magnetooptical Kerr effect (TMOKE) In transverse configuration, the magnetization is perpendicular to the incidence plane of the light and it is located on the plane of the sample.Using this configuration, reflectivity variations for the p polarized component of the light, which are proportional to the magnetization of the material at first order, are observed[25]. The sample is placed in between of two magnetic coils, where a static magnetic field is applied by minimum steps of 0.1 mT with maximum amplitude of 35 mT. The light is originated from a solid-state laser with λ=532 nm and

linearly polarized by a polarizer that only transmits the p-component of the light. That p-polarized light reaches a beam splitter which divides the beam in two. One beam impinges onto the magnetized sample at an incidence angle of 45º and then it is reflected to an optical attenuator and reaches a photodiode (sample photodiode). The other beam goes directly to an optical attenuator and reaches a reference photodiode (observe Fig. II. 15.). The function of the reference photodiode is to compensate the fluctuations and noise coming from the laser signal within the loop measurement.

The normalized variation between the two intensities (TMOKE signal) is recorded for each step of the applied magnetic field or magnetized state of the sample. being $R_{pp}(H)$ and $R_{pp}(H=0)$ the signals measured by the sample photodiode and the reference photodiode respectively. The signal of the two photodiodes are equalized previously to the loop measurement without magnetic field thus the signal of the reference photodiode can be considered as $R_{pp}(H=0)$ during the loop measurement. Thus this TMOKE signal is measured as a function of the applied magnetic field and averaged over typically 100 loops. This way, a magnetic hysteresis loop is obtained with the TMOKE signal defined as in the equation [II.23.]:

$$\frac{\Delta R_{pp}}{R_{pp}} \approx \frac{R_{pp}(H) - R_{pp}(H=0)}{R_{pp}(H=0)} \quad \text{[II.23]}$$

II.5.D- TMOKE measurements in Kretschmann configuration.

It is impossible to excite SPP waves with light impinging directly on a thick metal film[26]. This arises from the comparison between the wavevectors of the light and the SPP. The in-plane component of the wavevector for the incident light and the SPP are described by:

$$k_x^{light} = k_0 \sqrt{\varepsilon_d} \sin\theta$$

$$k_x^{SPP} = k_0 \sqrt{\frac{\varepsilon_m}{\varepsilon_d + \varepsilon_m}} \quad \text{[II.24]}$$

being k_0 the wavevector of the light in vacuum, ε_d and ε_m the dielectric permitivities of the insulator and metallic media respectively and θ the angle of incidence of the light. If we compare these wavevectors for the light and the SPP, we can state for any incident angle of the light:

$$\left|k_x^{light}\right| < \left|k_x^{SPP}\right| \quad \text{[II.25]}$$

This behavior is also observed in the SPP dispersion relation for any frequency lower than the ω_{SPP} (see figure II.16.). For achieving the k_{extra} to obtain the SPP excitation, diverse techniques are used, mainly: the Kretschmann configuration[27], the Otto configuration, the diffraction grating, near-field excitation and with a waveguide[28]. In this thesis work, the Kretschmann configuration[27] has been chosen to excite SPPs.

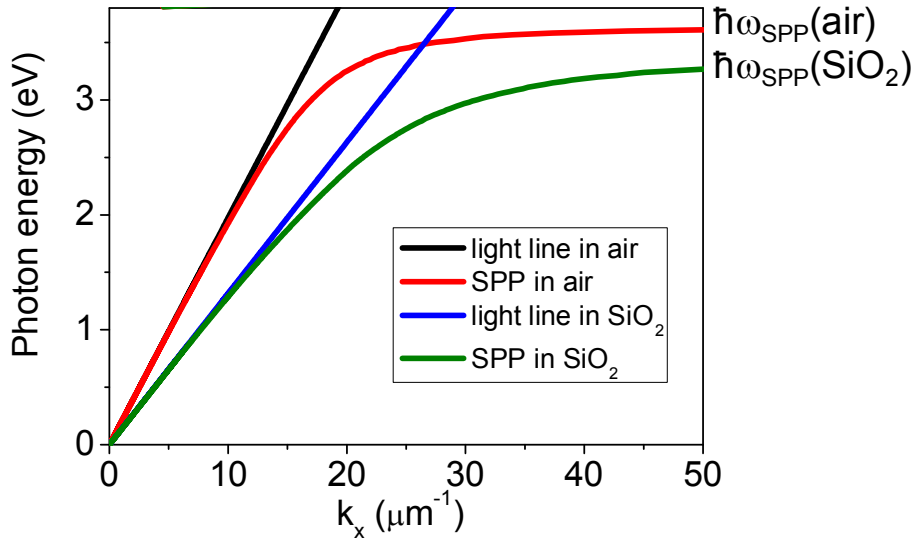

Fig. II. 16. Dispersion relations of two SPP excited in the interface of a Ag film and a dielectric with two different refractive index: air (red line) and SiO_2 (green line). These relations are compared with the light line in air (black line) and in SiO_2 (blue line).

That method is also known as prism coupling and it allows exciting the SPP confined at the metal-air interface (it is also possible at metal-water interfaces). The key factor is the use of a prism with a refractive index higher than the dielectric medium where the SPP would be excited. For example, we can consider air as the dielectric medium (ε_d=1) and Au, Ag, Co and Fe as the metallic media (the metals used in this thesis work) with the real part of ε_m= -12.8, -19.9, -5.15 and -5.36 respectively at our work wavelength (632.8 nm). The SPP wavevector for these metals is smaller than $1.12*k_0$ at the mentioned wavelength and therefore:

$$k_x^{SPP} = k_0\sqrt{\frac{\varepsilon_m}{1+\varepsilon_m}} < k_P = k_0\sqrt{\varepsilon_P} = 1.52 * k_0 \quad \text{[II.26]}$$

being k_p and ε_P the wavevector of the light inside the prism and the dielectric permitivity of a BK7 glass prism respectively. Thus the light coming from a typical BK7 prism gives the possibility to excite SPP waves in the metal-air interface of a metal thin film (please observe the sketch of Fig.II.17.(a)).

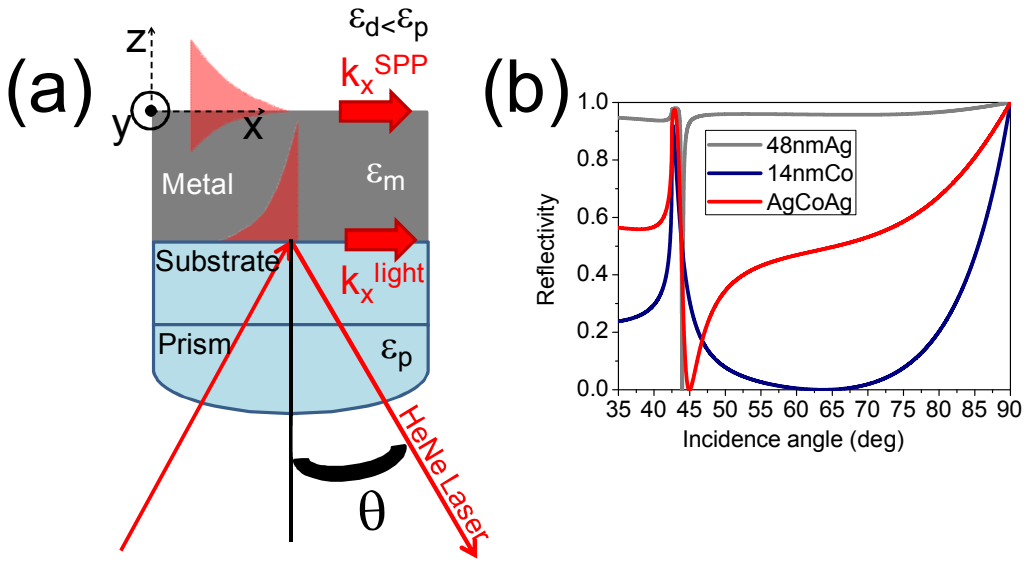

Fig. II. 17. (a) Kretschmann configuration sketch . (b) Simulated angular reflectivity curves for a 48 nm Ag/Glass (grey line), a 14 nm Co/Glass (purple line) and a 10 nm Ag/6 nm Co /9 nm Ag/Glass (red curve) exhibiting a minimum caused by the SPP excitation.

This relation is valid for any metal thickness above the cutoff thickness (thickness too low for confining the SPP field inside the metal). However, if the metal thickness is too high, the evanescent field of the incident light (that is coupled with the SPP resonance) does not reach the air-metal interface due to the optical absorption inside the metal. Therefore the optimum thickness of the metal layer for the SPP excitation has to be taken into account. This optimum thickness is dependent of the optical constants of the metal layer. The figure II.17.(b) shows three reflectivity curves performed via Transfer matrix simulations for a Ag film, a Co film and a Ag/Co/Ag multilayer on BK7 glass substrates (n=1.52). Around 42 degrees the three curves exhibits the characteristic maximum for the Total Reflection (TR) caused by the light travel between the glass and air media. Immediately, the reflectivity signal decreases due to the Attenuated Total Reflection (ATR) related to the SPP excitation into the metal-air interfaces[26,28]. The angular position and broadness of the Reflectivity minima are governed by the real and imaginary components of the Plasmon wavevector respectively. In particular, higher optical absorption leads to broader minima. It explains the great differences between the reflectivity curves for the Ag and Co film due to the higher optical absorption of Co compared to Ag in the visible region. Finally, the almost

zero reflectivity signal at the minimum positions for the three curves means that the light coupling to the SPP excitation is optimum for each layer thickness. Those optimum thickness for the Ag/Glass, Co/Glass, Ag/Co/Ag/Glass structures are 48 nm, 14 nm and 10 nm/6 nm /9 nm (for the sake of simplicity, the thicknesses of the top Ag layer and the Co layer were fixed, and that of the bottom Ag layer was varied). Therefore we can conclude that the higher optical absorption of the metal layer, the lower optimum thickness for the SPP excitation.

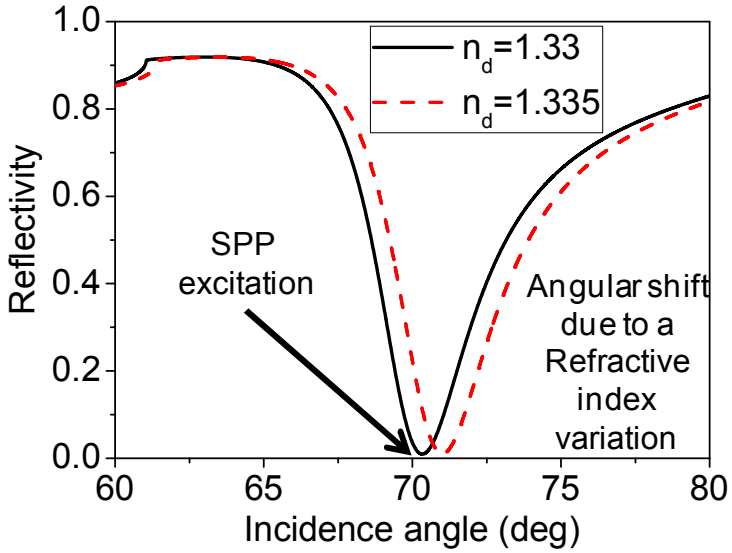

Fig. II. 18. Simulated Reflectivity as a function of the incidence angle of a 50 nm Au film over a BK7 glass substrate in a water medium. A curve is simulated with a refractive index n_d=1.330 (black continuous line) and the second one is simulated with a refractive index of n_d=1.335 (dashed red line).

The SPP resonance in a metal-insulator interface is highly dependent of the refractive index of the insulator medium as it can be verified in the equation [II.24.]. Therefore the variation of this refractive index changes the conditions for the excitation of the SPP in this interface or the same interface in a metallic thin film. As it is well known, these variations of the SPP resonance are widely used to the realization of optical sensor and biosensors with high sensitivity[29,30].

The Surface Plasmon Resonance (SPR) sensors can be divided by their excitation method: Prism coupling[31,32,33], diffraction gratings[34,35], integrated waveguides[36,37] and optical fibers[38,39]. The sensors based in the prism coupling are the most used and commercialized due to their simplicity.

In order to satisfy the condition for the surface Plasmon resonance there are two parameters of the incident light that can be changed: the wavelength and the incidence angle of the incident light (see equation [II.24]). In a sensor using the Kretschmann configuration[27] (schemed in figure II.17. (a)), we can simulate via Transfer matrix method the intensity of the reflected light as a function of the incident light for a medium with a refractive index of 1.33 (water) (see the figure II.18.). In this case, the total reflection is located around 62º. Then, the SPP resonance takes place as a

reflectivity minimum around 71º. Varying the refractive index of the dielectric medium, the reflectivity curve is angular shifted as it can be observed on the figure II.18. The measurement of this angular shift leads to an estimation for the refractive index variation of the dielectric medium. However, the usual way (and the way used in this thesis work) to detect the refractive index variations is performed with the light incident angle fixed around the half height of the resonance curve (68º on the figure II.18.) and measuring the variations for the intensity of the reflected light in real time.

Two experimental setups have been used for measuring the TMOKE signal under SPP excitation. The first one located at Instituto de Microelectrónica de Madrid (IMM-CSIC, Madrid, Spain) has been used to characterize the intertwined MO properties with the SPP resonance for magnetoplasmonic multilayers. On the other hand, the second one located at Istituto de Microelettronica e Microsistemi (IMM-CNR, Lecce, Italy) has been used for performing measurements of these magnetoplamonic multilayers as transducers for gas sensing and biosensing during two short stays under the supervision of the Dr. Mariagrazia Manera and the Prof. Roberto Rella.

II.5.D (i) Magnetoplasmonic characterization (Madrid system)

This experimental setup is sketched in figure II.19 (a) and is very similar to the previous one for measuring magnetic loops, since both systems measure the TMOKE of thin films. Again a laser is used as light source (in this case is a He-Ne laser with λ=632.8 nm), a polarizer for obtaining the p-component of the light, an electromagnet for magnetizing the sample in the transverse configuration and a photodiode for collecting the light reflected off the magnetized sample. Additionally, in this case, a lock-in amplifier and an AC magnetic field (with an amplitude around 350 Oe enough for achieving the saturation state of the sample and a frequency 18 Hz) are used. The time modulation is used to increase the signal-to-noise ratio (SNR) and to decrease the time consumed for each measurement. It can be performed since we are only interested in the TMOKE measurement at the saturation state of the magnetized sample in this setup.

On the other hand, the goniometer platform where the sample is mounted allows for measuring the reflectivity and TMOKE as a function of the incidence angle for the light impinging into the substrate side of the sample. In order to neglect the angular dependence of the reflectivity due to the air-substrate interface, the sample is coupled with a semispherical prism. The substrate is mounted onto the semispherical prism using immersion oil, which matches the refractive index of both substrate and prism allowing an optimum optical coupling between them. This part of the experimental

setup permits the excitation of the SPP confined in the metal-air interface of the sample and it is the aforementioned *Kretschmann configuration*[27].

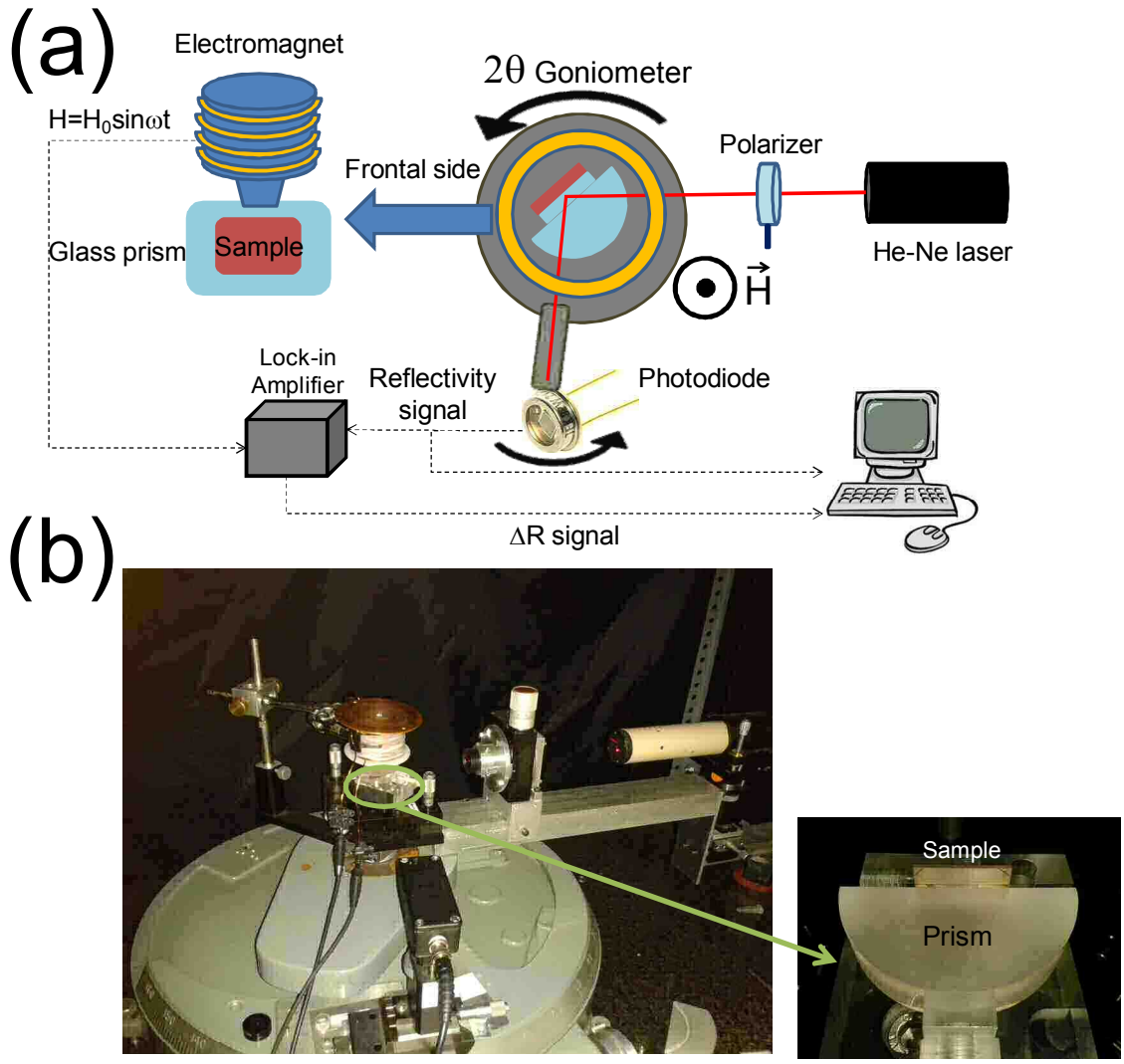

Fig. II. 19. Scheme (a) and photographs (b) of the setup for angular TMOKE measurements with Kretschmann configuration in order to excite SPPs.

II.5.D. (ii) Magnetoplasmonic sensing (Lecce system)

The second system is located at the Istituto de Microelettronica e Microsistemi (IMM-CNR) in Lecce, Italy. Reflectivity and TMOKE measurements have been performed under SPP excitation in order to test the SPR and MagnetoOptical Surface Plasmon Resonance[40] (MOSPR) sensing behavior of the magnetoplasmonic (MP) transducers. The setup for measuring the TMOKE is analogous to the previous one located at Madrid. SPP resonances have been excited by *Kretschmann configuration*[27] and TMOKE measurements have been performed via an AC magnetic field (with an amplitude around 50 Oe enough for achieving the saturation state of the sample and a frequency of 800 Hz since the SNR is a key factor in sensing experiments).

A suitable Teflon SPR test chamber has been used in order to analyze the sensing activity of these MP multilayers (see figure II.20.). The sensing performances of these MP samples have been investigated with different concentrations of vapours mixed in dry-air as carrier gas. As concerns the investigated organic vapours, at standard temperature and pressure they are liquid analytes: their saturated vapours (obtained by dry air bubbling at constant temperature) were diluted in a 20 mL vial with a dry air gas carrier and injected into the measurement cell. Dilution ratios for each Volatile Organic Compound (VOC) as well as defined mixtures of different VOCs were accurately regulated by a set of mass flow controllers (MKS Instruments) and a system of stainless steel pipelines and switching valves.

The obtained concentration of the saturated vapours depends on their saturated vapour pressure and the temperature at which the sample is kept. The maximum vapour concentration C_{max} formed in a closed test chamber can be calculated by dividing the vapour pressure at a given temperature by the atmospheric pressure (P_{atm}). For example, at 25 ºC the methanol vapour pressure is p_{25} = 16.9 *kPa* and the maximum vapours concentration is:

$$c_{\max} = \frac{p_{25}}{p_{atm}} \times 100 = 16.6 \times 10^4 \, ppm \quad \text{[II.27]}$$

To obtain different concentrations of the analyte vapours sent in the test chamber, the air flow carrying the saturated vapours was diluted to the reference flow of dry air in different suitable ratios for each vapour. As regards nitrogen dioxide and ammonia, certified bottles were used to obtain the desired concentration to be sent into the test chamber.

In each measurement the MP film was exposed to vapour(s) for about 20 min (necessary to reach a steady state for the sensor signal); then, after the measurements it was flushed with a pure dry air flow for about 20 min to restore the initial conditions. All measurements were performed at room temperature in a thermally conditioned

laboratory. Concerning the biosensing experiments, a flow system composed of a flow cell, a flow-injection valve, and a peristaltic pump allowed easily interchanging the liquid solutions, which carry the biomolecules towards the MP sensor.

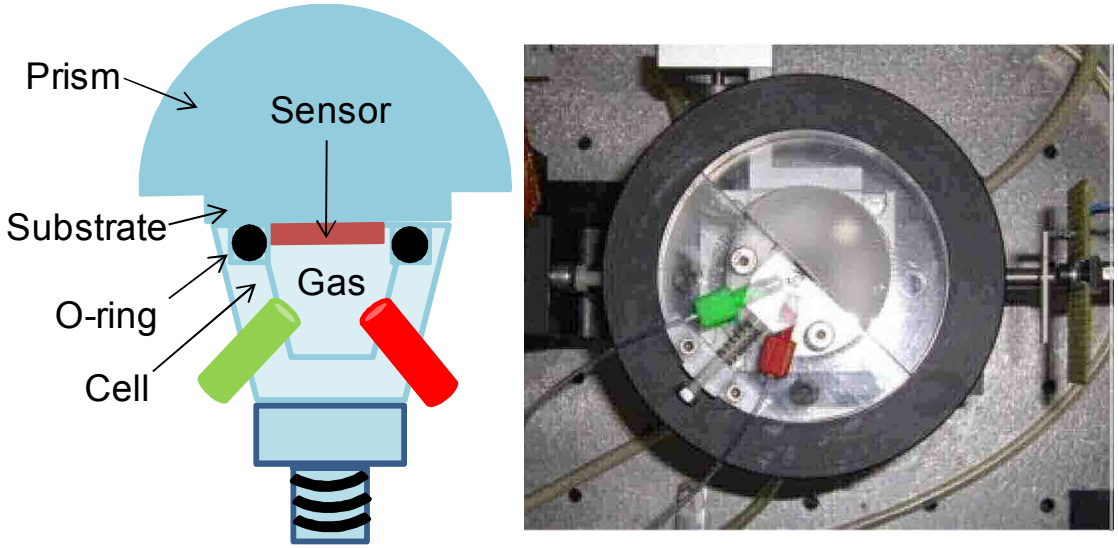

Fig. II. 20. Scheme (left side of the figure) and photograph (right side of the figure) of the setup for MOSPR sensor characterization located at IMM (Lecce, Italy).

II.6.-REFERENCES

[1] S. I. Shah, "*Sputtering: Introduction and general discussion*", Ed. D. A. Glocker and S. I. Shah, "Handbook of Thin Film Process Technology", IOP Publishing (1995).

[2] E. B. Graper, "*Electron Beam Evaporation*", Ed. D. A. Glocker and S. I. Shah, "Handbook of Thin Film Process Technology", IOP Publishing (1995).

[3] 1951 British patent 754 210.

[4] 1969 US patents 3230 110.

[5] C. Hammond, " The basics of Cristallography and Diffraction", Oxford Science Publications, New York (2001).

[6] B. K. Vainshtein, "Modern Crystallography", Spinger-Verlag, Berlin (1981).

[7] G. Binnig, C. F. Quate and Ch. Gerber, "Atomic Force Microscope", *Phys. Rev. Lett.* **56**, 930 (1986).

[8] Y. Martin, C. C. Williams, and H. K. Wickramasinghe, "Atomic force microscope–force mapping

and profiling on a sub 100-Å scale", *J. Appl. Phys.* **61**, 4723 (1987).

[9] T. R. Albrecht, P. Grütter, D. Horne, D. Rugar, "Frequency modulation detection using high-Q cantilevers for enhanced force microscope sensitivity", *J. Appl. Phys.* **69**, 668 (1991).

[10] A. K. Zvezdin and V. A. Kotov, "Modern Magnetooptics and Magnetooptical materials", Institute of Physics Publisshing Bristol and Philadelphia, Bristol (1997).

[11] WVASE32, Guide to using.

[12] H. TompKins and E. Irene, eds. Handbook of Ellipsometry, William Andrew Publishing, New York, 2005.

[13] E. Hecht, "Optics", Addison-Wesley Publishing Company, (1987).

[14] Complete Ease, Guide to using.

[15] M. Faraday, "Experimental researches in electricity. Nineteenth series", *Phil. Trans. Soc.* **136**, 1 (1846).

[16] J. Kerr, "On rotation of the plane of polarization by reflection from the pole of a magnet", *Phil. Mag.* **3**, 332 (1877).

[17] W. Voigt, "Magneto und elektrooptik", Leipzig (1908).

[18] J. L. Erskine and E. A. Stern, "Magneto-Optic Kerr Effects in Gadolinium", *Phys. Rev. B* **8**, 1239 (1973).

[19] K. H. J. Buschow, "Ferromagnetic Materials", Vol. **4**, *Elsevier Science Publishers B. V.* (1988).

[20] D. Weller, "Spin-orbit influenced spectroscopies of magnetic solids", Springer, Berlin, 1996.

[21] K. Sato, "Measurement of Magneto-Optical Kerr Effect Using Piezo-Birefringent Modulator", *Jap. J. Appl. Phys.* **20**, 2403 (1981).

[22] W. S. Kim, M. Aderholz, W. Kleemann, "Calibration of polar Kerr rotation and ellipticity measurements", *Meas. Sci. Technol* **4,** 1275 (1993).

[23] A. K. Zvezdin and V. A. Kotov, "Modern Magnetooptics and Magnetooptical Materials", *Institute of Physics Publishing Bristol and Philadelphia*, Bristol (1997).

[24] T. C. Oakberg, "Relative variation of stress-optic coefficient with wavelength in fused silica and calcium fluoride", *Meas. An. Rem. Sen. II,* 3754 (1999).

[25] C. Dehesa-Martínez, L. Blanco-Gutiérrez, M. Vélez, J. Díaz, L. M. Alvarez-Prado, and J. M. Alameda, "Magneto-optical transverse Kerr effect in multilayers", *Phys. Rev. B* **64**, 024417 (2001).

[26] H. Raether, *Surface Plasmons on Smooth and Rough Surfaces and on Gratings*, vol. 111 of *Springer Tracts in Modern Physics* (Springer-Verlag, Berlin, 1988).

[27] Kretschmann and H. Raether, *Z. Naturforsch*. A 23, 2135 (1968); E. Kretschmann, *Z.Phys* .241, 313 (1971).

[28] S. A. Maier, Plasmonics: Fundamentals and Applications (Springer, Berlin, 2007)

[29] Homola J., Yee S.S., Gauglitz G., "Surface plasmon resonance sensors: review", Sensors and Actuators B, **54** 528 (1999).

[30] Homola J., "Present and future of surface plasmon resonance biosensors", Analytical And Bioanalytical Chemistry **377,** 3 (2003).

[31] Nylander C., Liedberg B., Lind T., "Gas-Detection by Means of Surface-Plasmon Resonance", Sensors and Actuators **3**, 79 (1982).

[32] Flanagan M.T., Pantell R.H., "Surface-Plasmon Resonance and Immunosensors", Electronics Letters **20**, 968 (1984).

[33] Homola J, "Model of a Chemo-Optical Sensor Based on Plasmon Excitation in thin Silver Films", Sensors And Actuators B-Chemical **11**, 481 (1993).

[34] Cullen D.C., Brown R.G.W., Lowe C.R., "Detection of Immuno-Complex Formation Via Surface-Plasmon Resonance on Gold-Coated Diffraction Gratings", Biosensors **3**, 211 (1987).

[35] Homola J., Koudela I., Yee S.S., "Surface plasmon resonance sensors based on diffraction gratings and prism couplers: sensitivity comparison", Sensors and Actuators B **54,** 16 (1999).

[36] Homola J, Ctyroky J, Skalsky M, Hradilova J, Kolarova P, "A surface plasmon resonance based integrated optical sensor", Sensors And Actuators B **39,** 286 (1997).

[37] Dostalek J, Ctyroky J, Homola J, Brynda E, Skalsky M, Nekvindova P, Spirkova J, Skvor J, Schrofel J, "Surface plasmon resonance biosensor based on integrated optical waveguide", Sensors and Actuators B **76**, 8 (2001).

[38] Homola J, "Optical-Fiber Sensor-Based on Surface-Plasmon Excitation", Sensors and Actuators B **29**, 401 (1995).

[39] Bueno F.J., Esteban O., Diaz-Herrera N., Navarrete M.C., Gonzalez-Cano A., "Sensing properties of asymmetric double-layer-covered tapered fibers", Applied Optics **43**, 1615 (2004).

[40] Sepúlveda, B., Calle, A, Lechuga, L. M., Armelles, G. "Highly sensitive detection of biomolecules with the magneto-optic surface-plasmon-resonance sensor". Optics letters, *31*(8), 1085-1087 (2006).

Chapter III: Ag/Co/Ag multilayers

III.1.- INTRODUCTION **54**

III.2.- DETERIORATION OF THE MULTILAYERS IN AMBIENT CONDITIONS **56**

III.2.A.- Surface morphology 56

III.2.B.- Magnetoplasmonic characterization 57

III.2.C.- X-Ray photoelectron spectroscopy (XPS) 59

III.3.- Pt CAPPING LAYER STRUCTURES **62**

III.3.A.- Fabrication and morphology 62

III.3.B.-Magnetic characterization 63

III.3.C.-Magnetooptical characterization 63

III.3.D.-Magnetoplasmonic characterization 65

III.4.- Au CAPPING LAYER STRUCTURES **69**

III.4.A- Motivation of the structures 69

III.4.B.- Morphology 70

III.4.C.- Magnetic characterization 71

III.4.D.- Optical and Magneto-Optical characterization 72

III.4.E.- Magnetoplasmonic characterization 74

III.4.E.(i)- Surface plasmon resonance effects on the MO activity **75**

III.4.E.(ii)- Magnetic modulation of the SPP resonance **77**

III.4.F.- Comparison of the different magnetoplasmonic multilayers studied 79

III.6.-CONCLUSIONS **80**

III.7.-REFERENCES **81**

III.1.- INTRODUCTION

Although Au is the most common material on plasmonics, Ag is becoming a typical material for plasmonic applications in the form of nanowires[1,2], optical resonators[3,4] , nanoparticles[5,6], waveguides[7,8]... The use of Ag instead of Au is mainly carried out in experiments where the quality factor (Q factor) of the Plasmon resonance is a key parameter, since Ag exhibits more intense plasmon resonances than Au in the visible region due to its lower optical absorption and higher plasma frequency[9,10]. As an example of this fact, reflectivity maps have been calculated using the Transfer matrix[11] formalism for 50 nm Au/ BK7 Glass substrate and 50 nm Ag/ BK7 Glass substrate systems. In the figure III.1. the calculated maps as a function of both photon energy and wavevector with the light impinging from the glass side of the structure (Kretschmann configuration[12]) are shown. At low photon energies, the sharp lines following the minima of Reflectivity are related to the SPP excitation in the metal-air interfaces for the two metals. Both dispersion relations are quite similar in the low photon energy range (see the reflectivity curves for 800 nm of wavelength of both metals) however the SPP resonance for the Au film becomes very broad compared to the SPP resonance of the Ag film due to the mentioned optical losses of the Au metal in the visible range (see the reflectivity curves for 633 and mainly 514 nm wavelength of both metals). Therefore we can expect that Ag would provide enhanced performances compared to Au in magnetoplasmonic , since the sharper resonances of the Ag structures would allow longer propagation lengths of the excited SPPs (interesting for active plasmonic modulators) and higher sensitivity with refractive index variations of the dielectric medium (interesting for magnetooptical surface plasmon resonance sensing).

It is worth to mention that unfortunately Ag presents a serious drawback for the realization of these magnetoplamonic structures: Ag is chemical unstable in ambient conditions. Kovacs et al. have reported drastic variations in the SPP resonance of Ag films due to the formation of a Ag_2S layer over the Ag surface exposed to air in the laboratory[13,14], even though a possible oxidation of these Ag layers cannot be excluded as a possibility[15]. For this reason, the deposition of a thin capping layer over the Ag to protect it from deterioration has been already used for sensing applications. For instance, a comparison of the sensitivity of Ag and Au films covered by an ITO layer as transducers for SPR sensing has been reported[16]. However, an appreciable degradation is observed for the ITO/Ag systems after several weeks storage in ambient atmosphere.

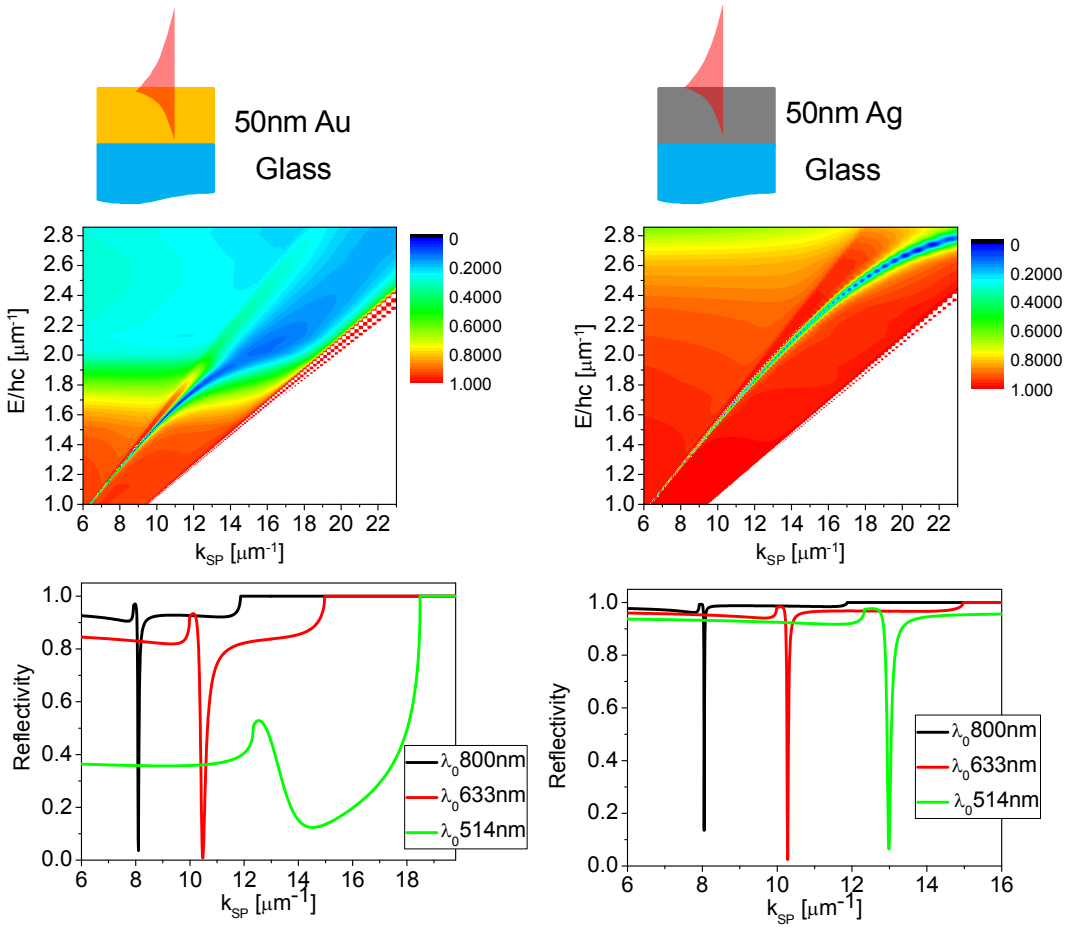

Fig III.1. Simulated Reflectivity maps as a function of both photon energy and wavevector (dispersion relations) for a 50 nm Au (left column of the figure) and 50 nm Ag (right column of the figure) films. Reflectivity profiles for 800 nm (black lines), 633 nm (red lines) and 514 nm (green lines) wavelength are presented in the bottom part of the figure.

In this chapter, we have explored the actual need of such a capping layer by the use of two different materials to protect Ag from deterioration: Pt and Au. Both materials are noble metals and generally non-reactive elements since they do not oxidize in ambient conditions, being therefore both good candidates to protect the multilayer system. In fact, Au exhibits sharper SPP resonances compared to Pt[17] (actually, Pt exhibits observable SPP resonances in the near-infrared but their SPP resonances are not observable in the visible region) thus the Au is a better option for the plasmonic applications. Nevertheless, the main aim of the capping layer is the protection of the Ag/Co/Ag trilayer using a minimum thickness of protecting material. Au and Pt capping layers were successfully used in our group for the protection of ferromagnetic materials (such as Co[18] or Fe[19]). A better conformational growth of a 2.5 nm Pt capping layer over a nanoparticulate Co film compared to the Au (with higher surface diffusion) capping layer has been reported[20]. In conclusion, the first option for the capping layer was a 2 nm Pt film due to the better conformational behavior with respect to Au, but finally better results were obtained with 5 nm Au capping layer.

To have a reference in absolute terms of the protective effects of the explored capping layer, it is necessary first to carry out a study of the air deterioration of unprotected Ag/Co/Ag multilayers. Subsequently, the morphological, magnetic, magnetooptical and magnetoplasmonic properties of Ag/Co/Ag systems with two different metals (Pt[21] and Au[22]) as capping layers will be presented.

III.2.- DETERIORATION OF THE MULTILAYERS IN AMBIENT CONDITIONS

In order to prove the need of a capping layer, we will describe the evolution of both the MO activity and the SPP resonance for Ag/Co/Ag multilayers with and without a Au capping layer in long term periods of time. As it is usually known the Ag chemically reacts with some agents present in the room atmosphere. Oxides and sulfides layers can be formed over the multilayer leading to a change of the optical properties, and therefore of the SPP resonance of the studied system. Moreover the buried Co layer can be affected by the reactive agents and it can loose its ferromagnetic nature and thus its high MO activity. For this study, two samples have been deposited over BK7 glass substrates in the sputtering system with the nominal structures: 5 nm Au/5 nm Ag/5 nm Co/7 nm Ag and 10 nm Ag/5 nm Co/7 nm Ag.

III.2.A.- Surface morphology

AFM measurements have been performed to control the eventual surface changes produced by the formation of new chemical compounds in the multilayered system. The first AFM measurements were done after a month after the multilayer deposition (see figure III.2. (a) and (b)). The AFM images for the two samples exhibit a granular surface characteristic of the sputtering deposition with an average height and diameter around 4 nm and 50 nm respectively as shown in the AFM profiles. These images are similar to those obtained just after the deposition, and therefore we can state that the surface morphology is not clearly affected by the ambient conditions within a month. On the other hand, some differences appear between the surfaces of the two kinds of structures for the AFM measurements performed after two years of the multilayer growth (see figure III.2. (c) and (d)). The AFM image for the Au/Ag/Co/Ag sample is still exhibiting the same morphology of the previous AFM measurements in contrast with the AFM image for the Ag/Co/Ag sample. Higher (around 50 nm height) and wider (around 200 nm width) structures are present in the surface compared to the pervious AFM image for the sample without Au capping layer. This drastic change of

the surface morphology must be related to the subsequent chemical reactions along the time, which are easily produced in the sample without a stable capping material.

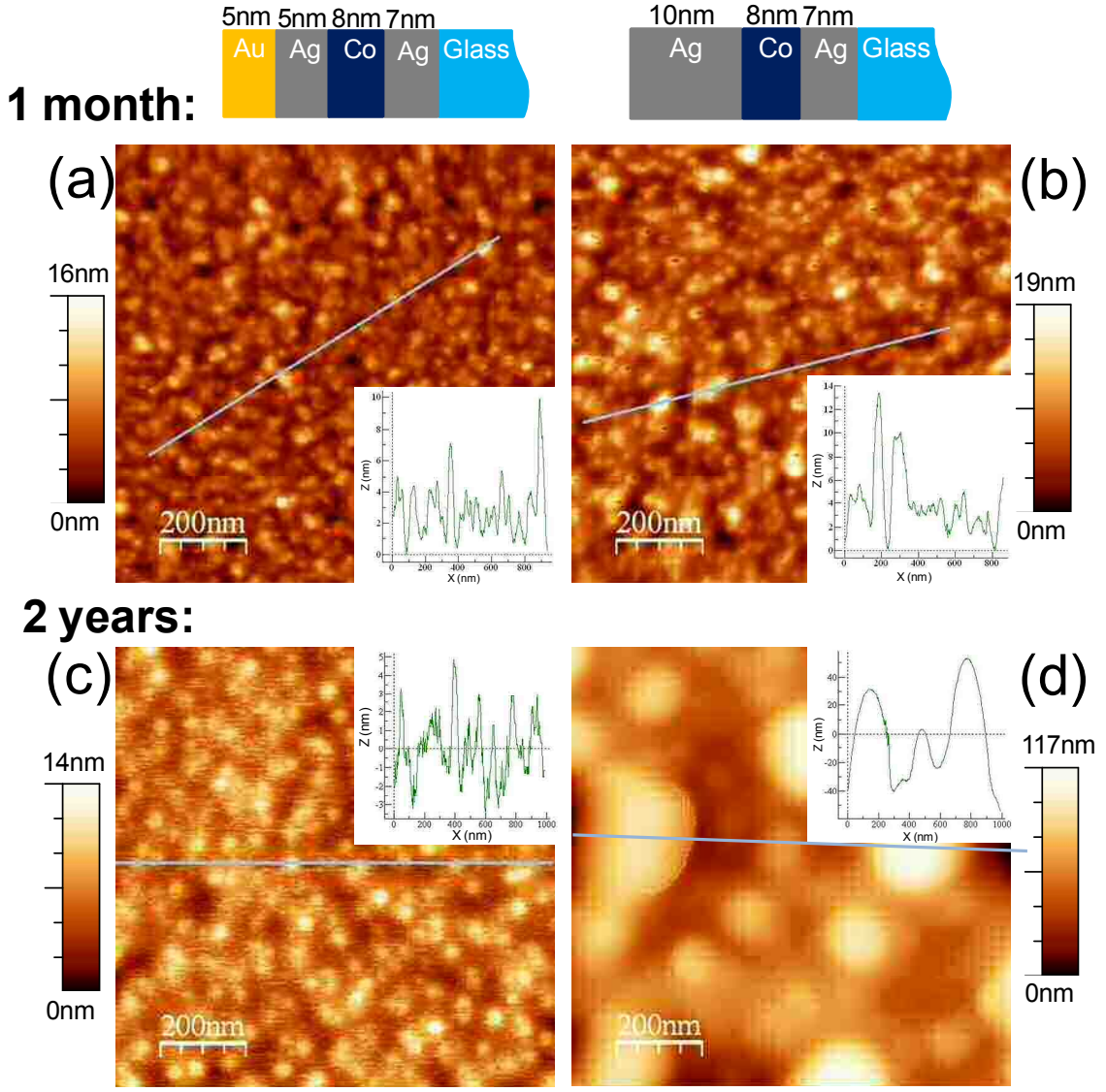

Fig. III.2. AFM images of the Au/Ag/Co/Ag (left column of the figure) and Ag/Co/Ag (right column of the figure) samples in two periods of the time: after 1 month ((a) and (b)) and after 2 years ((c) and (d)) from the multilayer growth. The insets of the respective figures show the AFM profiles taken along the mark indicated in each AFM image.

III.2.B.- Magnetoplasmonic characterization

Angular Reflectivity and TMOKE curves were measured under Kretschmann configuration to excite the SPP resonance for both samples in different periods of time. In the case of the Au/Ag/Co/Ag structure, both the Reflectivity minima (figure III.3.(a)) and the TMOKE maxima (figure III.3.(c)) exhibit an angular shift with time under

ambient conditions. This angular shift could be due to the formation of a dielectric layer over the Au/Ag/Co/Ag by condensation of the vapours from the room atmosphere, in a similar way to what happens in a SPR sensor[23]. It is important to remark that the line shape of the reflectivity curve does not vary with time (which indicates that the optical properties of the metallic multilayer are almost unaltered[24]) and the maximum of the TMOKE signal is very similar along the time (which provides information of the preservation of the Co layer from oxidation).In clear contrast, the Reflectivity minima of the sample without capping layer (Ag/Co/Ag trilayer) (figure III.3.(b)) become wider and present a higher angular shift compared to the Au/Ag/Ag/Co/Ag one with time. These two phenomena could be related to the chemical formation of some compound from mainly the Ag material and reactive elements of the room atmosphere[13]. Moreover, the decrease of around one order of magnitude for the TMOKE signal (figure III.3.(d)) with time is attributed to a high chemical deterioration (possible oxidation) of the Co layer.

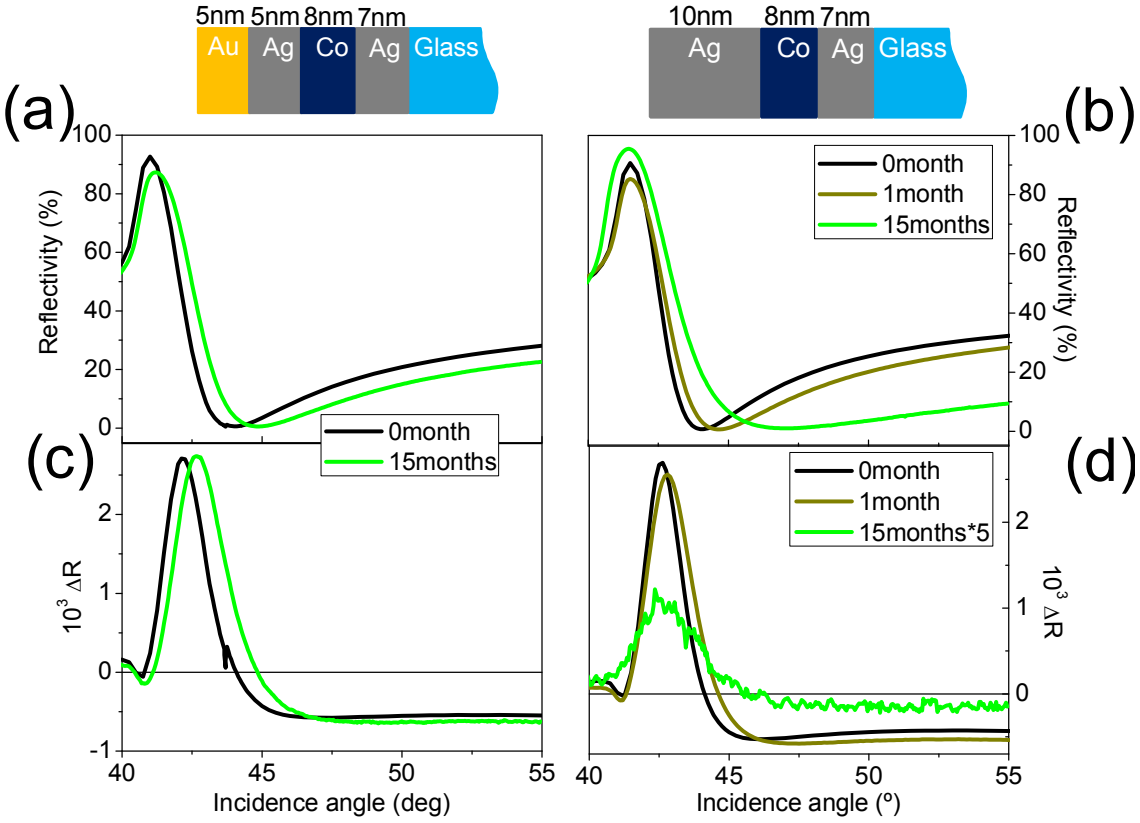

Fig. III.3. Angular measurements of the TMOKE effect using Kretschmann configuration in order to achieve SPP excitation for both structures with 0 month (black curves), 1 month (yellow curves) and 15 months (green curves) since their fabrication. The upper panels of the figure show the Reflectivity curves for both the (a)Au/Ag/Co/Ag sample and (b) Ag/Co/Ag sample. The bottom panels of the figure show the TMOKE curves for the (c)Au/Ag/Co/Ag sample and (d) Ag/Co/Ag sample. Please take care that the TMOKE signal for the 15 months in Ag/Co/Ag has been multiplied by 5 for the sake of clarity.

III.2.C.- X-Ray photoelectron spectroscopy (XPS)

Finally, XPS experiments were performed in the two samples (after two years of their fabrication) by Yves Huttel and Elisa Román-García from the group of Low-Dimensional Advanced Materials at the Instituto de Ciencia de Materiales de Madrid (ICMM). The aim of these experiments has been to indentify and to localize the diverse chemical compounds in the multilayer after the interaction with the chemical agents of the ambient atmosphere within 2 years for both structures.

The only unexpected chemical element observed in the Au/Ag/Co/Ag multilayer is C (see figure III.4.(a)) its presence being mainly located on the sample surface (on the Au layer). Probably this presence of C is due to the adsorption of organic vapours present in the laboratory environment over the sample surface. It is worth to mention that no traces of O are detected inside the structure. O is only present at the multilayer surface and at the multilayer-glass substrate interface (where Si is also detected). This proves that both Ag and Co layers have been effectively protected from the chemical interaction with O or other components by the deposition of the Au capping layer.

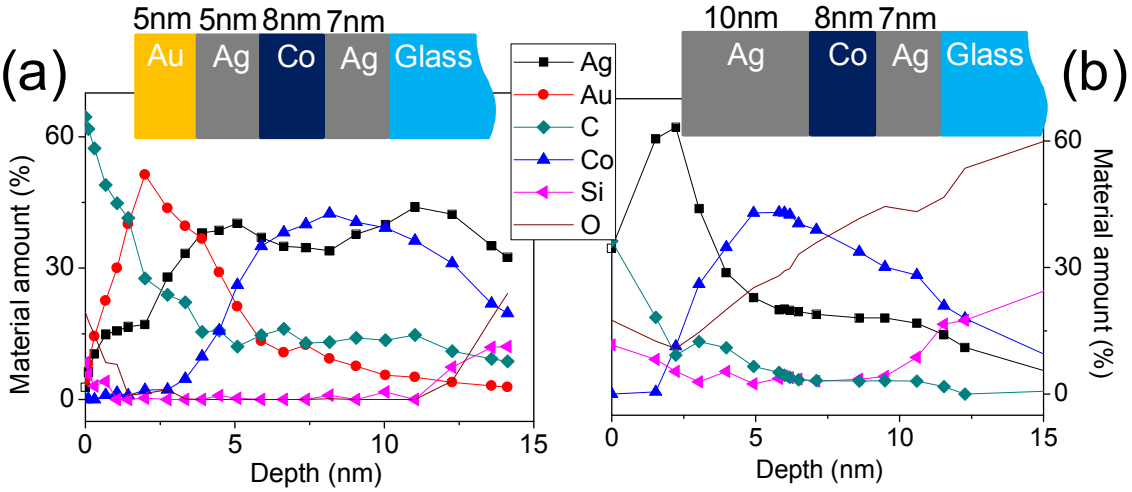

Fig. III.4. XPS measurements as a function of depth inside Au/Ag/Co/Ag(a) and Ag/Co/Ag(b) samples after two years maintained in ambient conditions since their fabrication.

On the other hand, the Ag/Co/Ag system presents a totally different O distribution inside the multilayer, being detected inside the whole structure. As a matter of fact, the O concentration is increasing with the depth of the structure achieving a 50% of concentration in the Co layer region. This explains why, after long exposure to ambient conditions, the TMOKE signal has almost disappeared and the SPR resonance has been strongly modified compared to the first measurements performed. It is worth

to mention that there is no evidence of the presence of S inside both multilayers, in opposition to the results of Kovacs[13]. Even though a conclusive justification for this difference is not obvious, it may be due to different ambient conditions between Kovacs experiments and those presented in this thesis work.

The presence of Oxygen inside the Co layer does not completely guarantee the existence of a chemical reaction between these two elements. In order to study that, XPS spectra as a function of the Binding Energy (BE) have been performed at different depths inside the two structures. In the figure III.5. (a) the spectra for the Au/Ag/Co/Ag multilayer present the two characteristic peaks corresponding to the $2P_{3/2}$ (778 eV) and $2P_{1/2}$ (793 eV) orbitals of the metallic Co. This metallic behavior of the Co is maintained for any depth inside the Au/Ag/Co/Ag rejecting any oxidation inside the Co layer. In opposition, the spectra for the structure without capping layer (fig. III.5. (b)) exhibits four peaks: the $2P_{3/2}$ and $2P_{1/2}$ peaks of the metallic Co and two extra peaks. These extra peaks are called "shake-up satellites", being typical for the 3d transition metal compounds or complexes[25]. These shake-up satellites and the energy shift towards higher BE of the $2P_{3/2}$ and $2P_{1/2}$ peaks indicate the formation of paramagnetic Co^{2+} ions[26,27,28], which is confirmed by the decreased TMOKE signal obtained from the corresponding magnetoplasmonic characterization. Besides, the relative intensity for these satellite peaks increases with the depth inside the multilayer. This indicates that the Co layer is highly composed of Co^{2+} ions, discarding a marginal formation of these compounds on the sample surface. Several works report the predominant formation of $Co(OH)_2$ compounds from a metallic Co film exposed to ambient atmosphere or water vapours under ambient conditions[27,29,30]. However, the formation of CoO oxide is also possible in rich O_2 atmospheres in ambient conditions.

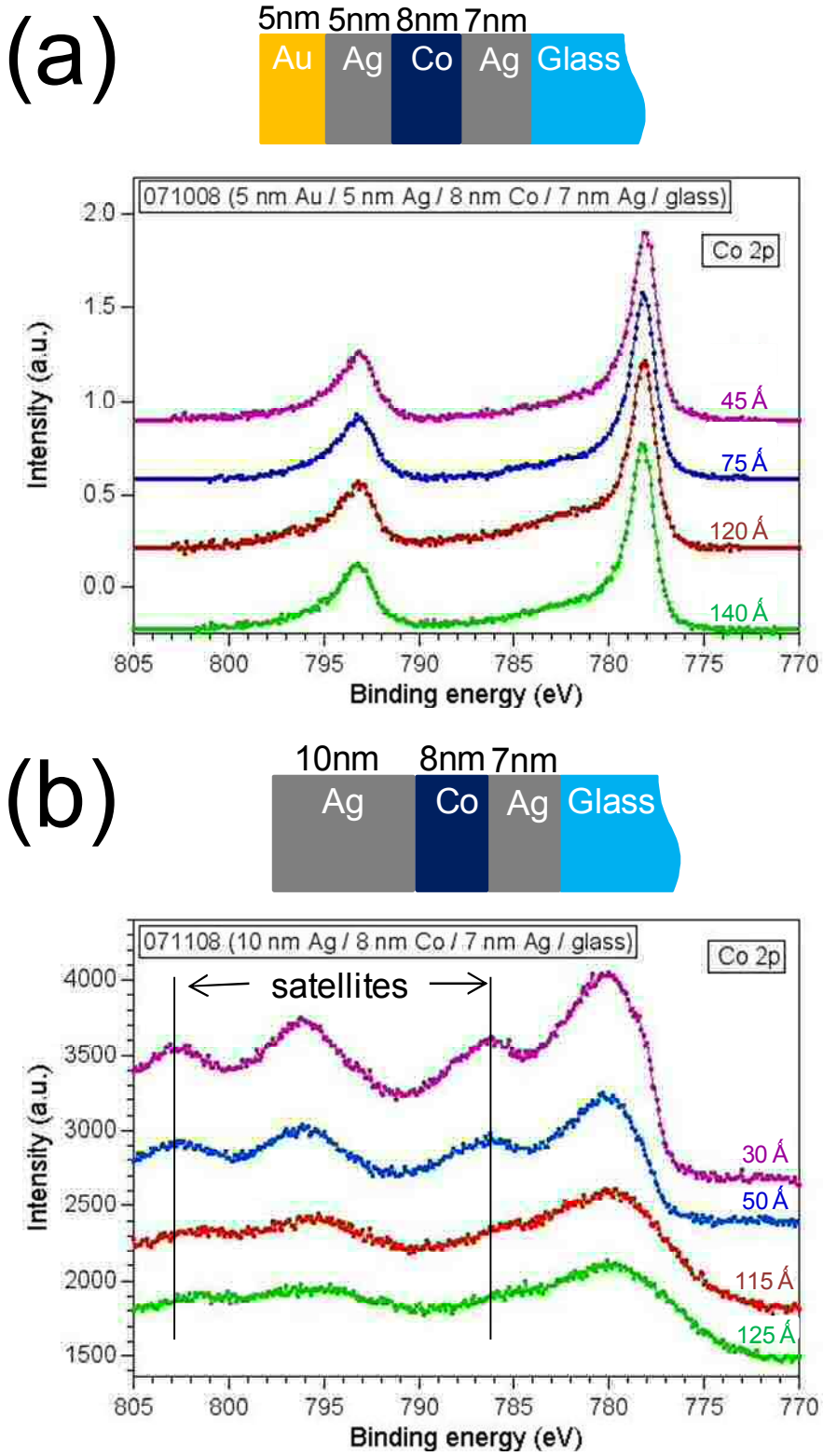

Fig. III.5. XPS Co 2P spectra at different depths inside the Au/Ag/Co/Ag(a) and Ag/Co/Ag(b) samples after two years maintained in ambient conditions since their fabrication.

III.3.- Pt CAPPING LAYER STRUCTURES

III.3.A.- Fabrication and morphology

Two series of 2 nm Pt/7 nm Ag/Co X nm/16 nm Ag structures have been grown simultaneously by magnetron sputtering at RT, one over glass substrates and another one over polycrystalline quartz in the Instituto Potosino de Investigación Científica y Tecnológica IPICYT (San Luís Potosí, Mexico) by Dr. David Meneses Rodríguez and Prof. Emilio Muñoz Sandoval. The Co thickness X was varied between 0 and 7 nm. Samples grown on glass have been used in transverse Kerr experiments with SPP excitation, and samples grown on quartz have been used in the rest of experiments. The morphology of the fabricated structures has been investigated both by SEM and AFM measurements. In Fig. III.6. we show both an AFM image (a) and a topographic profile (b) of the 3.5 nm Co thickness sample that is representative of the series. As it can be seen, the surface presents a granular morphology with a characteristic roughness that indicates a deviation from 2D growth.

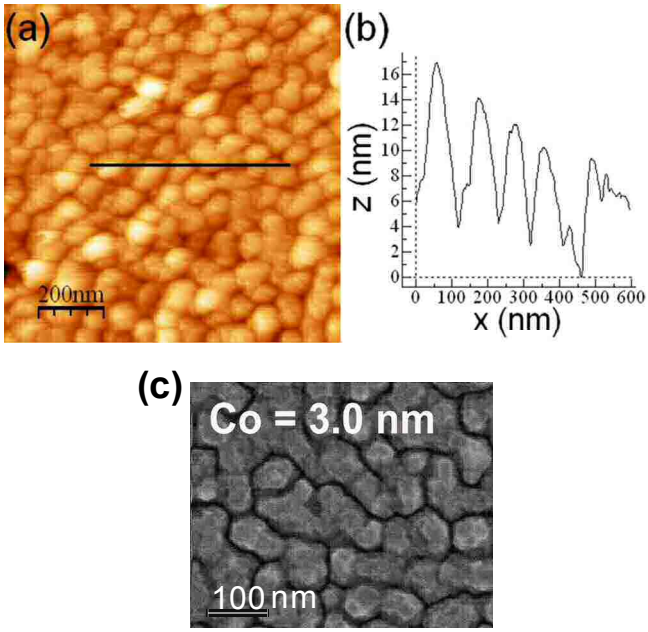

Fig III.6. (a) AFM image of the 3.5 nm Co thick sample. (b) Line profile taken along the mark indicated on (a). In both images the high roughness of the surface can be appreciated. (c) SEM image of the 3 nm Co thickness sample.

Mounds of about 50 nm diameter and 10 nm depth cover the surface. Since the total thickness of the fabricated structures ranges between 25 and 32 nm, this morphology is attributed to the first Ag layer, with a characteristic roughness that propagates upon deposition of successive Co, Ag and Pt layers (this fact will be studied in detail in Appendix I). The Scanning Electron Microscope (SEM) image for the 3 nm Co thickness sample (figure III.3.(c)) confirms this granular shape and rough surface for

these samples.

III.3.B.-Magnetic characterization

Both transverse and polar Kerr rotation hysteresis loops (sensitive to in-plane and out-of-plane magnetization, respectively) are measured for all the samples to determine the magnetic anisotropy. The low saturation field and the high remanent magnetization observed for the transverse loops, compared with the polar ones, evidence an in-plane magnetic anisotropy for all the samples (transverse (a) and polar (b) loops of a representative sample are given in Fig. III.7.). We have verified that the loops are similar in all in-plane directions, as expected from the isotropic mounds observed by AFM. Taking into account such morphology and the polycrystalline structure of the samples, it can be stated that shape anisotropy dominates.

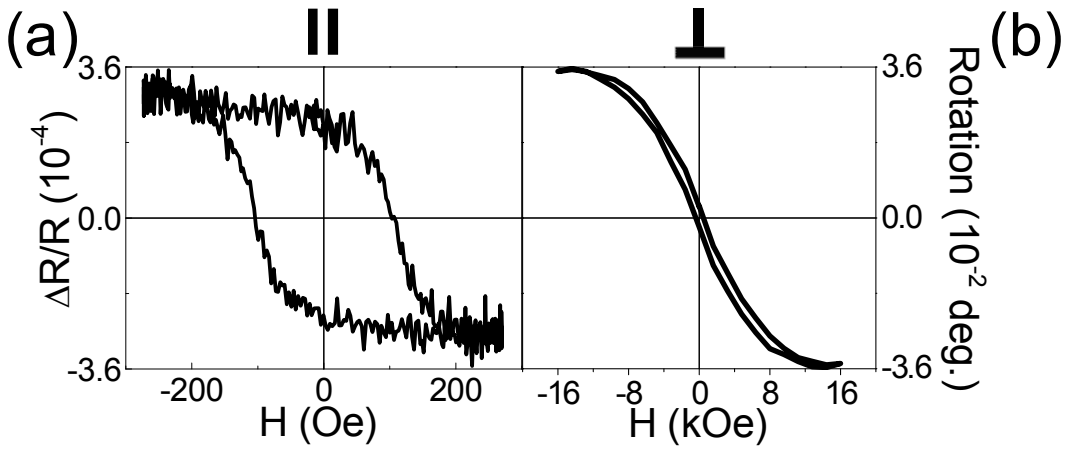

Fig. III.7. Kerr loops of a representative sample (4.5 nm Co thickness) measured in (a) Transversal and (b) Polar configurations.

III.3.C.-Magnetooptical characterization

The MO response has been studied using the Kerr effect in polar configuration, i.e. applying a 1.6 T magnetic field perpendicular to the sample surface and measuring the light at normal incidence reflected by the magnetized sample, in particular the rotation of the polarization plane and the change in the ellipticity state with respect to the incident linearly polarized light.

Fig. III.8. shows the rotation and ellipticity spectra for all the samples. The experimental ellipticity spectra (upper panel of the left column) show a characteristic negative peak around 3.75 eV that can be attributed to the bulk plasmon resonance of Ag[31]. Kerr rotation spectra (lower panel of the left column) also varies gradually with

increasing amount of Co, with a broad minimum around 3.4 eV only clearly observed for Co thickness above 3.5 nm, and a well defined maximum at around 3.9 eV. Such gradual variation of the MO ellipticity and rotation spectra with Co thickness has been qualitatively reproduced using simulations made with the Transfer Matrix method[11], even though some differences are observed. Regarding the theoretical ellipticity spectra, the zero crossing occurs at lower photon energies and the position of the minimum around 3.75 eV is basically independent of the amount of Co, while in the experiments the zero crossing occurs at higher energies and the position of the minimum shifts with Co thickness to higher energies.

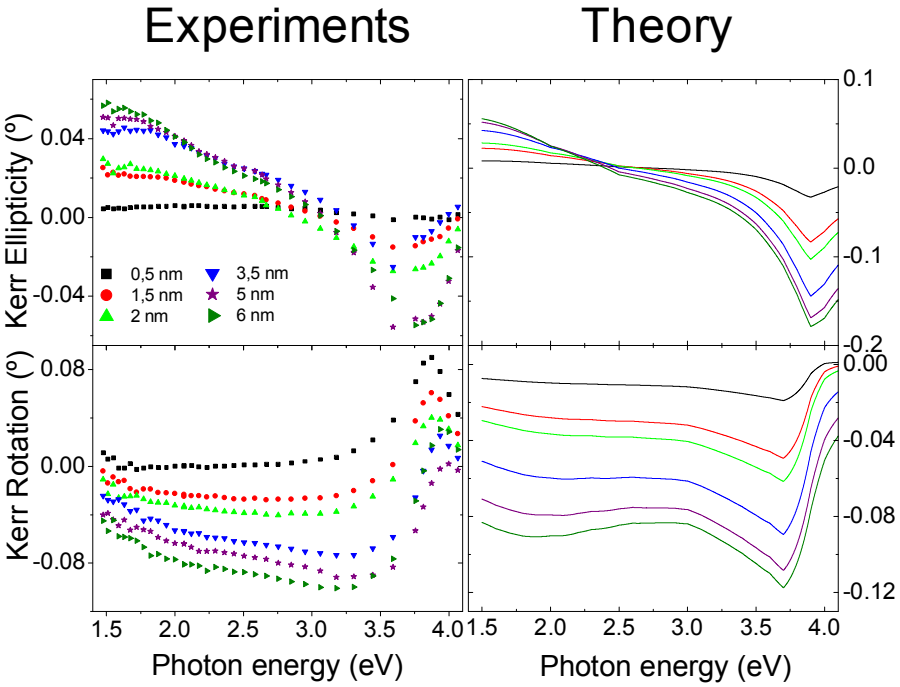

Fig. III.8. Experimental (left column) and theoretical (right column) ellipticity and rotation spectra (upper and lower panels, respectively) of the samples.

On the other hand, the calculated Kerr rotation spectra (lower panel of the right column) show a sharp minimum at 3.75 eV together with a maximum above 4 eV, while the minimum is hardly observed experimentally and the maximum occurs at somehow lower energies. In addition, both calculated ellipticity and rotation values are systematically larger than the corresponding experimental ones. All these discrepancies are very likely due to the rough morphology of the structures that implies a deviation from the flat interface structures used in the calculations. Moreover, a possible Ag and Co oxidation induced by a poor Pt protection of the structure can also contribute to the observed differences. However, qualitatively both the spectral behaviour and their overall trend with the amount of Co are reproduced.

III.3.D.-Magnetoplasmonic characterization

To study this first point, measurements of the transverse MO Kerr effect were carried out with and without SPP excitation. To excite the SPP we use the Kretschmann configuration[12] (see Fig. III.9. (a)). When the reference value of the transverse MO Kerr signal without SPP excitation is needed, the measurement is performed with light coming from the air side, i. e. incoming from the left in Fig. III.9. (a), where SPP excitation is not allowed.

In figure III.9. (b) we show the reflectivity versus incidence angle curve for the 2 nm Co sample as an example, together with the transverse Kerr signal (ΔR/R). The SPP excitation manifests itself as a minimum on the reflectivity at a specific angle of incidence ($\theta_{min} \cong 44^o$ here) above the critical angle for total internal reflection (around 41.5º in this case). The angle for SPP excitation corresponds to the matching between the in-plane component of the wavevector of the incident light and that of the SPP, therefore the SPP wavevector (k_{SPP}) can be obtained from:

$$k_{SPP} = \frac{2\pi}{\lambda}\sin\left(\theta_{\min}\right) \qquad [III.1]$$

where λ is the wavelength of the incident light in vacuum.

The variation of reflectivity when applying opposite magnetic fields (ΔR) also exhibits a maximum in this angular region, and as a consequence the transverse Kerr signal is characterized by a sharp resonance-like angular behaviour at around 44º, i.e. when the SPP is excited (figure III.9. (b)). When the SPP is not excited (illuminating the structure from the left hand side in figure III.9. (a)) neither R nor ΔR/R exhibit basically any angular dependence. Previously, values for ΔR/R in Au/Co/Au under SPP excitation conditions up to one order of magnitude larger than those without SPP excitation have been obtained[32,33,34], due both to a simultaneous reduction in the reflectivity of the system and to an enhancement of the electromagnetic field at the MO active layer, i.e. the Co layer.

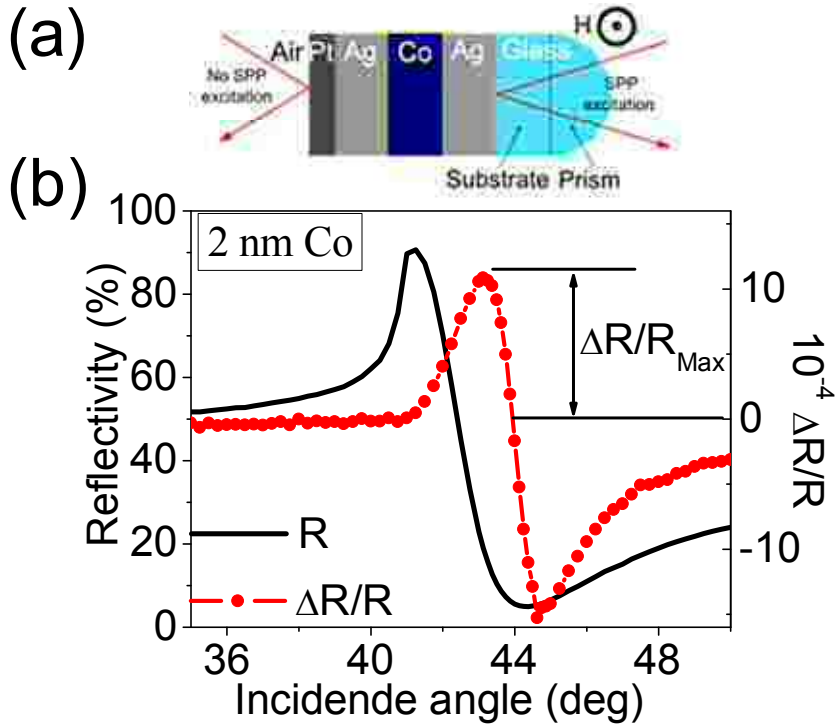

Fig. III.9. (a) Schematic view of the sample configuration. If the light is incident from the left, no SPP excitation occurs; if light is incident from the right the prism allows SPP excitation (Kretschmann configuration). (b) Measurements of the reflectivity and MO signal for the 2 nm Co thickness sample. A large enhancement on the MO signal when the SPP is excited (absorption peak of reflectivity) can be appreciated.

By defining the maximum of the reflectivity variation, $\Delta R/R_{Max}$, as its maximum positive value (see Fig III.9. (b)) we can study the Co thickness dependence of this magnitude and compare it with its counterpart obtained without plasmon resonance excitation. In Fig. III.10. (a) we show the experimentally determined transverse Kerr signals, both with and without SPP excitation, as a function of Co thickness. As it can be observed, when no SPP excitation is present, the MO signal exhibits the expected behaviour and monotonously increases with Co amount. However, when the SPP resonance is excited, a maximum is observed at around 2nm Co thickness, gradually decreasing for thicker Co layers. This is due to the optimum excitation of the SPP at this specific Co thickness and to the subsequent maximization of the electromagnetic field at the MO active (Co) layer. For thicker Co thickness, the higher optical absorption of the system makes the SPP excitation not optimal anymore. It is worth mentioning that this behaviour is similar to that obtained in Au/Co/Au trilayers[34] where the maximum was obtained for about 6 nm Co thickness. This different Co thickness for optimal SPP excitation and therefore maximum MO transverse Kerr signal is due to the different optical constants of the Au/Co/Au trilayers compared to the Pt/Ag/Co/Ag multilayers and the different thickness of the layers involved.

The transverse Kerr signal, with and without SPP excitation for such structures, has been calculated via Transfer Matrix method simulations using bulk values for the optical constants of the materials, and is presented in Fig. III.10.(b). As it can be seen, in the absence of SPP excitation ΔR/R gradually increases with the amount of Co, while it exhibits a maximum for 2 nm of Co when SPP is excited, in excellent agreement with the experimental results. However, both the magnitude of the effect and the sharpness of the curve are much higher in the calculations than in the experiment. This is probably due to the deviation from the ideal structures that the theory is treating. The growth mode is far from 2D, yielding a rough morphology and the absence of sharp interfaces in lateral areas of hundreds of nm. As a consequence, a good protection of the layers by the Pt capping is not easily guaranteed and partial oxidation of Ag, Co or both cannot be excluded. Taking this into account, the actual optical and magnetooptical constants of the layers may differ from the bulk ones used in the calculations. For example, these differences can give rise to the breadth of the SPP resonance in the experimental Reflectivity curve for the 2 nm Pt/7 nm Ag/2 nmCo/16 nm Ag sample compared to the simulated one (see figure III.10.(c)). In fact, the experimental curve for the PtAgCoAg sample is broader than a simulated reflectivity curve for a 6 nm Au/6 nm Co/16 nm Au sample[34]. Therefore we can conclude at this stage that the potential advantages of using Pt capped Ag instead of Au were not actually reached in these real systems.

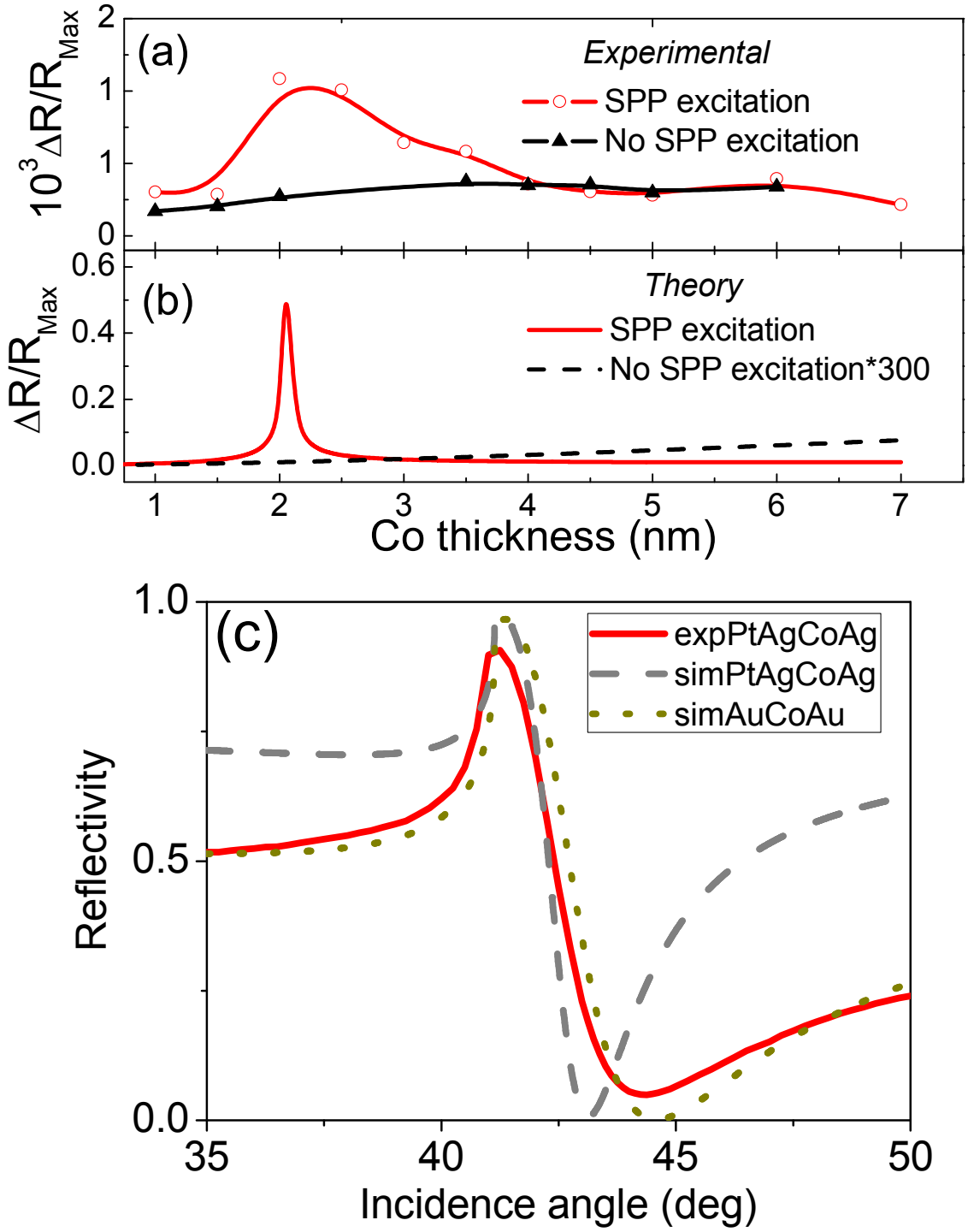

Fig III.10. Co thickness dependence of the transversal MO signal with and without SPP excitation. (a) Experimental results for 633 nm light (lines are just a guide for the eyes). (b) Simulation using transfer matrix formalism. We can see a strong Co dependence peak around 2 nm when SPP is excited, contrary to the non excitation case, where the MO signal gradually increases with Co thickness. (c) Reflectivity curves of the 2 nm Pt/7 nm Ag/2 nm Co/16 nm Ag and a 6 nm Au/6 nm Co/16 nm Au sample. The Pt/Ag/Co/Ag curve has been experimentally measured (continuous red line) and theoretically calculated by Transfer matrix simulations (dashed grey line). The Au/Co/Au curve (pointed golden line) has been only done by simulations.

III.4.- Au CAPPING LAYER STRUCTURES

III.4.A- Motivation of the structures

Since the results of the Pt/Ag/Co/Ag samples pinpointed the mentioned problems with the Co deterioration, the next step was the use of a new material as capping material instead of Pt. Au presents excellent performance for plasmonic applications in the visible range. Besides it is highly chemically stable in ambient conditions, and therefore using a Au thin film as capping layer was a logical choice at this stage.

The simulated Reflectivity curves via Transfer Matrix method of the figure III.11.(a) present the SPP resonances for three different samples: 6 nm Au/6 nm Co/16 nm Au, 10 nm Ag/6 nm Co/7 nm Ag and 5 nm Au/5 nm Ag/5 nm Co/7 nm Ag samples. The Au/Ag/Co/Ag sample exhibits a compromise between the sharpest SPP resonance of the Ag/Co/Ag sample and the widest SPP resonance of the Au/Co/Au. It is important to remark that the thickness of the Au capping layer (5 nm) was increased with respect to the Pt thickness of the previous section (2 nm) in order to fully protect the Ag/Co/Ag trilayer despite of the surface roughness for the grown system.

A series of 5 nm Au/5 nm Ag/X nm Co/7 nm Ag structures (see figure III.11.(b)), with Co thickness varying between 0 and 11 nm, has been grown at room temperature (RT) over microscope slide glass (BK7) substrates in the sputtering system. Additional structures, namely 20 nm Au/Glass, 10 nm Au/20 nm Ag/Glass and 10 nm Au/20 nm Co/Glass, were grown under the same conditions to extract the optical constants of Au, Ag and Co.

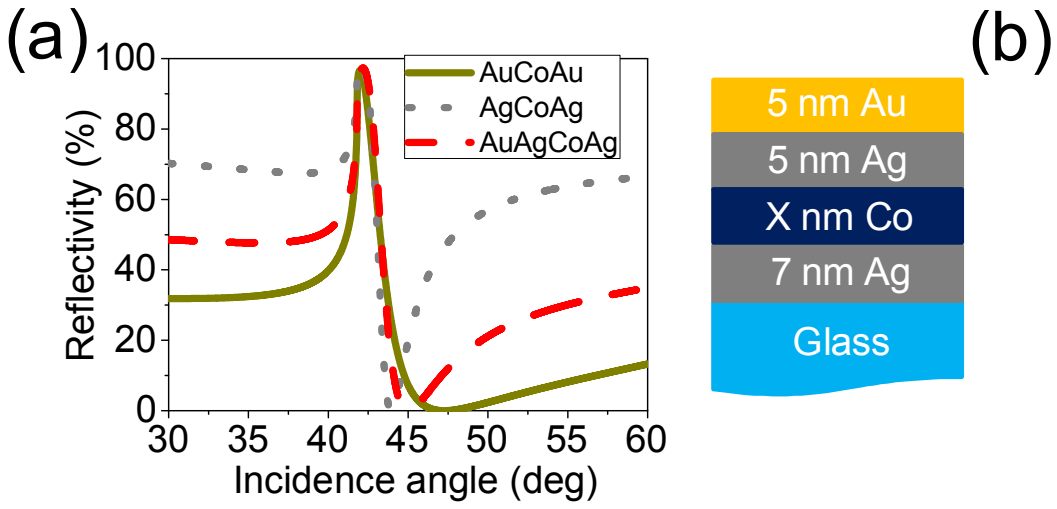

Fig. III.11. (a) Simulated reflectivity curves of 6 nm Au/6 nm Co/16 nm Au, 10 nm Ag/6 nm Co/7 nm Ag and 5 nm Au/5 nm Ag/5 nm Co/7 nm Ag samples via Transfer Matrix Method.(b) Scheme of the structure fabricated for the AuAgCoAg series.

III.4.B.- Morphology

The morphology of the samples has been analyzed by AFM, a representative image is shown in Fig. III.12.(a). Mounds are clearly observed on the sample surface. The lateral size of the mounds is similar (typical width around 50 nm) for all the samples, but their height decreases as the Co thickness increases, as shown in Fig. III.12.(b) for two representative topographic profiles corresponding to samples with 2 and 11 nm Co thickness. The profile of the glass substrate is also included as a reference. The substrate is rather flat, with 0.3 nm root mean square (rms) roughness value, whereas the samples exhibit a deviation from ideal 2D growth, with mounds whose height varies from 5 nm for the 2 nm Co sample, down to 3.5 nm for the 11 nm Co one. Fig. III.12.(c) shows the evolution of the average height of the mounds as a function of the Co thickness. The height decreases from 2 nm to 6 nm of Co thickness and above such value the mound height is almost constant. Taking into account that all the samples have the same layers on top of the Co one, it can be assumed that the initial mound height is mainly due to the first Ag layer grown over the glass substrate and that Co grows preferentially onto the valleys. When the Co thickness reaches 5 nm, the actual surface is now flatter and a continuous Co thin film can be formed: as a result, the final height of the structures is notably decreased.

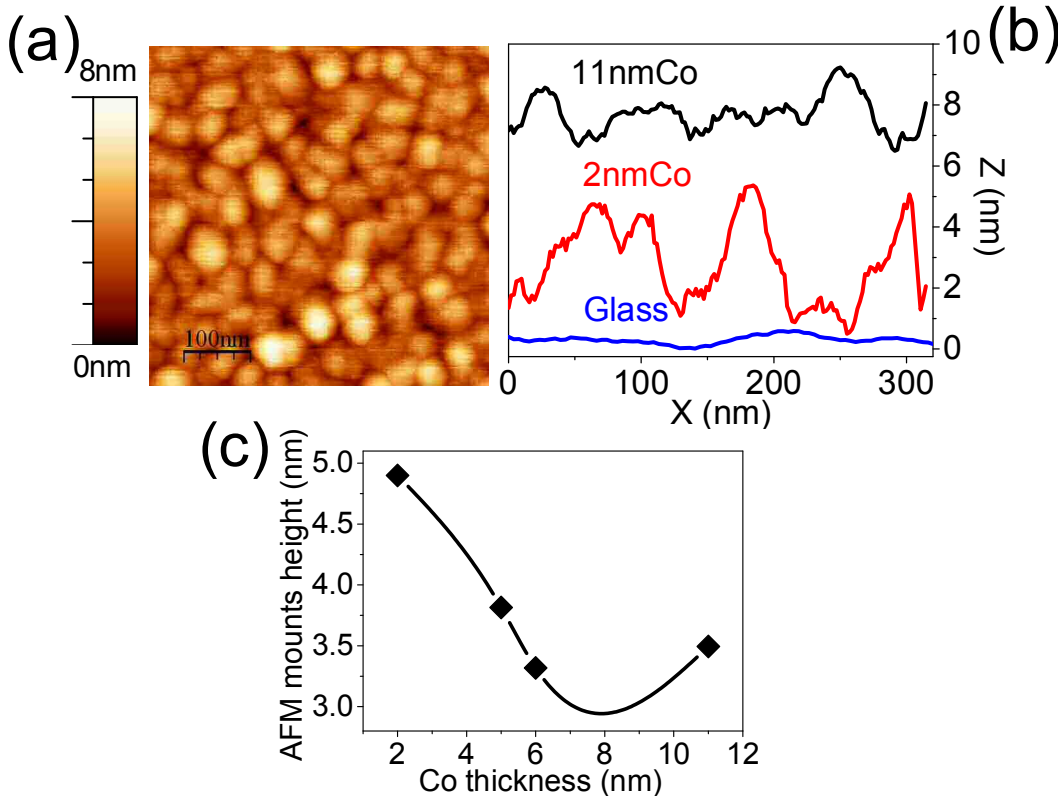

Fig. III.12. (a) AFM image of the 5 nm Co thick sample. (b)AFM profiles of two Au/Ag/Co/Ag multilayers with 2 and 11 nm Co thickness, respectively. The topographic profile of a glass substrate is also included as a reference. (c) Evolution of the mounts height with the Co thickness.

III.4.C.- Magnetic characterization

Kerr hysteresis loops in polar and transverse configurations (sensitive to out-of-plane and in-plane magnetization, respectively) have been measured for all the samples. Figure III.13.(a) shows the polar (left) and transverse (right) loops of representative samples. As expected, the MO signals (rotation angle in the polar configuration, changes in the reflected light intensity in the transverse one) increase with the Co amount. At a first glance, from the low saturation field and the high remanent magnetization for the transverse loops, compared with the high saturation field and low remanent magnetization for the polar ones, an in-plane magnetic anisotropy can be deduced for all the samples. More relevant information can be obtained by analyzing the evolution with the Co thickness of two of those properties, as depicted in Fig. III.13.(b): the *polar* saturation field H_s^p and the *transverse* coercivity H_c^t. For low Co thickness, H_s^p monotonously increases up to 7 nm; above such value, it is almost constant. Taking into account the aforementioned assumption that Co preferentially grows in the valleys of the rough Ag surface, such evolution can be explained as follows: For low thickness, the Co layer is not continuous but formed of mainly disconnected islands. The applied magnetic field must overcome the demagnetizing field in the perpendicular direction of those islands to saturate them. As the thickness increases, some islands become connected and their effective demagnetizing field increases (the ratio between their lateral dimensions and their height increases). Finally, when all the islanded regions coalesce, a continuous thin film of Co is formed, so the demagnetizing field reaches a maximum value and does not change for increasing thickness in the nm range: as a result, H_s^p saturates. It must be noticed that such continuous Co film is rough, and as a consequence the maximum H_s^p is lower than that expected for a completely flat thin film (17 kOe). Such explanation can also account for the evolution of H_c^t. Once the continuous Co film is formed, the magnetization reversal for in-plane field takes place by domain wall nucleation and propagation. With increasing thickness above 7 nm, the continuous film becomes more homogeneous: the number of pinning points for the domain wall movement decreases and as a result H_c^t decreases.

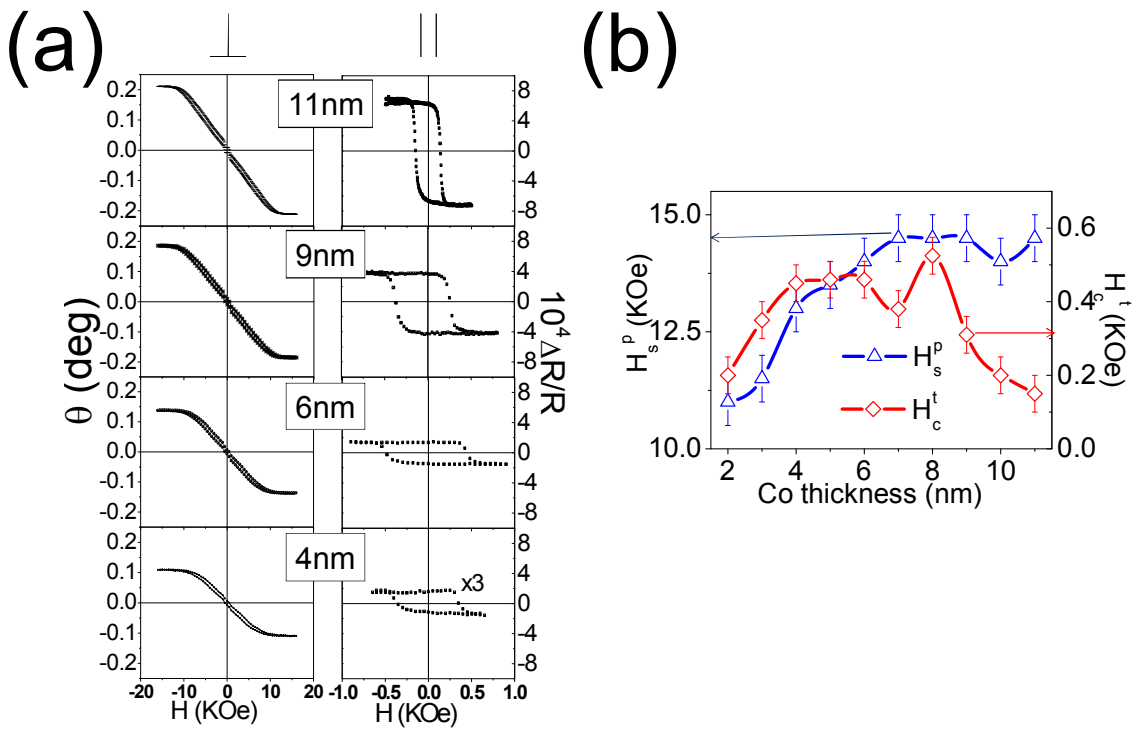

Fig. III.13. (a) Kerr loops of some representative samples (4-6-9-11 nm Co thickness) measured in polar (left side of the figure) and transversal (right side of the figure) configuration. (b) Evolution of the polar saturation field and the transverse coercivity with Co thickness.

Finally, we would like to mention that the magnetic field needed to saturate the samples in the transverse configuration, which is the one used for SPP wavevector modulation is always lower than 0.75 kOe (75mT), an easily achievable value for the characterization as well as for the development of applications.

III.4.D.- Optical and Magneto-Optical characterization

As the optical and magneto-optical properties of thin metal layers are influenced by the growth conditions, we have extracted the dielectric constants of our films by means of spectroscopic ellipsometry and polar Kerr spectroscopy. The optical constants of Au, Ag and Co and the magneto-optical constants of Co were obtained from 20 nm thick layers grown on glass substrates, where the Ag and Co were capped with a 10 nm Au protective film to avoid oxidation. First, the 20 nm Au/Glass thin film was characterized by spectroscopic ellipsometry, its experimental optical constants being then used for the determination of those of the Au capped Ag and Co layers. In Fig. III.14. the real and imaginary parts of the diagonal elements of the dielectric tensor determined in this way for Au (a), Ag (b) and Co (c) are shown. Figure III.14. (d) shows the magneto-optical constants of Co (real and imaginary parts), obtained from the experimental Polar Kerr spectra of the mentioned 20 nm Co/Glass thin film.

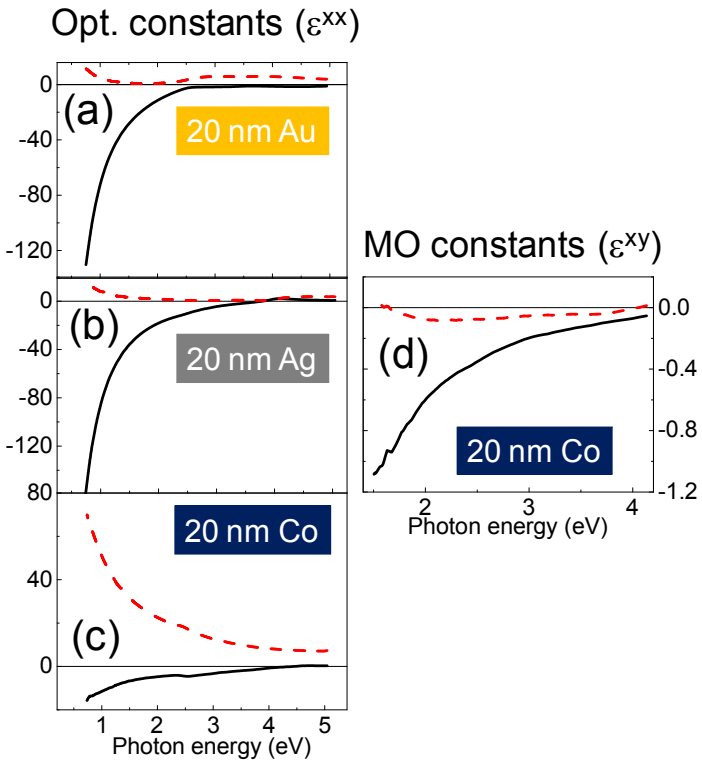

Fig. III.14. Optical and magneto-optical constants (real part ε_1 as continuous black line and imaginary part ε_2 as dashed red line) of the metals composing the multilayers analyzed in this work, obtained by ellipsometric (optical constants) and Polar Kerr (MO constants) spectra: (a) Au; (b) Ag; (c) Co;(d) MO constants of Co. All the data have been extracted from 20 nm thick films. In the case of Ag and Co, they were covered by a 10 nm Au layer to prevent oxidation.

Next, spectral MO characterization of the Au capped Ag/Co/Ag trilayers was carried out. In Figs. III.15. (a) and (b) we show polar Kerr rotation (θ) and ellipticity (φ) spectra for representative samples (11, 8, 5 and 2 nm Co). As expected, a gradual increase in the overall MO activity with Co amount is observed. The minimum of the Kerr rotation roughly shifts with Co amount from around 3.75 eV for 2 nm Co (Ag bulk plasmon position) to around 4 eV for for 11 nm Co (Co bulk plasmon position). The overall behavior of both Kerr rotation an ellipticity is well reproduced by a theoretical calculation based on continuous layers with sharp interfaces (figure III.15. (c) and (d)), where the used optical and MO constants are those experimentally obtained from the 20nm thick layers (see Fig. III.14.). The agreement is much better in the visible range, where the Kerr rotation roughly scales with the amount of Co, than in the UV range. In particular, the dip in the rotation at around 3.7 eV for the thinnest Co layer is not well captured. To understand the origin of this dip and the overall disagreement between theory and experiment in the UV range, we have to keep in mind that the layers have certain roughness, implying that for low Co thickness the layer continuity may be lost and therefore a continuous layer model is not valid. Taking into account this fact we have simulated the effect of having a layer of Ag with large Co inclusions, while keeping the same nominal Co amount. The result (shown in crosses in figures (c) and (d)) is a much more defined dip at around 3.7 eV (see inset in Fig III.15.(c)) which

corresponds pretty well with the location of the experimentally observed dip. On the other hand the value of the Kerr rotation in the visible range is hardly affected.

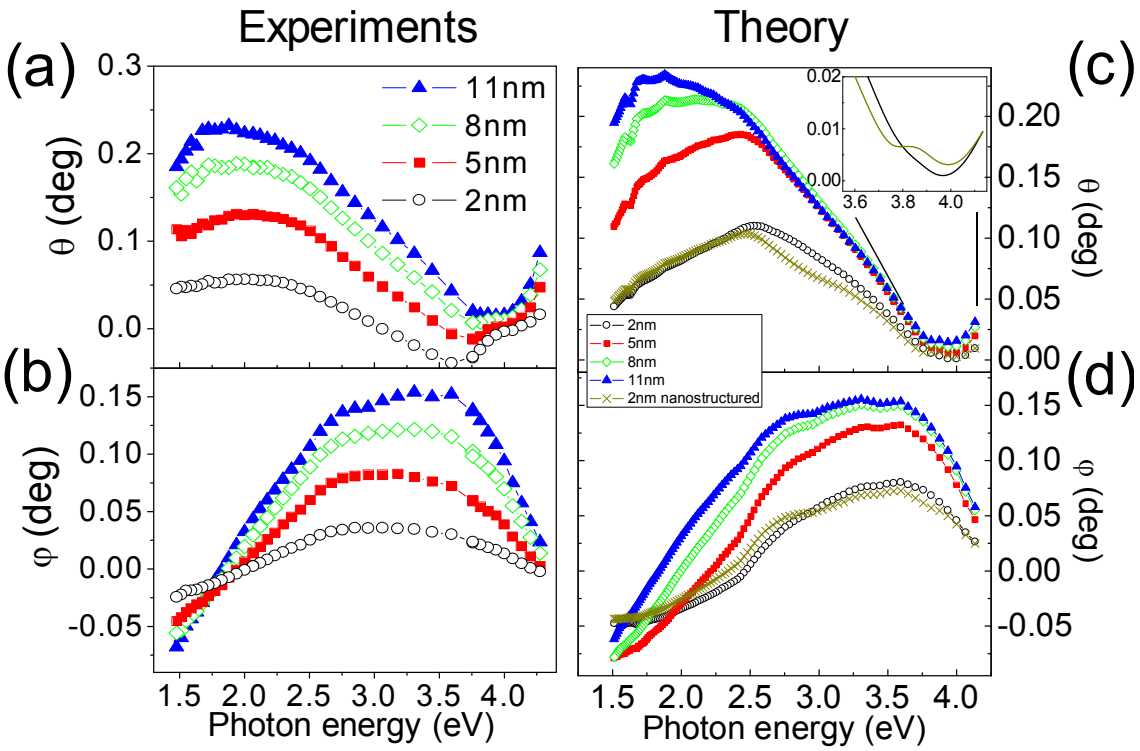

Fig. III.15. Experimental (left column of the figure) and theoretical (righ column of the figure) Kerr rotation and ellipticity spectra of the Au/Ag/Co/Ag layers for 4 representative values of Co thickness: 2, 5, 8 and 11 nm (symbols), and a simulation of a nanostructured thin film (crosses) , in particular Co islands on an Ag matrix, to estimate the effect of loosing the film continuity. The inset focuses on the high energy region for the continuous and nanostructured film with the same Co amount (2nm).

Therefore we can conclude that the dip in the rotation observed at energies between 3.5 and 4 eV for the 2 and 5 nm Co sample is due to the bulk plasmon resonance of Ag, since at such small Co thicknesses it is likely to have a not totally continuous Co film. This is supported by the disappearance of the dip upon increasing the nominal Co thickness.

III.4.E.- Magnetoplasmonic characterization

In what follows, the analysis of the MO activity of the Au/Ag/Co/Ag multilayers upon SPP excitation is presented, followed additionally by the study of the modification of the SPP wavevector when a magnetic field is applied. The experimental results will be presented and compared with theoretical calculations using the optical and MO constants determined in the previous section.

III.4.E.(i)- Surface plasmon resonance effects on the MO activity

Like for the series of structures capped with Pt, we have also carried out a systematic study of the ΔR/R enhancement when the SPPs are excited as a function of Co thickness in the series of Au/Ag/Co/Ag fabricated structures. Figure III.16. (a) shows a compilation of the ΔR/R versus incidence angle in Kretschmann configuration as a function of Co thickness. The characteristic resonance-like shape is observed for all Co thickness, with a clear maximum in amplitude for 8 nm Co. By defining the maximum of the reflectivity variation, $(\Delta R/R)_{Max}$, as its maximum positive value (as in the case for the Pt/Ag/Co/Ag samples) we can quantify this magnitude, analyze it as a function of Co thickness, and compare it with the measured ΔR/R in the absence of SPP excitation. The results are presented in figure III.16. (b) together with the theoretically calculated values obtained using the optical and MO constants determined in the previous section (please note that the experimental and simulated values without SPP excitation are multiplied by 10). As it can be observed, when no SPP excitation is present, the MO signal exhibits the expected monotonous increase with Co thickness, with very similar experimental and theoretical values. This is in contrast with the already mentioned behaviour when the SPP resonance is excited, where a maximum is observed at around 8 nm (experiments) and 6.5 nm (simulations) Co thickness, gradually decreasing for thicker Co layers. This behavior has been observed and explained in the previous section for the Pt capped Ag/Co/Ag structures[21] (also for Au/Co/Au trilayers[34]) and it is due to the optimum excitation of the SPP at a specific Co thickness and the subsequent maximization of the electromagnetic field at the MO active (Co) layer for that thickness, therefore optimizing the enhancement of the MO activity[35,36]. For higher Co thickness, the higher optical absorption of the system makes the damping to dominate, therefore preventing an optimal SPP excitation and leading to a reduction in the observed MO signal. As it can be seen in figure III.16. (b), the position of the maximum in the theoretically determined $(\Delta R/R)_{Max}$ differs about 1.5 nm from the experimental one. Both deviations of the actual Co thickness with respect to the nominal one and the intrinsic interface roughness present in the actual structures may be responsible for this difference.

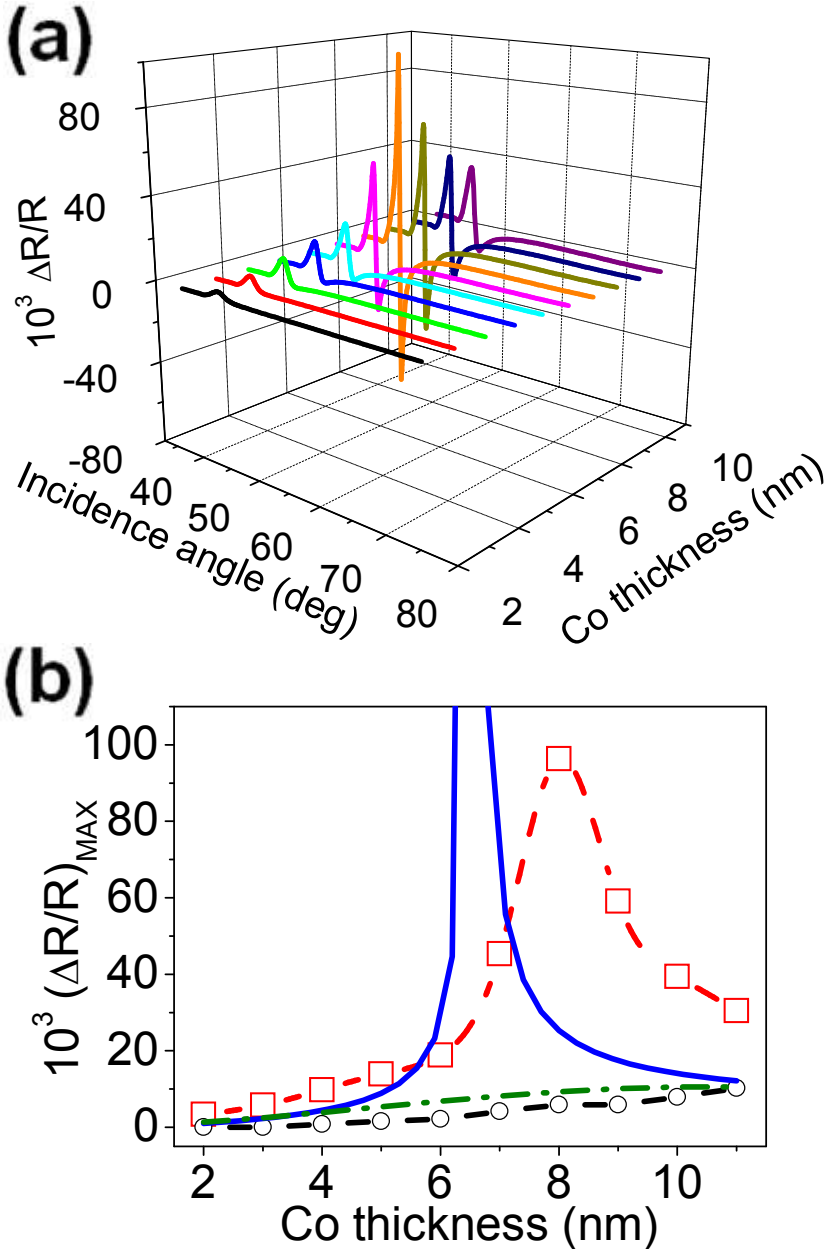

Fig. III.16. Co thickness dependence of the transversal MO Kerr signal (ΔR/R). (a) Experimental ΔR/R versus incidence angle curves for different Co thickness upon SPP excitation. (b) Co thickness dependence of the $(\Delta R/R)_{MAX}$, obtained both experimentally (dashed lines with open symbols) and from simulations (lines). The continuous blue line and the dashed red line with squares correspond to the $\Delta R/R_{MAX}$ values upon SPP excitation, whereas the green line and the dashed black line with circles correspond to $(\Delta R/R)_{MAX}$ values multiplied by 10 without SPP excitation.

III.4.E.(ii)- Magnetic modulation of the SPP resonance

So far we have discussed the effects that plasmon resonances can play in the MO activity of structures where materials with good plasmonic and magnetic properties coexist.

Due to the presence of the magnetic layer, the optical properties of this system no longer correspond to an isotropic system, but to an anisotropic one which has to be described by a dielectric tensor with non-zero off diagonal components. It is known that the dispersion relation of SPP for anisotropic media also depends on these non-diagonal elements of the dielectric matrix[37]. Since for ferromagnetic metals these elements depend on the magnetization, the application of an external magnetic field can produce a modulation in the SPP wavevector. This modulation has also been recently observed in complex Au/Co/Au structures[34,38], where the ferromagnetic material present in the structures contributes with large non-diagonal elements due to its MO activity, and therefore to a sizable modulation of the SPP wavevector at low magnetic fields.

An analytical expression for the SPP wavevector modulation in these complex structures cannot be obtained, but a reasonable approximation can be reached when considering a very simple system consisting of a dielectric, a thin layer of ferromagnetic material, and a very thick layer of noble metal. Assuming that the MO element ε_{xz} at saturation is much smaller than ε_{xx}, it is possible to obtain the modification of the plasmon wavevector k_{SPP} to the first order in ε_{xz} as:

$$\pm\Delta k_{SPP} \equiv k_{SPP}(\pm H) - k_{SPP}(0) = \frac{i2d(\varepsilon_d\varepsilon_m)^2}{(\varepsilon_d+\varepsilon_m)(\varepsilon_d^2-\varepsilon_m^2)}\left(\frac{2\pi}{\lambda}\right)^2\left(\pm\frac{\varepsilon_{xz}}{\varepsilon_{xx}}\right). \qquad \text{[III.2]}$$

where ε_m and ε_d are the diagonal elements of the dielectric tensor of the noble metal and the dielectric material respectively and d is the film thickness. From this expression it is readily seen that the magnitude of the SPP modulation depends linearly on the values of the non-diagonal elements of the dielectric tensor and on the film thickness.

The analytical expression provided in Eq. [III.2] gives estimation of the order of magnitude of the modulation for the SPP wavevector in our multilayered system. An exact way to obtain the SPP wavevector modulation is measuring the variations of the reflectivity minimum in reflectivity versus incidence angle curves with the sample magnetization saturated along opposite directions. Due to the limited angular resolution of the experimental setup, this direct measurement cannot be performed, but it can be simulated using the Transfer matrix formalism to calculate the reflectivity. Figure III.17. (a) shows the simulated reflectivity curves for 5nmAu/5nmAg/7nmCo/7nmAg/Glass structure at λ=633nm. The simulations exhibit an angular shift of the position of the minima due to the magnetic field, being the angular shift $\Delta\theta=\theta_{min}(H_+)-\theta_{min}(H_-)$ of the order of 10^{-2} degrees. Due to the small $\Delta\theta$ values, it is possible to relate them with the values of Δk_{SPP} by means of the angular derivative of Eq. [III.1] when the angle of incidence is θ_{min}:

$$\left(\frac{\Delta k}{k}\right)_{SPP} = \cot\left(\theta_{\min}\right)\Delta\theta \qquad \text{[III.3]}$$

The limited angular resolution of our experimental setup does not allow to have direct access to the actual Δθ values. However, we can compare the experimental ΔR/R versus incidence angle curves with the angular derivatives of reflectivity normalized to the reflectivity [(δR/δθ)/R]. In Fig. III.17. (b) we show these two magnitudes for the 8 nm thick Co layer, which exhibit a very close agreement both in shape and in intensity. The proportionality factor between ΔR/R and (δR/δθ)/R, taken as a parameter to adjust the amplitude of the curves, corresponds to Δθ, which in this way can be experimentally deduced. In this case, the obtained value is $\Delta\theta=1.55*10^{-2}$ deg.

We can now explore the evolution of the magnitude of the magnetic modulation of the SPP wavevector as a function of the Co thickness for the different fabricated structures. In figure III.17 (c) we show the experimentally deduced and the theoretical values of $(\Delta k/k)_{SPP}$ for our Au/Ag/Co/Ag structures as a function of the Co thickness, together with the simulated ones for a Au/Co/Au structure as in Ref.[34]. A monotonous increase of $(\Delta k/k)_{SPP}$ with Co thickness is observed in both cases, with similar experimental and theoretical values, reaching a similar modulation value of $2.8\text{x}10^{-4}$ for the maximum Co thickness (11 nm) for both Au and Ag based structures. This indicates that within the experimental conditions the main responsible for the SPP wavevector modulation is the magnetic material. Then again, Ag being a metal with smaller absorption that Au and therefore providing longer propagation distances, and since both metals confer a similar modulation potential, the use of Ag in the development of active plasmonic devices based on magnetoplasmonic systems appears to be a better option.

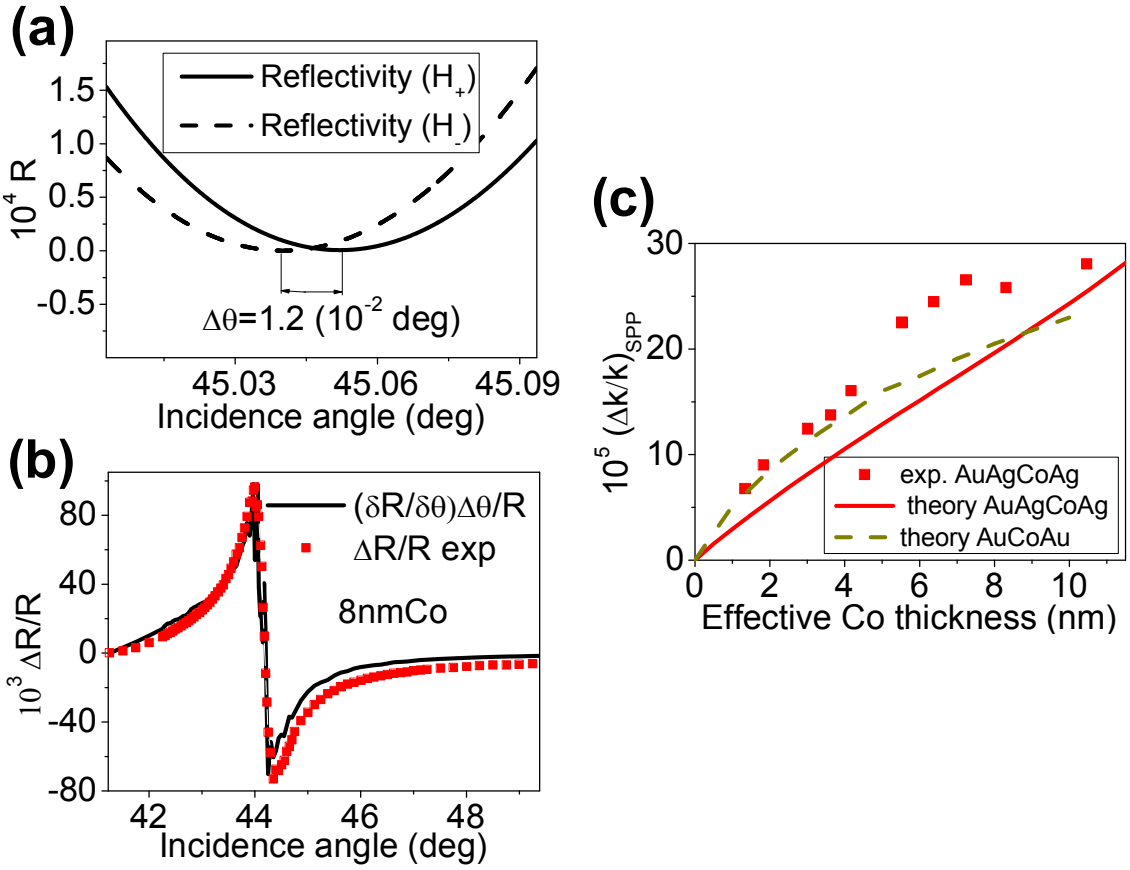

Fig. III.17. (a) Simulated reflectivity versus angle of incidence curves obtained for the sample 5nmAu/5nmAg/7nmCo/7nmAg/Glass with the magnetization saturated in one direction $\theta_{min}(H_+)$ (continuous line) and in the opposite direction $\theta_{min}(H_-)$ (dashed line). The angular shift due to the magnetic field modulation, $\Delta\theta = \theta_{min}(H_+) - \theta_{min}(H_-)$, is shown. (b) Angular derivative of the experimental reflectivity curve divided by the reflectivity and times $\Delta\theta$ [i.e. $(\delta R/\delta\theta)\Delta\theta/R$] compared with the experimental transverse MO Kerr signal ($\Delta R/R$). $\Delta\theta$ is the only fitting parameter. (c) Co thickness dependence of the $(\Delta k/k)_{SPP}$ experimental (points) and simulated (line) values. The dashed line corresponds to a simulation for a Au/Co/Au structure.

III.4.F.- Comparison of the different magnetoplasmonic multilayers studied

The observed MO enhancement in the Au/Ag/Co/Ag can be compared with that previously obtained in the Au/Co/Au[34] or Pt/Ag/Co/Ag[21] systems exploring the effect of the substitution of Au by Ag and its associated improvement of plasmonic properties. In Fig.III.18. (a) we show ΔR/R versus incidence angle curves for optimum SPP excitation in both systems, i.e., 8 nm Co for the Au/Ag/Co/Ag structure and 5.5 nm Co for the Au/Co/Au[34] Not only the value of $(\Delta R/R)_{Max}$ is a factor of 5 higher in the Au/Ag/Co/Ag structure compared to the Au/Co/Au one and one order of magnitude compared to the Pt/Ag/Co/Ag one, (see the table of figure III. 18. (b)) but also the slope of the resonance in the area of SPP excitation is one order of magnitude higher than for the Au/Co/Au and a factor of 20 higher when compared to the Pt/Ag/Co/Ag. This is due to the sharper plasmon resonance of Ag compared to Au (Au/Co/Au samples) or deteriored Ag

(Pt/Ag/Co/Ag samples), which comes from more negative real part of the dielectric constant of Ag at the working wavelength (633 nm)[17]. This bigger slope has special relevance in the MO surface plasmon resonance sensing applications[39] where the slope of the resonance is the relevant parameter that may lead to enhanced sensitivity of the device.

(a)

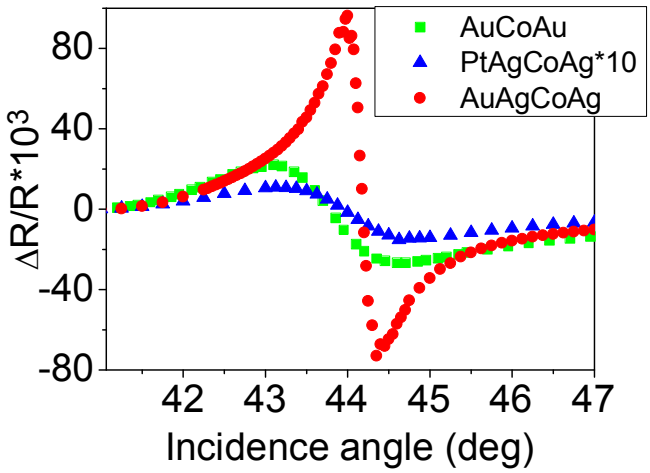

(b)

	$\Delta R/R_{max}$	SPP_{ON}/SPP_{OFF}	Sensing slope
Au/Co/Au	$2.2*10^{-2}$	40	52
Pt/Ag/Co/Ag	$1.1*10^{-3}$	4	26
Au/Ag/Co/Ag	$9.6*10^{-2}$	210	516

Fig. III.18. (a) Comparison between Au/Co/Au (green squares), Pt/Ag/Co/Ag (blue triangles) and Au/Ag/Co/Ag (red circles) structures. The Au/Co/Au curve comes from reference [34]. In both multilayers, the nominal Co thickness corresponds to the case of maximum SPP excitation and thus maximum $\Delta R/R_{MAX}$ (5.5 nm Co for Au/Co/Au, 2 nm for Pt/Ag/Co/Ag and 8 nm for Au/Ag/Co/Ag). (b) Table with $\Delta R/R_{MAX}$ values, the ratio between the TMOKE signal with and without SPP excitation and the slope values of the linear region inside the SPP resonance of the TMOKE curves for the three structures.

III.6.-CONCLUSIONS

Ag/Co/Ag multilayers have been fabricated and characterized. Special attention has been devoted to their magnetoplasmonic properties: the enhancement of the TMOKE signal under SPP excitation and the magnetic modulation of the SPP wavevector. Two capping layers have been used to protect the Ag and Co from the chemical reactions with room atmosphere. The 2 nm Pt capping layer has demonstrated a poor performance to maintain the magnetoplasmonic properties of the Ag/Co/Ag system. Nevertheless, the multilayers with a 5 nm Au capping layer have exhibited a

high and sharp resonance of the MO activity with SPP excitation (in fact, better performance than previous Au/Co/Au[34] trilayers) and a significant magnetic modulation of the SPP wavevector (almost equivalent to the Au/Co/Au[34] trilayers). Moreover, these systems with Au capping layer maintain these magnetoplasmonic properties in ambient conditions for long periods of time (confirmed for up to two years). In contrast, the Ag/Co/Ag trilayer without any capping layer suffers important modifications after two years exposed to ambient conditions, losing its original magnetoplasmonic properties. Therefore the key role is the use of a capping layer with good optical properties and to completely avoid the chemical reactions inside the Ag/Co/Ag as it has been obtained for Au/Ag/Co/Ag.

III.7.-REFERENCES

[1] Oulton, R. F., Sorger, V. J., Zentgraf, T., Ma, R.-M., Gladden, C., Dai, L., Bartal, G., et al. (2009). Plasmon lasers at deep subwavelength scale. *Nature*, *461*(7264), 629-32. Nature Publishing Group.

[2] Pyayt, A. L., Wiley, B., Xia, Y., Chen, A., & Dalton, L. (2008). Integration of photonic and silver nanowire plasmonic waveguides. *Nature nanotechnology*, *3*(11), 660-5.

[3] Min, B., Ostby, E., Sorger, V., Ulin-Avila, E., Yang, L., Zhang, X., & Vahala, K. (2009). High-Q surface-plasmon-polariton whispering-gallery microcavity. *Nature*, *457*(7228), 455-8. Nature Publishing Group.

[4] Kuttge, M., García de Abajo, F. J., & Polman, A. (2010). Ultrasmall mode volume plasmonic nanodisk resonators. *Nano letters*, *10*(5), 1537-41.

[5] Jin, R., Jureller, J. E., Kim, H. Y., & Scherer, N. F. (2005). Correlating second harmonic optical responses of single Ag nanoparticles with morphology. *Journal of the American Chemical Society*, *127*(36), 12482-3.

[6] Futamata, M., Maruyama, Y., & Ishikawa, M. (2003). Local Electric Field and Scattering Cross Section of Ag Nanoparticles under Surface Plasmon Resonance by Finite Difference Time Domain Method. *The Journal of Physical Chemistry B*, *107*(31), 7607-7617.

[7] Verhagen, E., Dionne, J. a, Kuipers, L. K., Atwater, H. a, & Polman, A. (2008). Near-field visualization of strongly confined surface plasmon polaritons in metal-insulator-metal waveguides. *Nano letters*, *8*(9), 2925-9.

[8] Verhagen, E., Kuipers, L., & Polman, A. (2007). Enhanced nonlinear optical effects with a tapered plasmonic waveguide. *Nano letters*, *7*(2), 334-7.

[9] P. B. Johnson and R. W. Christy, "Optical constants of the noble metals," *Phys. Rev .B*, vol. 6, p. 4370, (1972).

[10] L. Novotny and B. Hetch, *Principles of Nano-Optics*. Cambridge, U.K.: Cambridge Univ. Press, (2006), pp. 391–392.

[11] M. Schubert, "Polarization-dependent optical parameters of arbitrarily anisotropic homogeneous layered systems," *Phys. Rev. B*, vol. 53, p.4265, 1996; M. Schubert, T. E. Tiwald, and J. A. Woollam, "Explicit Solutions for the Optical Properties of Arbitrary Magneto-Optic Materials in Generalized Ellipsometry", Appl. Opt. **38**, 177 (1999).

[12] Kretschmann and H. Raether, *Z. Naturforsch*. A 23, 2135 (1968); E. Kretschmann, *Z.Phys* .241, 313 (1971).

[13] G. J. Kovacs, Surf. Sci. Lett. **78**, L245 (1978).

[14] Bennett, H., Peck, R., Burge, D., & Bennett, J. (1969). Formation and growth of tarnish on evaporated silver films. *Journal of applied physics*, *40*(8), 3351–3360.

[15] Zheludkevich, M. L., Gusakov, a. G., Voropaev, a. G., Vecher, a. a., Kozyrski, E. N., & Raspopov, S. a. (2004). Oxidation of Silver by Atomic Oxygen. *Oxidation of Metals*, *61*(1/2), 39-48.

[16] S. Szunerits, X. Castel, and R. Boukherroub, J. Phys. Chem. C **112**, 15813 (2008).

[17]Sambles, J., Bradbery, G., & Yang, F. (1991). Optical excitation of surface plasmons: an introduction. *Contemporary physics*, *32*(3), 173–183.

[18] Arbiol, J., Peiró, F., Cornet, a., Clavero, C., Cebollada, a., Armelles, G., & Huttel, Y. (2005). Capping layer effects in the structure and composition of Co nanoparticle ultrathin films. *Applied Physics Letters*, *86*(3), 032510.

[19] Navarro, E., Huttel, Y., Clavero, C., Armelles, G., & Cebollada, a. (2004). Capping-layer-induced magnetic coupling in a two-dimensional nanostructured system. Applied Physics Letters, 84(12), 2139.

[20] Clavero, C., Martínez, L., García-Martín, a., García-Martín, J., Huttel, Y., Telling, N., van der Laan, G., et al. (2008). Morphology and capping effects in the magnetic and magneto-optical properties of nanoparticulate Co films. Physical Review B, 77(9).

[21] E. Ferreiro-Vila et al., IEEE Trans. Magn. **44**, 3303-3306 (2008).

[22] E. Ferreiro-Vila et al., Phys. Rev. B **80**(12), 125132 (2009).

[23] J. Homola, Chem. Rev. **108**, 462–93 (2008).

[24] H. Raether, Surface Plasmons on Smooth and Rough Surfaces and on Gratings, vol. 111 of Springer Tracts in Modern Physics (Springer-Verlag, Berlin, 1988).

[25] Yin, L., Adler, I., Tsang, T., Matienzo, L. J., & Grim, S. O. (1974). PARAMAGNETISM AND SHAKE-UP SATELLITES IN X-RAY PHOTOELECTRON SPECTRA. Chemical Physics Letters, 24(1), 81-84.

[26] Haber, J., Stoch, J., & Ungier, L. (1976). X-RAY PHOTOELECTRON SPECTRA OF OXYGEN IN OXIDES OF Co, Ni, Fe AND Zn. *Journal of Electron Spectroscopy and Related Phenomena*, *9*, 459-467.

[27] Brundle, C., Chuang, T., & Rice, D. (1976). X-ray photoemission study of the interaction of oxygen and air with clean cobalt surfaces. *Surface Science*, *60*(2), 286–300.

[28] Cebollada, a., García Martín, J., Clavero, C., Balcells, L., Estradé, S., Arbiol, J., Peiró, F., et al. (2009). Growth and magnetic characterization of Co nanoparticles obtained by femtosecond pulsed laser deposition. *Physical Review B*, *79*(1), 1-13.

[29] Tompkins, H. G., & Augis, J. a. (1981). The oxidation of cobalt in air from room temperature to 467°C. *Oxidation of Metals*, *16*(5-6), 355-369.

[30] Moyes, R., & Roberts, M. (1977). Interaction of cobalt with oxygen, water vapor, and carbon monoxide. *Journal of Catalysis*, *49*(2), 216–224.

[31] S. R. Barman, C. Biswas, and K. Horn, "Collective excitations on silver surfaces studied by photoyield," in *Surface Science*, September 20, 2004, vol. 566–568, Part 1, Proceedings of the 22nd European Conference on Surface Science, pp. 538–543.

[32] V.I. Safarov, V. A. Kosobukin, C. Hermann, G. Lampel, J. Peretti and C. Marlière, Phys. Rev. Lett. **73**, 3584-3587 (1994).

[33] C. Hermann, V. A. Kosobukin, G. Lampel, J. Peretti, V.I. Safarov and P. Bertrand, Phys. Rev. B **64**, 235422 (2001).

[34] J. B. González-Díaz, A. García-Martín, G. Armelles, J. M. García-Martín, C. Clavero, A. Cebollada, R. A. Lukaszew, J. R. Skuza, D. P. Kumah and R. Clarke, Phys. Rev. B **76**, 153402 (2007).

[35] G. Armelles, J. B. González-Díaz, A. García-Martín, J.M. García-Martín, A. Cebollada, M. U. González, S. Acimovic, J. Cesario, R. Quidant and G. Badenes, Optics Express **16**, 16104-6112 (2008).

[36] Armelles, G., Cebollada, a, García-Martín, a, García-Martín, J. M., González, M. U., González-Díaz, J. B., Ferreiro-Vila, E., et al. (2009). Magnetoplasmonic nanostructures: systems supporting both plasmonic and magnetic properties. Journal of Optics A: Pure and Applied Optics, 11(11), 114023.

[37] R. F. Wallis, J. J. Brion, E. Burstein and A. Hartstein, Phys. Rev. B **9,** 3424–37 (1974).

[38] V. V. Temnov et al., Nat. Photonics **4,** 107-111 (2010).

[39] B. Sepúlveda, A. Calle, L. M. Lechuga and G. Armelles, Opt. Lett. **31**, 1085-1087 (2006).

Chapter IV:

The role of the structure and interface roughness: A comparison between epitaxial and polycrystalline multilayers

IV.1- INTRODUCTION 87

IV.2- FABRICATION TECHNIQUES 88

IV.3.- STRUCTURE AND MORPHOLOGY 89

IV.4.- MAGNETIC CHARACTERIZATION 92

IV.5. OPTICAL CHARACTERIZATION 96

IV.6. MAGNETOOPTICAL CHARACTERIZATION 97

IV.7. MAGNETOPLASMONIC CHARACTERIZATION 100

IV.7.A.-Surface plasmon resonance effects on the MO activity 100

IV.7.B.- Magnetic modulation of the SPP resonance 103

IV.7.C.- Propagation length of the SPPs 105

IV.8.-CONCLUSIONS 107

IV.9.-REFERENCES 107

IV.1- INTRODUCTION

The improvement of the plasmonic properties (lower optical losses of the Ag compared to the Au ones) for the noble metal-ferromagnetic heterostructures was studied on the previous chapter. Now, the key effect of both crystallinity (grain size or grain boundary scattering) and surface and interface roughness in the magnetic, optical, MO and mainly magnetoplasmonic properties of these multilayered heterostructures will be studied on this chapter. In fact, many previous works have shown that surface flatness[1,2], grain size[3,4,5,6] and epitaxial growth[7] play an important role in the optical constants of plasmonic nanostructures. For instance, Kuttge et al. have reported the differences in propagation length when the SPP is excited in a monocrystalline Au film or in two polycrystalline Au films with different grain sizes[4] (see figure IV.1.(a)), finding longer propagation lengths for the monocrystalline case and, when comparing polycrystalline structures, for those with larger grain sizes.

On the other hand, different works indicate that the magnetic and MO properties of multilayered structures may also be affected by the morphology[8,9,10] and the interface flatness[11,12] of the ferromagnetic layer inside a heterostructure. As an example of that, Clavero et al. have studied the differences of the MO constants for nanoparticulate Co films varying their morphology by the control of the temperature for the Co deposition[10] (see the figure IV.1.(b)). The reduction of the electronic relaxation time for smaller Co nanoparticles leads to a decrease of the Drude MO constants due to the confinement effects of these nanoparticles inside a dielectric matrix. Even polycrystalline Au/Fe/Au trilayers, used for biosensing purposes as a magneto-optical Surface Plasmon Resonance (MOSPR) sensor, exhibit lower MO performance than the theoretically expected ones[13], probably due to the reduced MO properties of Fe in contact with Au. All these facts indicate that if the structural and morphological characteristics can strongly determine the MO constants of a magnetoplasmonic multilayered system, thus the MO activity and the magnetic modulation of the SPP wavevector, both dependent of the MO constants, would be strongly modified as well.

A way to control the interface quality of metallic ultrathin films lies in the choice of the adequate deposition technique. Molecular beam epitaxy (MBE), sputter deposition and pulsed laser deposition (PLD) are widely used deposition techniques, each of them capable of obtaining structures with different structural characteristics. For the specific purpose of this chapter, PLD has a unique capability to produce ultraflat, high quality thin films[14], both due to the energy of the deposited atoms and the characteristic deposition rates. Therefore, this work will focus on the influence that the use of different deposition techniques (PLD vs. MBE) for the buffer layer growth of otherwise equivalent structures has on their magnetoplasmonic properties, and more specifically on the magnetic field induced modification of the SPP wavevector. For this study, we have fabricated Au/Fe/Au trilayered structures deposited onto MgO substrates

by using PLD Fe and MBE Cr buffer layers.

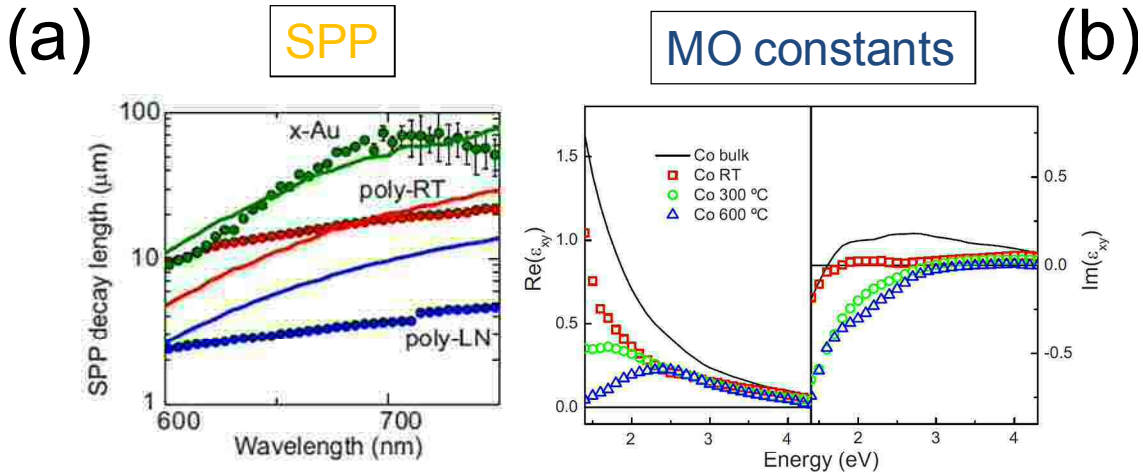

Fig.IV.1. (a) SPP propagation length as a function of wavelength for three different samples: The green dots are for single-crystalline gold (*x*-Au) and the red and blue dots are for polycrystalline gold films deposited at room temperature (poly-RT) and liquid-nitrogen temperature (poly-LN), respectively. The solid lines are propagation lengths calculated from the dielectric constants measured for the respective samples (figure taken from ref [4]). (b)Experimental MO constants of the different nanoparticulate layers (symbols), together with bulk MO constants (black line), consisting of Co deposited at room temperature (RT) (red squares),300ºC (green circles) and 600 ºC (blue triangles) with a Al capping layer (figure taken from ref [10]).

IV.2- FABRICATION TECHNIQUES

Sample growth was performed by M. Iglesias and F. J. Palomares in the Instituto de Ciencia de Materiales de Madrid (ICMM) under ultra high vacuum conditions in a system equipped with a combination of Pulsed Laser Deposition (PLD) and Molecular Beam Epitaxy (MBE) techniques. Two series of 7 nm Au/X nm Fe/7 nm Au structures, with Fe thickness varying between 0 nm and 6 nm, have been grown at room temperature (RT) on MgO(001) substrates. Buffer layers, namely 1 nm Fe and 2 nm Cr, were used to fabricate the otherwise equivalent series of samples. The Fe buffer layers were grown by PLD whereas the Cr ones were grown by MBE. Fe layers were deposited by using a Nd-YAG laser (λ = 532 nm, 4 ns pulses, 25 mJ/pulse, 10 Hz repetition rate) and the deposition rate was 0.5 nm/min. Au layers were also deposited by MBE and the deposition rates for Au and Cr layers were 1 nm/min. Prior to deposition, the MgO substrates were outgassed at 200 ºC for 25 minutes for water desorption purposes and then cooled down to RT for thin film deposition.

IV.3.- STRUCTURE AND MORPHOLOGY

The crystalline structure of both series of samples, with Fe buffer layer grown by PLD and with Cr buffer layer grown by MBE, has been studied by XRD. Fe and Cr are elements with body centred cubic structure and very similar lattice parameter (0.287 nm and 0.288 nm, respectively). It is well known that both can grow epitaxially on MgO (001) substrates[15,16] upon 45º in plane rotation of their crystalline lattice to match the 0.4213 nm lattice parameter of the substrate. Therefore they both are excellent candidates as buffer layer to promote the epitaxial growth of a wide variety of metallic systems. However, we have found significant differences between the two series. Symmetric scans of samples with Fe interlayer thickness of 6 nm are shown in figure IV.2. (a). As it can be seen, the growth by PLD of a Fe buffer layer clearly promotes (001) oriented growth along the out-of-plane direction, with the observation of Au (200) and MgO (200) diffraction peaks. The epitaxial nature of PLD buffer sample is also confirmed by the asymmetric XRD ϕ scans shown on figure IV.2. (b), where scans for MgO (220), Au (111) and Fe (110) diffraction peaks are shown. On the other hand, the samples with Cr buffer layer grown by MBE exhibit a polycrystalline, textured growth, with the observation of the Au (111) diffraction peak on the figure IV.2. (a).

Important differences have been obtained in XRR measurements and AFM analysis, which indicate that PLD deposition has a unique capability to produce ultraflat films due to the energy of the deposited atoms and the characteristic deposition rates[14,17].

Representative AFM images of the topmost surface of two samples without Fe interlayer and other two equivalent ones with Fe interlayer (4.5 nm and 5 nm of Fe interlayer thickness, respectively) for both the epitaxial and polycrystalline series are shown in Fig. IV.3. (a). It is interesting to remark that the AFM images are displayed with the same height and lateral scale for better comparison. As it can be observed, the two samples without Fe interlayer and the epitaxial sample with 4.5 nm Fe interlayer exhibit a very flat surface with global differences in height of around 0.5 nm over the scanned area. On the other hand, the polycrystalline 5 nm Fe sample shows a rougher surface including granular structures around 7 nm in height, correlated with the different buffer growth technique. In Fig. IV.3. (b) we have plotted the Fe interlayer thickness dependence of the RMS roughness obtained from AFM measurements of the topmost layer for both series of samples, which is systematically at least a factor of two larger in the polycrystalline samples than in the epitaxial ones for every Fe interlayer thickness.

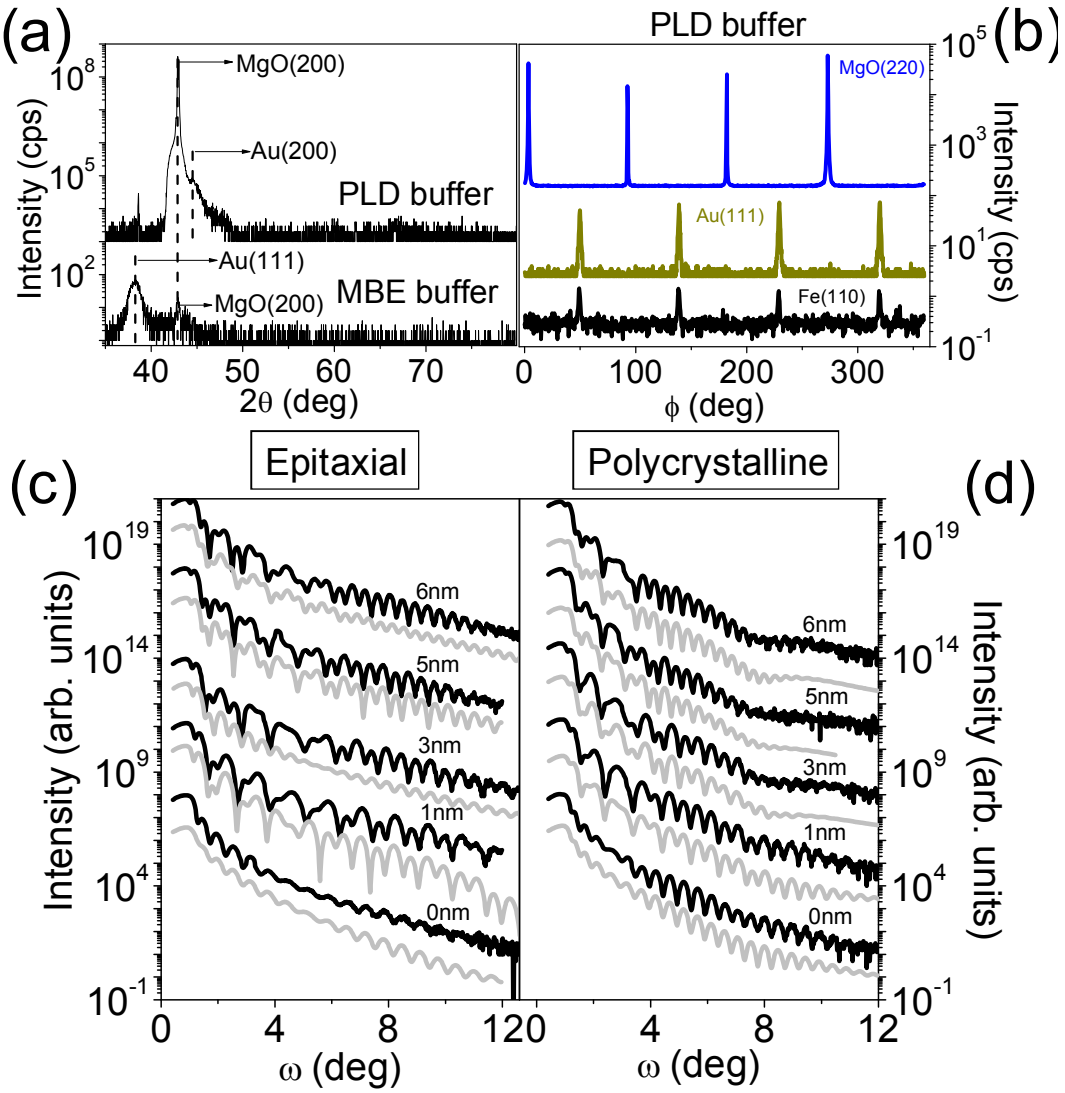

Figure IV.2: (a) High angle symmetric X-ray diffraction scans for representative epitaxial and polycrystalline trilayers, respectively. (b) Phi scans of asymmetric reflections of MgO, Au and Fe, showing the epitaxial nature of the structures grown by PLD. X-ray reflectometry scans (black curves) together with best fits (grey curves) for the epitaxial (c) and polycrystalline (d) structures.

In this sense, XRR is a very suitable tool to extract quantitative information about, not only the roughness of the topmost layer in a multilayered system, but also to determine the thickness and roughness of buried interfaces. In the bottom panel of figure IV.2., we show XRR curves and their corresponding best fits for both series of samples, epitaxial and polycrystalline ones (Fig. IV.2. (c) and (d), respectively). The XRR curves of epitaxial structures show that the oscillations extinguish at higher 2θ angles compared to the polycrystalline ones due to the higher flatness of the interfaces in the epitaxial multilayers. In fact, the roughness analysis of the XRR curves fits yields values of 0.2 nm for the Au topmost layer in the epitaxial sample with 6 nm Fe interlayer thickness compared to 0.5 nm for the same Fe interlayer thickness in the

polycrystalline one. The obtained results for the Fe interlayer – top Au layer interface from XRR measurements are also shown in figure IV.3. (b). Although similar slope values of the Fe interlayer roughness are found in both types of structures, the same trend to that mentioned in the case of AFM results is observed, i.e., lower roughness for the epitaxial case. This result confirms the major role of the buffer layer morphology, which affects substantially the growth of consecutive Au, Fe and Au layers and gives rise to systematically larger roughness for the entire multilayer. Summarizing, the epitaxial growth of the Fe interlayer and the whole layered structure for this set of samples favors the reduction of the roughness and the improvement of the overall morphology providing very smooth continuous surfaces and high quality interfaces in terms of flatness[17].

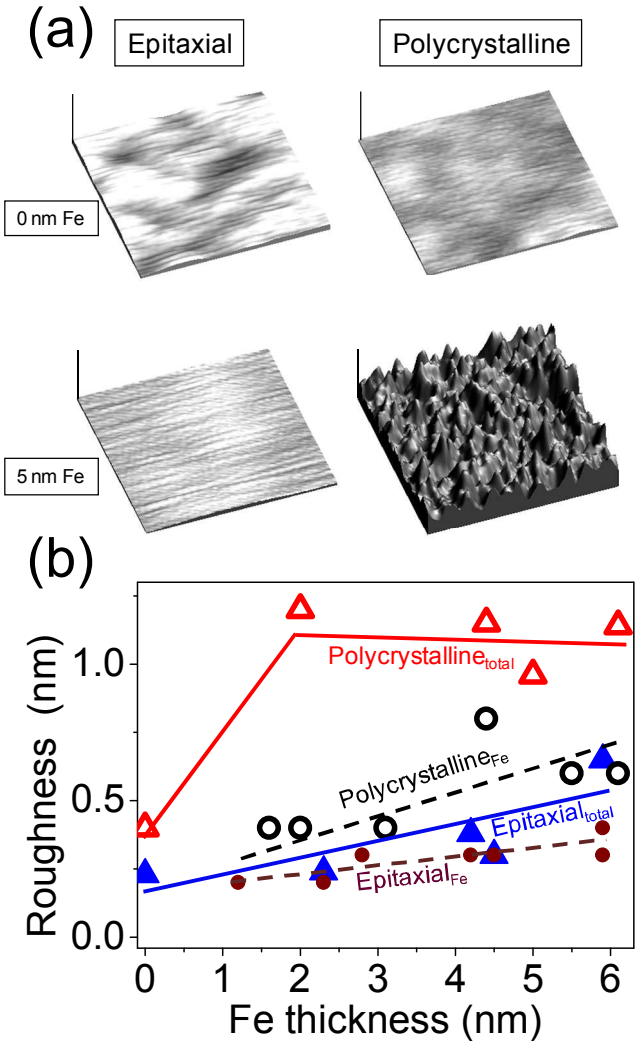

Figure IV.3. (a) AFM images for the two samples without Fe interlayer and the two representative Fe interlayer samples (4.5 nm and 5 nm Fe thickness, respectively) for the epitaxial (left column) and polycrystalline (right column) series. The AFM images have the same scale (7 nm vertical and 400 nm lateral). (b) Evolution of the surface (triangles) and Fe interlayer (circles) roughness, deduced from AFM and XRR measurements, respectively, with the Fe interlayer thickness for epitaxial (full symbols) and polycrystalline (empty symbols) structures.

IV.4.- MAGNETIC CHARACTERIZATION

The effect of the crystalline nature on the magnetic anisotropy and magnetization reversal process for the two series of structures is studied by measuring both in-plane and out-of-plane magnetic hysteresis loops using transverse and polar Kerr effect, respectively. The obtained loops are shown in figure IV.4.(a) for the epitaxial series, and figure IV.5. for the polycrystalline one. In the first case, a clear in plane four-fold magnetic anisotropy, characteristic of a (001) oriented cubic Fe lattice is observed, as evidenced by the easy [100] and hard [110] in-plane magnetocrystalline axes shown for selected samples in the left column of figure IV.4.(a). Analyzing these hysteresis loops, we can extract the normalized remanence M_r/M_s (where M_r is the remanent magnetization and M_s is the magnetization at saturation) along the hard [110] axis. In our epitaxial series an averaged M_r/M_s value of 0.73±0.02 is determined, which confirms 45º between the magnetization and the magnetic field direction (i.e. the magnetization lies along the [100] direction) in the remanent state (see the sketch of fig. IV.4.(b)). Worth to notice, even the sample without Fe interlayer, i.e., 14 nm Au / 1 nm Fe / MgO(001), exhibits a clear in plane anisotropy with well defined easy and hard axes hysteresis loops. This indicates that this buffer layer has a great degree of continuity, enough to evidence the typical biaxial in-plane anisotropy of a cubic thin film. However, in the out-of-plane magnetic characterization performed by polar Kerr measurements and shown on the right column of figure IV.4.(a), the loop of the sample with 0 nm Fe interlayer shows a magnetic saturation field about 8 kOe, well below than that expected for a continuous Fe thin film (21 kOe). This suggests that the Fe buffer film might be in the form of platelets (incomplete layer)[18]. The loop of the sample with 1.2 nm Fe interlayer exhibits a saturation field higher than 16 kOe, which indicates that the continuity of such Fe interlayer is better than that of the buffer. Finally, for higher Fe interlayer thickness, the tendency of the loops points to the formation of continuous Fe interlayers.

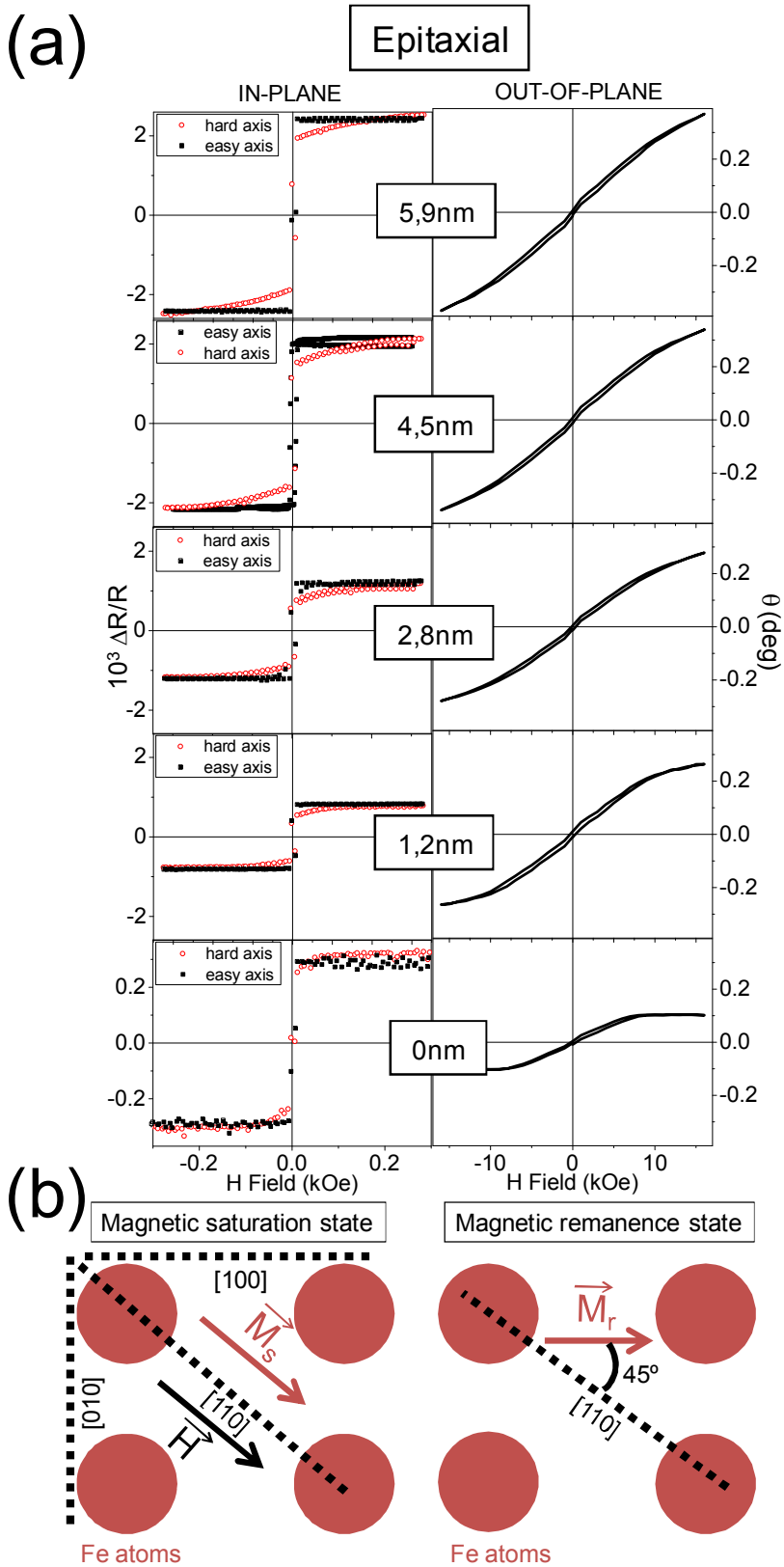

Figure IV.4.(a) Kerr magnetooptical loops of representative epitaxial samples measured in transverse (left panel) and polar (right panel) configurations. In transverse configuration, the open and closed symbols correspond to the hard and easy magnetic axes, respectively. (b) Sketch showing the variation of the magnetization for the cubic Fe lattice between the magnetic saturation and remanence states when the magnetic field is located along the hard magnetic [110] axis.

On the other hand, the corresponding hysteresis loops for the polycrystalline samples are shown in figure IV.5. Rounded loops are obtained in the transverse configuration, with total absence of in-plane anisotropy (loops at 0 and 45º yield identical results), as it should be expected for a polycrystalline structure, therefore with isotropic magnetic behavior. In the polar configuration, the behavior observed for the epitaxial layers with very low saturation field, related to incomplete layers at low Fe thickness (1.6 nm), are reproduced for this polycrystalline samples. Besides, the higher in-plane coercive field for polycrystalline samples compared to the corresponding epitaxial ones (figure IV.6.) can be mainly ascribed to the higher interface roughness of the former, as already discussed in section IV.3. Fig. IV.6. displays the in-plane coercive field vs. Fe interlayer thickness for epitaxial and polycrystalline samples. In the case of the epitaxial series it remains constant, which clearly indicates the existence of a continuous and flat Au-Fe interlayer for each Fe thickness. On the other hand, the polycrystalline series shows a coercive field increase with Fe thickness up to 3 nm Fe, probably due to an islanded morphology. At higher Fe interlayer thickness, once coalescence forms a continuous Fe interlayer, the coercive field decreases due to an improved homogeneity. This can be attributed to a decrease in the number of pinning points for domain-wall motion when the magnetization reversal takes place.

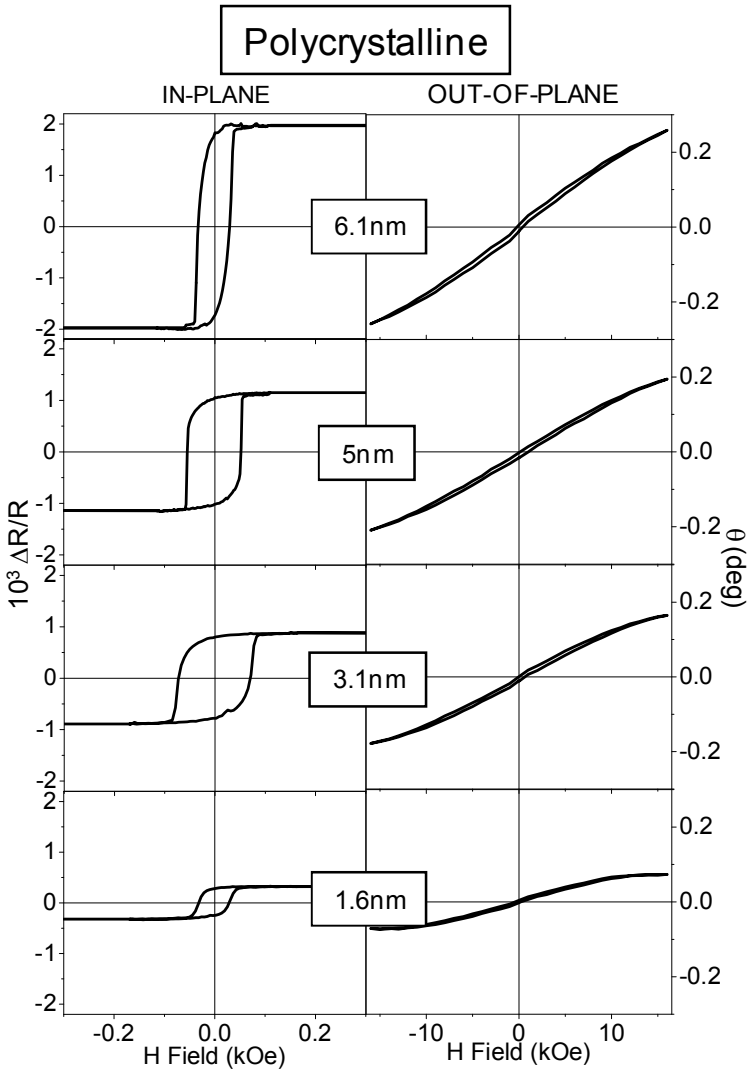

Figure IV.5. Kerr magnetooptical loops of representative polycrystalline samples measured in transverse (left panel) and polar (right panel) configurations.

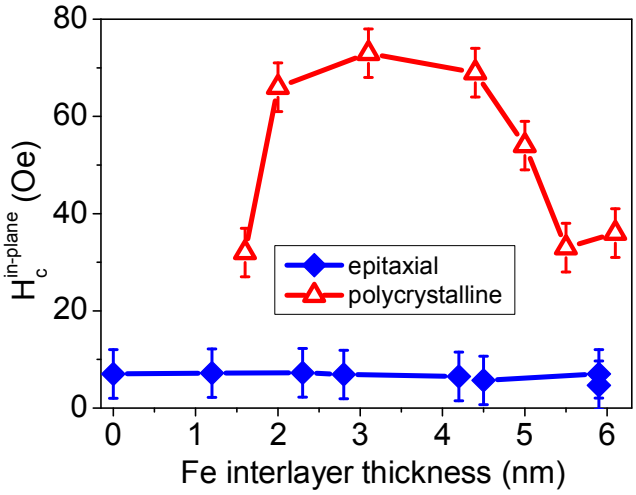

Figure IV.6. In-plane coercive magnetic field ($H_c^{in\text{-}plane}$) *vs.* Fe interlayer thickness for epitaxial and polycrystalline sets of samples.

IV.5. OPTICAL CHARACTERIZATION

As it has been reported on the previous chapter, the growth conditions affect the optical and magnetooptical (MO) properties of thin metal layers. For this reason, we have performed ellipsometric measurements in order to calculate the optical constants for the topmost Au layer (most relevant for the SPP excitation under Kretschmann configuration) of both series of samples. The classical Drude-Lorentz model has been used to get the dielectric constants of the epitaxial and polycrystalline Au layers:

$$\varepsilon(\omega) = \varepsilon_{\infty} - \frac{\omega_p^2}{\left(\omega^2 + i\alpha\Gamma\omega\right)} + G_1(\omega) + G_2(\omega) \qquad \text{[IV.1.]}$$

where ε_∞ is the high-frequency limit dielectric constant, ω_p is the plasma frequency , Γ is the damping constant, and the G terms represent the interband transitions in the visible region as two Lorentz oscillators:

$$G_n(\omega) = \frac{f\omega_n^2}{\omega_n^2 - \omega^2 - i\Gamma_n\omega} \qquad \text{[IV.2.]}$$

Using the Drude parameters and amplitude, frequency and damping constant of the n oscillators (f, ω_n and Γ_n respectively) from ref [5], we have fitted the free parameter α for our ellipsometric measurements. This loss factor (α) is used to quantify the differences between the damping term in Au bulk from the literature[19] and our fabricated samples. The obtained results *vs.* Fe interlayer thickness are plotted in Fig. IV.7. (a), showing an overall increase of the loss factor with Fe interlayer thickness. It is significant that the two samples without Fe interlayer exhibit a loss factor very close to 1, proving the good quality of epitaxial and polycrystalline Au thickest layers. The main remark of this optical characterization is the similarity of the Au loss factors for the two series. This indicates that the cristallinity, grain size and roughness are not critical parameters for the optical constants of the Au topmost layers. The actual Au optical constants from the representative 6 nm Fe samples of the two series of samples are shown in Fig. IV.7. (real (b) and imaginary parts (c)), further confirming the mentioned resemblance between the optical properties of the topmost Au in the epitaxial and polycrystalline samples, although higher absorption is obtained in the polycrystalline sample, as can be observed in the imaginary part at low photon energy[20].

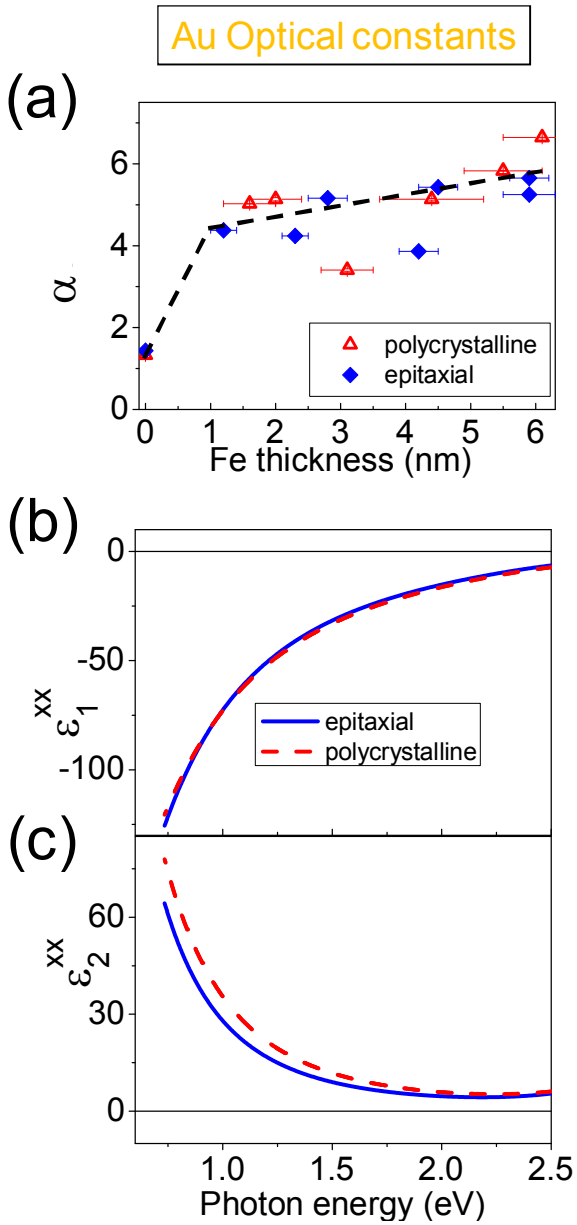

Figure IV.7. Optical properties, obtained by ellipsometric measurements, of the Au topmost layers from both sets of samples: (a) Loss factor (α) *vs.* Fe interlayer thickness. Epitaxial and polycrystalline optical constants (Real (b) and imaginary (c) parts) for the Au topmost layer in the 6 nm Fe samples.

IV.6. MAGNETOOPTICAL CHARACTERIZATION

In order to extract the effective MO constants of the different Fe layers, Polar Kerr spectra have been measured for all the samples in both series (figure IV.8.). An increase of rotation (θ) and ellipticity (ϕ) is observed with Fe thickness in the two series of samples. In every spectrum, the inverted s-shape feature found in the rotation curves (and the corresponding maxima found in the ellipticity ones) around 2.5 eV is related to the bulk plasmon resonance of Au. Interestingly, the overall MO activity of the

polycrystalline samples is lower (roughly a factor two) than that of the equivalent epitaxial samples. Surely, we have to take into account the contribution of the 1 nm Fe buffer layer in the epitaxial series to the MO activity. However, the rotation and ellipticity spectra for the 1 nm Fe interlayer epitaxial structure (with 2 nm of total Fe thickness) exhibit an overall magnitude similar to the spectra for the 6 nm Fe polycrystalline one. This indicates that the differences between the two sets of samples are not originated simply by the presence of a MO active buffer layer on epitaxial multilayers. In advance, we can anticipate that this reduction in the MO activity for the polycrystalline Fe layers is originated from differences in the MO constants of both structures.

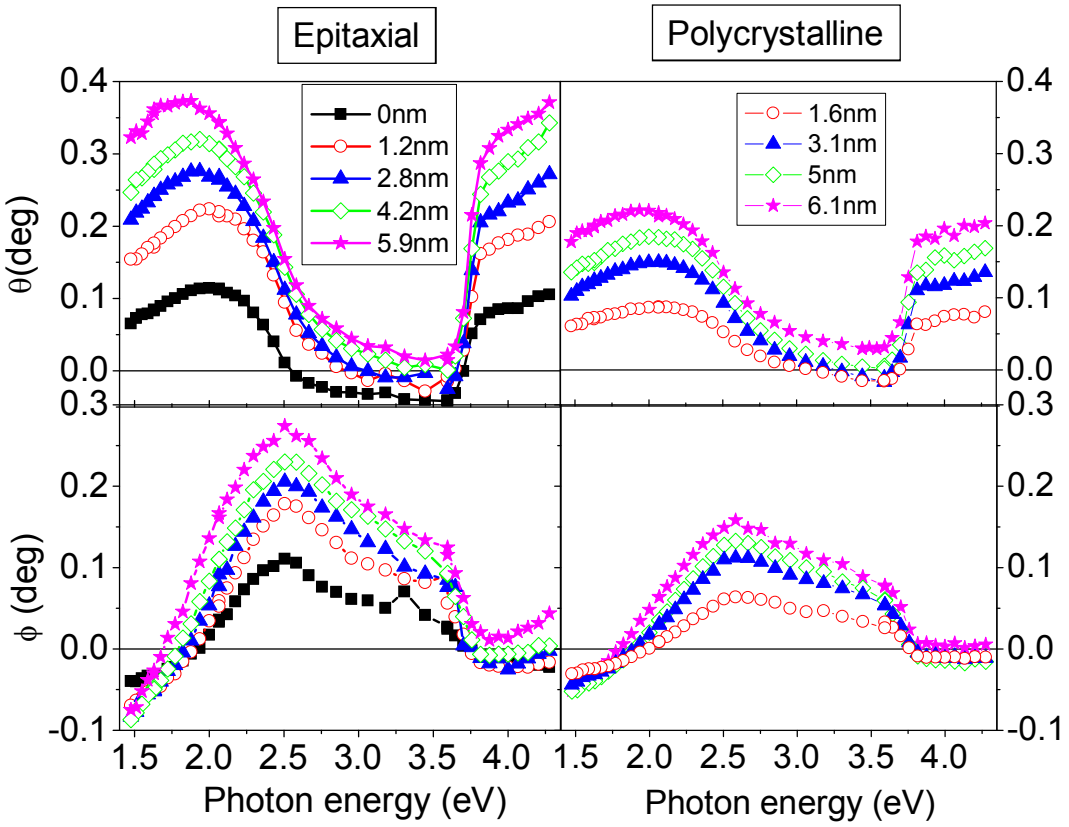

Figure IV.8. Rotation (θ) and ellipticity (ϕ) spectra of representative samples for both series of structures.

When analyzing the MO constants we have to take into account that there are two Fe layers in each epitaxial multilayer (except for the 0 nm Fe sample): buffer layer and interlayer. Therefore three representative MO constants can be extracted: epitaxial interlayer, epitaxial buffer (1 nm Fe) and polycrystalline interlayer Fe MO constants. In Fig. IV.9. we have plotted the MO constants corresponding to the epitaxial buffer, 6 nm Fe epitaxial interlayer and 6 nm Fe polycrystalline interlayer. Worth to mention, no relevant differences are observed looking at the MO constants of the buffer layer and interlayer for epitaxial structures. On the other hand, polycrystalline and epitaxial interlayers exhibit remarkable differences. First, the value of the real part of the MO

constants for the epitaxial interlayer is about two times larger than for the polycrystalline one at low photon energies (1.8 times at He-Ne laser wavelength). Second, the zero-crossing of the imaginary part of the MO constants for the epitaxial interlayer is located around 1.8 eV whereas for the polycrystalline one is located around 2.5 eV. In order to understand the origin of these relevant differences, we can use the Drude model for simulating the MO properties of the intraband contribution in a Fe layer [IV.3.]. This approximation, considering only the intraband contribution, is enough to describe the MO constants in the low photon energy region (1-5 eV), because the interband contribution on the MO activity from Fe or Co is not very important in this spectral region[21,22] and can be neglected. Therefore the MO constants are described by:

$$\varepsilon_{xy}^{drude}(w) = i\frac{w_c w_p{}^2}{w\left[(\Gamma - iw)^2 + w_c{}^2\right]} \qquad \text{[IV.3.]}$$

using a value of plasma frequency of 10.2 eV, cyclotron frequency of 0.0973 eV (w_p and w_c, respectively) from ref.[21] in this equation. Two theoretical curves corresponding to two different damping constants 1.6 eV (bulk Fe) and 2.5 eV have been plotted in figure IV.9. They exhibit a good qualitative agreement with the curves experimentally obtained for the epitaxial and polycrystalline structures if we keep in mind that the interband contribution has not been taken into account in the theory. This points to a possible contribution to the different MO properties observed between epitaxial and polycrystalline Fe layers coming from these different Drude damping constants (Γ) or electron scattering times in the two kinds of metallic layers. The higher Γ used to match the polycrystalline curve indicates a higher ratio of electronic collisions inside the polycrystalline Fe layer and at their rough interfaces compared to the epitaxial or bulk one[8,9].

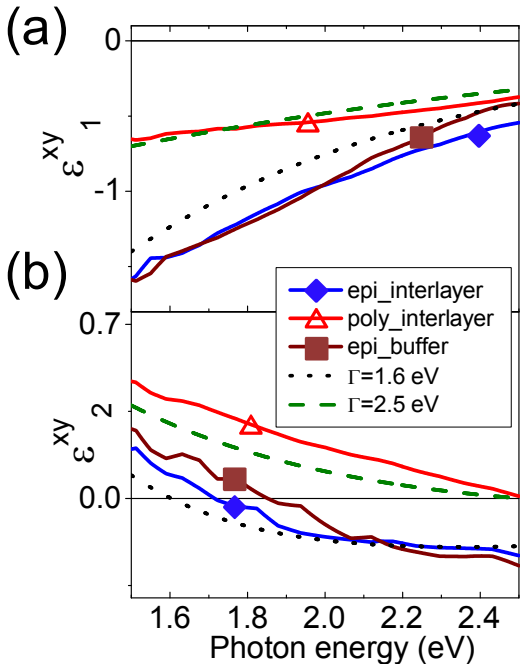

Figure IV.9. Real (a) and imaginary (b) parts of experimental magnetooptical (MO) constants for epitaxial Fe interlayer (6 nm thick), epitaxial Fe buffer layer (1 nm thick) and polycrystalline Fe interlayer (6 nm thick). In addition, two theoretical curves, using a Drude model with Γ as 1.6 and 2.5 eV (dotted and dashed curves, respectively), were added in order to compare with the experimental MO constants.

IV.7. MAGNETOPLASMONIC CHARACTERIZATION

IV.7.A.-Surface plasmon resonance effects on the MO activity

Once the different structural, morphological and MO characteristics of both series of samples are determined, the possible influences on their magnetoplasmonic properties can be studied. This has been carried out by measuring the reflectivity and transverse MO Kerr effect (TMOKE) signal using the Kretschmann configuration for a given wavelength λ=632 nm as it has been schemed in figure IV.10. (a).

Standard reflectivity versus incidence angle measurements as a function of the Fe interlayer thickness are shown in figure IV.10. (b) for the epitaxial (left panel) and polycrystalline (right panel) structures. Focusing first our attention on the series of epitaxial samples, we can see a strong dependence of the minimum in the reflectivity as a function of the Fe interlayer thickness, with values of 0.4 for the sample without Fe interlayer, 0.1 for the sample with 1.2 nm Fe, and much lower values for the rest of epitaxial samples. The lowest value of the reflectivity minimum is observed for the epitaxial sample with 4.5 nm Fe, since this thickness is very close to the optimum SPP excitation thickness.

With Fe interlayer thicker than 4.5 nm, the reflectivity minimum increases because the multilayer system goes far from the optimum SPP excitation parameters.

On the other hand, this dependence is much less pronounced in the polycrystalline series, with all the minima in the reflectivity reaching values between 0.1 and 0. The lowest reflectivity minimum value is obtained for the sample of 3.1 nm Fe (optimum SPP excitation), the reflectivity minimum increasing again with thicker Fe interlayers.

Considering now the transverse Kerr signal ($\Delta R/R$) measured for both series of samples, in figure IV.10. (c) we show the obtained results as a function of both the Fe interlayer thickness and the incidence angle. Remarkably, the largest $\Delta R/R$ signal values are obtained for both the epitaxial structure with 4.5 nm Fe interlayer and polycrystalline one with 3.1 nm Fe interlayer. For the specific thickness of these two structures the SPP excitation is optimum, therefore exhibiting a very small (close to zero) reflectivity upon SPP excitation, and as a consequence an enhanced MO activity, which actually might diverge if values of reflectivity very close to zero were achieved. The different optimum SPP excitation thickness in both structures are due to the different optical absorption of the two buffer layers used, being 2 nm of Cr more absorbing than 1nm of Fe, and consequently being necessary a lower Fe interlayer thickness for almost optimum plasmon excitation in the polycrystalline series. It is worth noticing that there is no clear influence of the crystalline nature of the structures on the plasmon excitation of the different samples.

Finally we can represent $(\Delta R/R)_{MAX}$, which is the positive maximum value of TMOKE angular measurement [14, 18], as a function of the Fe interlayer thickness for the two sets of samples with and without SPP excitation (see figure IV.10. (d)). When SPP is excited (left panel of figure IV.10. (d)), the $(\Delta R/R)_{MAX}$ exhibits a maximum at the mentioned optimum SPP thickness for polycrystalline and epitaxial structures (3.1 nm and 4.5 nm Fe thickness respectively), decreasing for thicker Fe layers. In contrast, when no SPP is excited (right panel of figure IV.10. (d)), $(\Delta R/R)_{MAX}$ shows a typical monotonous increase with Fe amount for both sets of samples. The influence of the higher MO constants of the epitaxial samples with respect to the polycrystalline ones is clearly observed, with the higher TMOKE signal increase with Fe amount for the epitaxial structures compared to that for the polycrystalline ones (a factor of 3).

In summary, the very large $\Delta R/R$ ratios with SPP excitation obtained in the polycrystalline and epitaxial systems at different Fe interlayer thickness (3.1 nm and 4.5 nm, respectively) are simply due to the proper thickness obtained in these two samples for optimum plasmon excitation, being the different optimum Fe interlayer thickness attributed to the different absorption of Cr and Fe buffer layers. On the other hand, the $\Delta R/R$ signal without SPP excitation is directly related to the MO constants of both series of samples following the same trend but exhibiting a larger linear increase for the epitaxial multilayers.

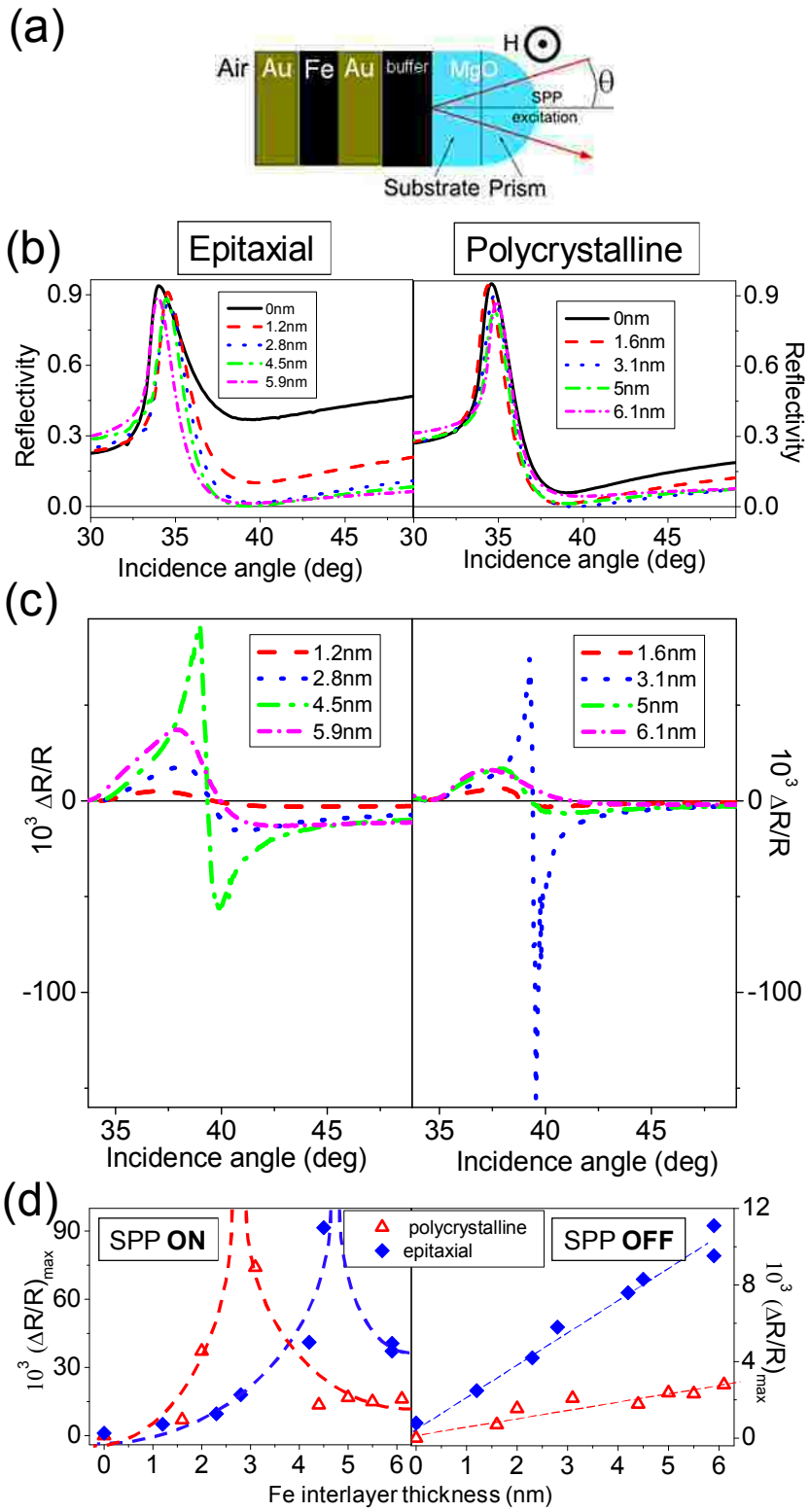

Figure IV.10. (a) Sketch of the Kretschmann configuration which allows the angular measurements of the (b) Reflectivity and (c) ΔR/R as a function of the Fe interlayer thickness for epitaxial (left panels) and polycrystalline (right panels) structures. (d) $(\Delta R/R)_{MAX}$ vs. Fe interlayer thickness for both polycrystalline (red triangles) and epitaxial (blue diamonds) samples, with (left panel) and without (right panel) SPP excitation. Dashed lines are guides for the eyes. Notice the different vertical scales when comparing the left and right panel.

IV.7.B.- Magnetic modulation of the SPP resonance

Another issue of interest is the potential use of these magnetoplasmonic structures in active plasmonic devices. The ferromagnetic layer in the multilayered structure introduces sizeable off diagonal components in the dielectric tensor of the whole system. Thus the application of a low external magnetic field can produce a modulation in the wavector of the SPP. This SPP modulation has been studied in the previous chapter using Co as the ferromagnetic layer[23,24,25,26]. Here, we have measured this effect in both epitaxial and polycrystalline structures with Fe as the ferromagnetic layer.

With the measurements shown in section IV.7.A. and following the formalism detailed in the previous chapter, based on the comparison between the angular derivative of the reflectivity and the angular dependence of ΔR/R, the magnetic field-induced modulation of the SPP wave vector can be determined. In figure IV.11. we present in symbols the experimentally obtained modulation as a function of the Fe interlayer thickness for both epitaxial and polycrystalline structures. As it can be seen, Δk/k increases with Fe interlayer thickness for both series of samples, with systematically larger values for the epitaxial samples, for Fe thickness above 2.5 nm, whereas the observed modulation is similar for both series below this value. Obviously, the non-zero wavevector modulation obtained for the epitaxial sample without Fe interlayer is due to the effect of the Fe buffer layer, whereas in the polycrystalline series the Cr buffer does not contribute to the modulation since Cr is not ferromagnetic.

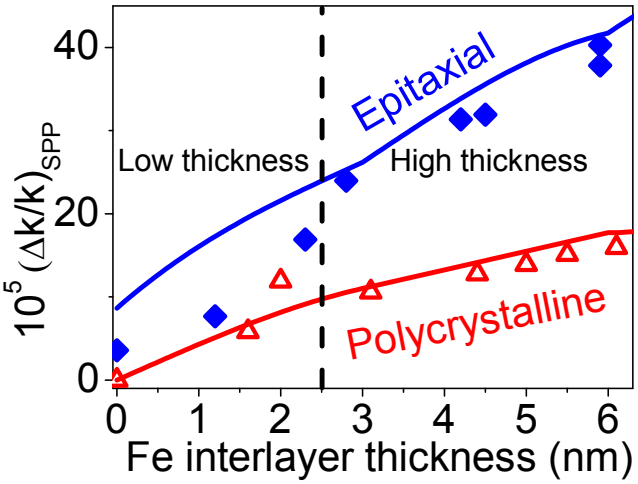

Figure IV.11. Fe interlayer dependence of experimentally (symbols) and simulated (continuous lines) $(\Delta k/k)_{SPP}$ using the actual MO constants obtained from epitaxial (diamonds) and polycrystalline (triangles) sets of structures.

To understand the observed differences, the modulation of the SPP wavevector as a function of the Fe interlayer thickness has been calculated using the transfer matrix formalism[27], assuming sharp interfaces between the different layers and using the effective magnetooptical (MO) constants experimentally determined by polar Kerr spectroscopy (see section IV.6.) for the 6 nm Fe epitaxial and polycrystalline interlayer samples. Note that the effective magnetooptical constant of the Fe layer is roughly a

factor of two lower in the polycrystalline sample than in the epitaxial one for the considered wavelength. The calculated results are shown in figure IV.11. as continuous lines, with a very good agreement with the experimental data corresponding to both series of samples, with the only exception of the epitaxial samples having Fe interlayer thickness below 2.5 nm.

This observed difference in $\Delta k/k$ is therefore ascribable to the reduced effective MO constants of the Fe interlayer for the polycrystalline series with respect to the epitaxial one. This reduction of the effective Fe MO constants can be interpreted in two ways: either because a system with a rough interface can be optically considered as an effective medium composed by Fe and Au, and therefore with effective MO constants lower than those of bulk Fe, or just by a purely interfacial effect where the MO constants of the Fe atoms at the Fe-Au interface are smaller from bulk Fe due to hybridization effects[12], and therefore proportional to the interface area, which will be larger for a system with rough interfaces. On the other hand, the deviation from the expected trend in the epitaxial series for Fe thickness below 2.5 nm (mainly for the 1.2 nm Fe sample) can be understood from the lack of completeness of the Fe interlayer at this thickness range as discussed in section IV.4. This lack of completeness gives rise to a region where Fe and Au coexist, and therefore can be considered as a layer with effective MO constants lower than those of bulk Fe.

Interestingly, as shown in the figure IV.12., the magnetic modulation of the SPP and the TMOKE signal without SPP excitation exhibit the same trend with the Fe interlayer thickness for both series of samples. This is due to the lower MO constants for the polycrystalline samples compared to the epitaxial ones, constants that in the end govern those two magnitudes.

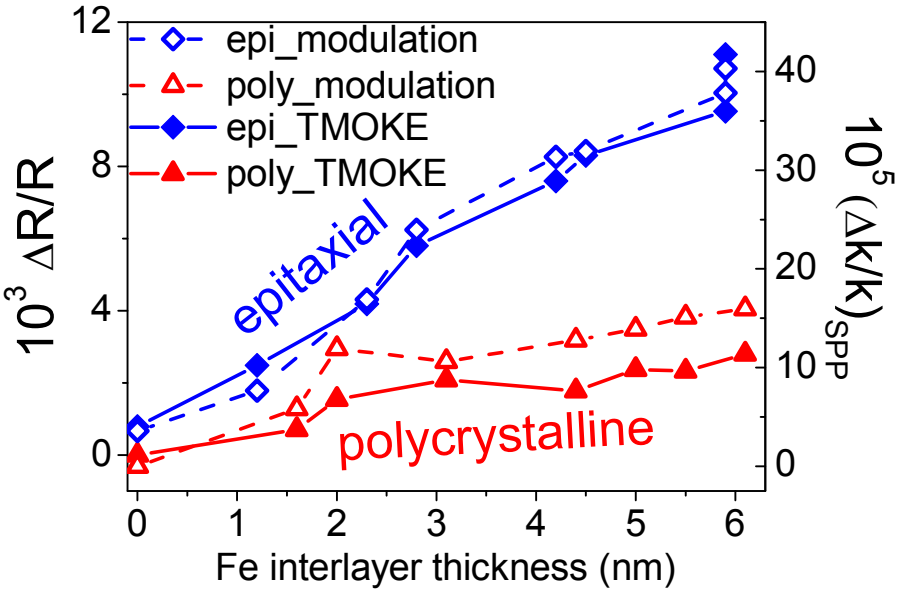

Figure IV.12. Fe interlayer dependence of experimental TMOKE without SPP excitation (closed symbols) and $(\Delta k/k)_{SPP}$ (open symbols) obtained from epitaxial (blue diamonds) and polycrystalline (red triangles) sets of structures.

IV.7.C.- Propagation length of the SPPs

From the viewpoint of applications, another relevant parameter for example for the development of a magnetic field driven plasmonic modulator is the propagation length of SPPs (L_{SPP}). Although there exist a number of experiments that provide accurate measurements of the L_{SPP} [4], for the purposes of this thesis the method based on the fitting of the minimum of reflectivity to a Lorentzian curve will be sufficient. The equation showing the reflectivity as a function of the in-plane light wavevector (k_x) of a metal layer under Kretschmann configuration can be written as[28]:

$$R = 1 - \frac{4\Gamma_i \Gamma_{rad}}{\left[k_x - \left(k_x^0 + \Delta k_x\right)\right]^2 + \left(\Gamma_i + \Gamma_{rad}\right)^2} \qquad [IV.4.]$$

where k_x^0 is the SPP wavevector of a semi-infinite metal layer, Δk_x is the wavevector correction for a finite metal layer, Γ_i are the inherent losses of a metal and Γ_{rad} are the radiantive losses. Close to the thickness for optimum SPP excitation, we can approximate Γ_{rad} being equal to Γ_i[28]. Then we can extract Γ_i as the FHWM from a fitting to a Lorentzian curve as it is shown in the Fig. IV.13. (a) for the curve of the 4.5 nm Fe interlayer thickness epitaxial sample. Finally L_{SPP} is defined as:

$$L_{SPP} = \frac{1}{2\Gamma_i} \qquad [IV.5.]$$

The L_{SPP} of the 3.1 nm Fe and 4.5 nm Fe samples, which are the samples with optimum SPP excitation, for the polycrystalline and epitaxial sets respectively, are shown in the table from Fig. IV.13. (b). The L_{SPP} of the two samples are very similar pinpointing the mentioned same SPP characteristics for the two series. For the sake of comparison, the $(\Delta k/k)_{SPP}$ and L_{SPP} of the optimum SPP excitation sample for the polycrystalline Au/Ag/Co/Ag series of the previous chapter are also shown in the table of Fig. IV.13. (b). Due to the lower optical absorption of Ag compared to Au, this L_{SPP} for the Ag-Co based system is the double of the L_{SPP} for the two Au-Fe based systems. Besides, the optimum SPP excitation thickness of Co (8 nm) in this Au/Ag/Co/Ag multilayer is higher than the optimum SPP excitation Fe thickness for the two series studied in this work. As the modulation is proportional to the thickness of the ferromagnetic layer in systems with similar roughness, this larger amount of magnetic material justifies in part the enhanced $(\Delta k/k)_{SPP}$ for the Ag-Co based system compared to the polycrystalline Au-Fe one.

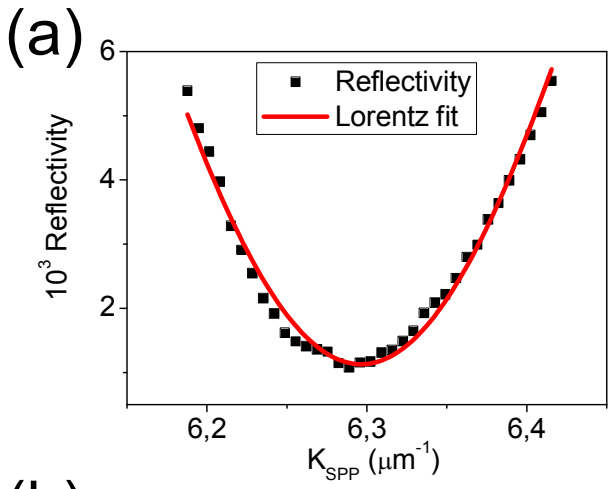

(b)

	Epitaxial (5nmFe)	Polycrystalline (3nmFe)	AuAgCo (8nmCo)
$(\Delta k/k)_{SPP}$	$32*10^{-5}$	$11*10^{-5}$	$24*10^{-5}$
L_{SPP}	1.7±0.3 μm	1.9±0.3 μm	3.6±0.9 μm
$10^3\ (\Delta kxL)_{SPP}$	10±1.7	4.0±0.6	18±4.5

Figure IV.13. (a) Fit of a reflectivity minimum to a lorentzian curve for the 4.5 nm Fe interlayer sample of the epitaxial set. (b) Table showing $(\Delta k/k)_{SPP}$, L_{SPP} and $(\Delta k \times L)_{SPP}$ of the samples with optimum SPP excitation for the epitaxial Au/Fe/Au, polycrystalline Au/Fe/Au and polycrystalline Au/Ag/Co/Ag series.

Finally, we can define a figure of merit[25] for the three structures that exhibit optimum SPP modulation by taking into account both magnitudes relevant for modulator applications ($(\Delta k/k)_{SPP}$ and L_{SPP}) as the $(\Delta k \times L)_{SPP}$ product. This last magnitude is shown for the three structures in the last line of the table of Fig. IV.13. (b). The Ag-Co based system exhibits the highest $(\Delta k \times L)_{SPP}$ due to its highest L_{SPP}, with the values for the Au-Fe epitaxial structure yielding almost 50%, and the Au-Fe polycrystalline showing the lowest $(\Delta k \times L)_{SPP}$ value(less than the half of Au-Fe epitaxial one) due to its lowest $(\Delta k/k)_{SPP}$.

IV.8.-CONCLUSIONS

In this chapter, we have carried out a systematic study comparing the structural, morphological, magnetic, optical, MO and magnetoplasmonic properties of epitaxial and polycrystalline Au/Fe/Au trilayers as a function of the Fe interlayer thickness.

We find a direct effect of the higher crystalline and interface quality of the epitaxial structures on the MO constants of Fe, which as a consequence gives rise to an increase in the MO activity without SPP excitation (threefold) and in the magnetic modulation of the SPP wavevector (twofold) with respect to their equivalent polycrystalline ones.

On the other hand, the MO activity with SPP excitation mainly depends on the achievement of the exact layers thickness that leads to optimum Plasmon excitation, and as a consequence to a minimum in the reflectivity and a maximum in the TMOKE signal.

From the SPP propagation length L_{SPP}, the $FoM \equiv (\Delta k \times L)_{SPP}$ can be defined and the optimized epitaxial structure exhibit double performance than the optimized polycrystalline one. Finally, the values of the optimized polycrystalline Au/Ag/Co/Ag structure were presented in order to evaluate the possibility of epitaxial Ag-based modulator studies.

IV.9.-REFERENCES

[1] P. Nagpal, N. C. Lindquist, S.–H. Oh and D. J. Norris, Science **325,** 594 (2009).

[2] X. Zhu et al., Adv. Mater. **22,** 4345-4349 (2010).

[3] V. Krishan and R. H. Ritchie, Phys. Rev. Lett. **24,** 1117 (1970).

[4] M. Kuttge, E. J. R. Vesseur, J. Verhoeven, H. J. Lezec, H. A. Atwater and A. Polman, Appl. Phys. Lett. **93,** 113110 (2008).

[5] K.-P. Chen, V. P. Drachev, J. D. Borneman, A. V. Kildishev and V. M. Shalaev, Nano Lett. **10,** 916 (2010).

[6] Y. Saito, J. J. Wang, D. N. Batchelder and D. A. Smith, Langmuir **19,** 6857-6861 (2003).

[7] M. Grzelczak, B. Rodríguez-González, J. Pérez-Juste and L. M. Liz-Marzán, Adv. Mater. **19,** 2262-2266 (2007).

[8] C. Clavero, B. Sepúlveda, G. Armelles, Z. Konstantinovic, M. García del Muro, A. Labarta and X. Batlle, J. Appl. Phys. **100,** 074320 (2006).

[9] C. Clavero, A. Cebollada, G. Armelles, Y. Huttel, J. Arbiol, F. Peiró and A. Cornet, Phys. Rev. B **72,** 024441 (2005).

[10]Clavero, C. et al. (2008). Morphology and capping effects in the magnetic and magneto-optical properties of nanoparticulate Co films. *Physical Review B*, *77*(9).

[11] A. A. Sidorenko, C. Pernechele, P. Lupo, M. Ghidini, M. Solzi, R. De Renzi, I. Bergenti, P. Graziosi, V. Dediu, L. Hueso and A. T. Hindmarch, Appl. Phys. Lett. **97,** 162509 (2010).

[12] L. Uba et al., Phys. Rev. B **62**(20), 13731-13747 (2000).

[13] D. Regatos, D. Fariña, A. Calle, A. Cebollada, B. Sepúlveda, G. Armelles and L. M. Lechuga, J. Appl. Phys. **108,** 054502 (2010).

[14] J. Shen *et al.*,Surf. Sci. Reports **52**, 163 (2004).

[15] C. Martínez Boubeta et al., J. Appl. Phys. **93**(4), 2126-2134 (2003).

[16] A. Singh et al., Appl. Phys. Lett. **87,** 072505 (2005).

[17] E. Paz et al., Nanotechnology **21,** 255301 (2010).

[18] C. Martínez Boubeta, C. Clavero, J. M. García-Martín, G. Armelles, A. Cebollada, Ll. Balcells, J. L. Menéndez, F. Peiró, A. Cornet and M. F. Toney, Phys. Rev. B **71,** 014407 (2005).

[19] Johnson P. B. and Christy R. W., Phys. Rev. B **6**, 4370 (1972).

[20] Fedotov, V., & Uchino, T. (2012). Low-loss plasmonic metamaterial based on epitaxial gold monocrystal film. *Optics Express*, *20*(9), 9545-9550.

[21] G. S. Krinchik, J. Appl. Phys. **35,** 1089 (1964).

[22] R. Carey and B. W. J. Thomas, J. Phys. D: Appl. Phys. **7,** 2362 (1974).

[23] J. B. González-Díaz, A. García-Martín, G. Armelles, J. M. García-Martín, C. Clavero, A. Cebollada, R. A. Lukaszew, J. R. Skuza, D. P. Kumah and R. Clarke, Phys. Rev. B **76**, 153402 (2007).
[24] E. Ferreiro-Vila et al., Phys. Rev. B **80**(12), 125132 (2009).
[25] D. Martín-Becerra,J. B. González-Díaz, V. V. Temnov, A. Cebollada, G. Armelles, T. Thomay, A. Leitenstorfer, R. Bratschitsch, A. García-Martín and M. U. González, Appl. Phys. Lett. **97,** 183114 (2010).

[26] Temnov, V. V *et al.* (2010). Active magneto-plasmonics in hybrid metal – ferromagnet structures. *Nature Photonics*, (January), 1-5.

[27] M. Schubert, Phys. Rev. B **53**(8), 4265-4274 (1996).

[28] H. Raether, *Surface Plasmons on Smooth and Rough Surfaces and on Gratings*, Springer Tracts in Modern Physics, Vol. 111 (Springer-Verlag, Berlin, 1988).

Chapter V:

Sensing

Applications

V.1- INTRODUCTION 110

V.2.- GLAD TiO_2 FUNCTIONALIZED GAS SENSOR 111

V.2.A.-Preparation of magneto-optical transducing layers and TiO_2 sensing layer 113

V.2.B.-Morphological characterization 114

V.2.C.-Magnetoplasmonic characterization 115

V.2.E.-Gas sensing 119

V.3.- BIOSENSING 123

V.3.A.-Surface functionalization of the biosensor 123

V.3.B.-Biosensing experiment (antiBSA recognition) 124

V.3.C.-Comparison of different multilayers as transducers 128

V.4.. -CONCLUSIONS 130

V.5.. - REFERENCES 131

V.1- INTRODUCTION

As it is well known, the excitation of SPP waves leads to regions of enhanced electromagnetic (EM) fields in the direct proximity of the metal-dielectric interface that are extremely sensitive to the local changes of refractive index occurring at such interface, and this property provides a capability for a label-free form of analytical detection[1]. As a result, this technique is widespread to monitor the binding of biomolecules to the Au or Ag surface, as well as to monitor interactions between biomolecules of different nature in the nanomolar to picomolar range in real time. Applications of this technology can be found in biology, food safety, medical diagnostics and environmental monitoring[2,3,4,5,6].

For this sensing application of SPR's, an "active sensing layer" is needed onto the Au or Ag transducing substrate. Its active role consists in the change of its optical constants upon the interaction with the investigated analyte (gas or biomolecules) which can be sensitively detected as a change in the reflectivity SPR curve (the details of a SPR sensor are explained in the chapter of Experimental Techniques). This variation of the Reflectivity curve is also present on the MO activity under SPP excitation. For example, a simulation via Transfer matrix method of the TMOKE signal around the SPP resonance for a Au/Co/Au trilayer performed with two different dielectric media named baseline (n=1) and analyte (n=1.095) above the upper Au layer of the multilayer is shown in figure V.1. (a). The resonance of the TMOKE signal exhibits an angular shift due to the variation of the refractive index. At a fixed incidence angle this angular shift is translated into a change in the TMOKE signal (figure V.1. (b)). This sensor configuration based on the measurement of the MO activity under SPP excitation is called MagnetoOptical Surface Plasmon Resonance (MOSPR) sensor and it was first proposed and studied by Sepulveda et al. [7]

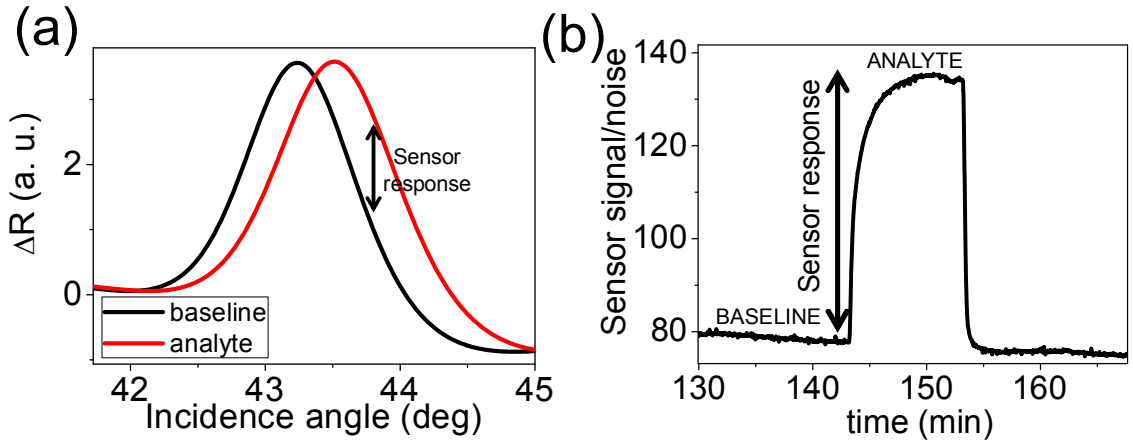

Fig.V.1. Simulated angular TMOKE curves for two dielectric media: baseline (n=1) and analyte (n=1.095). We can observe the angular shift that causes a variation in the TMOKE signal (sensor response). (b) Sensorgraph with the analyte response.

In this chapter, both a porous TiO_2 thin film and a bovine serum albumine (BSA) self-assembled multilayer (SAM) are proposed as sensing layers for the detection of alcohol vapours (gas sensing) and the specific detection for the antibodies of the BSA (biosensing) respectively. Both sensing experiments have been performed for the SPR and MOSPR sensors to compare their performance. The thickness for the metallic layers of the sensor transducers have been optimized via Transfer matrix simulations by Dr. J. B. González-Díaz and Dr. A. García-Martín to maximize the sensing performance of the multilayers, i.e., to achieve the higher slope for the reflectivity (SPR sensor) and TMOKE curves (MOSPR sensor). The comparison between SPR and MOPSR sensing platforms is made by using optimized layers in each case, i. e. Au layers for SPR and Au/Co/Au for MOSPR. Sepulveda et al. has reported a higher sensitivity for the MOSPR sensor compared to the SPR one detecting the unspecific adsorption of BSA protein on the Au layer of the Au/Cr/Co/Cr transducer[7]. Confirming this higher sensitivity of the MOSPR sensor, Regatos et al. has studied these two kinds of sensors for Au/Fe/Au transducers[8].

V.2.- GLAD TiO_2 FUNCTIONALIZED GAS SENSOR

A porous sensing layer is a good choice for gas sensing, since it provides a large surface area to be put in contact with the gaseous ambient to be monitored. Organic, inorganic or mixed active sensing materials can be chosen, with various structural and morphological features for these purposes[9,10,11]. Also, nanostructured semiconductor metal oxides, such as SnO_2, ZnO, TiO_2, and NiO, are promising sensing materials for a wide range of gases and vapours. The enhanced sensing features are determined by the high chemical activity and porosity of the active materials, which are direct consequences of their nanostructure. Because of this, gas sensing capabilities depend critically on the synthesis method and parameters that allow for tailoring of selectivity and sensitivity toward the target species. Previously, TiO_2 thin films with Au nanoparticles[12] and TiO_2 nanocrystals on Au films[13], have succesfully been used as sensing layers for a SPR sensor to detect alcohol vapours. This justifies our election of a nanostructured TiO_2 film as sensing layer for these vapours.

In our case, thin films of nanoporous columnar TiO_2 deposited by Glancing angle deposition (GLAD) have been chosen as sensing material to detect the presence of different alcohol vapours of interest in food applications. GLAD is a physical vapour deposition method capable of producing thin films with a large variety of highly porous nanostructures (see the figure V.2.)[14,15,16] that can be tuned to meet the needs of different applications[17,18,19].

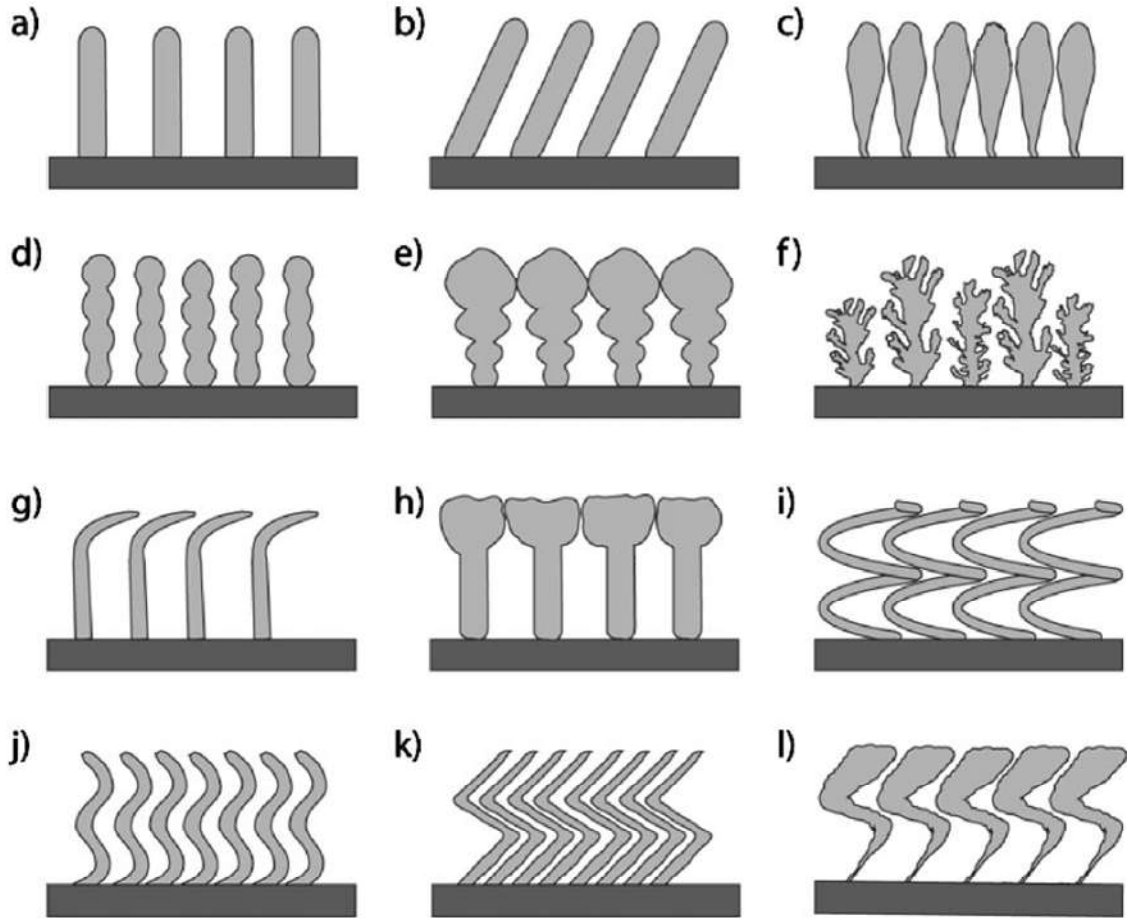

Figure V.2. Schematic depiction of various nanostructures obtained in GLAD thin films: (a) straight pillars, (b) inclined columns, (c), (d), (e) pillars with variable diameter, (f) fractal-like structures, (g), (h) columns with capping layers, (i) helix, (j) waved columns, (k) zig–zag, (l) zig–zag pillars with varying diameter. (Figure taken from ref [14]).

During deposition, the zenithal angle α (angle of vapour incidence) and the azimuthal angle ω (angle of substrate rotation around substrate normal) are adjusted in response to real-time measurement of vapour deposition rates to yield a specific film nanostructure (see figure V.3.). The enhanced surface area observed in GLAD films has been exploited in a variety of applications, particularly in fabricating sensor devices[20,21]. Due to their inherently porous nature, gaseous species in the ambient environment are free to diffuse through the structure producing detectable changes in the dielectric constant of the system[18]. Moreover, the inner surface of the oxide films (such as SiO_2, TiO_2, and Al_2O_3) fabricated using GLAD, may promote the capillary condensation of water vapour within the porous structure, thus being used for humidity sensors[22].

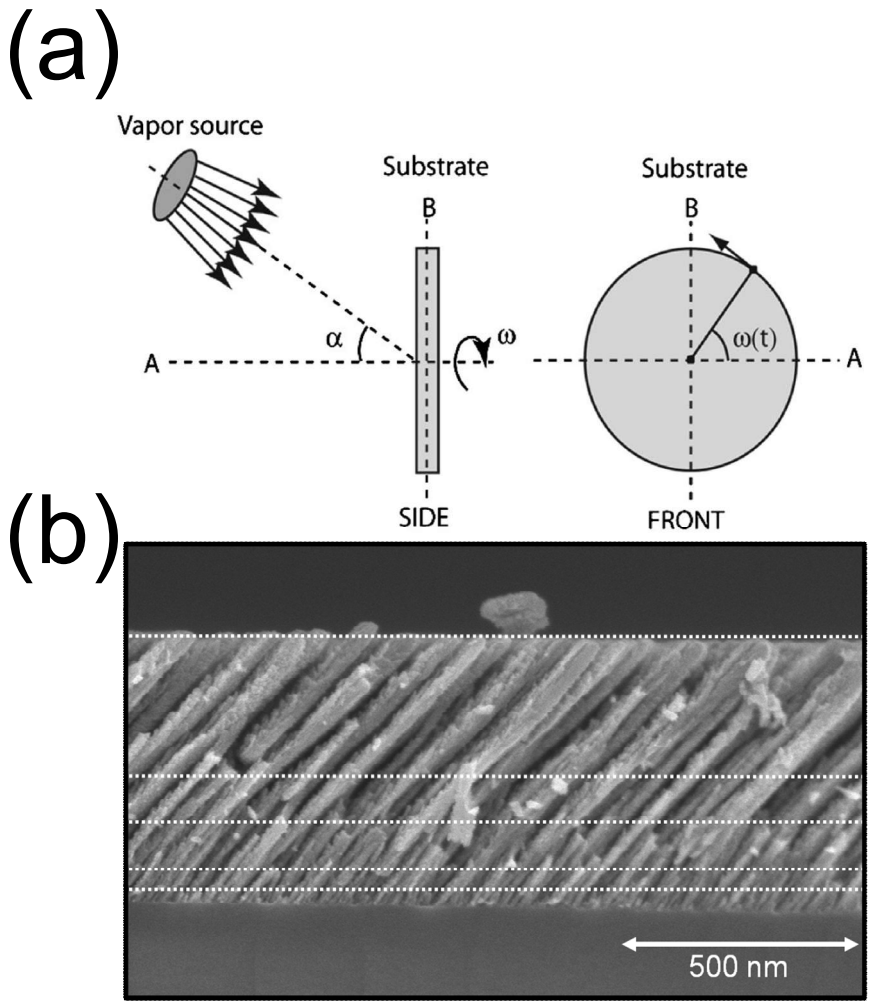

Fig.V.3. (a) Schematic description of the GLAD process. Angles of substrate tilt α and azimuthal rotation ϖ(*t*)=const (Figure taken from ref. [14]).(b) SEM picture showing a cross section of a TiO_2 thin film deposited by GLAD at ICMSE, using e-beam evaporation with incidence angle of 70º without rotation around the azimuthal angle.

V.2.A.-Preparation of magneto-optical transducing layers and TiO_2 sensing layer

A set of 15 nm Au/ 6 nm Co/ 25 nm Au/2nm Cr multilayers were deposited on Corning glass substrates. The 2 nm thick Cr layer between the substrate and the 25 nm Au layer improves the adherence of the magnetoplasmonic structure. All layers were deposited by dc magnetron sputtering at room temperature in an ultrahigh-vacuum chamber with a base pressure of 10^{-9} mbar using a circular mask of Ta with 8 mm diameter over the glass substrate. The samples exhibit two zones: a circular core with the metallic layers (for the gas sensing experiments) and an outer region with the bare glass substrate (see the inset of the figure V.5. (a)). In these conditions all the constituents layers are polycrystalline and the Co layer has in-plane magnetization. The choice of these thickness values comes from the need to prevent Co oxidation while maximizing the magneto-optical ΔR signal upon the change in the real part of refractive index n[23].

Once the transducer layers are grown, they were transferred to a different deposition system where 10, 20 and 50 nm amorphous TiO_2 thin films were deposited on top by the group of Prof. A. R. González-Elipe at the Intituto de Ciencia de Materiales de Sevilla (ICMSE) using glancing-angle deposition (GLAD) technique without any mask over the sample.In this way we can compare the GLAD TiO_2 grown over the metallic multilayer and over the bare glass substrate. Reference TiO_2 layers were also grown onto Au/Cr/glass and bare glass substrates. The porous nanocolumnar layer of TiO_2 was grown by electron beam evaporation from a TiO_2 source under a residual oxygen pressure of $5x10^{-4}$ torr at a zenithal angle of incidence of 70º. No rotation around the azimuthal angle was intended for the prepared films which, in this way, presented a tilted columnar nanostructure[18,19]. The deposition rate and film thickness were controlled with a calibrated quartz crystal monitor placed at a normal angle besides the substrates. Further details on the deposition process and optical features of the realized materials can be found in [18].

V.2.B.-Morphological characterization

As it is known the GLAD deposition leads to a thickness dependent surface morphology, with the characteristic nanocolumnar structures becoming more isolated and defined at high GLAD film thickness. Therefore some differences on the surface morphology (key factor in gas adsorption) were expected for the different TiO_2 thickness. For analyzing the surface morphology, the AFM is a very suitable technique as can be seen in Fig. V.4. The AFM images of the 20 nm TiO_2 show the early stages of the formation of nanocolumns. On the Au/Co/Au region, the TiO_2 nanostructures preserve the granular morphology of the metallic grains below them, whereas those over the bare substrate do not exhibit a regular morphology yet. Similar results (not shown) are obtained for a 10 nm TiO_2 deposit.

On the other hand, AFM images for a 50 nm TiO_2 deposit show well defined columnar structures over both Au/Co/Au trilayer and substrate regions. The AFM profiles make more clearly observable these TiO_2 columns , which are higher over the Au/Co/Au region than over the substrate region. This column height difference suggests that there is a better atomic shadowing produced over the grained Au/Co/Au surface than over the flat glass surface. Contrary to this, 10 and 20 nm TiO_2 deposits do not exhibit such a remarked nanostructured morphology.

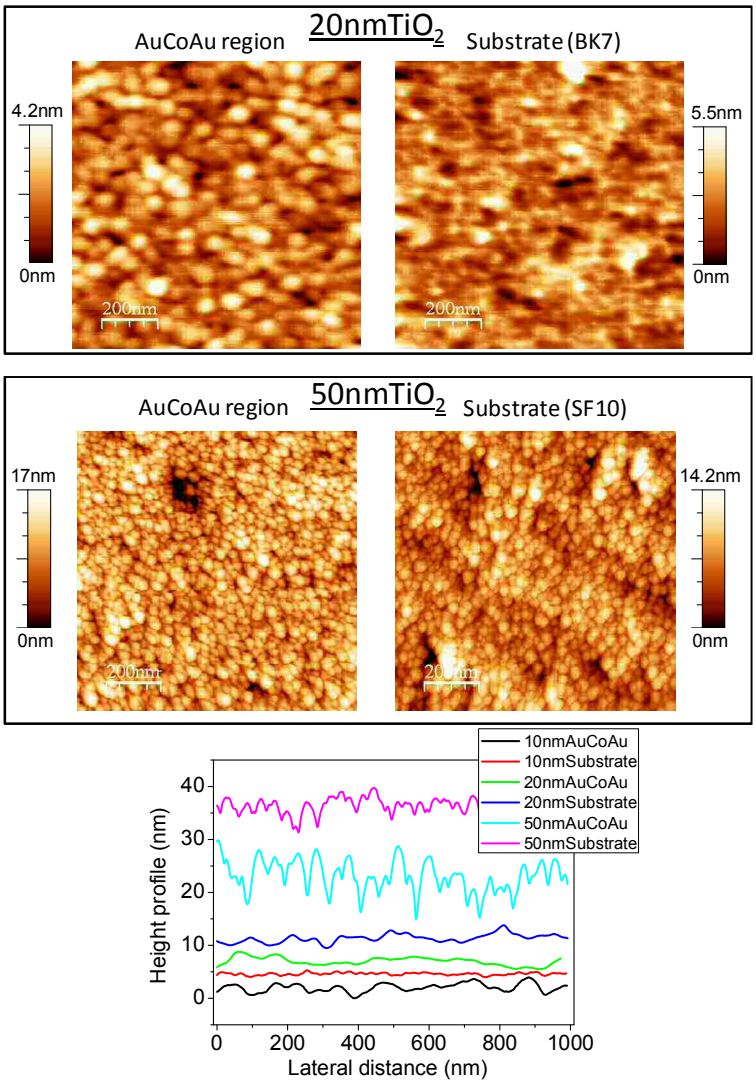

Fig.V.4. AFM images and profiles of different thickness TiO_2 samples on both Au/Co/Au and substrate regions.

V.2.C.-Magnetoplasmonic characterization

We first briefly discuss the peculiar optical properties of structures grown by GLAD. It is worth to mention that Wang et al. have reported that the GLAD TiO_2 structures exhibits birrefringence ($\Delta n=0.067$) with a incidence flux angle of 65 degrees higher than common bulk materials as quartz ($\Delta n=0.009$) or MgF_2 ($\Delta n=0.012$)[24].

Taking into account the directional growth of GLAD TiO_2 layers, the elipsometric measurements have been taken at different azimuth angles (see inset Fig. V.3. (a)). The 10 and 20 nm TiO_2 samples did not exhibit any dependence of azimuth angle on the elipsometric measurements. This indicates that in the early stages of the growth by GLAD the nanostructures are not asymmetric within the plane of the sample. Therefore an Effective Medium Approximation (EMA) was used for modelling the GLAD TiO_2 layer as a combination of TiO_2 bulk and air with these two thickness. The

refractive index obtained from the fit between experiments and model is shown in Fig. V.5. (a). In both cases, a refractive index of 1.682 was obtained at 632.8nm wavelength, which is significantly smaller than that of bulk TiO_2 (2.494). However, this value is in agreement with previously reported refractive indices of TiO_2 thin films prepared by GLAD[18]. This indicates that the porosity is very similar for these two TiO_2 thickness.

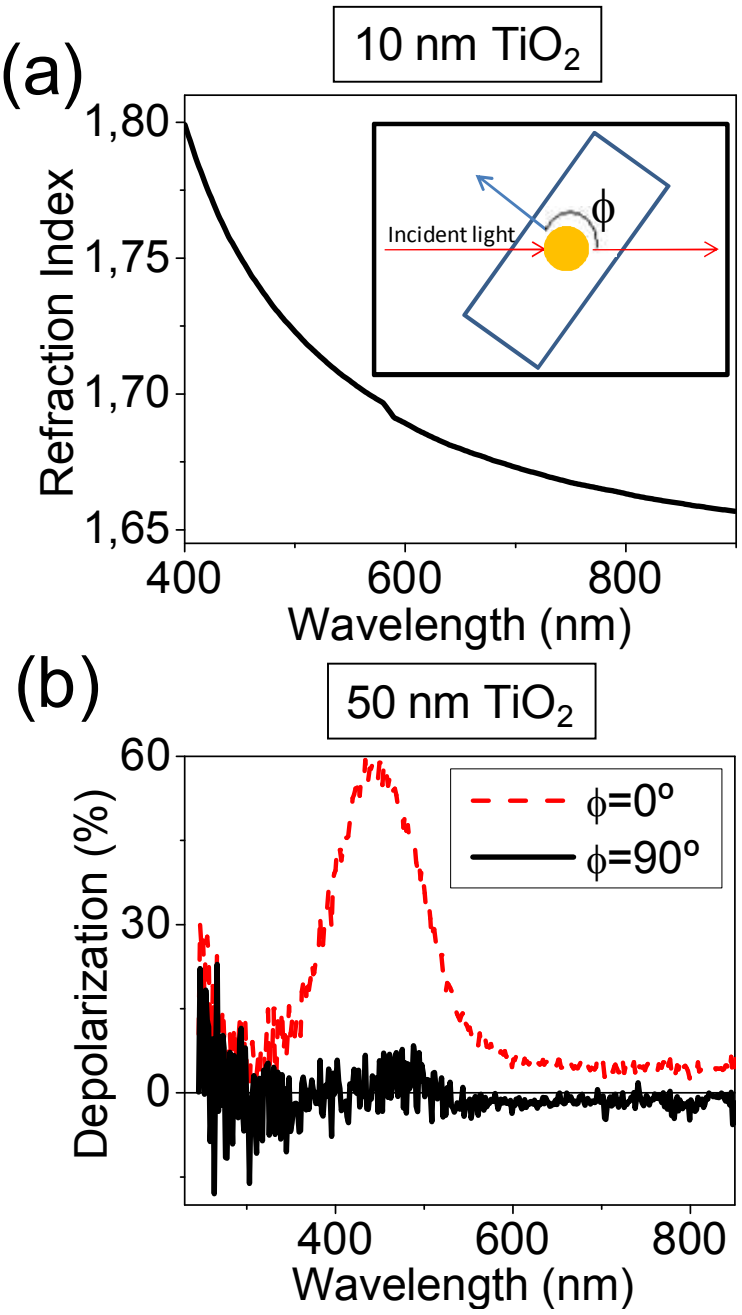

Fig.V.5. (a) Deduced refractive index of 10 nm TiO_2 thickness sample using an EMA. (b)Depolarization spectra for different azimuth angles of 50 nm TiO_2 thickness sample.

On the other hand, the 50 nm TiO_2 sample presented a distinctive morphology as AFM measurements indicated in the previous section. As the depolarization ratio

(which represents the lost of the polarization state after the light being reflected on the sample[25]) from ellipsometric experiments is a good parameter for checking the presence of possible optical anisotropies (Fig. V.3. (b)), it has been used to characterize this sample for two different azimuthal light incidence angles. The obtained spectra show a peak around 475 nm wavelength related to scatering proccess, the intensity of which in the 0º azimuth curve being much higher than that of the 90º azimuth curve. This difference indicates the existence of an optical anisotropy for this specific TiO_2 thickness making in turn not straightforward to univoquely determine the refractive index of this sample. It is precisely this complex behavior associated to the anisotropic nature of the 50 nm TiO_2 which makes it not a good candidate for sensing experiments. Moreover, the 20 nm TiO_2 sample exhibits a SPP resonance very broad due to its high thickness, and therefore only the magnetoplasmonic properties (by means of Kretschmann configuration and the Transverse Kerr Magnetooptical Kerr Effect (TMOKE)) for the 10 nm TiO_2 thickness sample have been measured and used for gas sensing experiments. In Fig. V.6. the SPR reflectivity curves for the Au/glass and TiO_2/Au glass (a) as well as Au/Co/Au/glass and TiO_2/Au/Co/Au/glass (b) are reported. In both cases, when the TiO_2 layer is on top, the incident angle θ_{spr} at which the reflectivity minimum takes place exhibits a shift to higher angles with respect to the bare metal/glass samples. This difference can be ascribed to a change in the actual refractive index above the gold layer when the metal surface is covered by the TiO_2 film. The shift magnitude in the SPR angle typically depends on both the thickness and the refractive index *n* of the titania deposited layer; we can estimate that this angular shift corresponds to a 10 nm layer with a refractive index of 1.628 above the Au layer (this refractive index value is close to the elipsometric one of 1.682). It is also worth noticing the broadening of the curve around the minimum in the case of Au/Co/Au when compared to Au, since the presence of a Co layer increases the absorption losses compared to pure Au.

ΔR curves also experience a shift in the angular position when a thin TiO_2 layer is deposited onto the Au/Co/Au multilayers substrate (Fig V.6.(c)). Also in this case, this change can be ascribed to the change of refractive index due to the presence of a thin film at the interface air/Au.

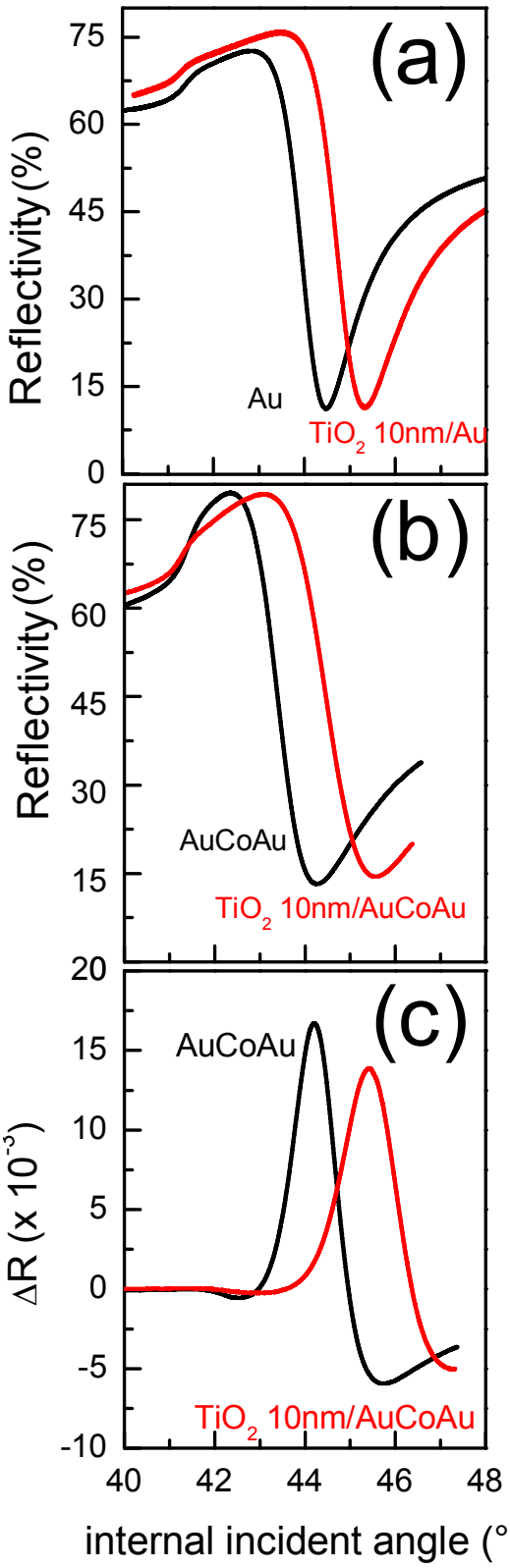

Fig. V.6 R vs angle of Au(50nm)/glass and TiO2(10nm)/Au/glass (a), R vs angle of Au/Co/Au/ glass TiO2 (10nm)/ AuCoAu/ glass (b) and ΔR vs angle of the same samples (c).

V.2.E.-Gas sensing

The sensing experiments described in what follows have been performed within a short stay at the Istituto de Microelettronica e Microsistemi (IMM-CNR, Lecce, Italy) under the supervision of Dr. M. G. Manera and Prof. R. Rella (the details of the experimental setup used are explained in the last section of the chapter II Experimental Techniques).

Two different sensing approaches can be used to test the ability of the TiO_2 layers to detect the presence of different alcohol vapour molecules such as ethanol, methanol and isopropanol. The Au/Co/Au multilayer has been used as transducing layer both in a traditional SPR sensing configuration and in the proposed MOSPR gas sensor configuration. In the first case, the reflectance of the active sensing layers, recorded in the Kretschmann configuration, is monitored during time at a fixed angle, corresponding to the maximum slope of the SPR curve reported in fig V.6. (a). In the second case, the ΔR magneto-optical signal, recorded in the presence of an oscillating magnetic field in transversal configuration, is monitored during time, at a fixed angle, corresponding to the maximum slope of the ΔR curve reported in fig V.6. (b). Increasing concentrations of alcohol vapours mixed in dry air were sent into the test chamber spaced out by a flux of pure N_2 (dry air) with the aim to evaluate the reversibility of the sensors after interaction with the investigated analytes. The interaction of the sensing layer with the alcohol vapours produced a change in the optical properties of the sensing TiO_2 films, namely a change in the refractive index[18], since the alcohol vapours are allowed to penetrate into the porous structure of the sensing layers. This effect produces a change in the plasmon wavevector, which, in turn, translates into a change both in the SPR and the MOSPR curves. Thus, the two recorded signals have the role to monitor the optical changes of the TiO_2 active layer upon the interaction with the investigated alcohol vapours.

In figure V.7. the calibration curves relative to SPR and MOSPR sensors are reported. The curves show the obtained sensor responses corresponding to different alcohol vapours. These curves represent the signal variation in presence of the analyte/dry-air mixtures with different concentrations compared to the value of the signal in dry-air. Here the signal corresponds to the reflectivity or the magnetoopical ΔR signal for the two different SPR and MOSPR configurations, respectively. The gas sensing measurements were done in the same experimental setup, with the same sample, and flowing the same alcohol vapour analytes obtained under the same experimental conditions.

Due to the different nature of reflectance measurements in the SPR sensor and of the MO measurements in the MOSPR sensor, the comparison of their sensing performances, namely of their calibration curves, must be done taking into account the signal-to-noise ratio (SNR) of the experimental measurements. Noise in this sense is anything which contributes to the detected signal but which is not due to the parameter

being measured. It is generated in all parts of the electrical circuitry, but in light measurement systems it is dominated by noise from the detector or noise associated with the optical signal. The system noise here is defined as the RMS deviation of the experimental signal (during 1000 s) when in the test chamber flows dry air.

Sensitivity information can be obtained from the slope of the calibration curves.[26] The experimental results yield a significant enhancement of the MOSPR sensor sensitivity towards the investigated alcohol vapours with respect to the intensity-interrogated SPR sensor, using the same Au/Co/Au layer as sensing transducer, as can be noticed in Table V.1.

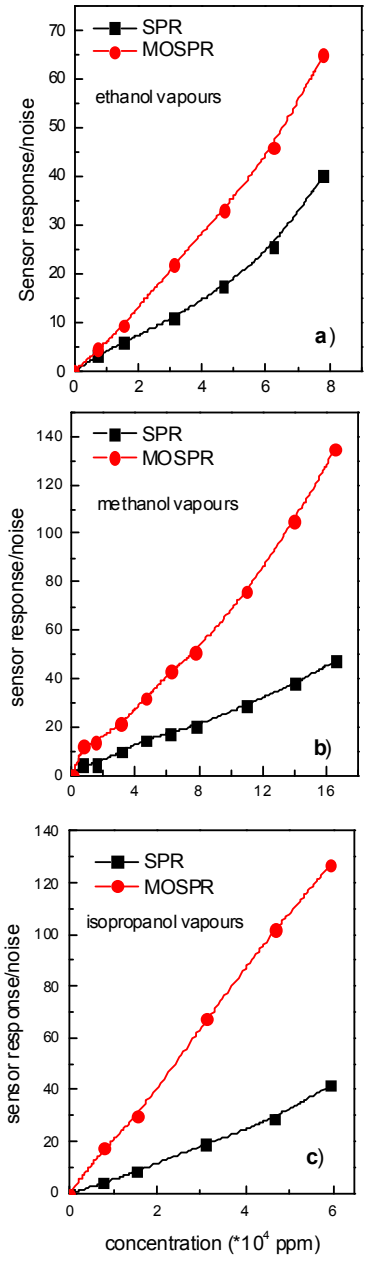

Fig.V.7. Calibration curves of the sensor relative to different concentration of ethanol vapours (a), methanol vapours (b) and isopropanol vapours (c) mixed in dry-air.

For the sake of completeness, the sensing performances of the TiO_2 active layers were also investigated in a SPR configuration using as transducing layer the conventional Au/glass substrates (in the optimal configuration 48nm Au/2nm Cr/ glass). Both Au/glass and Au/Co/Au/glass structures were deposited on the same kind of Corning glass substrate, using the same growth conditions, as well as the same TiO_2 sensing layer deposited on them. The obtained sensitivity results are reported in Table V.1.

Table V.1. Sensitivity comparison (ppm^{-1})

Analyte	MOSPR sensor ($\times 10^{-4}$)	SPR sensor Au/Co/Au transducer ($\times 10^{-4}$)	SPR sensor Au transducer ($\times 10^{-4}$)
Ethanol	7.2	3.6	6.0
Methanol	7.8	2.8	4.2
Isopropanol	21.9	6.3	16.0

Under the same conditions of sensing technique, the highest sensitivity is obtained for isopropanol alcohol vapours. This result can be explained taking into account the higher refractive index of isopropanol (i.e., 1.380) with respect to that of methanol (i.e., 1.329) and ethanol (i.e., 1.361).

But if we compare the sensitivity obtained for the different sensing techniques, methanol vapour is the analyte resulting in a higher MOSPR sensing performance: almost double than conventional SPR sensing (Au film as transducer). In order to justify this result, we have to take into account that the values reported in table **V.1.** represent the sensitivity, i.e., the speed at which the sensor signal changes upon a change of concentration of analyte. As it is known from SPR theory, a variation in the dielectric constant ε_d of the medium in contact to the air/Au interface upon the change in refractive index, causes a variation in the plasmon wavevector k_{sp}. The electromagnetic field exponentially decaying at the air/Au interface becomes therefore a sensing probe for changes of refractive index at this interface, translating into a variation of SPR signal. The speed of this variation depends on the speed of the wavevector to follow the changes at the transducer interface, which in turns depends on the ability of the decaying field to penetrate deeply into the dielectric and follow the changes of its optical parameters.

In the MOSPR signal the plasmon wavevector k_{sp} is modulated at a certain frequency by the modulation of the magnetization in Co layer. The modulated wavevector Δk is now responsible for the detection of refractive index changes at the

air/Au interface. The speed the modulated wavevector takes to follow such optical variations dictates the sensitivity with respect to the different analytes. Small gas molecules such as methanol will allow the electromagnetic field to follow more quickly the changes in gas concentration resulting in a more rapid change in Δk with respect to bulky analyte molecules such as isopropanol. In addition, small analyte molecules will interact with the sensing layer in proximity of the MO active layer region where the electromagnetic field, responsible for the enhancement of the magnetooptical signal, is drastically enhanced allowing to probe analyte changes rapidly.

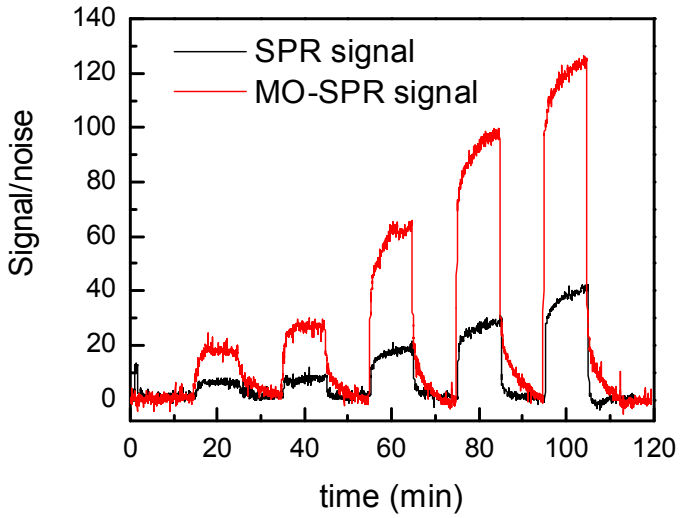

Fig. V.8. Dynamic response curves (R and ΔR vs time) towards isopropanol vapours by alternating increasing gas concentrations and dry-air with time.

These considerations come from the comparison of the traditional SPR and the MOSPR configurations using Au film and Au/Co/Au multilayer films as transducing layers, respectively. In the two cases the probing electromagnetic field at the air/Au interface is the best for each experimental sensing configuration (remember that the thickness of the transductor multilayers were optimized via simulations). As shown in the table, a reduction of sensitivity of SPR sensor using Au/Co/Au as transducing layer with respect to traditional SPR sensor is obtained. This can be ascribed to the reduced probing ability of the decaying electromagnetic field at the air/Au interface interface of the Au/Co/Au multilayer, due in turn to a damped plasmon excitation in the Au/Co/Au structure with respect to classical air/Au interface interface.

The comparison of sensitivity values obtained for the investigated transducing sensor platforms highlights the significant and important enhancement obtained with MOSPR sensor over conventional SPR approach[7,8].

Dynamic curves relative to the analyte exhibiting the best sensing performance, namely isopropanol vapours, are shown in fig. V.8. as representative of the behaviour of all tested alcohol vapours. The stability of the signal and reversibility in the absorption and desorption processes is observed in all the concentration range and for all investigated analytes for the two SPR and MOSPR configurations. A large increase in the signal is observed in the sensorgram corresponding to MOSPR measurements, thus

confirming the achieved objective of this study. However, this configuration presents a slight reduction in the recovery times as can be noticed in the figure. Reproducibility of the measurements is ensured by repeating the measurements for more cycles.

V.3.- BIOSENSING

The use of the MOSPR sensor using Au/Co/Au trilayers as transducers to detect some biomolecules has been reported for first time with BSA protein[7] and very recently with the DNA hybridization[27].

The detection of the interaction of the Bovine Serum Albumin (BSA) protein and its respective antibody (antiBSA) has been the biosensing experiment proposed to systematically test the sensitivities of the SPR and MOSPR sensors considered in this thesis work. The realization of this experiment is motivated by the relevance of the formation of the anti-BSA/BSA immune complex to the studies of the receptor site of the red blood cells[28]. Besides, the BSA protein is widely used to block active sites on surfaces, which indicates its high performance to be immobilized on the transducer multilayer.

V.3.A.-Surface functionalization of the biosensor

An immobilization of the receptor biomolecules on the Au surface of the SPR and MOSPR transducers is required for the detection of the target biomolecules (sensing experiment). Generally, a self assembled monolayer (SAM) is attached to the metal surface by the covalent bond formed between the Au atoms and the S atoms of the thiol groups (SH-) using alkanthiolates organic compounds[29,30,31].

According to the published works relative to this process, the immobilization protocol used for the biosensing experiments performed in this thesis work is sketched in the fig.V.9.:

1. Using a mercaptoundecanoic acid (11-MUA) 10 mM in ethanol solution within 48 hours, the covalent bond (Au-S) is formed.
2. The sample surface is activated with a mixture of N-ethyl-N'-(3-dimethylaminopropyl)-carbodiimide (EDC 30 mM) and N-hydrosuccinimide (NHS 50 mM) dissolved in a solution of 10% of ethanol in water.
3. An intermediate compound is formed via NHS, which allows the covalent bond of the receptor biomolecules using their amine groups (-NH_2). This biomolecule immobilization is a key point for the sensitivity of the biosensor with the target biomolecules.

4. Ethanolamine (1 M) is used to block the surface of non-specific interactions from the target biomolecule.
5. Finally, the target biomolecules solutions are introduced into the system.

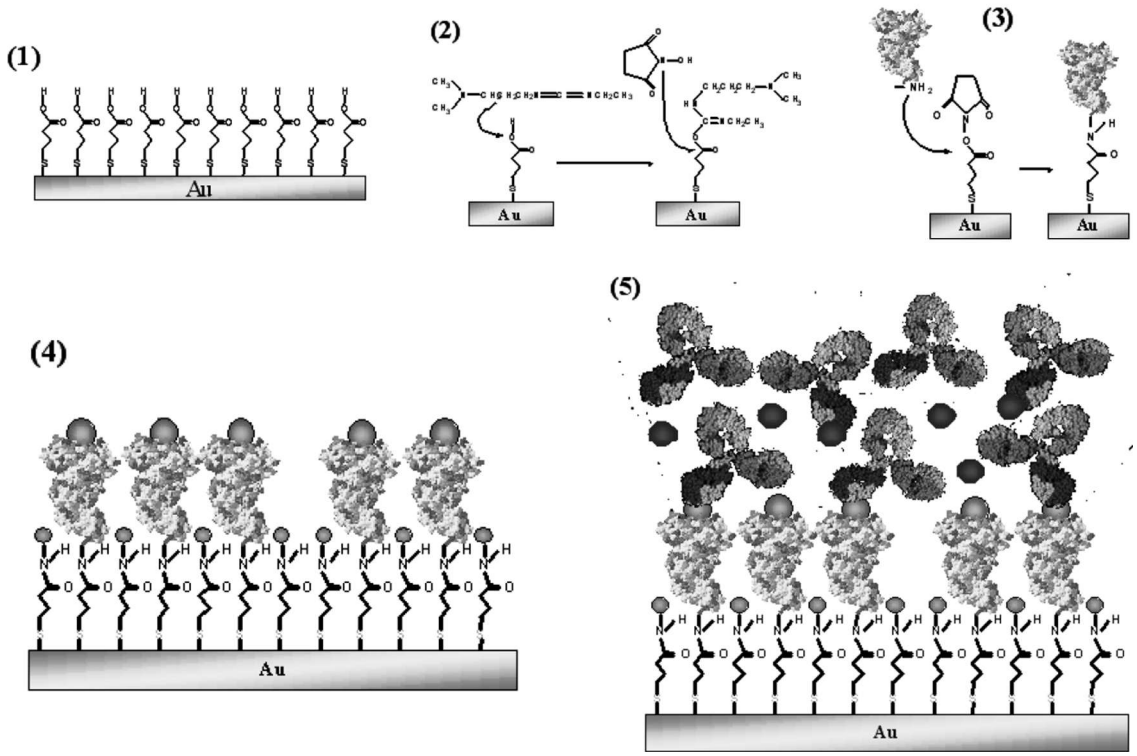

Fig V.9. Covalent immobilation protocol based in Thiol SAM on Au. Image taken from reference [31].

V.3.B.-Biosensing experiment (antiBSA recognition)

The figure V.10. shows the reflectivity and TMOKE curves corresponding to the SPR and MOSPR measurements respectively for each stage of the biosensing experiment using a 10 nm Au/6 nm Co/21 nm Au/2 nm Cr/SF10 multilayer as sensor transducer. These layer thickness were optimized via Transfer matrix simulations performed by Dr. A. García-Martín and Dr. J. B. González-Díaz. The refractive indices (around 1.33) involved for these experiments in aqueous medium are quite higher than those for the gas experiments (around 1) therefore the SPP resonance in aqueous medium is quite different from the respective one in air medium (thus its optimum layer thickness varies too). The functionalization of the Au surface with the 11-MUA acid leads to an unexpected angular shift towards lower incidence angles (i. e. lower effective refractive index) compared to the bare Au/Co/Au due to the higher effective refractive index of MUA compound (n=1.45[32]) compared to the pure water (n=1.33). The Au-S covalent bond gives rise to a strong charge transfer of the Au to the S atoms

of the surface causing this variation of the SPP resonance[33](shown in the reflectivity curves and also in the TMOKE ones). Subsequently, the BSA protein is attached to the functionalized Au surface with a solution of 100 parts per million (ppm) in water, exhibiting an angular shift towards higher incidence angles (i. e. higher effective refractive index) for both reflectivity and TMOKE curves compared to the previous ones for the thiol functionalization. The antibody recognition for a concentration of 5 ppm exhibits the highest angular shift for all the curves. Moreover, the use of a solution of HCl (1 mM) regenerates the sample surface (i. e. it removes the antibody from the surface) returning the reflectivity and TMOKE curves to the BSA state (without the presence of antibody-protein complex on the sample surface) in order to start another antibody recognition again. It is worth to mention that the TMOKE curve cannot return to the exactly same state than the previous BSA functionalization. However, a series of 3 or 4 cycles of HCl have been performed for the same sample obtaining a stable return curve.

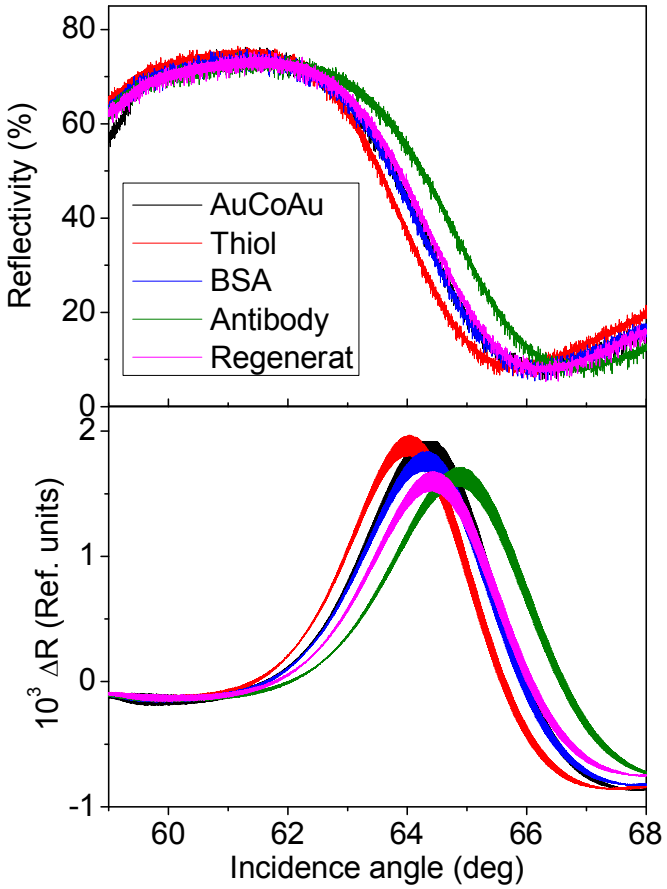

Fig V.10. R vs. angle of bare Au/Co/Au/glass sample (black curve) with a Thiol layer (red curve), with BSA proteins (red curve), with antiBSA-BSA complex (green curve) and after the regeneration of the sensing layer (pink curve). (b) ΔR vs angle of the same samples.

Two sensorgraphs are presented in the figure V.11. showing this biosensing experiment in detail. The MOSPR sensor measures the variation of the TMOKE signal at an incidence angle of 65.06º and 65.65º for the BSA immobilization (fig V.11.(a)) and the antibody recognition (fig. V.11. (b)) sensorgraphs respectively. The election of

these two angles corresponds to the points with higher slope (thus higher sensitivity of the sensor) for the initial TMOKE curves in the BSA immobilization (Thiol curve) and antibody recognition (BSA curve). The first sensorgraph related to the BSA immobilization shows two preliminary cycles of a solution of 10% ethanol in water and pure water to clean the sample surface and to get a stable baseline of the signal for the MOSPR sensing. Then, the mixture of NHS/EDC (introduced to activate the thiol surface) gives rise to the highest variation of the refractive index into the cell chamber. After that, the sample was cleaned with the solute of 10% ethanol in water and pure water. Finally, the solution of 100 ppm of BSA protein in water leads to a permanent variation of the sample surface (the BSA immbolization via amine coupling) since the signal is maintained although the solution was changed to pure water.

The figure V.11. (b) exhibits the abtiBSA recognition at different concentrations. It first shows the blocking or deactivation of the unreacted surface sites of the sample using ethanolamine (EA 1M), manifested as a high and fast variation of the sensor signal. Next, and previously to the antiBSA recognition, the sample was cleaned with pure water and the baseline was recorded in Phosphate Buffered Saline (PBS) solution (with a higher refractive index than pure water), since the antibodies of the BSA protein were dissolved in PBS solution. Next, the antiBSA solutions were injected increasing the concentration of the antibodies. Notice that the injection of the antiBSA solution results in a rapid rise in the baseline, indicating that the association reaction between BSA and antiBSA is rather easy. This is in contrast with the dissociation reaction, which shows a very slow (almost negligible) decay. The combination of rapid binding and slow decay suggests that the binding of antiBSA to BSA is quite strong. As it was expected, the sensor signal increases with the antibody concentration, which demonstrates that the BSA-Au/Co/Au surface is being specifically covered by the antiBSA and therefore the effective refractive index of the surface is increasing.

The sensor response can be defined as $\Delta S=S_{Ab}-S_{base}$ where S_{Ab} is the sensor signal when the association reaction of the BSA-antiBSA is saturated and S_{base} is the baseline signal with pure PBS solution previously to the antiBSA injection. Although the signal and sensitivity[7] measured for the SPR and MOSPR sensors are different, the dependence of the sensor response with the antibody concentration (calibration curve) must be similar for the two sensors. The figure V.12. shows two calibration curves performed in two Au/Co/Au transducers for SPR and MOSPR sensing configurations (i.e. measuring the variation of the reflectivity and TMOKE signals respectively).

The two curves exhibit a quite linear behaviour at low antiBSA concentrations (0-2 ppm), saturating at high antiBSA concentrations (around 10 ppm). This indicates that the sensor surface is completely covered by the BSA/antiBSA complex at around 10 ppm of antiBSA concentration, avoiding the association of a higher amount of antiBSA on the sensor surface. The trends of the two calibration curves exhibit the well known Langmuir adsorption isotherm[34,35] for the association of the antiBSA with the BSA protein present on the sensor surface.

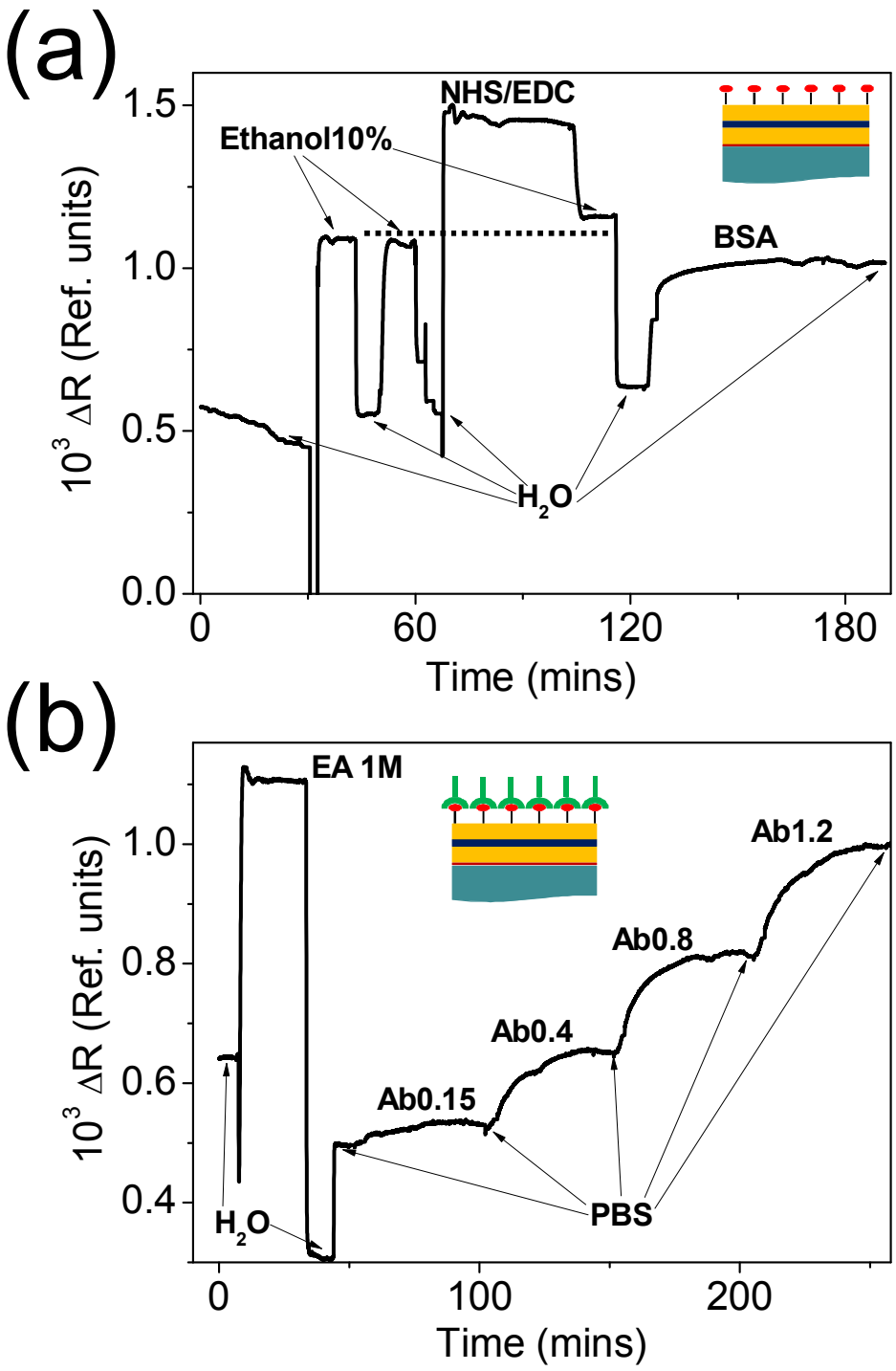

Fig V.11. Sensorgraphs for both the functionalization of the BSA sensing layer (a) and the antiBSA recognition at different concentrations (b). The pointed line of the figure (a) highlights the reproducibility of the MOSPR signal in 10% ethanol solution..

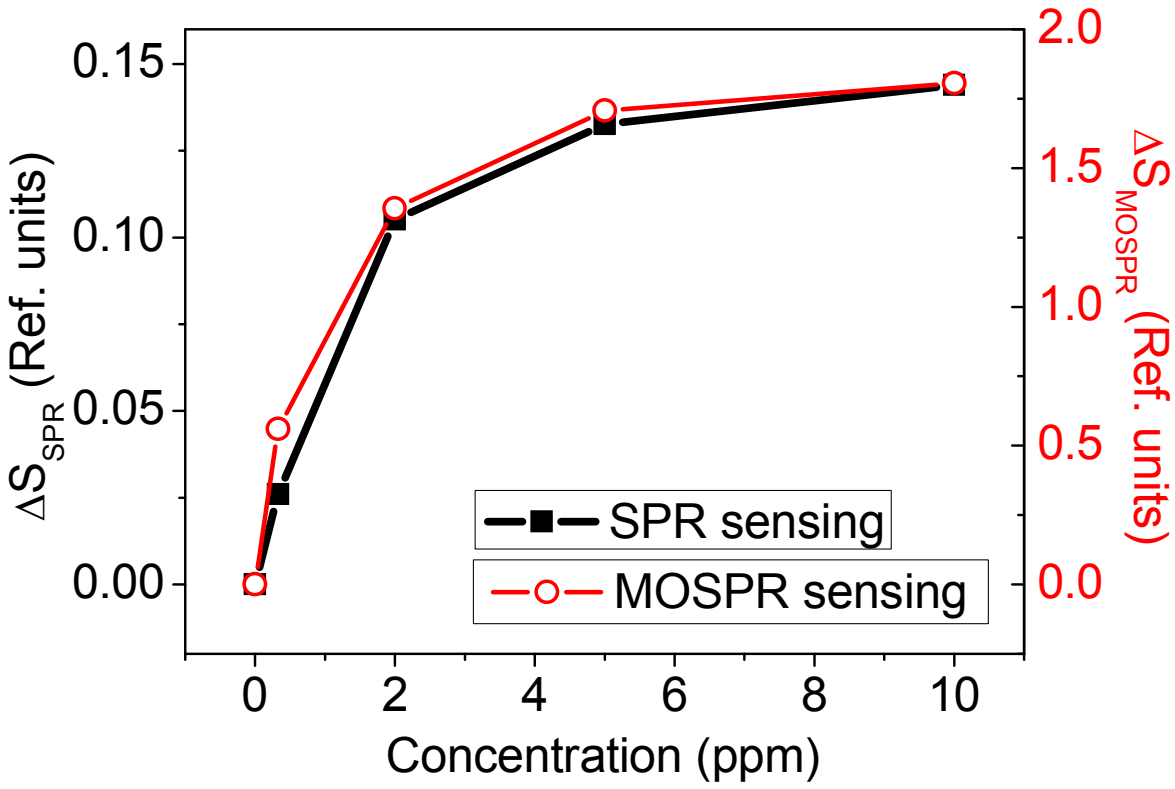

Fig V.12. Calibration curves for the SPR (black squares) and MOSPR (red circles) sensors detecting the antiBSA analyte.

V.3.C.-Comparison of different multilayers as transducers

Additionally, a Au/Ag/Co/Ag multilayer and a Au thin film have been also used as transducers to perform MOSPR and SPR sensing experiments respectively to compare their performances with the corresponding one for the Au/Co/Au trilayer used as MOSPR sensor. The figure V.13. (a) shows the calibration curves of the already discussed Au/Co/Au trilayer and a 10 nm Au/5 nm Ag/6 nm Co/17 nm Ag/2 nm Cr/SF10 multilayer for the recognition of the antiBSA. The two curves exhibit the Langmuir adsorption[34,35] behavior. However, the magnitudes of the sensor responses for the same concentration of analyte are quite different (a factor 1.75 for the 5 ppm concentration) for the two multilayers. Taking into account that the amounts of the attached antibody on the surface must be very similar for the two transducers used, we can conclude that the sensitivity of the Au/Co/Au system is higher than the Au/Ag/Co/Ag one: this fact is in opposition with what can be expected after the conclusions of the chapter III. Nevertheless, observing the angular TMOKE curves of the figure V.13.(b), the causes of the lower sensitivity for the Au/Ag/Co/Ag system can be identified: the TMOKE curve becomes wider after 20 minutes of water flux on the Au/Ag/Co/Ag surface, which indicates that probably some degree of oxidation of the Ag and/or Co layers takes place, leading to a poorer sensing performance with respect

to the Au/Co/Au trilayer. However, this oxidation of the system is partial and saturates, since the TMOKE curve becomes stable after the first 20 minutes of exposure to the water flux. It must be noticed that in chapter III we showed that a 5 nm thick Au capping layer was able to preserve Ag and Co in ambient conditions. Unfortunately, the liquid environment needed to perform biosensing is more aggressive and even a 10 nm thick capping layer has not been able to completely preserve Ag and Co.

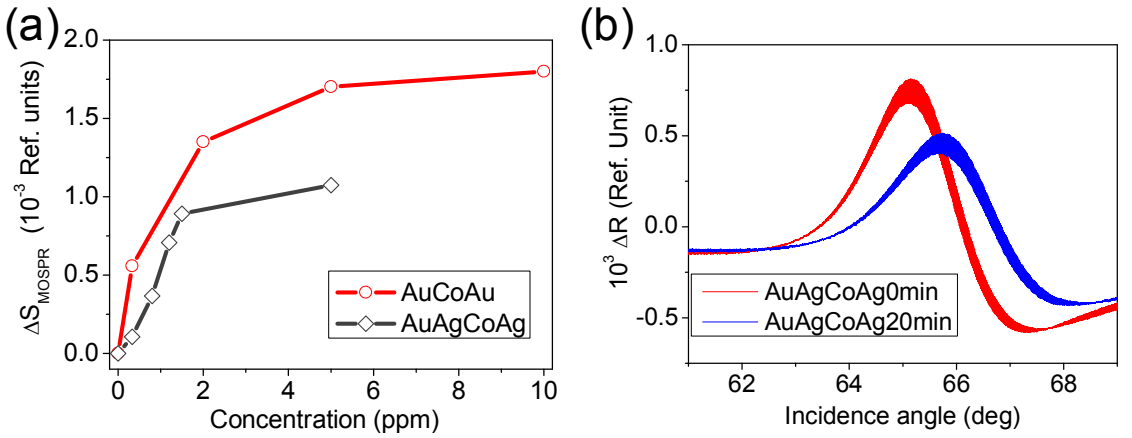

Fig V.13. (a) Calibration curves for a Au/Co/Au (red circles) and Au/Ag/Co/Ag (grey diamonds) multilayers. TMOKE vs. incident angle for the Au/Ag/Co/Ag sample starting the water flux (red curve) and after 20 min with the water flux (blue curve) inside the cell chamber.

A reallistic comparison of the MOSPR and the SPR sensing capabilities must be done using the best candidate transducers for each configuration, as it has been performed in the gas sensing section. Thus a 48 nm Au/2 nm Cr/SF10 multilayer has been selected as SPR transducer for the antiBSA recognition. Due to the different nature of the signals measured for the SPR and MOSPR sensors, the responses of both of them are normalized to the signal of the baseline (signal with pure PBS). The normalized calibration curves for the two sensors are shown in the figure V.14. , exhibiting the Langmuir isotherm behavior. In the 0-1.5 ppm concentration range the responses of both sensors are linear. Therefore the sensitivity for each sensor can be obtained from the slope of the calibration curves in these linear regions[7]. With this methodology, the calculated sensitivities are 0.81 and 0.47 ppm^{-1} for the MOSPR and SPR sensors respectively. This confirms the higher sensitivity of the MOSPR sensor compared to the "classical" SPR one for a real biosensing experiment such as the association of the antiBSA with the BSA protein.

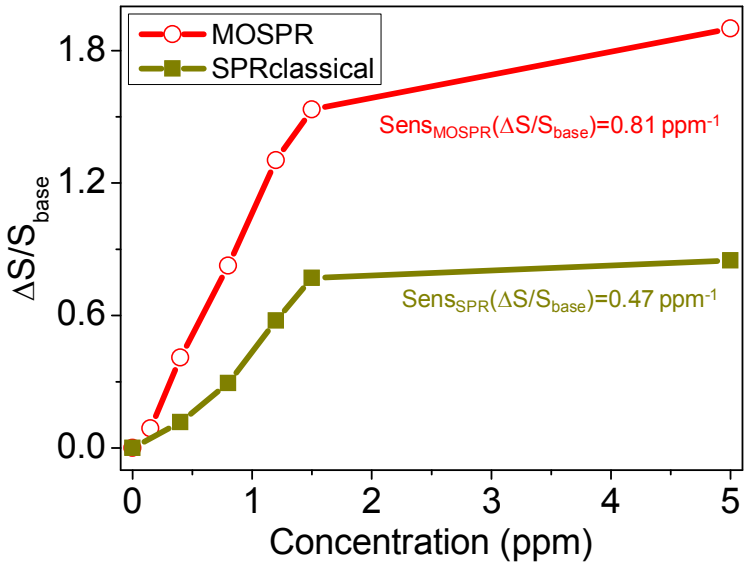

Fig V.14. Normalized calibration curves for the MOSPR sensor (red circles) using Au/Co/Au as transducer and the "classical" SPR sensor (yellow squares) using a Au film as transducer. The sensitivities of both sensor are calculated using a linear fit in the 0-1.5 ppm concentration range.

V.4.. -CONCLUSIONS

In this chapter we have shown how the different magnetoplasmonic (MP) multilayers developed along it have successfully been used as transducers in SPR and MOSPR configurations for the detection of alcohol vapours in air medium and the specific formation of antibody-protein complex in aqueous medium. Concerning the gas sensing experiments, an innovative GLAD TiO_2 porous layer has been used as sensing layer, showing a good performance for trapping methanol, ethanol and isopropanol molecules due to its high porosity (thus high surface/volume ratio). Moreover the MOSPR sensor demonstrates a higher sensitivity with respect to the SPR sensor using Au/Co/Au trilayer or Au film ("classical" SPR) as sensor transducers for the alcohol vapours detection.

This higher sensitivity of the MOSPR sensor compared to the SPR one has also been confirmed in aqueous conditions for an immunological experiment. A protocol has been performed using thiol-based SAMs to bind the biomolecules with the top Au layer of the MP transducers. A BSA functionalized transducer has been used as sensing layer for the recognition of the antiBSA analyte. A typical saturation state has been achieved at high analyte concentrations (Langmuir isotherm behavior) for the response of SPR and MOSPR sensors. A Au/Ag/Co/Ag multilayer as MOSPR transducer has exhibited lower sensitivity compared to the Au/Co/Au transducer due to a possible partial oxidation of Ag and Co layers leading to a deterioration of the TMOKE angular curve. Besides, the normalized sensitivity is higher for the MOSPR sensor (Au/Co/Au as transducer) compared to the corresponding one for the "classical" SPR sensor (Au film as transducer).

V.5.. - REFERENCES

[1] M. Piliarik, H. Vaisocherová, J.Homola, *Methods Mol Biol.* **2009**, *503*, 65.

[2] M. Piliarik, M . Bocková, J. Homola, *Biosens Bioelectron.* **2010,** *26*, 1656.

[3] F. Fernández, K. Hegnerová, M. Piliarik, F. Sanchez-Baeza, J . Homola, MP. Marco, *Biosens Bioelectron.* **2010**, *26*, 1231.

[4] J. Spadavecchia , M.G. Manera , F. Quaranta , P. Siciliano , R. Rella, *Biosens Bioelectron.* **2005**, *21,* 894.

[5] J. Hottin, J. Moreau, G. Roger, J. Spadavecchia, M. Millot, M. Goossens, M. Canva, *Plasmonics* **2007**, *2*, 201.

[6] S. Herminjard, L. Sirigu, H. P. Herzig, E. Studemann, A. Crottini, J. Pellaux, T. Gresch, M. Fischer, J. Faist, *Opt. Express*, 2009, *17*, 293.

[7] Sepúlveda, B., Calle, A., Lechuga, L. M., & Armelles, G. (2006). Highly sensitive detection of biomolecules with the magneto-optic surface-plasmon-resonance sensor. *Optics letters*, *31*(8), 1085-1087.

[8] Regatos, D., Fariña, D., Calle, a., Cebollada, a., Sepúlveda, B., Armelles, G., & Lechuga, L. M. (2010). Au/Fe/Au multilayer transducers for magneto-optic surface plasmon resonance sensing. *Journal of Applied Physics*, *108*(5), 054502.

[9] M.G. Manera, L. Valli, S. Conoci, R. Rella, (2009) *J. Porphyrins Phtalocyanines*, *13,* 1140.

[10] H. Denga, D. Yanga, B. Chena, C- Linb, *Sens. Actuat. B-Chem* **2008**, *134,* 502.

[11] M.G.Manera, G. Leo, M.L.Curri, R. Comparelli, R. Rella, A. Agostiano, L. Vasanelli, *Sens. Actuat. B-Chem* **2006**, *115*, 365.

[12] M. G. Manera, J. Spadavecchia, D. Buso, C. de Julián – Fernández, G. Mattei, A. Martucci, P. Mulvaney, J. Pérez- Juste, R. Rella, L. Vasanelli, P. Mazzoldi, *Sens. Actuat. B-Chem* **2008,** *132***,** 107.

[13] M.G.Manera, P.D.Cozzoli, G. Leo, M.L.Curri, A.Agostiano, L. Vasanelli, R. Rella, Sens. Actuat. B-Chem **2007**, 126, 562.

[14] Robbie, K., Beydaghyan, G., Brown, T., Dean, C., Adams, J., & Buzea, C. (2004). Ultrahigh vacuum glancing angle deposition system for thin films with controlled three-dimensional nanoscale structure. *Review of Scientific Instruments*, *75*(4), 1089.

[15] M. J. Brett and M. M. Hawkeye, Science **2008**, 319, 1192.

[16] Smith, D. O., Cohen, M. S., & Weiss, G. P. (1960). Oblique-Incidence Anisotropy in Evaporated Permalloy Films. *Journal of Applied Physics*, *31*(10), 1755.

[17] M.M. Hawkeye, M. J. Brett, *J. Vac. Sci. Technol.* A **2007**, *25*, 1317.

[18] González-García, L., Lozano, G., Barranco, A., Míguez, H., & González-Elipe, A. R. (2010). TiO2–SiO2 one-dimensional photonic crystals of controlled porosity by glancing angle physical vapour deposition. *Journal of Materials Chemistry*, *20*(31), 6408.

[19] Gaillard, Y., Rico, V. J., Jimenez-Pique, E., & González-Elipe, A. R. (2009). Nanoindentation of TiO 2 thin films with different microstructures. *Journal of Physics D: Applied Physics*, *42*(14), 145305.

[20] G. K. Kiema, M. J. Colgan, and M. J. Brett, *Sol. Energy Mater. Sol. Cells* **2005**, *85*

[21] K. D. Harris, A. Huzinga, and M. J. Brett, *Electrochem. Solid-State Lett.* **2002**, *5*, H27.

[22] J.J. Steele, M.T. Taschuk, M.J. Brett, *Sens. Actuat. B-Chem* **2009**, *140,* 610

[23] González-Díaz, J.B. et al. (2007). Surface-magnetoplasmon nonreciprocity effects in noble-metal/ferromagnetic heterostructures. *Physical Review B*, *76*(15), 1-4.

[24] Wang, S., Xia, G., He, H., Yi, K., Shao, J., & Fan, Z. (2007). Structural and optical properties of nanostructured TiO2 thin films fabricated by glancing angle deposition. *Journal of Alloys and Compounds*, *431*(1-2), 287-291.

[25] H. TompKins and E. Irene, eds. Handbook of Ellipsometry, William Andrew Publishing, New York, 2005.

[26] J. Homola, Anal.Bioanal.Chem. **2003**, 377, 528.

[27] Regatos, D., Sepúlveda, B., Fariña, D., Carrascosa, L. G., & Lechuga, L. M. (2011). Suitable combination of noble / ferromagnetic metal multilayers for enhanced magneto- plasmonic biosensing. *Optics Express*, *19*(9), 8336-8346.

[28] Varga, L., Thiry, E., Fust, G. *Immunology*, 1988, 64, 381-384.

[29] Lawrence, H., & Ralph, G. (1992). SYNTHESIS, STRUCTURE, AND PROPERTIES OF MODEL ORGANIC SURFACES. *Annu. Rev. Phys. Chem.*, *43*, 437-463.

[30] Sigal, G. B., Bamdad, C., Barberis, A., Strominger, J., & Whitesides, G. M. (1996). A Self-Assembled Monolayer for the Binding and Study of Histidine-Tagged Proteins by Surface Plasmon Resonance. *Analytical Chemistry*, *68*(3), 490-497.

[31] PhD thesis: "**Efectos Magneto-Ópticos en dispositivos biosensores de campo evanescente",** Borja Sepúlveda, Universidad Complutense de Madrid (2005).

[32] Jordan, C., Frey, B., & Kornguth, S. (1994). poly-L-lysine adsorption onto alkanethiol-modified gold surfaces with polarization-modulation Fourier transform infrared spectroscopy and surface plasmon resonance. *Langmuir*, *10*(5), 3642-3648.

[33] Sheridan, a, Ngamukot, P., Bartlett, P., & Wilkinson, J. (2006). Waveguide surface plasmon resonance sensing: Electrochemical desorption of alkane thiol monolayers. *Sensors and Actuators B: Chemical*, *117*(1), 253-260.

[34] Langmuir I., *J. Am. Chem. Soc.,* 37, 1139 (1915).

[35] Duff, D. G., Ross, S. M. C., & Vaughan, D. H. (1988). Adsorption from solution: An experiment to illustrate the Langmuir adsorption isotherm. *Journal of Chemical Education*, *65*(9), 815.

Chapter VI:

MP-MIM

cavities

VI.1.- INTRODUCTION 134

VI.2.- DESIGN OF STRUCTURES 135

VI.3.- EXPERIMENTAL AND THEORETICAL METHODS..... 141

VI.4.- PLASMONIC MIM CAVITY..... 141

VI.4.A. -Morphology and plasmonic characterization ($Ag/SiO_2/Ag$)..... 142

VI.5.- MAGNETOPLASMONIC MIM CAVITIES..... 144

VI.5.A.- Samples and multilayer optimization 144

VI.5.B.- Morphological characterization..... 146

VI.5.C.- Magnetic characterization 148

VI.5.D.- Magnetoplasmonic characterization..... 149

VI.5.D.(i)-Optical characterization of the modes 149

VI.5.D.(ii)- Magnetic modulation of the modes 152

VI.6.- CONCLUSIONS 158

VI.7.- REFERENCES 159

VI.1.- INTRODUCTION

Optical cavities are powerful tools to control the interaction of light with matter and have been employed in a wide range of fields from quantum optical devices[1] to ultrasensitive optical sensors[2]. These applications rely on the effective confinement of light in a small cavity mode volume. While most of cavity designs so far are based on dielectric material assemblies, the confinement of light using metallic nanostructures has recently become a topic of great interest. In contrast to the dielectric cavities, such plasmonic cavities can overcome the diffraction-limited size and in principle support a subwavelength mode volume[3].

The strong confinement of light is particularly interesting for SPPs guided in a nanosized dielectric gap between two metals[4,5,6]. Such a metal-insulator-metal (MIM) geometry serves as a plasmonic gap waveguide (PGW), since "squeezing" the SPP field into the dielectric core could be a way to overcome the problem for the light coupling into a waveguide of nanometric transversal dimensions, as Gizburg et al. have proposed (Figure VI.1.(a))[7]. In fact, Dionne et al. have experimentally studied MIM-SPPs guided in waveguides with very small transverse dimensions[8]. As a result, the wavelength along the direction of propagation is shortened significantly for these MIM-SPPs and therefore they can allow the realization of nanocavities with extremely small mode volumes[9,10] or nonlinear optical device applications[11]. In comparison to other SPP guiding geometries, the cost of extra losses that are linked to the increase in confinement is relatively low[4,5,12].

Regarding the advantages in sensing applications, these MIM-SPPs are split into two optical (symmetric and antisymmetric) modes, with different distribution of the electromagnetic field that is highly desirable to achieve the compensation of cross-sensitivity to background refractive index variations for SPR sensors. Slavík et al. have studied this novel symmetric/antisymmetric (S/A) SPR sensor (Figure VI.1.(b)) proposing a Au film between the sensing medium and a Teflon film as the opposite insulator-metal-insulator (IMI) system (which exhibits the reciprocal properties of the MIM system) [13,14].

In this chapter, we will focus our attention on the magnetic field driven k_{SPP} modulation by proposing a step forward in this research area: the incorporation into the metallic multilayers studied so far in this thesis of an insulator layer, forming therefore magnetoplasmonic MIM (MP-MIM) cavities. Thanks to the mentioned benefits of their improved confinement properties, these systems open new routes for the realization of integrated magnetic SPP modulators. In particular, here we analyze in detail the magnetic field modulation of the wavevector of the two MIM-SPP modes, symmetric

and antisymmetric, supported by Ag/SiO_2/Ag-Co multilayered structures grown on SF10 glass substrates.

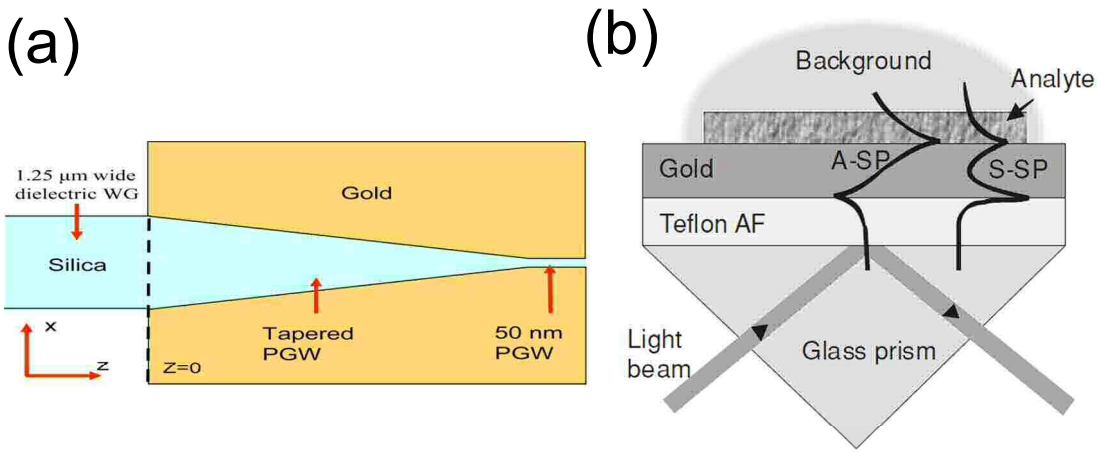

Figure VI.1. (a) Tapered plasmon gap waveguide: a 1.25µ m wide input dielectric waveguide, and a 50 nm output plasmon gap waveguide (figure extracted from ref. [7]). (b) Sensor configuration for excitation of A/S-SPR in a IMI system (figure extracted from ref. [13]).

VI.2.- DESIGN OF STRUCTURES

A Metal-Insulator-Metal (MIM) structure is a well known system with two metal-dielectric interfaces[4]. When these interfaces are uncoupled, each of them supports a SPP (observe the inset of figure VI.2.(a)). When they are coupled in a cavity, a more complex behavior appears, with several optical modes present. To explain this behavior, we have simulated by means of a transfer matrix formalism a system consisting of 70nm Ag/w_0 SiO_2/40nm Ag/SF10 glass substrate (n=1.723). Figure VI.2(a) shows the reflectivity of this system as a function of both the incidence angle and the SiO_2 thickness, w_0, for a p-polarized plane wave light impinging on the substrate at 632.8 nm wavelength. The minima of this reflectivity map account for the modes that can be excited in the structure at those illumination conditions. As SPPs are transversal magnetic (TM) modes, we restrict our discussion to p-polarized illumination which only excites TM modes.

From Fig. VI.2.(a), it can be seen that at high core widths (w_0 > 800 nm), the waveguide supports several optical modes, TM_n, with n>2, as well as two uncoupled SPP at each Ag-SiO_2 interface, which are therefore degenerated and collapse in the same reflectivity minimum (around 58º). The number of optical modes depends on the particular thickness of the core and decreases as w_0 gets smaller. For example, for w_0 = 1000 nm the system shows three optical modes while only one remains at w_0 = 500 nm, with cut-off at w_0 ~ 400 nm. Moreover, when the insulator thickness decreases below w_0 = 800 nm, the two surface waves start to couple by means of the interaction of their evanescent electromagnetic fields inside the optical cavity, giving rise to a splitting of the degenerate SPP into two modes, TM_1 and TM_0. These two SPP modes are named

the antisymmetric (AM) and the symmetric (SM) ones attending to the profiles of the normal electric (E_z) components of their electromagnetic fields inside the waveguide core, as shown in Fig. VI.2.(b). The AM and SM modes are excited at lower and higher angles of incidence respectively, implying a smaller and higher wavevector for each mode[8]. As the MIM cavity core width is further reduced, the wavevector of the AM mode decreases, in such a way that this mode loses its plasmonic character (once it crosses the light line) and it is progressively less confined inside the waveguide. This mode reaches a zero wavevector, and therefore cut-off, at w_0 = 180 nm. The SM mode, on the other hand, increases its in-plane wavevector as w_0 decreases, keeping always a plasmonic nature and increasing its confinement inside the waveguide. In figure VI.2.(a), the SM mode disappears for $w_0 \sim 100$ nm as the wavevector becomes too large to allow for excitation by means of illumination through a SF10 glass substrate, but no cut-off exists for this mode. Therefore this SM mode is the only one supported by PGW structures[7]. Since we are interested in analysing the magnetic field induced modulation on the wavevector of the two SPP modes, the region of interest for the design of our MIM cavities is within 180-400 nm core width. Being the AM mode highly dispersive compared with the SM one in this region, this will lead to significant differences for the wavevector modulation of the two modes.

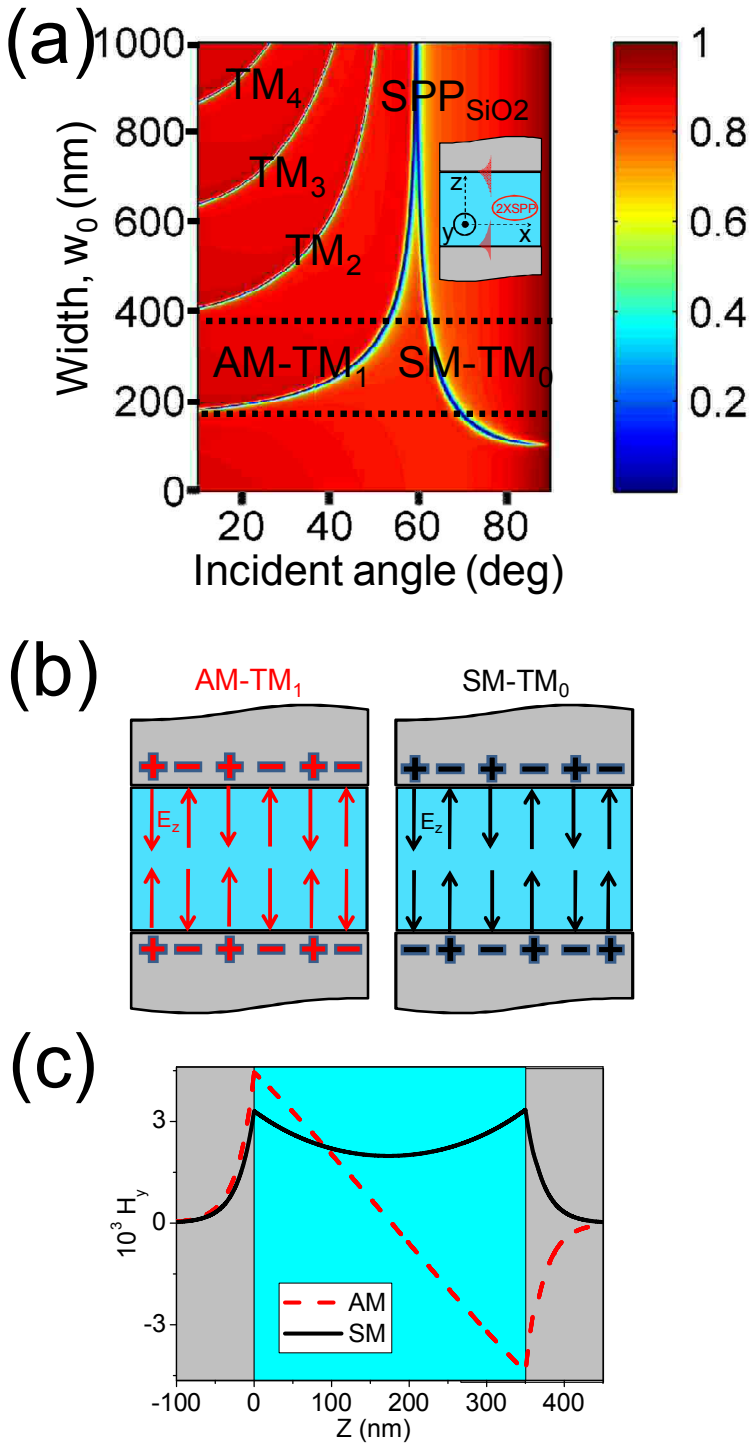

Figure VI.2. (a) Simulated reflectivity map as a function of SiO_2 thickness and angle of incidence showing the different optical and plasmonic modes confined inside a Metal-Insulator-Metal (MIM) structure. The SiO_2 thickness of the insulator layer for the MIM magnetoplasmonic cavities fabricated in this work are located between the two dashed black lines indicated in the figure. Inset: Scheme of a MIM structure, where it is possible to excite one SPP at each metal-dielectric interface (thus two SPPs) inside the optical nanocavity. (b) Sketches for both charge and normal electric field (E_z) distributions along the two metal-dielectric interfaces of the MIM system for the antisymmetric, AM (left side of the figure) and symmetric, SM (right side of the figure) modes originated from the interaction of the two uncoupled SPPs. (c) Normalized magnetic field amplitude (H_y) distributions for the two plasmonic modes inside the MIM nanocavity: AM (red dashed line) and SM (black solid line).

Figures VI.2.(b) and (c) further extend the description of the electromagnetic (EM) field distribution of the two SPP modes inside the cavity. In particular, Fig. VI.2.(b) shows a sketch of the normal electric field (E_z) and surface charge distributions for the two modes, whose behaviors are opposite. The AM mode presents a change of the sign for its E_z amplitude in the core center (and therefore a zero crossing) whereas the SM mode exhibits a minimum of the E_z amplitude in the core center but no change of E_z sign (or zero crossing) inside the insulator core. Figure VI.2.(c) shows for both modes the calculated normalized magnetic field amplitude (H_y), which exhibits the same symmetry as E_z, in order to compare their relative confinement. While SM mode presents an electromagnetic profile more confined on the interfaces, the EM field of the AM mode spreads out towards the metal regions.

Connecting with the studies carried out in this thesis, when a ferromagnetic metallic layer is inserted into the Ag one of the MIM system, the same AM and SM plasmonic modes exist and, most importantly, the application of a magnetic field parallel to the interface and perpendicular to the SPP propagation direction induces a measurable modification on the wavevector of the SPP modes, as mentioned in the introduction. This property is well-known and has been widely characterized in single-interface SPPs as it has been studied for Ag/Co/Ag and Au/Fe/Au trilayers (chapters III and IV, respectively), and some preliminary studies have also been done on IMI configurations[15,16]. The objective of this chapter is to analyze, both theoretically and experimentally, the modulation effect for the above described MIM plasmonic symmetric and antisymmetric modes. To get an insight on the expected phenomenology and determine the most appropriate structures to be fabricated and characterized, preliminary simulations of the magnetic modulation of the SPP wavevector were done on several symmetric and asymmetric magnetoplasmonic MIM cavities. The MIM cavities were modeled again using Transfer matrix formalism with a dielectric tensor that takes into account the magnetooptical activity of the ferromagnetic metal layer. The wavevector modulation is determined by calculating the SPP modes with and without applied magnetic field (finite and zero values for the off-diagonal elements of the dielectric tensor respectively).

Figure VI.3.(a) and (b) show the obtained results for the AM and SM modes respectively in a magnetoplasmonic MIM cavity with only one Co layer (air/70nm Ag/ SiO_2/10 nm Ag/6 nm Co/11 nm Ag/SF10) and in a perfect symmetric MIM cavity with two identical Co layers (SF10/11 nm Ag/ 6 nm Co/10 nm Ag/SiO_2/10 nm Ag/6 nm Co/11 nm Ag/SF10). As a reference, the magnetic modulation undergone by the single interface SPP of a silica capped fully metallic multilayer with Co inside (SiO_2/10 nm Ag/6 nm Co/11 nm Ag/SF10) also appears. Note that the Co film is always sandwiched between Ag layers, due to its high optical absorption. If the Co layers were positioned directly into the metal-dielectric interfaces, this would lead to a strong SPP damping, broadening the reflectivity minima associated with each mode and preventing from

distinguishing them easily. This effect is reduced when the Co layer is moved away from the interface because of the evanescent nature of the SPP wave[17]. As it can be seen in Fig. VI.3.(a) and (b), at high SiO_2 thickness the three systems produce the same modulation (that of a single interface) due to the loss of coupling of the two SPP modes in the MIM structures. In contrast, the modulation exhibits different trends for the two MIM systems in the low thickness region in which the SPP coupling exists. Regarding the AM mode in the MIM cavity with one Co layer, the magnetic modulation is increased compared to that for the SPP mode in the silica capped fully metallic multilayer, indicating the advantage of the MIM system. In contrast in the case of the SM mode in the MIM cavity with one Co layer, the magnetic modulation is decreased compared to that for the SPP mode in the silica capped fully metallic structure. This is possibly due to the higher confinement of the EM field into the insulator region of the MIM system (thus lower EM field in the Co layer) for the SM mode at low SiO_2 thickness (Plasmon gap waveguide behavior) compared to that of the SPP mode in the silica capped fully metallic structure.

For the fully symmetric cavity, on the other hand, the modulation tends to zero as the cavity gets narrower for both modes, and becomes null at 200 nm of SiO_2 thickness for the AM mode. This is related to the non-reciprocity of the SPP wavevector in presence of a magnetic field:[18,15] the wavevector of the forward SPP differs from that of the backwards SPP. This translates to reversed modulations also for the upwards and downwards SPPs in opposite interfaces (see sketch in Fig. VI.3.(c)) In fact, it has been demonstrated in an IMI system that the modulation signal for coupled SPPs is completely canceled if the system is perfectly symmetric[15].

Summarizing, in order to analyze the magnetic field induced modulation on both AM and SM modes of MIM systems, which can be excited through a SF10 glass substrate, we will restrict to cavities with an insulator thickness between 180 and 400 nm (indicated with dashed black lines in figure VI.2.(a)). Moreover, we can expect tuning the magnetic field modulation of the modes with the SiO_2 thickness and using one or two Co layers inside the MIM structure, so different configurations of MIM magnetoplasmonic (MIM-MP) cavities taking these aspects into account will be analyzed.

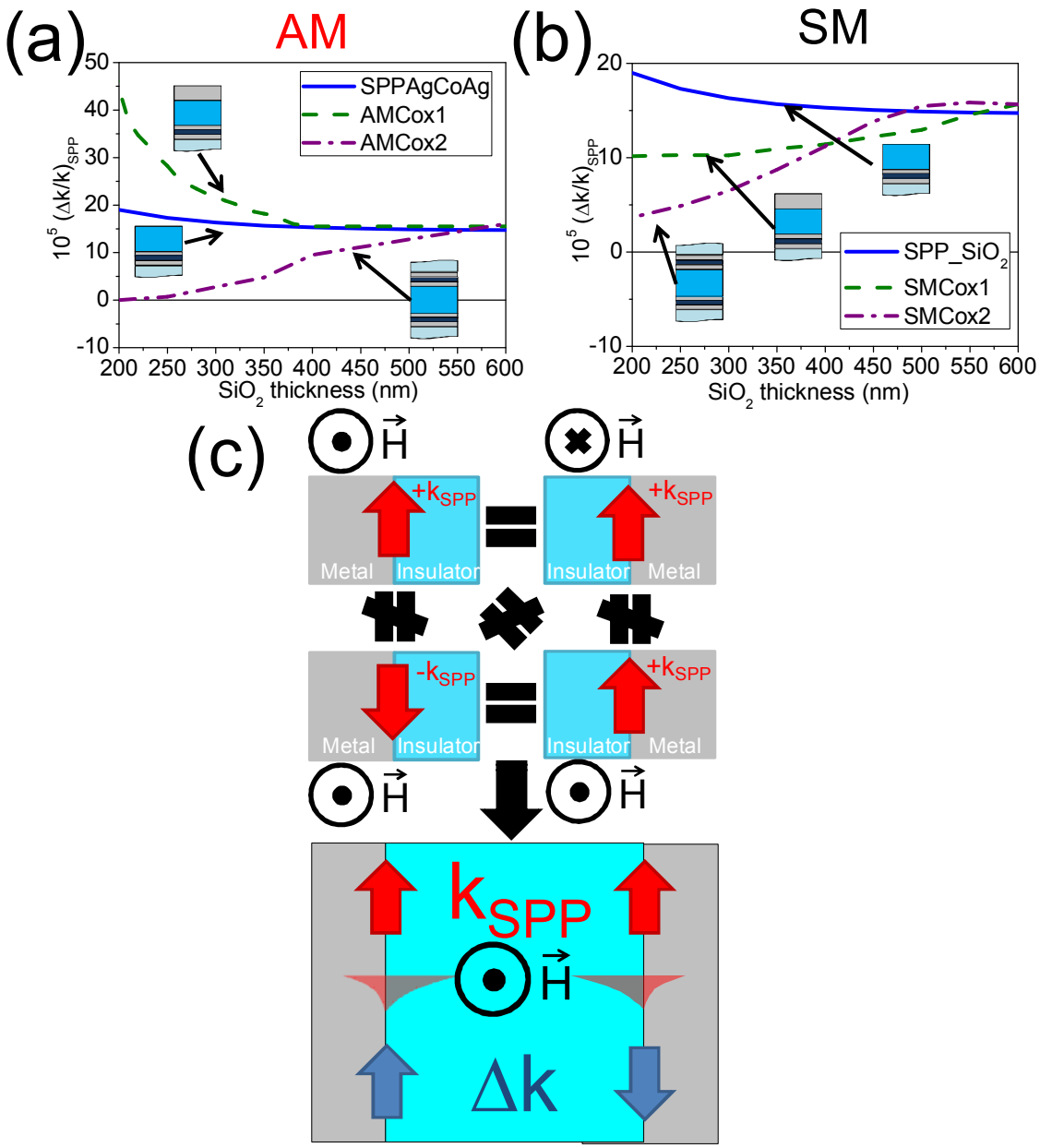

Figure VI.3. Simulation of the surface plasmon polariton (SPP) modulation as a function of SiO_2 thickness for a single-interface SPP mode in a silica capped fully metallic multilayer [SiO2/10 nm Ag/6 nm Co/11 nm Ag/SF10] (blue solid line) and for the antisymmetric (AM) (a) and symmetric (SM) (b) modes in two MIM systems with one Co layer [air/70nm Ag/ SiO2/10 nm Ag/6 nm Co/11 nm Ag/SF10] (green dashed line) and two Co layers [SF10/11 nm Ag/ 6 nm Co/10 nm Ag/SiO2/10 nm Ag/6 nm Co/11 nm Ag/SF10] (purple dash-point line). (b) Sketch of the equivalence relations for the magnetic modulation in single interfaces depending on the magnetic field and wavevector directions and the magnetic modulation contribution to the SPP wavevector from each insulator-metal interface in a symmetric MIM structure.

VI.3.- EXPERIMENTAL AND THEORETICAL METHODS

Sample growth was performed in the deposition system, with a combination of DC magnetron sputtering and e-beam evaporation techniques (for more details see the section II.2.). Due to the better performance of the optical properties of Ag compared to those of Au in the visible region, MIM structures have been fabricated using Ag instead of Au as plasmonic material in order to enhance the magnetoplasmonic properties (see the section III.1.). A thin Ti layer is used to promote Ag adhesion to glass (see Appendix I), and a Au capping layer is placed on top of the last Ag layer to prevent the chemical deterioration of Ag in ambient conditions (see the Chapter III)[29]. The Au, Ag and Ti layers were deposited by magnetron sputtering whereas the Co and SiO_2 ones were deposited by e-beam evaporation.

Simulations of the Reflectivity, TMOKE signal and the magnetic modulation for the wavevector of the plasmonic modes signals, carried out in order to compare with the experimental results, were performed via transfer matrix method using experimental optical and MO constants of the materials obtained from spectral measurements. The optical constants used to simulate the layers were experimentally obtained via spectral ellipsometry from specific samples grown for this purpose (the specific samples, the optical constants and more details are shown in the section III.4.). On the other hand, the MO constants for the Co layers used for the simulations have been obtained by combined spectral ellipsometry and polar Kerr spectroscopic measurements (more details appear in Appendix II). As will be justified later, two sets of optical and MO constants have been used for the simulations of the Co layer due to the different morphology and interface roughness of this film (see chapter IV for the case of Fe films) when it is deposited in different positions inside the MIM structures. For the Co layer grown underneath the SiO_2 layer (Co down and Co double series), which shows a very flat morphology, the optical and MO constants of an epitaxial Co film, calculated from the measurements of Ref. [[19]], have been used. On the other hand, the optical and MO constants for a polycrystalline Co film from the specific samples of chapter III have been used in order to simulate the much rougher Co layer deposited on top of the SiO_2 layer (Co up and Co double series).

VI.4.- PLASMONIC MIM CAVITY

First, a preliminary Ag/SiO_2/Ag sample was grown in order to observe the splitting of the SPP degeneration, due to the two metal-insulator interfaces in the MIM structure, into two different optical modes (SM and AM modes) by means of attenuated total reflection (ATR) measurements using the Krestchmann configuration[20]. These two optical modes present different energy distribution, which leads to different propagation

constants (effective refractive index and propagation losses) of the optical modes that can be observed in the mentioned ATR measurements.

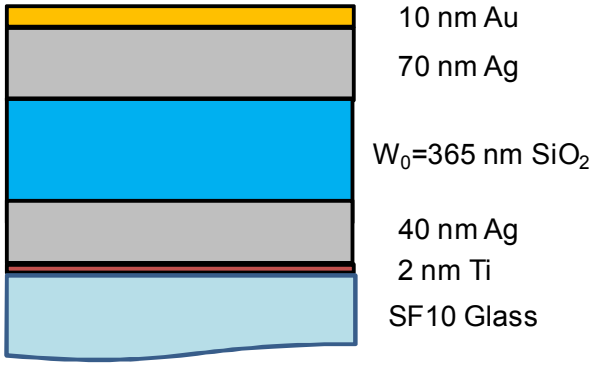

Fig.VI.4. Scheme of the fabricated plasmonic MIM structure with the layer thickness.

A SiO_2 thickness (w_0) of 365 nm was chosen in order to fabricate the sample that exhibits the two plasmonic modes. The thickness of the layers below the dielectric core were optimized taking into account the Kretschmann configuration for exciting the plasmonic modes (see Fig. VI.4. (b)). On the other hand, the Ag upper layer is chosen thick enough to avoid the excitation of SPP in the air-metal interface. Finally the 10 nm Au topmost layer is used as a capping to prevent the degradation of Ag.

VI.4.A. -Morphology and plasmonic characterization (Ag/SiO_2/Ag)

As it is well known the optical properties of nanostructures depend strongly on the morphology (see chapter IV). For this reason, AFM measurements of the MIM system were performed. The fig. VI.5. (a) shows an AFM image of the topmost surface for the SPP cavity. It is worth to mention the rougher surface compared to the Ag/Co/Ag/Ti multilayers of the Appendix I. Large mounds are observed in the AFM profile of Fig. VI.5. (b) with an average width of 50 nm and a height of 8 nm. Such mounds can be ascribed to the roughness of the underneath 40 nm Ag layer which the insulator layer has been deposited onto.

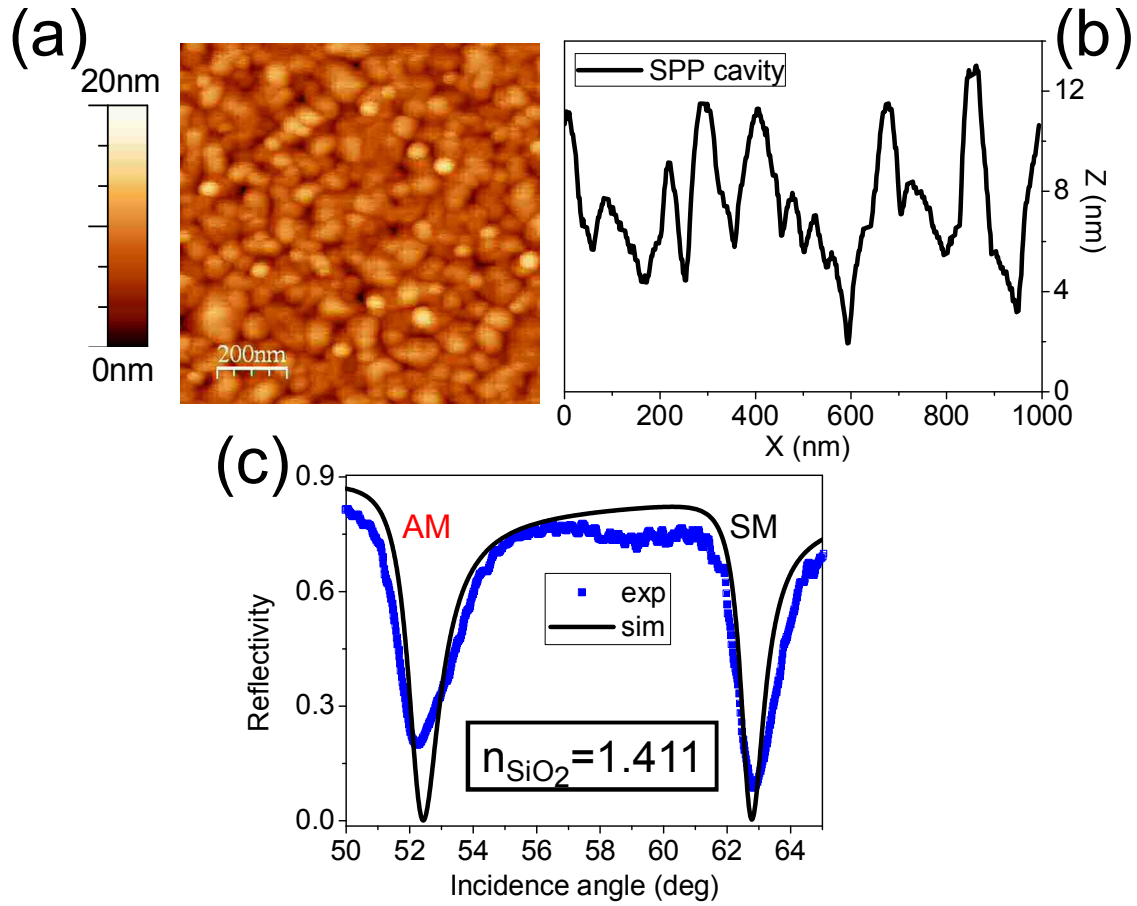

Fig.VI.5. AFM image (a) and profile (b) of the MIM multilayer. (c) Reflectivity angular measurement (blue squares) under Kretschmann configuration of the MIM structure, showing the symmetric and antisymmetric modes. Besides, the fitted curve (black line) obtained using a SiO_2 refractive index of 1.411.

Subsequently, angular reflectivity measurements were performed under Kretschmann configuration in order to excite the two optical modes supported by the MIM structure. As we can see in Fig. VI.5.(c), the reflectivity curve presents two minima around 52 and 63 degrees that are related to the AM and SM modes respectively. Besides, a simulated reflectivity curve is fitted to the experimental one in the figure. The experiment and simulation show an AM mode with a broader minimum compared to the SM one. This is due to the different distribution of the electromagnetic (EM) field in each mode, since the AM mode confines the EM field in the metal region whereas the SM confines the EM field inside the insulator core[5].

It is worth to notice that the refractive index of the SiO_2 core fitted in the simulation is 1.411 at 632.8 nm of wavelength. Since the refractive index for bulk SiO_2 is 1.458, this suggests that the insulator layer is porous, a conclusion which agrees with the results of the AFM measurements shown in the previous figure. The overall roughness of the SPP cavity causes an increase of radiation losses[21]. Such radiation losses are responsible of the high reflectivity values at the minima shown in the experimental reflectivity curve compared to the lower reflectivity values at the minima of the simulated reflectivity one. Moreover, the radiation losses change the conditions

for the optimum SPP excitation thickness, and also explain the higher breadth of the two experimental minima compared to the simulated ones.

VI.5.- MAGNETOPLASMONIC MIM CAVITIES

As we could see in previous chapters, it is possible to modulate the wavevector of a SPP upon the insertion of a ferromagnetic (for example Co or Fe) thin film in a metallic multilayer. By means of ATR measurements, we can also study this magnetic modulation on the two optical modes of the previously described Ag/SiO_2/Ag system (AM and SM modes). Interestingly enough, the different EM distribution inside the MIM structure for the two modes will determine the intensity of the magnetic modulation of the SPP wavevector. However, other properties of the fabricated multilayers are important too. The flatness of the Co layer and the overall roughness of the studied system govern the MO properties (see chapter IV concerning a Fe layer) and propagation losses of the system respectively. By these reasons, a complete characterization of the fabricated magnetoplasmonic MIM cavities was performed, including morphology, magnetic and magnetoplasmonic characterizations.

VI.5.A.- Samples and multilayer optimization

According to the results presented in section VI.2., three series of magnetoplasmonic MIM cavities with three different MO active layer positions, namely Co down, Co up and Co double, were fabricated. The particular structure of each series, shown in Fig. VI.6., is: 10 nm Au/70 nm Ag/w_0 SiO_2/10 nm Ag/6 nm Co/11 nm Ag/2 nm Ti/SF10 (Co down series); 10 nm Au/70 nm Ag/6 nm Co/10 nm Ag/w_0 SiO_2/23 nm Ag/2 nm Ti/SF10 (Co up series); and 10 nm Au/70 nm Ag/6 nm Co/10 nm Ag/w_0 SiO_2/10 nm Ag/6 nm Co/11 nm Ag/2 nm Ti/SF10 (Co double series). The SiO_2 thickness (w_0) varies between 180 nm and 380 nm (see the table VI.1. with the samples fabricated for each series).

W_0 (SiO_2 thickness)	Co_{down}	Co^{up}	2xCo
	-	180 nm	180 nm
	260 nm	260 nm	260 nm
	380 nm	380 nm	380 nm

Table.VI.1. Samples fabricated for the Co down (yellow), Co up (red) and Co double (blue) series with their respective SiO_2 thickness for each sample.

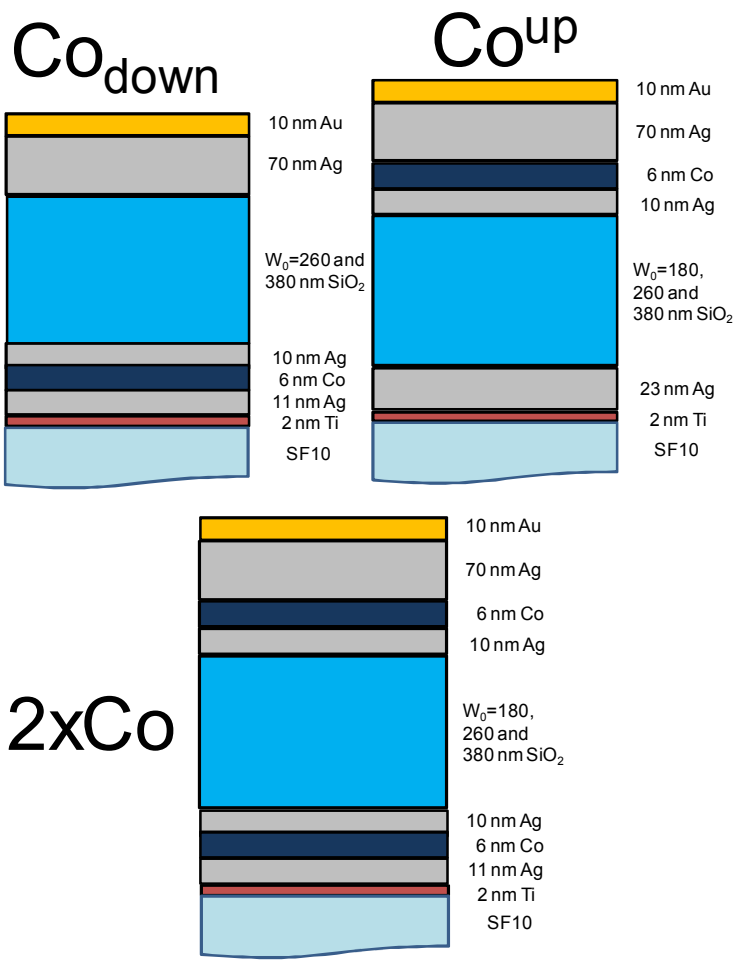

Fig.VI.6. Schemes of the three series of MIM-MP cavities fabricated on SF10 substrates varying the Co layer position: below the SiO_2 layer (Co_{down}), on top of the SiO_2 layer (Co^{up}) and in both positions (2xCo).

Using Transfer matrix simulations it was again possible to optimize the thickness of each layer for the SPP excitation in Kretschmann configuration. The figure VI.7. shows three reflectivity maps as a function of both the insulator thickness (w_0) and the incidence angle for the three Co position series. Despite the broadness of the optical modes due to the Co optical absorption, all the optical modes supported by the previous $Ag/SiO_2/Ag$ system are also observed now in the three reflectivity maps (compare with Fig. VI.2.(a)). As it can be expected, the Co up series reflectivity map (fig. VI.7.(b)) shows the lowest optical losses in its modes since the light does not travel across the Co layer before the light-SPP coupling in the Kretschmann configuration. On the other hand, the Co double series reflectivity map (fig. VI.7.(c)) presents the highest optical losses in its modes due to the presence of two Co layers. Finally we can remark that it is possible to differentiate between the AM and SM modes in the samples with SiO_2 thickness below 400 nm for the three reflectivity maps. Therefore this SiO_2 thickness will be our upper limit in order to confirm the observation of the SPP splitting for the ATR measurements with the MP-MIM cavities.

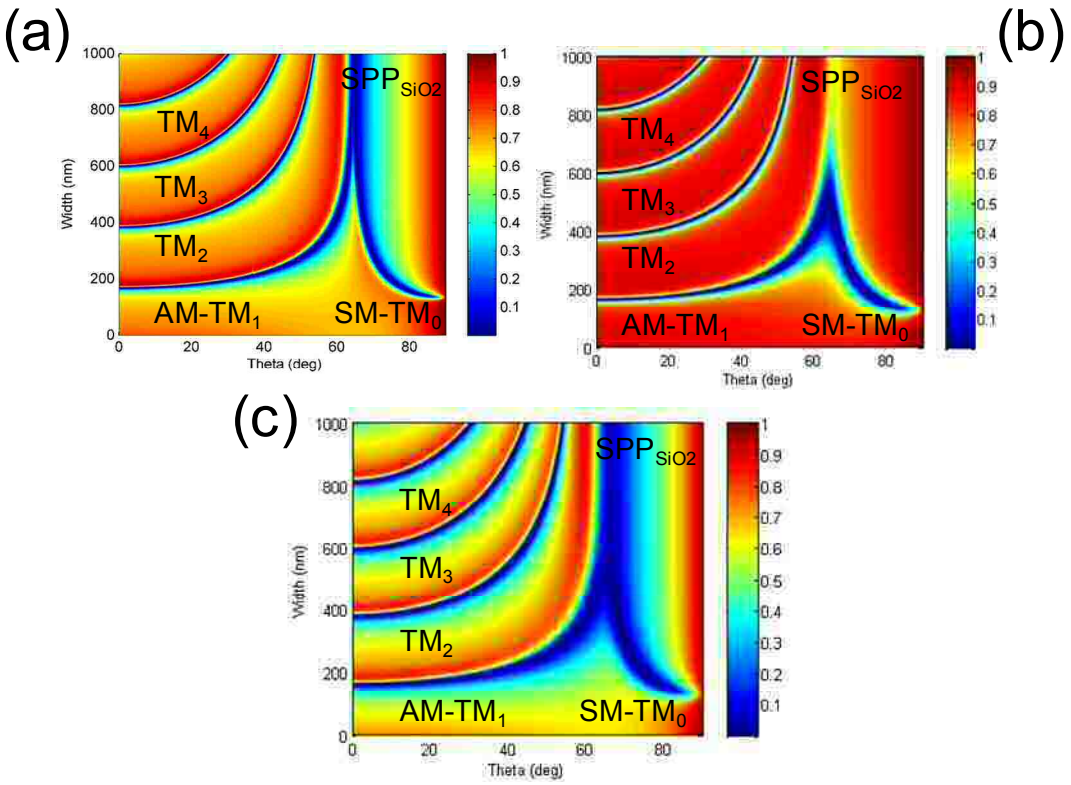

Fig.VI.7. Simulated reflectivity maps of the three series of MP-MIM cavities fabricated on SF10 substrates varying the Co layer position: Co down series(a), Co up series(b) and Co double series (c).

VI.5.B.- Morphological characterization

AFM measurements were performed for the samples of the three Co position series. Figure VI.8.(a) shows a representative image of a 380 nm SiO_2 sample of the Co down sample. Granular structures can be observed over the surface after the deposition of the multilayer thin film, but showing a clear state of coalescence. A comparison of AFM profiles for the three series of samples and a reference sample without SiO_2 layer is presented in the figure VI.8. (b). The AFM profile for the reference sample exhibits the flattest surface (RMS roughness value of 0.9 nm) indicating that the surface roughness of the MP-MIM cavities is mainly due to the deposition of the insulator layer. The profiles of the cavities are quite similar although a systematic difference can be found between the 260 nm and 380 nm samples. The 380 nm samples show rougher AFM profiles (RMS roughness values of 2.2, 2.5 and 2.1 nm for the Co down, Co up and Co double series respectively) than the 260 nm ones (RMS roughness values of 2.0, 2.1 and 1.4 nm for the Co down, Co up and Co double series respectively) due to the higher SiO_2 thickness. It is worth to mention that the 260 nm SiO_2 sample of the Co

double series presents the flattest surface of all cavities. According to chapter III, the Co layer deposition of a 6 nm Co layer between the Ag layers reduces the surface and interface roughness, and therefore the deposition of two Co layers gives rise to the smoothest surface.

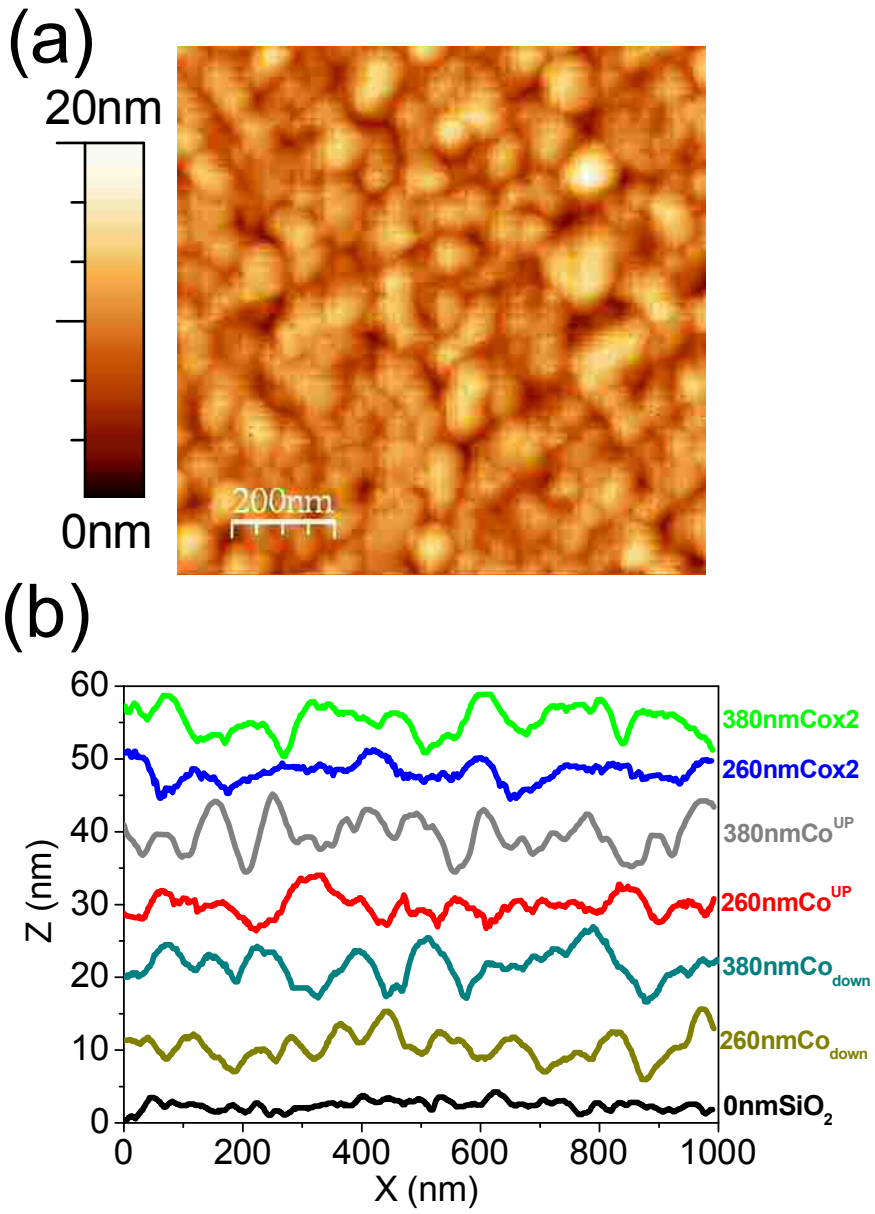

Figure VI.8. AFM image of a representative MP-MIM cavity (380 nm thickness SiO_2-Co down). (b) AFM profiles for a sample without SiO_2 (reference sample), and the 260 and 380 nm SiO_2 thickness samples of the three MIM-MP cavity series fabricated. The curves are vertically offset for clarity.

VI.5.C.- Magnetic characterization

TMOKE loops were measured for the three Co position series in order to determine the magnetization reversal process of the Co layers deposited in different places of the MIM structure. As it has been shown in the previous subsection, the surface morphology varies with different Co layer position, and therefore the Co layer morphology should vary too. An indirect suitable tool for studying the Co layer morphology is the use of TMOKE measurements, as it has been described in previous chapters.

The figure VI.9. shows the TMOKE loops of the 260 nm SiO_2 samples on the left side and the TMOKE loops of the 380 nm SiO_2 samples on the right side. On the first row, the two TMOKE loops for the Co down series are presented. They exhibit an almost rectangular shape and very low coercive field (around 30 Oe) that is characteristic of flat ferromagnetic films. On the second row, the two TMOKE loops for the Co up series can be observed (note that the differences of the TMOKE values with the SiO_2 thickness are originated by an optical effect, since the MIM structure act as a Fabry-Perot resonator). They exhibit higher coercive fields (around 150 Oe) compared to the TMOKE loops for the Co down series. The observed difference in magnetic behavior for the two Co position series can be ascribed to the difference of the interlayer roughness for the Co layers grown at the two different positions. The Co layer grown underneath the SiO_2 layer exhibits flat interfaces whereas the Co layer grown over the SiO_2 exhibits rougher interface due to the high roughness of the insulator layer where it has been deposited. Finally on the third row, the TMOKE loops for the Co double series are shown. The magnetization reversal exhibits two components: The first magnetization component shows a low coercive field similar to that of Co down loops, while the second magnetization component exhibits a higher coercive field similar to that of Co up loops. This indicates that the independent magnetization reversal processes of both Co layers are observed, the Co layer underneath of the SiO_2 layer reversing at low magnetic fields, and the Co layer on top of the SiO_2 layer switching at higher magnetic fields. It is important to remark that these differences between the magnetic properties of the Co layers are due to the interface roughness that leads to significant differences in the MO and magnetic modulation of the SPP wavevector too (see the chapter IV).

After this morphological and magnetic characterization, we can conclude that the ferromagnetic layer presents different physical properties depending of its position inside the MIM structure, due to the interface roughness mainly caused by the rough SiO_2 layer. Therefore two different sets of optical and MO constants, as has already been indicated in section VI.3., will be used for modeling the Co layers in the simulations of reflectivity, TMOKE signal and magnetic modulation of the SPP wavevector.

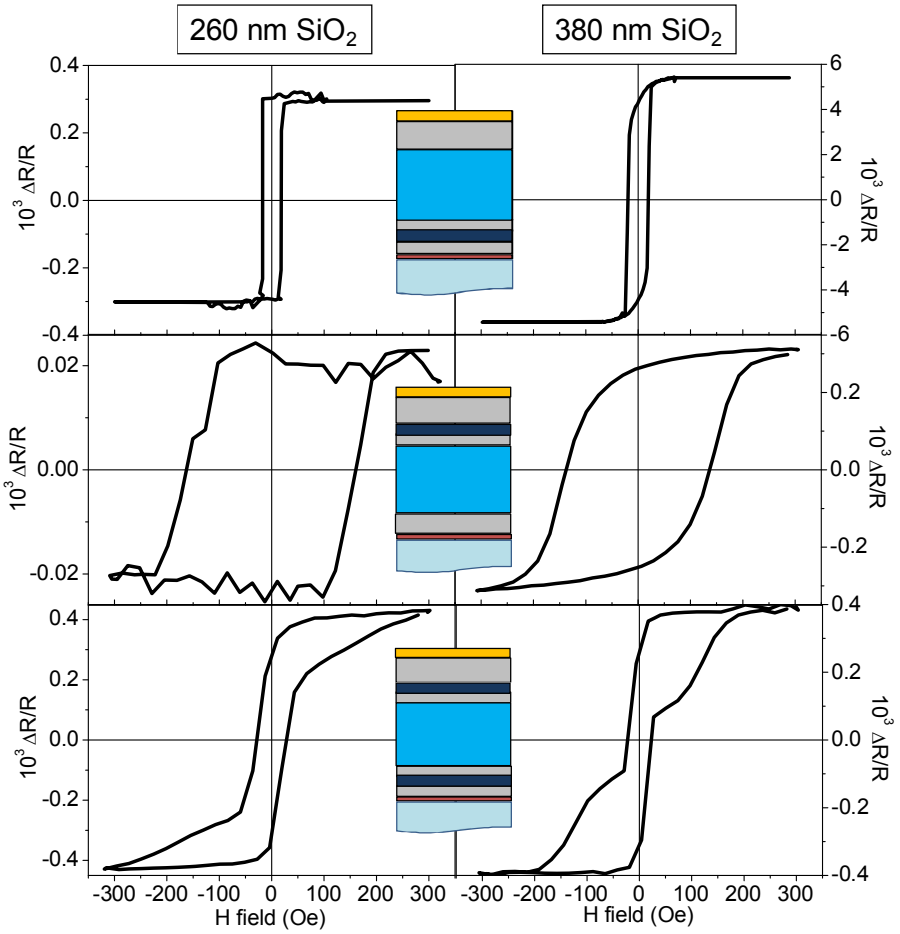

Fig.VI.9. TMOKE loops for 260 (left side of the figure) and 380 nm (right side of the figure) SiO_2 thickness samples of the three MOSPP cavity series fabricated.

VI.5.D.- Magnetoplasmonic characterization

After these preliminary studies have been carried out, it is possible to perform the mentioned ATR and TMOKE measurements in the magnetoplasmonic MIM cavities at 632.8 nm wavelength. From the angular reflectivity experiments, we will obtain the wavevector dependence with the insulator thickness of the AM and SM modes for the three series of samples. On the other hand, the magnetic modulation of the wavevector of the modes for the three series will be obtained from the TMOKE curves.

VI.5.D.(i)-Optical characterization of the modes

Reflectivity measurements for the three series of samples, using the Kretschmann configuration in order to excite the SPP modes, are shown in the figure VI.10. Two minima (θ_{min}) can be observed related to the excitation of the AM mode at

lower incidence angles and the SM mode at higher incidence angles for every reflectivity curve (as for the Ag/SiO_2/Ag reflectivity curve). It is worth to mention that the SPP splitting of the two modes agrees with the Transfer matrix simulations (see the section VI.4.), i.e., the AM mode increases its excitation angle (effective refractive index) with the SiO_2 thickness until reaching the standard SPP angle excitation in a Ag-SiO_2 interface (SPP coupling and mode splitting disappear). On the other hand, the SM mode decreases its excitation angle (effective refractive index) with the SiO_2 thickness until reaching the standard SPP excitation in SiO_2 (SPP coupling and mode splitting disappear). The AM modes exhibit broader minima (related to its optical losses) compared to the respective minima of the SM modes for the three series. This is due to the predominant confinement of the EM field inside the metal regions for the AM modes compared to the predominant confinement of the EM field inside metal-insulator interfaces for the SM modes[5]. The SPP modes in the Co double samples exhibit the highest optical losses as the simulation had predicted, due to the existence of two ferromagnetic layers.

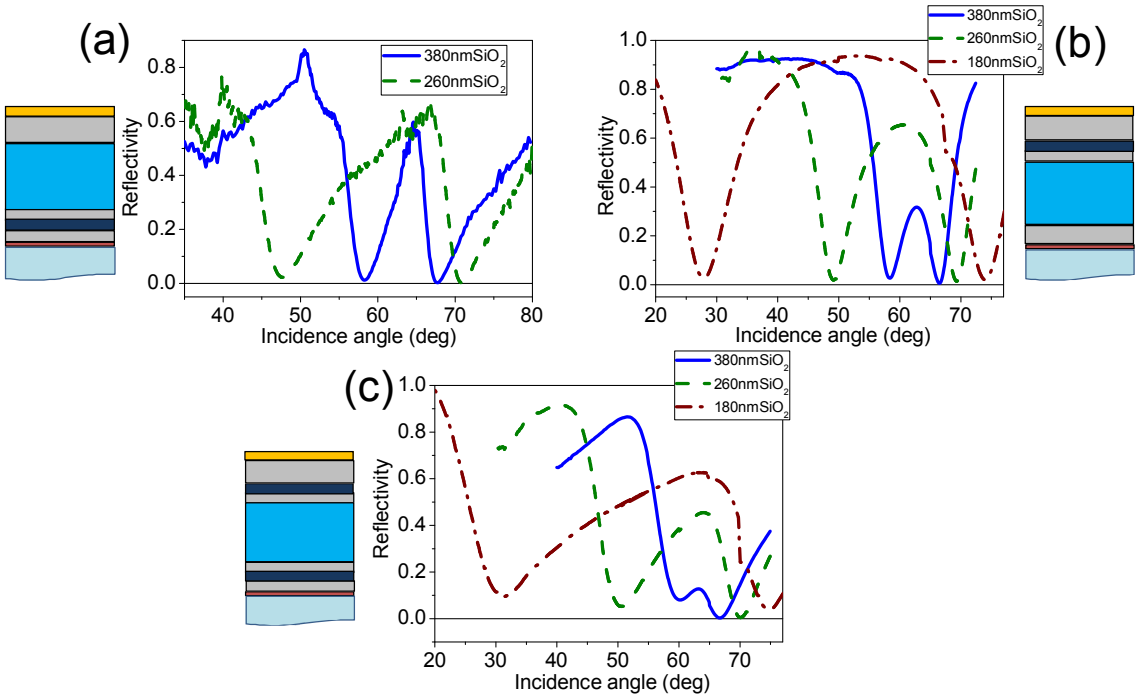

Fig.VI.10. Reflectivity curves as a function of the incidence angle for 380 nm SiO_2 thickness (solid blue line), 260 nm SiO_2 thickness (dashed green line) and 180 nm SiO_2 thickness (dashed-dotted brown line) samples. (a) Co down series, (b) Co up series and (c) Co double series.

Using the θ_{min} value of the AM and SM modes from each experimental reflectivity curve and the equation [VI.1.] it is possible to obtain the experimental real part of the wavevector (k_x) of the SPP modes normalized to the vacuum wavevector (k_0):

$$k_x / k_0 = n_{SF10} \sin(\theta_{\min}) \qquad [VI.1.]$$

where λ is the vacuum wavelength and n_{SF10} is the refractive index of the SF10 substrate (1.723). The figure VI.11. shows the dependence of the AM and SM wavevectors with the SiO_2 thickness for the three series of MOSPP cavities.

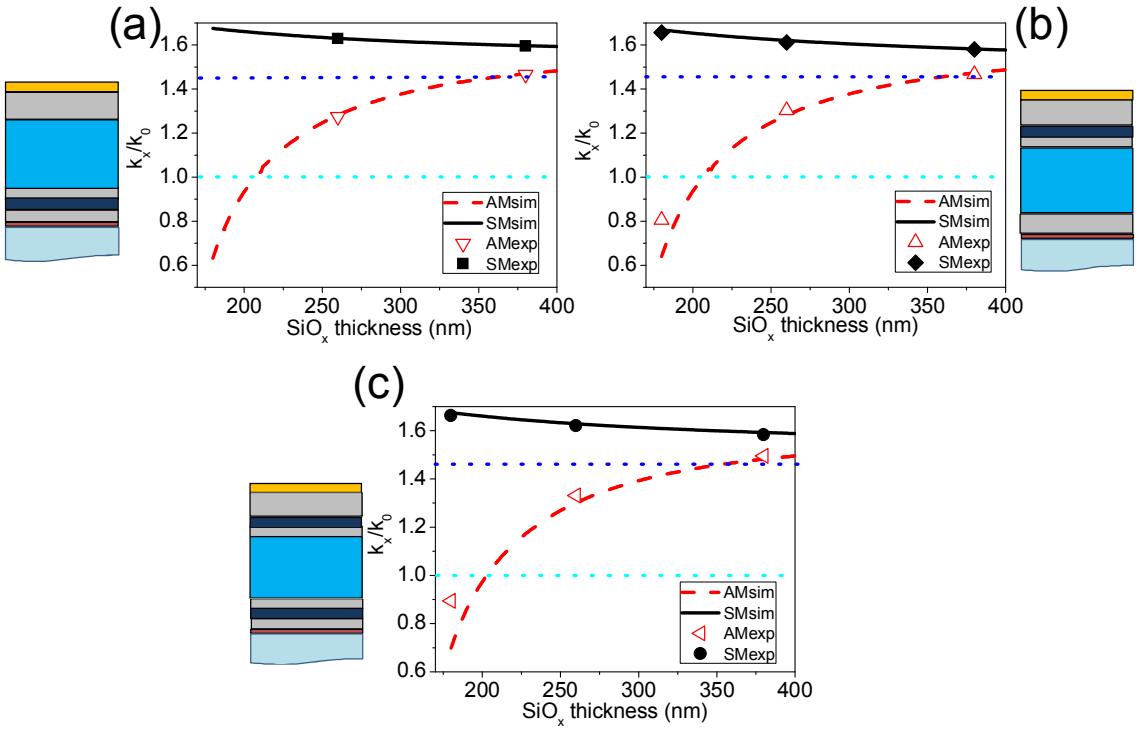

Fig.VI.11. Experimental (symbols) and simulated (lines) normalized real part of the wavevector as a function of the SiO_2 thickness for the AM (red empty triangles and dashed lines) and SM (black solid symbols and lines) modes. (a) Co down series, (b) Co up series and (c) Co double series. Also the SiO_2 light line (dark blue dotted line) and the vacuum light line (light blue dotted line) are included.

By a detailed analysis of the wavevector of the two modes for the MP-MIM cavities, we can observe at 380 nm SiO_2 thickness that the SPP coupling of the two insulator-metal interfaces is very weak, therefore the two modes exhibit very similar wavevectors or optical properties. Focusing on 260 nm SiO_2 thickness, the AM and SM wavevectors are quite separated, in fact the AM wavevector is lower than the light line in SiO_2 medium (below the dark blue dotted line). This implies that the AM mode cannot be considered as an actual SPP. Focusing on 180 nm SiO_2 thickness, the AM and SM wavevectors are highly separated. The AM wavevector is lower than the light line in the vacuum (below the light-blue dotted line), which means that the AM mode confinement inside the waveguide is very low.

All these facts will lead to consequences for the magnetic modulation of the mode's wavevector, since a poor confinement of the optical mode inside the core of the

MIM cavity enhances the EM field localization in the metallic part of the structure (and consequently in the Co layer).

The Transfer Matrix simulations exhibit a close agreement with the experimental wavevector values of the three series of MP-MIM cavities, with small deviations when the AM wavevector becomes very dispersive in the region of lower SiO_2 thickness, a fact that makes easier obtaining larger differences between experiments and simulations. It is worth mentioning that the AM and SM wavevectors of the three MOSPP cavities varying the Co layer position are almost identical, which remarks the negligible effect of the insertion of one or two Co layers inside the MIM optical system on the real part of the wavevector (dispersive properties). This fact has also been recently pinpointed comparing Au and Au/Co/Au nanodisks[22].

VI.5.D.(ii)- Magnetic modulation of the modes

The magnetic modulation of the SPP wavevector has been experimentally determined by measuring the reflectivity and transverse MO Kerr effect (TMOKE) signal using the Kretschmann configuration[20] for a given wavelength λ=632 nm as it has been sketched in Fig. VI.12.(a). Figure VI.12.(b) shows a representative angular reflectivity measurement for the 260 nm SiO_2 sample of the Co down series. A simulated reflectivity curve (black line) is fitted to the experimental curve (blue circles) using the refractive index and the thickness of the SiO_2 layer as fitting parameters, and obtaining a SiO_2 refractive index of 1.464 and a core thickness of 260 nm for this sample. This value of the refractive index for the insulator layer is very similar to the refractive index of bulk SiO_2 material, and therefore for the rest of the samples, the SiO_2 refractive index was fixed at that value and only the core thickness was fitted. We can deduce from their different refractive index that the SiO_2 layer deposited over the Ag/Co/Ag trilayer grows with lower porosity than the SiO_2 layer deposited over the 40 nm Ag layer of the plasmonic MIM structure (section VI.4.). It is also possible an Oxygen deficiency in the SiO_2 material of the plasmonic MIM structure due to the intrinsic nature of the process for the SiO_2 e-beam evaporation. As a consistency check, spectral ellipsometric measurements have also been performed for the magnetoplasmonic MIM cavities exhibiting a good agreement of the fitting between the measurements and the model for these refractive index and thickness of the insulator layer.

The corresponding angular TMOKE signal is shown in Fig. VI.12.(c), in which an enhancement with resonance shape of the TMOKE signal is found around the incidence angles for the excitation of the AM and SM modes. As it has been explained in detail in previous chapters (see chapter III), these resonances are related to the

magnetic modulation of the SPP wavevector. Moreover, the value of the k_{SPP} modulation can be deduced from the comparison between the TMOKE curve and the angular derivative of the experimental reflectivity. First, the angular derivative of the experimental reflectivity curve (black solid line in Fig. VI.12.(c)) is fitted to the TMOKE curve (red dots) in order to obtain the magnetic angular shift ($\Delta\theta$). Then, the magnetic modulation $(\Delta k/k)_{SPP}$ is obtained using the equation [III.3.] from the chapter III. As it can be seen from Fig. VI.12.(c), both SM and AS modes are modulated by the magnetic field.

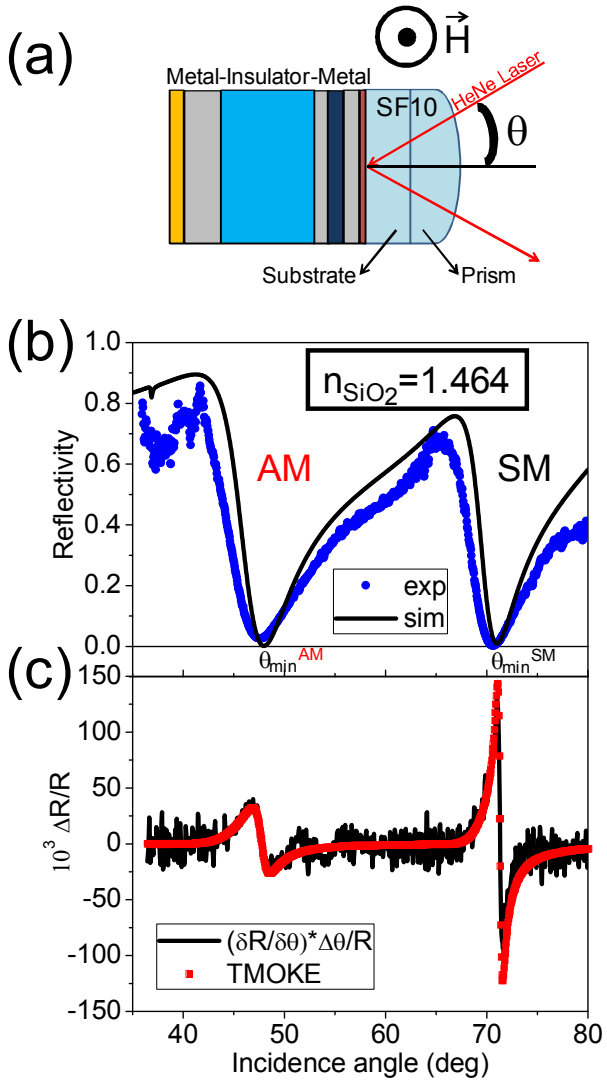

Figure VI.12. Scheme of the TMOKE measurement under Kretschmann configuration to allow SPP excitation. (b) Experimental (blue circles) and simulated (black line) reflectivity curves for a representative MIM-MP cavity (260 nm SiO_2 thickness of the Co down series). Both antisymmetric and symmetric plasmonic modes of the MIM cavity appear. (c) TMOKE signal (red dots) showing clear resonances around the excitation of the two plasmonic modes. The black solid line corresponds to the fitting of the angular derivative of the experimental reflectivity to the TMOKE curve for obtaining the $\Delta\theta$ parameter.

Special mention deserves the 380 nm SiO_2 (Co double series) structure. Figure VI.13.(a) shows the experimental TMOKE signal and the angular derivative for this structure. As it can be seen, while the agreement between both magnitudes is good for the SM mode, allowing the extraction of $\Delta\theta$, it is not so for the AM mode, and as a consequence an accurate value of $\Delta\theta$ can not be obtained using this method. This mismatch of the resonance shape between the angular derivative and the TMOKE signal for this mode is due to the sizeable TMOKE for this specific structure in the angular region containing this mode (i.e. without SPP excitation) and the low efficient light coupling to the mode. To clarify this interpretation, Transfer matrix simulations of Reflectivity and TMOKE curves for a particular sample with two MO identical Co layers (in order to simplify the system) have been performed (Fig. VI.13.(b)). Two TMOKE curves have been simulated with the two Co layers having identical optical constants and with either only one of them exhibiting MO activity (i.e. non null MO constants) or with the two layers having identical MO constants, labeled 1xMO and 2xMO in Fig.VI.13.(b), respectively. In the structure with only one MO active layer, the TMOKE curve exhibits two resonances related with the modulation of the two plasmonic modes. In clear contrast, the two resonances due to the excitation of both plasmonic modes are not observed (as we have explained in section VI.2. regarding the nonreciprocal modulation of the specular SPPs) for the system with two identical MO active layers. In fact, in this case there is a high MO activity in the angular region between the excitation of the modes, in qualitative agreement with the experimental curve shown in fig. VI.13.(a).

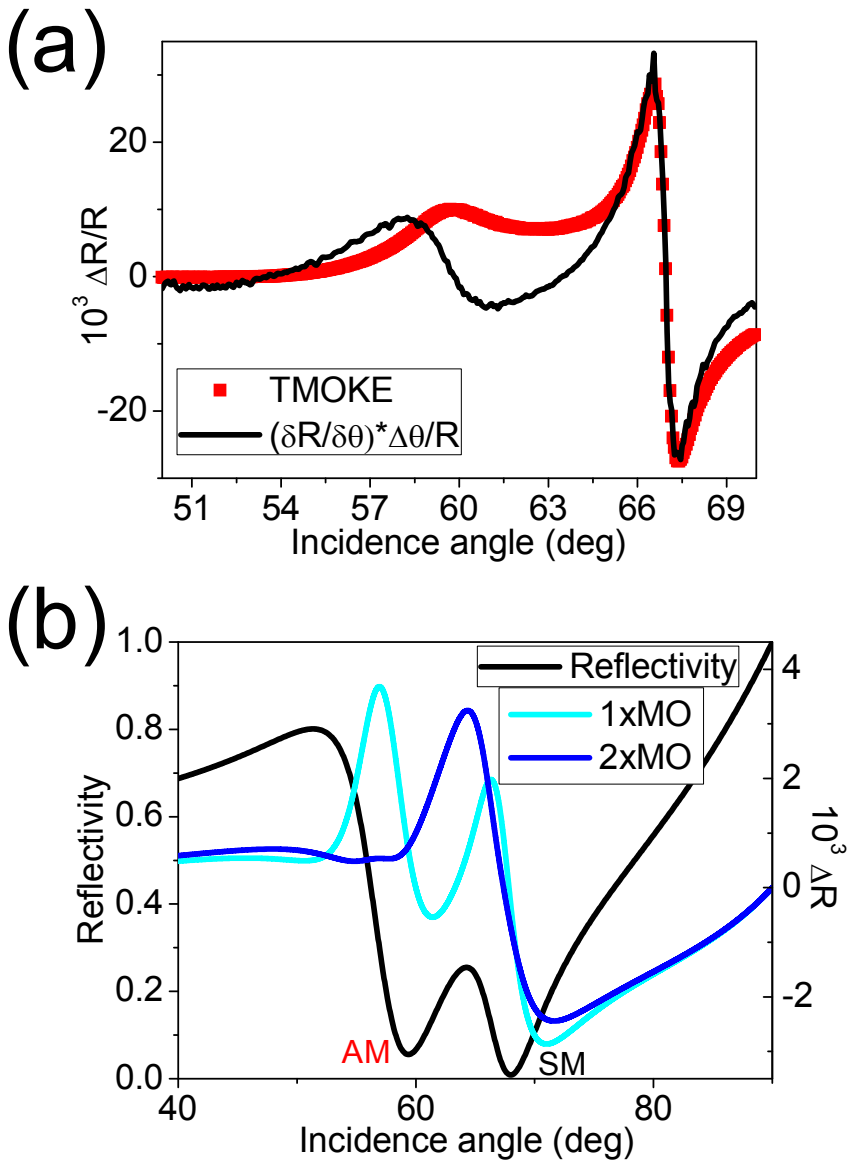

Figure VI.13. (a) Experimental TMOKE signal (red squares) does not fit with the angular derivative (black line) around the SPP resonance of the AM mode for the 380 nm SiO_2 sample of the Co double series. (b) Simulated Reflectivity (black curve) and TMOKE angular curves for this 380 nm SiO_2 sample with one (cyan curve) and two (blue curve) MO active Co layers.

Excluding this specific structure, the magnetic modulation of the surface plasmon wavevector has been determined with the above described procedure for all the other structures for the three magnetoplasmonic MIM cavities series. The obtained absolute values of SPP modulation are shown in Fig. VI.14. for both the antisymmetric and the symmetric MIM plasmonic modes. The symbols correspond to the experimental values, while the lines show the simulated ones. For the structures with only one Co layer, i. e. the Co down and Co up series, the AM modes of the MP-MIM cavities exhibit higher SPP modulation than the SM modes, especially at lower SiO_2 thickness; for instance more than three times at 180 nm SiO_2 thickness for the Co up series. Moreover, the modulation of the AM mode strongly increases with the reduction of the

SiO_2 thickness while that of the SM mode remains almost constant. We can explain this behavior with two main reasons related to the dispersion relations of the two modes. On the one hand, the wavevector of the AM mode exhibits a very dispersive behavior (see figure VI.10.) close to the cutoff thickness. Because of this, small modifications in the properties of the cavity can induce a strong change in the mode wavevector. In this way, the magnetic modulation of that AM mode is magnified compared to the SM one. On the other hand, the wavevector for the AM mode decreases with the SPP coupling (i.e. as the insulator width decreases) and therefore it loses its confinement inside the cavity. This loss leads to a spreading of the EM field into the metallic claddings (including the Co layer) for the AM mode. In contrast, the SM mode increases its wavevector remaining as a highly confined plasmonic mode for any insulator width whose EM field is well concentrated into the cavity core[5].

In the case of the Co double series, the magnetic modulation of the SPP wavevector is lower than that obtained for the series with only one Co layer, but both modes give non negligible modulation. This is in contrast to the null (for the AM mode) and almost null (for the SM mode) values expected for an ideal MIM cavity with two identical Co layers symmetrically positioned, as has been shown by the simulations in section VI.2. This apparent discrepancy can be ascribed to both the morphology of the Co layers (imposed by the SiO_2 growth) and the thickness structure (demanded for the Kretschmann configuration) that make that the actual samples of the Co double series are asymmetric. Therefore the distribution of the EM field intensity for each mode, which controls the magnetic modulation[17], is not exactly symmetric for the two Co layers inside the fabricated waveguide. Moreover, those two deposited Co layers show different optical and MO constants, as deduced above from the morphology and magnetic characterization. These different physical properties modify the magnetic modulation of the wavevector supported for each MO active layer, giving rise to an even stronger asymmetry. In other words: as the magnetic modulation of the plasmon at one metal-dielectric interface does not perfectly match that of the other interface, the system shows a net magnetic modulation of the modes. The simulations of the Co double series performed using the actual layer structure and the two sets of optical and MO constants mentioned in section VI.3. exhibit a good qualitatively agreement with the experiments. From these simulations it can also be seen that the observed magnetic modulation of the SPP wavevectors for the Co double series can be understood as the difference of the modulations obtained in the Co up and the Co down series, in accordance to the non-reciprocity argument exposed in section VI.2. (see Fig. VI.3.(b)). In fact, the bottom panel of figure VI.14. (Co double series) shows the calculated values of this difference between the two series with one Co layer compared to the modulation values for the Co double series. The modulation values are quite similar if we take into account the differences between the layer growth of the structures for the three series varying the position of the Co layer or adding another one.

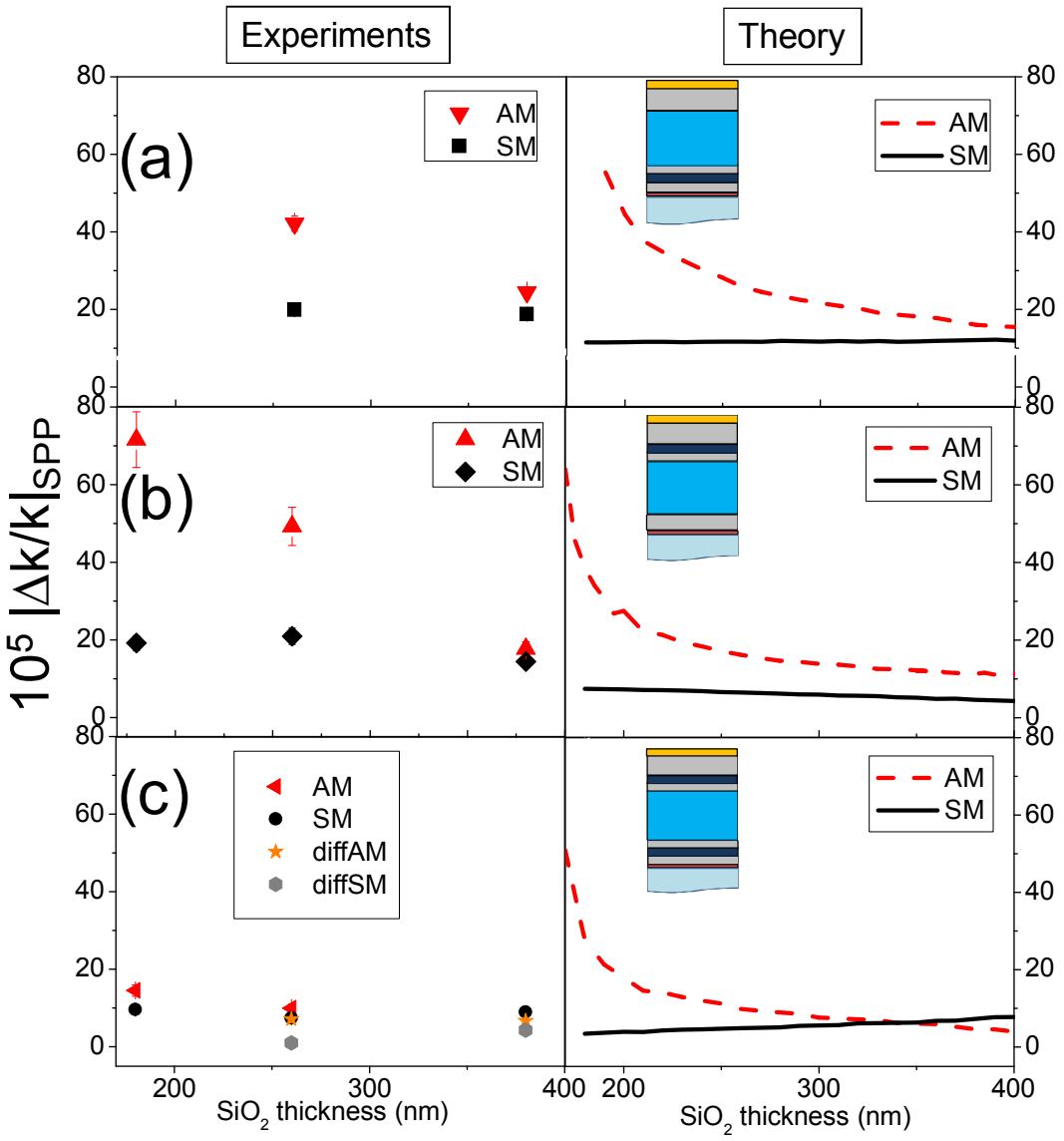

Figure VI.14. Experimental (left column of the figure) and simulated (right column of the figure) absolute values of the magnetic modulation of the SPP wavevector ($|\Delta k/k|_{SPP}$) as a function of SiO_2 thickness for AM (red triangles and dashed lines) and SM (black symbols and solid lines) plasmonic modes in Co down (a), Co up (b) and Co double (c) MP-MIM cavities. Moreover, the $|\Delta k/k|_{SPP}$ values of the Co double series are compared to the absolute difference of the Co down and Co up series experimental values for the AM (star symbols) and the SM modes (hexagonal symbols).

The trends of the measured magnetic modulation are well reproduced by the simulations for all the three series. The discrepancy about the actual values of the experiments and the theory is possibly caused by the differences between the actual optical, MO constants and thickness for the fabricated layers and the ones used in the simulations obtained from reference samples. It is worth to mention that our simulations have been performed with fixed parameters extracted from reference samples; therefore a perfect fitting between experiments and theory values is out of our possibilities. However, we can conclude that our study provides a comprehensive understanding of

the magnetic modulation achievable by the two modes present in a MP-MIM cavity and accessible in Kretschmann configuration, validated both experimentally and by means of transfer matrix simulations.

VI.6.- CONCLUSIONS

In this chapter, MP-MIM cavities have been designed, fabricated and characterized. A systematic study has been performed comparing the morphological, magnetic and magnetoplasmonic properties of these cavities as a function of both the SiO_2 thickness and the position of one or two Co layers for the MIM system. Experiments and simulations have shown the possibility of the magnetic modulation of the wavevector for the two AM and SM plasmonic modes. The differences in the dispersion relation of both modes, and thus on their confinement properties, give rise to a drastically different behavior for the magnetic modulation of the wavevector with the SiO_2 thickness: the modulation increases dramatically for the AM mode as the cavity gets narrower while it is almost constant for the SM mode. Moreover, there is at least a three times enhancement in the modulation for the AM mode compared to SM one at low SiO_2 thickness (180 nm). The strong modulation observed for the AM mode in a MIM configuration makes it an interesting alternative to be considered in plasmonic modulators or in magnetoplasmonic sensing configurations. Additionally, our results show that in a perfect symmetric MP-MIM cavity the modulation is cancelled, but that this modulation is not completely cancelled when some asymmetry is introduced in the cavity structure. However the high modulation values of the AM mode for the samples with only one Co layer (Co down and Co up series) could be also obtained in the Co double samples by simply applying a low magnetic field which would allow reaching the magnetization saturation for only one Co layer (remember that the Co layers present saturation of the magnetization at different magnetic fields for the samples of the Co double series). This would allow to magnetically switch between low and high modulation of the SPP wavevector in these MP-MIM structures with two Co layers.

VI.7.- REFERENCES

[1] K. J. Vahala, Nature **424**, 839–846 (2003).
[2] A. M. Armani, R. P. Kulkarni, S. E. Fraser, R. C. Flagan and K. J. Vahala, Science **317**, 783–787 (2007).
[3] S. A. Maier, Plasmonics: Fundamentals and Applications (Springer, Berlin, 2007).
[4] E. N. Economou, Phys. Rev. **182**, 539–554 (1969).
[5] J. A. Dionne, L. A. Sweatlock, A. Polman and H. A. Atwater, Phys. Rev. B **73**, 035407 (2006).
[6] R. Zia, M. D. Selker, P. B. Catrysse and M. L. Brongersma, J. Opt. Soc. Am. A **21**, 2442–2446 (2004).
[7] P. Ginzburg, D. Arbel, and M. Orenstein, Optics Letters **31**(22), 3288-3290 (2006).
[8] J. A. Dionne, H. J. Lezec and H. A. Atwater, Nano Lett. **6**, 1928– 1932 (2006).
[9] H. T. Miyazaki and Y. Kurokawa, Phys. Rev. Lett. **96**, 097401 (2006).
[10] S. A. Maier, Opt. Quantum Electron. **38**, 257–267 (2006).
[11] I. D. Rukhlenko, A. Pannipitiya, M. Premaratne, and G. P. Agrawal, Phys. Rev. B **84** 113409 (2011).

[12] P. Berini, Opt. Express **14**, 13030–13042 (2006).

[13] Slavík, R., Homola, J., & Vaisocherová, H. (2006). Advanced biosensing using simultaneous excitation of short and long range surface plasmons. *Measurement Science and Technology*, *17*(4), 932-938.

[14] Keathley, P. D., & Hastings, J. T. (2011). Nano-gap-Enhanced Surface Plasmon Resonance Sensors. *Plasmonics*, (April).

[15] B. Sepulveda, L. M. Lechuga and G. Armelles, Journal of Lightwave Technology **24**(2), 945-955 (2006).

[16] Y.-C. Lan and C.-M. Chen, Opt. Express **18**, 12470 (2010).
[17] Temnov, V. V., Armelles, G., Woggon, U., Guzatov, D., Cebollada, A., Garcia-martin, A., Thomay, T., et al. (2010). Active magneto-plasmonics in hybrid metal – ferromagnet structures. *Nature Photonics*, (January), 1-5.
[18] J. B. Khurgin, Appl. Phys. Lett. **89**, 251115 (2006).
[19] D. Weller, G. Harp, R. Farrow, A. Cebollada and J. Sticht, Phys. Rev. Lett. **72**(13), 2097–2100 (1994).

[20] Kretschmann and H. Raether, *Z. Naturforsch*. A 23, 2135 (1968); E. Kretschmann, *Z.Phys* .241, 313 (1971).
[21] H. Raether, *Surface Plasmons on Smooth and Rough Surfaces and on Gratings*, vol. 111 of *Springer Tracts in Modern Physics* (Springer-Verlag, Berlin, 1988).

[22] Meneses-Rodríguez, D., Ferreiro-Vila, E., Prieto, P., Anguita, J., González, M. U., García-Martín, J. M., Cebollada, A., et al. (2011). Probing the electromagnetic field distribution within a metallic nanodisk. *Small*, *7*(23), 3317-23.

Conclusions and future perspectives

Fully metallic MP multilayers:

- Ag/Co/Ag multilayers have been fabricated and characterized using two capping layers to protect the Ag and Co from the chemical reactions with room atmosphere. The 2 nm Pt capping layer has demonstrated a poor performance to maintain the magnetoplasmonic properties of the Ag/Co/Ag system. Nevertheless, the multilayers with a 5 nm Au capping layer have exhibited a high and sharp resonance of the MO activity with SPP excitation (in fact, better performance than previous Au/Co/Au trilayers) and a significant magnetic modulation of the SPP wavevector (almost equivalent to the Au/Co/Au trilayers). Moreover, these systems with Au capping layer maintain these magnetoplasmonic properties in ambient conditions for long periods of time (confirmed for up to two years). In contrast, the Ag/Co/Ag trilayer without any capping layer suffers important modifications after two years exposed to ambient conditions, losing its original magnetoplasmonic properties. Therefore the key role is the use of a capping layer with good optical properties and to completely avoid the chemical reactions inside the Ag/Co/Ag as it has been obtained for Au/Ag/Co/Ag.

- A systematic study comparing the structural, morphological, magnetic, optical, MO and magnetoplasmonic properties of epitaxial and polycrystalline Au/Fe/Au trilayers as a function of the Fe interlayer thickness has been carried out.We find a direct effect of the higher crystalline and interface quality of the epitaxial structures on the MO constants of Fe, which as a consequence gives rise to an increase in the MO activity without SPP excitation (threefold) and in the magnetic modulation of the SPP wavevector (twofold) with respect to their equivalent polycrystalline ones. On the other hand, the MO activity with SPP excitation mainly depends on the achievement of the exact layers thickness that leads to optimum Plasmon excitation, and as a consequence to a minimum in the reflectivity and a maximum in the TMOKE signal. From the SPP propagation length L_{SPP}, the $FoM \equiv (\Delta k \times L)_{SPP}$ can be defined and the optimized epitaxial structure exhibit double performance than the optimized polycrystalline one. Finally, the values of the optimized polycrystalline Au/Ag/Co/Ag structure were presented in order to evaluate the possibility of epitaxial Ag-based modulator studies.

Sensing applications:

- Regarding the sensing applications, we have shown how the different magnetoplasmonic (MP) multilayers developed along it have successfully been used as transducers in SPR and MOSPR configurations for the detection of alcohol vapours in air medium and the specific formation of antibody-protein complex in aqueous medium. Concerning the gas sensing experiments, an innovative GLAD TiO_2 porous layer has been used as sensing layer, showing a good performance for trapping methanol, ethanol and isopropanol molecules due to its high porosity (thus high surface/volume ratio). Moreover the MOSPR sensor demonstrates a higher sensitivity with respect to the SPR sensor using Au/Co/Au trilayer or Au film ("classical" SPR) as sensor transducers for the alcohol vapours detection. This higher sensitivity of the MOSPR sensor compared to the SPR one has also been confirmed in aqueous conditions for an immunological experiment. A protocol has been performed using thiol-based SAMs to bind the biomolecules with the top Au layer of the MP transducers. A BSA functionalized transducer has been used as sensing layer for the recognition of the antiBSA analyte. A typical saturation state has been achieved at high analyte concentrations (Langmuir isotherm behavior) for the response of SPR and MOSPR sensors. A Au/Ag/Co/Ag multilayer as MOSPR transducer has exhibited lower sensitivity compared to the Au/Co/Au transducer due to a possible partial oxidation of Ag and Co layers leading to a deterioration of the TMOKE angular curve. Besides, the normalized sensitivity is higher for the MOSPR sensor (Au/Co/Au as transducer) compared to the corresponding one for the "classical" SPR sensor (Au film as transducer).

Insulator-metal MP multilayers:

- Magnetoplasmonic-Metal-Insulator-Metal (MP-MIM) cavities have been designed, fabricated and characterized. A systematic study has been performed comparing the morphological, magnetic and magnetoplasmonic properties of these cavities as a function of both the SiO_2 thickness and the position of one or two Co layers for the MIM system. Experiments and simulations have shown the possibility of the magnetic modulation of the wavevector for the two AM and SM plasmonic modes. The differences in the dispersion relation of both modes, and thus on their confinement properties, give rise to a drastically different behavior for the magnetic modulation of the wavevector with the SiO_2 thickness: the modulation increases dramatically for the AM

mode as the cavity gets narrower while it is almost constant for the SM mode. Moreover, there is at least a three times signal enhancement in the modulation for the AM mode compared to SM one at low SiO_2 thickness (180 nm). The strong modulation observed for the AM mode in a MIM configuration makes it an interesting alternative to be considered in plasmonic modulators or in magnetoplasmonic sensing configurations. Additionally, our results show that in a perfect symmetric MP-MIM cavity the modulation is cancelled, but that this modulation is not completed cancelled when some asymmetry is introduced in the cavity structure. However, the high modulation values of the AM mode for the samples with only one Co layer (Co down and Co up series) could be also obtained in the Co double samples by using a low magnetic field, which allow reaching the magnetization saturation for only one Co layer (remember that the Co layers present saturation of the magnetization at different magnetic field for the samples of the Co double series). This would allow to magnetically switch between low and high modulation of the SPP wavevector in these MP-MIM structures with two Co layers.

Appendix I

The role of a buffer seed layer

The importance of both a capping layer with good performance for the protection of the Ag/Co/Ag trilayers and the interface roughness of a ferromagnetic layer for the magnetic modulation of the SPP wavevector in Au/Fe/Au trilayers has been shown in chapter III and IV, respectively.

On one hand, the capping layer thickness is dependent of the surface roughness. It means that a complete coverage of a flatten Ag/Co/Ag surface can be achieved with thinner capping layers. This thinner capping layers leads to systems with SPP resonances closer to the Ag/Co/Ag ones and with flatten surfaces that leads to sharper SPP resonances with lower optical scattering[1].

On the other hand, the flatness of the first Au or Ag layer promotes the subsequent growth of a ferromagnetic layer with lower interface roughness, and therefore with higher effective MO constants[2]. Moreover, the implementation of these magnetoplasmonic multilayers as sensor transducers needs multilayers firmly attached to the glass substrates. They have to be resistant to aggressive substances in aqueous conditions.

A method to improve the surface flatness and multilayer adherence to the substrates is the deposition of a thin buffer layer into the glass substrate prior the Ag/Co/Ag deposition. The most common buffer layers used are 2 nm of Ti or Cr: such layers exhibit similar performance. The 2 nm Ti buffer layer was used for sensing applications and for the MP-MIM cavities in chapter V and VI, respectively.

In the following, we will study the surface roughness of a Ag thin film using a Cr buffer layer. The figure A1.1. shows the surface morphology (via AFM measurements) of two 7 nm Ag layers deposited with and without a 2 nm Cr buffer layer over BK7 glass substrates. The Ag film without buffer layer grows with a high grain size (the mean grain height observed in the AFM profile is around 20 nm) over the glass substrate. In contrast, the Ag film deposited over the 2nm Cr/Glass system grows in form of smaller grains (the grain height observed is about 3 nm). Therefore we can conclude that the use of a buffer layer improves the surface flatness of a Ag film deposited over a glass substrate, which is advantageous for the performance of the Au/Ag/Co/Ag structures and the interlayer flatness of the ferromagnetic layers (which gives rise to higher effective MO constants) studied in this thesis work.

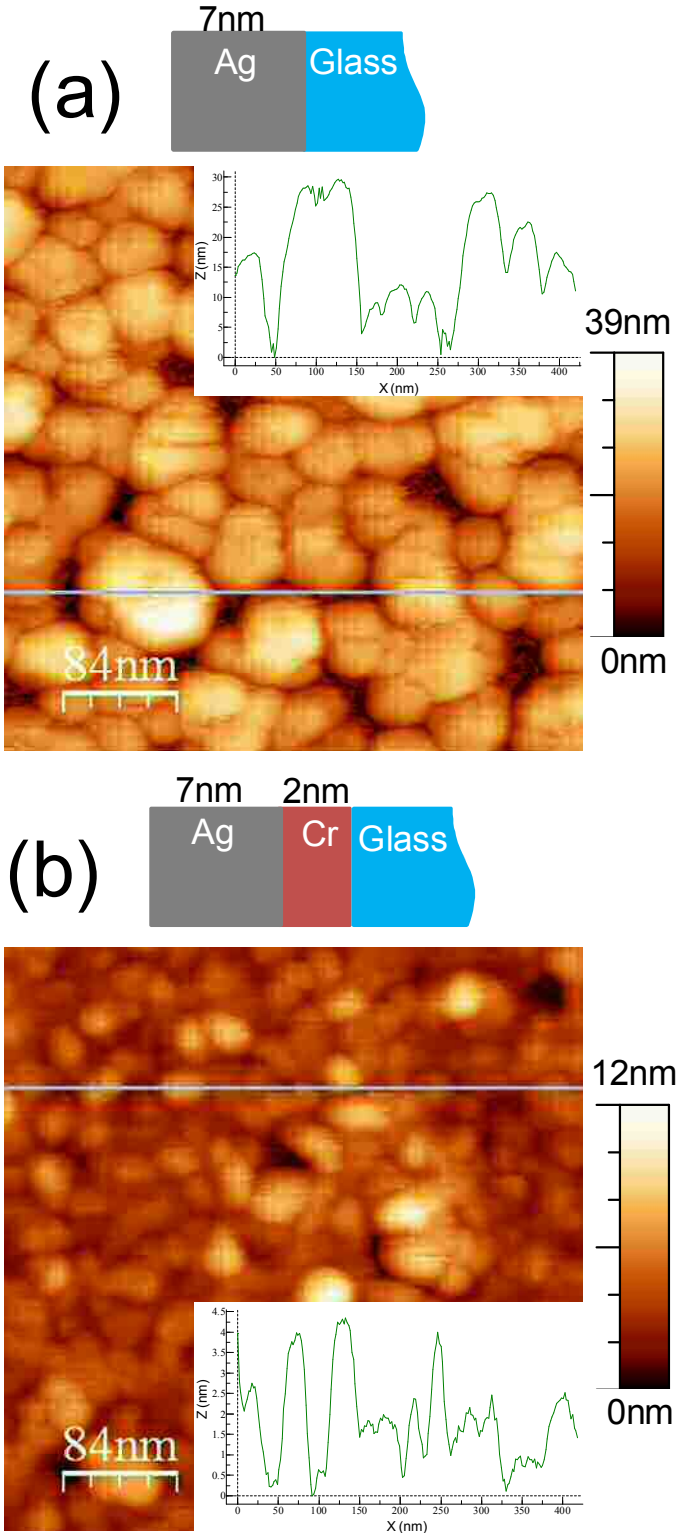

Fig. AI.1. AFM images of the 7 nm Ag sample without buffer layer (a) and 7 nm Ag/2 nm Cr buffer layer (b). The insets of the respective figures show the AFM profiles taken along the mark indicated in the AFM image.

References

[1] Liu, H., Wang, B., Leong, E. S. P., Yang, P., Zong, Y., Si, G., Teng, J., et al. (2010). Enhanced surface plasmon resonance on a smooth silver film with a seed growth layer. *ACS nano*, *4*(6), 3139–3146.

[2] Ferreiro-Vila, E., Iglesias, M., Paz, E., Palomares, F., Cebollada, F., González, J., Armelles, G., et al. (2011). Magneto-optical and magnetoplasmonic properties of epitaxial and polycrystalline Au/Fe/Au trilayers. *Physical Review B*, *83*(20), 1-8.

Appendix II

The Transfer Matrix Method

The optical and MO response of a multilayered structure formed by an indeterminate number of layers with isotropic or anisotropic dielectric constants can be simulated using a numerical method. This is the Transfer Matrix method (TMM)[1,2]. As an important application, the determination of actual MO constants for a magnetic layer inside in a multilayered system method will be explained using both this formalism and the experimental Polar Kerr spectra of the multilayer system at the end of the appendix.

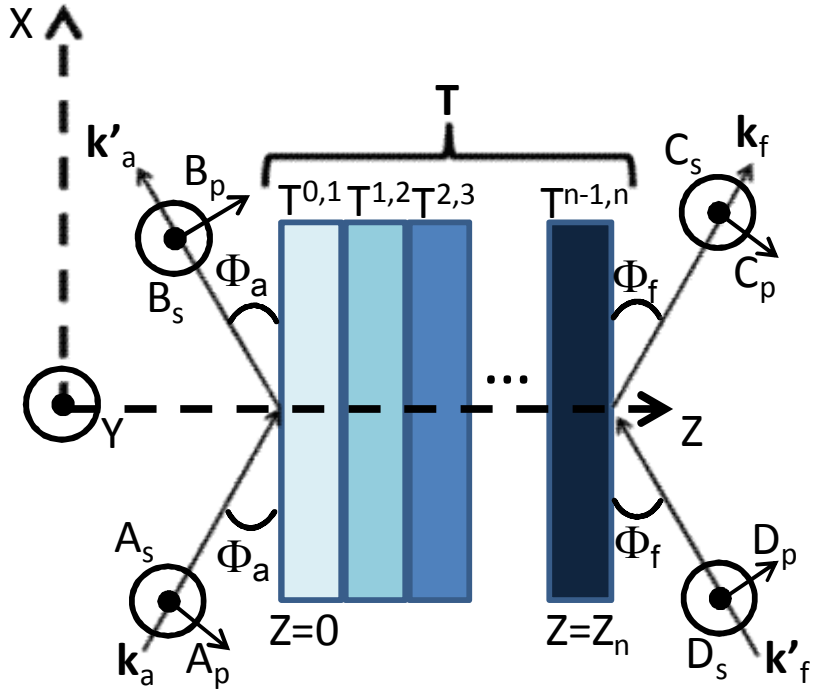

Figure AII.1. Sketch of a multilayer with *n* layers. The incident, reflected and transmitted waves are characterized by their p and s polarization vectors, angles and wavevectors.

We can consider an incident plane electromagnetic wave impinging at an angle Φ_a over a multilayered structure with parallel interfaces. It can be described by its p and s polarizations (A_p and A_s) and wave vector $\mathbf{k_a}$. We suppose that there is no incident light from the right side of the system (D_p=0 and D_s=0). Thus the p and s components of the reflected (B_p and B_s) and transmitted (C_p and C_s) waves can be treated in form of the Transfer matrix:

$$\begin{pmatrix} A_s \\ B_s \\ A_p \\ B_p \end{pmatrix} = \mathrm{T} \begin{pmatrix} C_s \\ 0 \\ C_p \\ 0 \end{pmatrix} \rightarrow \begin{pmatrix} T_{11} & T_{12} & T_{13} & T_{14} \\ T_{21} & T_{22} & T_{23} & T_{24} \\ T_{31} & T_{32} & T_{33} & T_{34} \\ T_{41} & T_{42} & T_{43} & T_{44} \end{pmatrix} \qquad [\mathrm{AII.1}]$$

Using this Transfer matrix, we can get the complex reflection coefficients of the optical system:

$$\mathbf{r}_{ps} = \left(\frac{B_s}{A_p}\right)_{A_s=0} = \frac{T_{13}T_{21} - T_{11}T_{23}}{T_{13}T_{31} - T_{11}T_{33}} \qquad \text{[AII.2a]}$$

$$\mathbf{r}_{pp} = \left(\frac{B_p}{A_p}\right)_{A_s=0} = \frac{T_{13}T_{41} - T_{11}T_{43}}{T_{13}T_{31} - T_{11}T_{33}} \qquad \text{[AII.2b]}$$

With the complex reflection coefficients, we can obtain the complex Kerr rotation and TMOKE signal as they have been defined in Chapter II:

$$\theta_k^p + i\varepsilon_k^p = \frac{\mathbf{r}_{sp}}{\mathbf{r}_{pp}}$$
$$\theta_k^s + i\varepsilon_k^s = \frac{\mathbf{r}_{ps}}{\mathbf{r}_{ss}} \qquad \text{[II.15]}$$

$$\frac{\Delta R_{pp}}{R_{pp}} = \frac{R_{pp}(+M_s) - R_{pp}(-M_s)}{2R_{pp}(0)} = \frac{\left|\mathbf{r}_{pp}(+M_s)\right|^2 - \left|\mathbf{r}_{pp}(-M_s)\right|^2}{2\left|\mathbf{r}_{pp}(0)\right|^2} \qquad \text{[II.9]}$$

The only step missing is the calculation of the Transfer matrix itself. We define the Maxwell equations in form of the in-plane components of the electric and magnetic field:

$$\partial_z \Psi(z) = ik_0 \Delta \Psi(z), \quad \Psi(z) = \left(E_x, E_y, H_x, H_y\right)^T(z) \qquad \text{[AII.3]}$$

where we have assumed harmonic time dependence for the electromagnetic fields and also a homogeneous non-diagonal dielectric tensor (containing the polar and transversal MO constants), being the Δ matrix defined as:

$$\Delta = \begin{pmatrix} k_x \varepsilon_{xz}/\varepsilon_{zz} & 0 & 0 & 1 - k_x^2/\varepsilon_{zz} \\ 0 & 0 & -1 & 0 \\ \varepsilon_{xy} & k_x^2 - \varepsilon_{xx} & 0 & 0 \\ \varepsilon_{xx} + \varepsilon_{xz}^2/\varepsilon_{zz} & \varepsilon_{xy} & 0 & -k_x \varepsilon_{xz}/\varepsilon_{zz} \end{pmatrix} \qquad \text{[AII.4]}$$

Now we need to use the matching conditions at each interface:

$$\Psi(z+d) = e^{i\omega\Delta d/c}\Psi(z) = T_p \Psi(z) \qquad \text{[AII.5]}$$

The matrix T_p relates the in-plane components of the electric and magnetic fields at a given interface. Applying the Cayley-Hamilton theorem[3], T_p can be expressed in a series expansion up to the power of n-1, being n the rank of the matrix:

$$T_p = e^{i\omega\Delta d/c} = \beta_0 I + \beta_1 \Delta + \beta_2 \Delta^2 + \beta_3 \Delta^3 \qquad [AII.6]$$

where β_i must obey the next condition:

$$e^{i\omega q_k d/c} = \sum_{j=0}^{3} \beta_j q_k^j, \quad k = 1,...,4 \qquad [AII.7]$$

being q_i the eigenvalues of the matrix Δ . Therefore, the total transfer matrix T can be constructed simply by a sequential multiplication of the partial transfer matrices at each interface:

$$\begin{pmatrix} A_s^i \\ B_s^i \\ A_p^i \\ B_p^i \end{pmatrix} = T_p^{i,i+1} \begin{pmatrix} C_s^{i+1} \\ D_s^{i+1} \\ C_p^{i+1} \\ D_p^{i+1} \end{pmatrix} \rightarrow \begin{pmatrix} A_s^0 \\ B_s^0 \\ A_p^0 \\ B_p^0 \end{pmatrix} = T_p^{0,1} \begin{pmatrix} C_s^1 \\ D_s^1 \\ C_p^1 \\ D_p^1 \end{pmatrix} = T_p^{0,1} T_p^{1,2} \begin{pmatrix} C_s^2 \\ D_s^2 \\ C_p^2 \\ D_p^2 \end{pmatrix} = ... = T_p^{0,1} ... T_p^{n-1,n} \begin{pmatrix} C_s^n \\ 0 \\ C_p^n \\ 0 \end{pmatrix}$$

$$T = L_a^{-1} \left[\prod_{i=1}^{n} T_p^{i-1,i} \right] L_f \qquad [AII.8]$$

where L_a and L_f are the projection of the in-plane components of the incident/reflected and transmitted waves through to the first and last interfaces

$$L_a^{-1} = \frac{1}{2} \begin{pmatrix} 0 & 1 & -n_a^{-1} \cos^{-1} \Phi_a & 0 \\ 0 & 1 & n_a^{-1} \cos^{-1} \Phi_a & 0 \\ \cos^{-1} \Phi_a & 0 & 0 & n_a^{-1} \\ -\cos^{-1} \Phi_a & 0 & 0 & n_a^{-1} \end{pmatrix} \qquad [AII.9]$$

$$L_f = \begin{pmatrix} 0 & 0 & \cos \Phi_f & 0 \\ 1 & 0 & 0 & 0 \\ -n_f \cos \Phi_f & 0 & 0 & 0 \\ 0 & 0 & n_f & 0 \end{pmatrix} \qquad [AII.10]$$

It is worth to mention that the transfer matrix method is a suitable tool to determine the MO constants of a MO active layer inside a multilayer structure. In this thesis, this method has been used for the extraction of the actual MO constants for a Co layer in a Au/Co bilayer (see chapter III section 4.D.) and for epitaxial and polycrystalline Fe layers in a Au/Fe/Au/Fe multilayer (see chapter IV section 6). Previously, it is necessary to know the optical constants of each layer, obtained from elipsometric measurements (see chapter II.4.), and the experimental rotation and ellipticity spectra (see chapter II.5.) of the multilayered system. The determination is based in the fact that, in a first approximation, the MO signal of the multilayer is linearly proportional to the real and imaginary parts of the MO constants of the MO active layer, i.e., the MO activity can be expressed as:

$$\theta(\lambda) = A(\lambda)\varepsilon_1^{xy}(\lambda) + B(\lambda)\varepsilon_2^{xy}(\lambda) \quad \text{[AII.11a]}$$

$$\phi(\lambda) = C(\lambda)\varepsilon_1^{xy}(\lambda) + D(\lambda)\varepsilon_2^{xy}(\lambda) \quad \text{[AII.11b]}$$

where the factors A, B, C and D are wavelength dependent and express the contribution of the real and imaginary parts of ε^{xy} to the rotation and ellipticity. These expressions represent a system of equations with two unknown parameters, which may be solved if the latter factors are deduced.

It is worth noticing that this approximation is reliable only if these factors are low enough. One method to prove the linearity is to simulate some MO signals of the system, in which the MO constants are: exclusively real (ε^{xy}=0.1), exclusively imaginary (ε^{xy}=0.1i), or a addition of them (ε^{xy}=0.1+0.1i). If the sum of the two first MO signals is equal to that of the last one, then the approximation is reliable. If not, it shows that the non linear terms cannot be neglected.

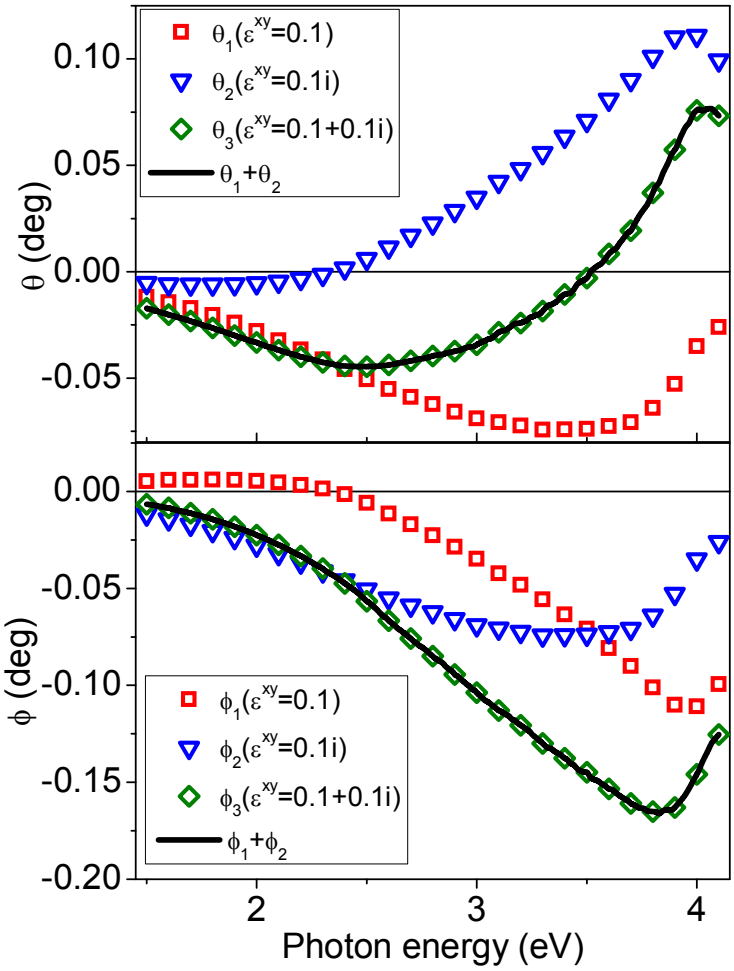

Figure AII.2. Simulated (a) Kerr rotation θ and (b) ellipticity ϕ spectra for an 5 nm Au/5 nm Ag/6 nm Co/6.6 nm Ag/2 nm Ti/BK7 glass substrate multilayered structure and using the next MO constants for the Co layer:ε^{xy}=0.1 (red squares), ε^{xy}=0.1i (blue triangles) and ε^{xy}=0.1+0.1i (green diamonds). The black line shows the sum of the two first spectra.

An example can be seen in figure AII.2., where we show the simulated Kerr rotation θ (a) and ellipticity ϕ (b) spectra for an 5 nm Au/5 nm Ag/6 nm Co/6.6 nm Ag/2 nm Ti/BK7 glass substrate multilayered structure and using the next MO constants for the Co layer: ε^{xy}=0.1 (red squares), ε^{xy}=0.1i (blue triangles) and ε^{xy}=0.1+0.1i (green diamonds). The black line shows the sum of the two first spectra (the exclusive real and imaginary MO constants). It can be observed that the linear dependence of the rotation and ellipticity on the real and imaginary parts of ε^{xy} is verified.

Under these conditions we have a way to obtain the spectral dependence of the A, B, C and D factors. As they depend on the structure, but not in the MO activity, they may be obtained through the calculated spectra for the ε^{xy}=0.1 and ε^{xy}=0.1i MO constants:

$$A(\lambda)=\frac{\theta_1(\varepsilon^{xy}=0.1)}{0.1} \quad \text{[AII.12a]} \qquad B(\lambda)=\frac{\theta_2(\varepsilon^{xy}=0.1i)}{0.1} \quad \text{[AII.12b]}$$

$$C(\lambda)=\frac{\phi_1(\varepsilon^{xy}=0.1)}{0.1} \quad \text{[AII.12c]} \qquad D(\lambda)=\frac{\phi_2(\varepsilon^{xy}=0.1i)}{0.1} \quad \text{[AII.12d]}$$

Finally, once these factors have been obtained, we can determine the real (ε^{xy}_1) and imaginary (ε^{xy}_2) parts of the MO constants using the equation [AII.11] and the experimentally acquired rotation (θ_{exp}) and ellipticity (ϕ_{exp}) spectra:

$$\varepsilon_1^{xy}(\lambda)=\frac{B\phi_{exp}-D\theta_{exp}}{BC-AD} \quad \text{[AII.13a]}$$

$$\varepsilon_2^{xy}(\lambda)=\frac{C\theta_{exp}-A\phi_{exp}}{BC-AD} \quad \text{[AII.13b]}$$

References

[1]Schubert, M. (1996). Polarization-dependent optical parameters of arbitrarily anisotropic homogeneous layered systems. *Physical review. B, Condensed matter*, *53*(8), 4265-4274.

[2] Schubert, M., Tiwald T. E. and Woollam J. A. (1999). Explicit solutions for the optical properties of arbitrary magneto-optic materials in generalized ellipsometry. Appl. Opt. 38, 177.

[3] Wöhler H., Fritsch M., Haas G. and Mlynski D. A.(1988). Faster 4x4 matrix method for uniaxial inhomogeneous media. J. Opt. Soc. Am. A 5, 1554.

List of publications:

Publications directly related with this thesis:

1. **E.Ferreiro**, X.Bendaña, J.B.González-Díaz, A.García-Martín, J.M.García-Martín, A. Cebollada, G.Armelles, D.Meneses-Rodríguez, E.Muñoz-Sandoval. "Surface plasmon resonance effects in the magneto-optical activity of Ag/Co/Ag trilayers." IEEE Transactions on Magnetics, Vol. 44 nº.11 (2008) 3303-3306. **DOI: 10.1109/TMAG.2008.2002381**

2. **E.Ferreiro-Vila**, J.B.González-Díaz, R.Fermento, M.U.González, A.García-Martín, J.M.García-Martín, A.Cebollada, G.Armelles, D.Meneses, and E.Muñoz Sandoval. "Intertwined magneto-optical and plasmonic effects in Ag/Co/Ag layered structures" Physical Review B, 80 (2009) 125132. **DOI: 10.1103/PhysRevB.80.125132**

3. G. Armelles, A. Cebollada, A. García-Martín, J. M. García-Martín, M. U. González, J. B. González-Díaz, **E. Ferreiro** and J. F. Torrado. "Magnetoplasmonic nanostructures: systems supporting both plasmonic and magnetic properties." Journal of Optics A: Pure and Applied Optics, 11 (2009) 114023. **DOI:10.1088/1464-4258/11/11/114023**

4. **E. Ferreiro-Vila**, M. Iglesias, E. Paz, F. J. Palomares, F. Cebollada, J. M. González, G. Armelles, J. M. García-Martín, and A. Cebollada "Magneto-optical and magnetoplasmonic properties of epitaxial and polycrystalline Au/Fe/Au trilayers" Physical Review B, 83 (2011) 205120 **Editor's suggestion. DOI: 10.1103/PhysRevB.83.205120**

5. M. G. Manera, G. Montagna, **E. Ferreiro-Vila**, L. González-García, J. R. Sánchez-Valencia, A. R. González-Elipe, A. Cebollada, J. M. Garcia-Martin, A. Garcia-Martin, G. Armelles and R. Rella "Enhanced gas sensing performance of TiO_2 functionalized magneto-optical SPR sensors" Journal of Material Chemistry, 21 (2011) 16049. **DOI: 10.1039/c1jm11937k**

6. **E. Ferreiro-Vila**, J. B. González-Díaz, G. Armelles, A. Cebollada, J. M. García-Martín, and M. U. González "Magnetic modulation for symmetric and antisymmetric modes in a MIM magnetoplasmonic cavity". In preparation.

Other publications:

1. E. Th. Papaioannou, V. Kapaklis, P. Patoka, M. Giersig, P. Fumagalli, A. Garcia-Martin, **E. Ferreiro-Vila**, G. Ctistis. "Magneto-optic enhancement and magnetic properties in Fe antidot films with hexagonal symmetry" Physical Review B, 81 (2010) 054424. **DOI: 10.1103/PhysRevB.81.054424**

2. David Meneses-Rodríguez, **Elías Ferreiro-Vila**, Patricia Prieto, José Anguita, María U. González, José M. García-Martín, Alfonso Cebollada, Antonio García-Martín, and Gaspar Armelles "Probing the Electromagnetic Field Distribution within a Metallic Nanodisk" Small, 7 nº23 (2011) 3317-3323**. DOI: 10.1002/smll.201101060**

3. D. Meneses-Rodríguez, **E. Ferreiro-Vila**, J. C. Banthí, P. Prieto, J. Anguita, A. García-Martín, M. U. González, J. M. García-Martín, A. Cebollada, and G. Armelles "Internal electromagnetic field distribution and magneto-optical activity of metal and metal-dielectric magnetoplasmonic nanodisks" eNanonewsletter nº23 p22-24 (October 2011)

4. M. G. Manera, **E. Ferreiro-Vila**, A. Cebollada, J. M. Garcia-Martin, A. Garcia-Martin, G. Giancane, L. Valli and R. Rella "Spectroscopic, Morphologic and Magneto-Optical Surface Plasmon Resonance of ethane-bridged Zn porphyrins dimers in Langmuir-Schäfer thin film for sensing applications" accepted for publication in the Journal of Physical Chemistry.